GALACTIC STAR FORMING REGIONS AND YOUNG STELLAR OBJECTS

A thesis
submitted for the degree of
Doctor of Philosophy

In
The Faculty of Science
University of Calicut, Calicut

by
MAHESWAR GOPINATHAN

Indian Institute of Astrophysics
Bangalore 560 034, INDIA
2005

To my PARENTS...

DECLARATION

I hereby declare that the matter contained in this thesis is the result of the investigations carried out by me at the Indian Institute of Astrophysics, Bangalore, under the supervision of Prof. H. C. Bhatt. This thesis has not been submitted for the award of any degree, diploma, associateship, fellowship etc. of any university or institute.

Prof. H. C. Bhatt	Maheswar Gopinathan
(Thesis Supervisor)	(Ph.D. Candidate)

Indian Institute of Astrophysics
Bangalore 560 034, INDIA
February, 2005

CERTIFICATE

This is to certify that the thesis entitled **"Galactic Star Forming Regions and Young Stellar Objects"** submitted to the University of Calicut by Mr. Maheswar Gopinathan for the award of the degree of Doctor of Philosophy in the faculty of Science, is based on the results of the investigations carried out by him under my supervision and guidance, at the Indian Institute of Astrophysics, Bangalore. This thesis has not been submitted for the award of any degree, diploma, associateship, fellowship etc. of any university or institute.

Prof. H.C. Bhatt
(Thesis Supervisor)

Indian Institute of Astrophysics
II Block, Koramangala
Karnataka
February, 2005

ACKNOWLEDGMENTS

It is a pleasure to thank the many people who made this thesis possible.

It is difficult to overstate my gratitude to my Ph.D. supervisor, Prof. H. C. Bhatt. With his enthusiasm, his inspiration, and his great efforts to explain things clearly and simply, he helped to make astronomy and astrophysics fun for me. Throughout my PhD period, he provided encouragement, sound advice, good teaching, good company, lots of good ideas and above all showed immence patience. I would have been lost without him.

I would like to thank the Head of the Physics department, University of Calicut, Prof. B. R. S. Babu, for his valuable advices and suggestions. I am very much grateful to him for his help during registration, conduction of the Pre-PhD examination and other formalities.

I would like to thank the many people who have taught me physics, especially, my graduate and post-graduate teachers, Dr. Vasudevan Nair and Dr. Mohana Kumaran Nair. I would also like to thank the many people who have taught me astrophysics, especially, all my course work teachers.

I thank Prof. J. H. Sastri, Acting Director of the Indian Institute of Astrophysics, and all the Board of Graduate Studies members, for providing the necessary facilities required for pursuing this study. I also thank my doctoral committee members, Dr. Raveendran, Dr. Mekkaden and Dr. Sushma Mallik for their timely advices and suggestions.

I am grateful to all the observing staffs at Kavalur, especially, Mr. Selvakumar, Mr. Appakutty and Mr. Moorty. I thank all the electonics, electrical and mechanical staffs at Kavalur for their support and help.

I thank the IIA library staff, and the Librarian Ms. Cristina Birdi for providing all the assistance required in making the books and journals available for reference. I thank Mr. J. S. Nathan and Mr. Baba Varghese for all the help they have provided to me whenever I encountered problems with the computers. I thank the staffs of the binding section, Mr. Kanagaraj and Mr. Thyagaraja for preparing the bound copies of the thesis.

All my friends at IIA have made working here an enjoyable experience, and I sincerely appreciate all that they have done. I thank Manoj, a senior, a friend, who introduced me for the first time to the wonderful world of Star Formation and with whom I made my first observations at Kavalur. Thank you Manoj !

I thank my beloved seniors, especially, Rajesh, Sivarani, Arun, Dilip, Suresh, Dharam and Preeti for giving me advices and wounderful company. I also thank all my batchmates for giving me company and help. I thank Ravinder for all those special sessions. I thank all my juniors especially those who play cricket with me.

I would like to thank Raji and Raja for caring me like a brother. A special thanks to Dr. Partho and Dr. Muneer.

I wish to thank three of my best friends, Kishore, Resmi and Vinod, for helping me get through the difficult times, and for all the emotional support, comraderie, entertainment, and caring they provided.

I thank Gopan chetan and Manju chechi for providing me with all the facilities that I required initially. Their help and support can not be forgotten.

Finally, I thank my family members for their support and encouragement. I thank Ajith chetan, who is more than a brother to me, Raji chechi and chichu for their love and care. I thank my in-laws for their support. I am extremely grateful to my parents for their wholehearted encouragement and support. I take this opportunity to thank my parents for letting me choose Astornomy & Astrophysics as my career. At the end, a Big "Thank You" to my wife, Swapna, for *everything*.

LIST OF PUBLICATIONS

- **Refereed publications**

  1. Photometric distances to dark clouds: Cometary globules CG 12, **Maheswar, G.**, Manoj, P., Bhatt, H. C., 2004, MNRAS, 355, 1272
  2. Magnetic Fields in cometary globules - III: CG12, H. C. Bhatt., **Maheswar, G.**, Manoj, P., 2004, MNRAS, 348, 83
  3. Optical spectroscopic and 2MASS measurements of Stephenson H_α stars, **Maheswar, G.**, Manoj, P., Bhatt, H. C., 2003, A&A, 402, 963.
  4. Circumstellar disks around Herbig Ae/Be stars: Polarization, outflows and binary orbits, **Maheswar, G.**, Manoj, P., Bhatt, H. C., 2002, A&A, 387, 1003
  5. Non-emission-line young stars of intermediate mass, Manoj, P., **Maheswar, G.**, Bhatt, H. C., 2002, MNRAS, 334, 419

- **Conference proceedings**

  1. Intermediate galactic latitude starforming region-CG 12, **Maheswar, G.**, Manoj, P., Bhatt, H. C., 2002, BASI, 30, 651
  2. Circumstellar environment around young stars in nearby OB associations, Manoj, P., **Maheswar, G.**, Bhatt, H. C., 2002, BASI, 30, 657

- IRAS 05436-0007, Maheswar, G., Bhatt, H. C., 2004, IAUC, 8295, 3

Table of Contents

List of Tables

List of Figures

GALACTIC STAR FORMING REGIONS AND YOUNG STELLAR OBJECTS

Chapter 1

Introduction

1.1 Star formation - An Overview

The physics of star formation determines the conversion of gas to stars. Stars are the primary constituents of galaxies, the most fundamental building blocks of the Universe, and yet the processes by which stars form are not well understood. Nearly all the luminous mass in the Galaxy, some $10^{11}M_\odot$, is in stars which formed billions of years ago. Star formation is a complex problem and this thesis deals with a small part of the question: how do stars form? Knowledge of the processes by which these stars are formed is essential to understand the structure and evolution of a galaxy, which depend on the environment in which stars form, the star formation rate, and their mass spectrum.

Stars are observed to be forming in dense regions of the interstellar medium, the molecular clouds, which are found to be strongly self-gravitating. The molecules in these self-gravitating clouds are formed when most of the background stellar ultraviolet radiation is absorbed owing to the high opacity due to dust. The exclusion of background starlight removes the heat input to the cloud and the cloud temperature drops from a typical value of $\sim$ 80K in a transparent cloud to $\lesssim$ 10K in an opaque cloud. H_2 and CO molecules are found to occur in regions where A_V exceeds $\approx$ 0.5 mag (Spitzer & Jenkins 1975; Bally & Langer 1982). About half the mass of the interstellar medium is contained in these high density or high opacity molecular clouds (10^9 $M_\odot$), most of which is in the form of hydrogen molecules. H_2 is the most abundant molecule in molecular clouds. However, H_2 is not easily observed because it does not radiate well from its lower rotational level owing to the absence of permanent electronic dipole moment. Cold molecular hydrogen in star forming regions has been recognized only by collisional excitation of other molecules. These molecular clouds constitute about one percent of the total mass of our Galaxy where new stars are forming at an estimated rate of $\sim 1 M_{\odot}\ yr^{-1}$. Molecular clouds, the birth places of stars within our Galaxy, fall into two categories:

- *Dark (or Dwarf) molecular clouds (DMCs)*
- *Giant Molecular Cloud (GMCs)*

Table 1.1: Physical characteristics of molecular clouds in the interstellar medium.

	Hot core	Warm clump	Cloud	Complex
Giant Molecular Clouds (GMCs)				
Mass ($M_{\odot}$)	$10 - 10^3$	$1 - 10^3$	$10^3 - 10^5$	$10^5 - 10^6$
Density (cm^{-3})	$10^7 - 10^9$	$10^4 - 10^7$	$10^2 - 10^4$	100-300
Temp (K)	100-200	25-70	$\gtrsim 20$	15-20
ΔV ($km\ s^{-1}$)	1-10	1-3	3-12	6-15
A_V (mag)	50-1000	5-1000	$\gtrsim 2$	1-2
Size (pc)	0.05-1	0.05-3	3-20	20-80
Dark Molecular Clouds (DMCs)				
Mass ($M_{\odot}$)		0.3-10	$10 - 10^3$	$10^3 - 10^4$
Density (cm^{-3})		$10^4 - 10^5$	$10^2 - 10^4$	$10^2 - 10^3$
Temp (K)		≈ 10	$\gtrsim 10$	$\gtrsim 10$
ΔV ($km\ s^{-1}$)		0.2-0.4	0.5-1.5	1-3
A_V (mag)		5-25	2-5	1-2
Size (pc)		0.05-0.4	0.2-4	6-20
Bok Globules (BGs)				
Mass ($M_{\odot}$)			5-500	
Density (cm^{-3})			$10^3 - 10^4$	
Temp (K)			10-20	
ΔV ($km\ s^{-1}$)			1-3	
A_V (mag)			1-25	
Size (pc)			0.1-2	

The cold and dark (or dwarf) molecular clouds are visible as dark patches in the sky, and have a complex morphology. The giant molecular clouds also have a complex morphology but differ from DMCs in their spatial distribution and in their physical properties. GMCs are distributed along the spiral arms of the Galaxy and have a typical life time of about a few 10^7 years. DMCs on the other hand are distributed throughout the galactic disk. Because they are not restricted to the spiral arms of the Galaxy, they can probably survive one or more galactic rotations and thus have lifetimes of 100 million years or more. The characteristic physical properties of DMCs and GMCs are given in

Table 1.1. Observations of these molecular clouds in CO and other higher density tracers (H_2CO & NH_3) showed that structurally they are not uniform but are always composed of numerous dense clumps which have a range of geometries from spherical to highly filamentary. These clumps or cores[1] are the sites of low mass star formation in the case of DMCs and massive stars in the case of GMCs. Cores in GMCs are found to be more massive and warmer than those in DMCs.

Observations of dense gas and associated young stellar objects (YSOs) in the nearest molecular clouds have revealed at least two modes or environments of star formation. In two of the well studied nearby DMCs, Taurus and ρ Ophiuchus, Taurus represents an isolated or distributed mode of star formation characterized by low stellar densities and low overall star formation efficiency. In contrast, clustered star formation, characterized by high stellar densities and high star formation efficiency is occurring in the ρ Ophiuchus cloud. In the nearest and well studied giant molecular cloud, Orion, most of the molecular material is concentrated in two large clouds, Orion A (L1641) and Orion B (L1630). While both clustered and isolated modes of star formation are occurring in L1641, clustered mode of star formation is dominant in L1630 molecular cloud (Lada, Strom, Myers 1993).

The binary frequency of pre-main sequence (PMS) stars in nearby DMCs (e.g., Taurus, Ophiuchus) in the surveyed mass range is found to be higher (roughly by a factor of 3) than that found in field stars. On the other hand binary frequency of PMS stars in Trapezium cluster (Petr 1998) indicates a result similar to that of field stars implying that most of the field stars are formed in environment typical of rich cluster like Trapezium rather than in poor groups such as in Taurus. Thus in order to understand how most of the stars form throughout the Galaxy, one must understand how massive cores form and produce rich clusters of stars with high efficiency. However, most of the present day theories of star formation deal with isolated, low mass star formation, the kind of situation that exists in DMCs.

The currently adopted hypothesis dealing with the formation of such individual low mass (sun-like) stars forming in a well-separated, small and dense cloud core, consists of

---

[1] clump is used to denote any region of enhanced density in a larger clouds, while the term core is used to denote particularly dense self-gravitating clumps that might collapse to form a star or a group of stars.

four conceptually distinct stages (Larson 1969; Shu et al. 1987). The first stage corresponds to the fragmentation of a molecular cloud into a number of gravitationally bound cores, which are initially supported by a combination of thermal, magnetic and turbulent pressures (Shu et al. 1987; Mouschovias 1991). The prestellar condensations slowly contract under their own gravity as a result of a mechanism, still poorly understood, that may involve ambipolar diffusion (e.g., Mouschovias 1991), the dissipation of turbulence (e.g., Nakano 1998), and an outside impulse (e.g., Bonnell et al. 1997). The principal feature in this stage involves a quasistatic evolution towards a $1/r^2$ density configuration appropriate for a singular isothermal sphere. The estimated lifetime of the prestellar core stage is a few times 10^6 yr. When the contracting core becomes sufficiently centrally concentrated, it enters the second stage wherein the cloud core gravitationally collapses from *inside-out*. It ends with the formation of an opaque, hydrostatic protostellar object in the centre (e.g., Larson 1969; Boss & Yorke 1995; Bate 1998) wherein the inner regions form an accreting but otherwise secularly evolving protostellar plus nebular disk. The evolving star plus disk system is covered by the infalling gas and dust envelope that rains down from the overlying, slowly rotating, molecular cloud core. The measured visual extinction of the central star ranges from several tens to a thousand magnitudes or more, making the object optically invisible. These objects are hence studied principally by means of the infrared, submillimeter, and millimeter radiation produced by the heated dust in the surrounding envelope. At some point during this phase of the evolution, a powerful wind breaks out along the rotational poles of the system. These outflows are believed to carry away the excess angular momentum of the infalling matter. The estimated time spent in the protostellar formation till the bipolar outflow stage (third stage) is roughly 10^5 yr, almost independent of mass. During the fourth stage, due to the action of stellar wind and outflows, the surrounding envelope of matter is cleared giving an exposed (optically visible) PMS star and associated circumstellar disc.

The protostars and PMS stars are collectively called YSOs. The majority of the known low-mass YSOs can be distinguished into three classes depending on the shape of the spectral energy distribution (SED) which can be parameterized by a SED spectral index. The variation in the shape of the SED represents a variation in the amount and distribution of luminous circumstellar material around YSOs and is therefore represents an evolutionary sequence. In this evolutionary sequence (Lada 1988), *Class I* sources are the youngest and least evolved objects, protostars, undergoing accretion and assembling the bulk of the mass they will ultimately contain when they arrive on the main sequence. Their SEDs are broader than a single blackbody and peak at far-infrared or sub-millimeter wavelengths. Towards longer wavelengths SED rises producing a huge “excess” compared to that from a stellar photosphere. *Class II* sources also have SEDs broader like class I sources but peak at near-infrared wavelengths. Therefore, these sources must be surrounded by considerably less gas and dust than Class I objects and hence are more evolved. *Class III* sources are the most evolved objects. Their SEDs peak at visible and infrared wavelengths and decrease longward of two microns more steeply than Class II sources. Thus their SEDs are interpreted as rising from extincted or unextincted photosphere of the young stars. However, some Class III sources are estimated to have similar ages as Class II sources suggesting that the duration of various phases may be different for different stars (with same mass), and could depend on the environments where they form.

The star forming environments of the kind that prevail in GMCs and DMCs are very complicated and the initial conditions which led to the formation of stars in these regions can get modified due to the presence of stellar winds and outflows which are very common in regions of high and low-mass star formation respectively. The study of molecular clouds which are isolated, small and structurally less complicated are thus the ideal star forming regions that can be used as “laboratories” for a better understanding of the star formation process.

1.2 Bok Globules

The absence of stars or presence of dark patches in certain regions of the sky, once thought to be as holes, are recognized as absorbing clouds of dust situated between the background star field and the observer. Bok and Reilly (1947) were the first to call attention to the isolated globules as the sites of star formation and hypothesized that they are in a state of gravitational collapse, ultimately leading to the formation of stars. Different studies of Bok globules have shown that, indeed, a significant fraction of these clouds are engaged in the process of low-mass star formation (e.g., Yun & Clemens 1990, 1992; Santos et al. 1998), whereas others seem to be rather quiescent and stable (Kane, Clemens, & Myers 1994; Kane & Clemens 1997). Using a variety of means namely, IRAS measurements, millimeter spectral line observations, and near-infrared imaging surveys the nature of the YSOs content in Bok globules has been assessed (Yun & Clemens 1994, 1995). The physical properties of BGs, given in Table 1.1, are comparable to that of the clumps in GCMs and DCMs making BGs the ideal sites for understanding the physics of star formation in simple and less complicated environments.

On the basis of their optical morphology, Bok globules are generally classified as elephant trunks and speck globules, cometary globules and bright-rimmed clouds, globular filaments, and isolated dark globules (Leung 1985). Among the different types of globules, cometary globules attracted early attention because of the presence of bright optical rims. In our work, presented in this thesis, we concentrated on a study of the star forming cometary globules.

1.3 Cometary Globules

During the inspection of hypersensitized IIIaJ plates taken for the ESO/SRC Southern Sky Survey with the UK 48-inch Schmidt telescope, Hawarden & Brand (1976) noticed several elongated, comet-like objects. They identified twelve such objects characterized by having compact, dusty heads which are almost or completely opaque. Long, faintly luminous tails extend several *arcmin* in apparent length from one side of the head while the other side often shows a narrow, bright rim. They named these objects as ***Cometary Globules (CGs)***. Plates taken with a narrow-band Hα mosaic filter (Elliot & Meaburn 1976) established that the tails and the bright rims are emission features. Ten of the twelve CGs identified lie in the outskirts of the Gum nebula. Sandqvist (1976) identified four more CGs in the Gum-Vela region. Later, Zealey et al. (1983) and Reipurth (1983) found a total of 38 CGs in a survey for CGs on IIaO-ESO and IIIaJ SRC Schmidt plates covering the whole Gum Nebula. Cometary globule, CG 1, identified towards Gum-Vela region is a classic example of a CG with an opaque head, long luminous tail extending from one side and a bright rim on the other side of the head (Figure 1.1). A list of

80 remnant clouds is given by Ogura & Sugitani (1998) towards Ori OB 1 association. Of these, 29 can be distinguished by having a cometary morphology with the head and tail of these clouds oriented roughly towards a common centre located somewhere in the Belt or Sword region (Ogura & Sugitani 1998). However, relatively isolated CGs are also known, for example CG 12 (Williams et al. 1977).

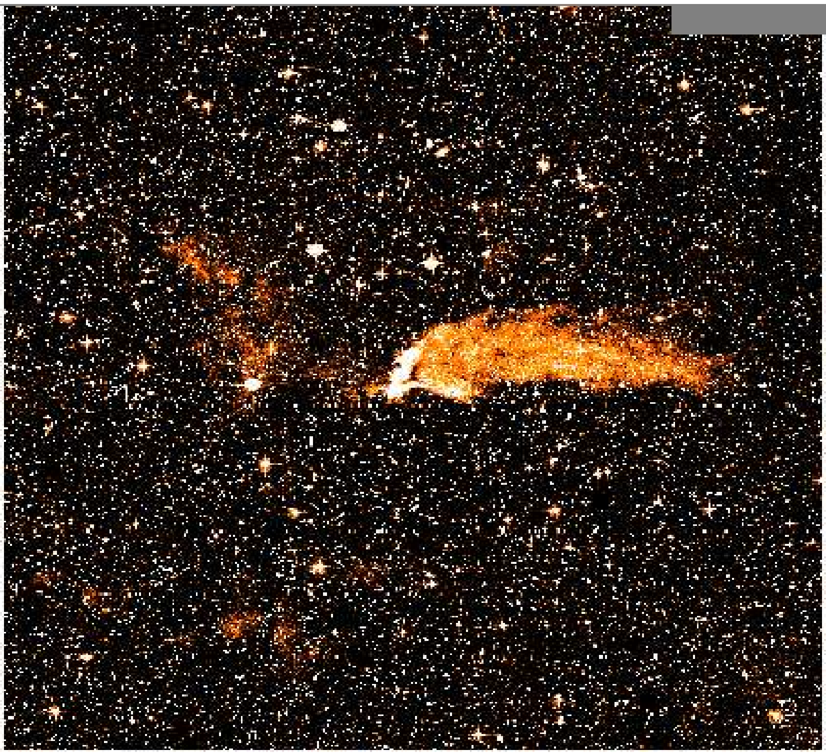

Figure 1.1: Cometary globule CG 1 is a classic example of a CG with an opaque head, long luminous tail extending from one side and a bright rim on the other side of the head. Bernes 135, a pre-main-sequence star, is located at the rim of the cloud. The 1° × 1° image of the field contain CG 1 is reproduced from Digitized Sky Survey. North is up and east is to the left.

There is evidence for current low mass star formation in a number of CGs. For example, Bernes 135, a pre-main-sequence star (PMS), is associated with CG 1 (Reipurth 1983; Brand et al. 1983), CG 30 contains the Herbig-Haro object HH 120 and the infrared source CG 30-IRS 4 (Pettersson 1984), emission line stars inside and in the vicinity of L 1616 (Alcala et al. 2004), A number of CGs in Gum Nebula have IRAS point sources with SEDs characteristic of young stellar or protostellar objects, associated with their compact heads, indicating star formation at relatively enhanced rates (Bhatt 1993).

Most of the CGs have been found to be associated with star-forming regions with massive OB type stars (e.g., Hawarden & Brand 1976; Sandqvist 1976; Schneps, Ho & Barret 1980; Zealey et al. 1983; Reipurth 1983; Gyulbudagyan 1986; Sugitani, Fukui & Ogura 1991; Block et al. 1992). The largest of such systems of CGs is associated with the Gum Nebula in Vela-Puppis with 32 CGs (Zealey et al. 1983; Reipurth 1983) centered around the Vela OB2 association. The radial velocity measurements (after removing the galactic differential rotation) of the system of CGs towards Gum-Vela region from ^{12}CO molecular line observations indicated that the CGs are expanding from a common centre (Sridharan 1992). They estimated an expansion age of $\sim$ 6 Myr. Radial velocities measured at different locations in the CGs, from the head towards the tail, showed that the tail is moving faster than the head. As part of a programme to map the magnetic fields in CGs by making optical polarization measurements of stars projected in the regions of these globules, Sridharan, Bhatt & Rajagopal (1996) observed CG 22 and Bhatt (1999) observed the CG 30-31 complex. In CG 22, a majority of the stars seen projected within the cloud boundaries were found to be polarized (at a level $\sim$ 1 %) with the electric vector oriented parallel to the CG tail. If the polarization is a result of non-spherical dust grains aligned by the magnetic field (Davis-Greenstein mechanism), then the results for CG 22 imply that the magnetic field in this CG is parallel to its tail. In the CG 30-31 complex, the field was found to be nearly perpendicular to the cometary tails and is more or less parallel to the bipolar molecular outflow from the YSO IRS 4 embedded in the head of CG 30. Both CG 22 and the CG 30-31 complex are part of the system of CGs around the Vela OB2 association.

From the survey of southern dark clouds of Hartley et al. (1986), a comprehensive list of 169 small southern molecular clouds (globules) were established by Bourke et al. (1995). The most opaque clouds with the angular diameter less than $10'$ were included in the list. Of these, 40 show cometary-globule-like appearance. This includes 32 CGs identified by Zealey et al. (1983) and Reipurth (1983) towards Gum-Vela region. These 32 CGs were observed for ammonia emission along with four globular dark clouds (GDC) in Vela identified by Reipurth (1983). Of the 36 globules observed, four were found to be strong emitters of ammonia (11%) and 23 had detections greater than 3σ (64%). Thus as a group, CGs are detected more frequently than the other Bok globules in their study

(75% compared with only 38%). Such a high detection rate for CGs would suggest that the external forces which have been working on CGs, have had a significant effect on their internal structure. Of the nine CGs with geometric head sizes $\lesssim 1'$, seven were not detected in ammonia. If beam dilution is the reason for their non-detections, then it may be that all CGs in the Gum-Vela region contain dense cores. The typical values of hydrogen column density and number density for the opaque heads of the Vela CGs are $N(H_2) \sim 6 \times 10^{21} cm^{-2}$ and $n(H_2) \sim 5 \times 10^{3} cm^{-3}$ respectively (Vilas-Boas, Myers & Fuller 1994; Bourke et al. 1995). Three out of four globules mapped in detail, showed the derived core sizes to be a close approximation of the optical size of the globule head.

The kinetic temperatures determined for some of the CGs like CG 1 ($T_K \sim 15K$, Harju et al. 1990), CG 4 and CG 6 ($T_K \sim 15K$, Gonz*á*lez-Alfonso, Cernicharo & Radford 1995), CG 12 ($T_K \lesssim 20K$, White 1993), CG 30 and CG 31A ($T_K \sim 13K$, Bourke et al. 1995) and Ori-I-2 ($T_K \sim 25K$, Cernicharo, 1991), appears to be slightly higher when compared to darker globules in which the derived kinetic temperature is typically in the range $T_K \sim 8 - 10K$ (Dickman 1975; Martin & Barrett 1978; Myers & Benson 1983; Clemens et al. 1991; Bourke et al. 1995).

The simple morphology and physical characteristics of these clouds have been known since early observations (Hawarden & Brand 1976; Zealey et al. 1983). The presence of a head-tail morphology and their being oriented roughly towards a common center indicate that their origin is due to some common mechanism which is external in nature. These objects provide an opportunity to understand better the star formation process in environments that can be relatively clearly defined and give useful insight into star formation in more complex environments.

We present an updated list of CGs compiled from the literature and from a search made by us in 100μm IRAS images to identify clouds with cometary morphology in different locations of the Galaxy in Table 1.2. Column 1 contains the right ascension-ordered identifying number of each globule, column 2 gives the globule identification, column 3 & 4 give 2000.0 epoch right ascension and declination. Columns 5 & 6 give the Galactic coordinates. Columns 7 & 8 contain remarks and references for individual globules respectively. Out of 93 CGs listed, twenty nine are associated with Orion OB 1 association, thirty two are associated with Gum nebula and rest are relatively isolated.

The cometary morphology of a cloud identified with LBN 131.54-08.16 (shown in Figure 3.3) was noted by us in our search.

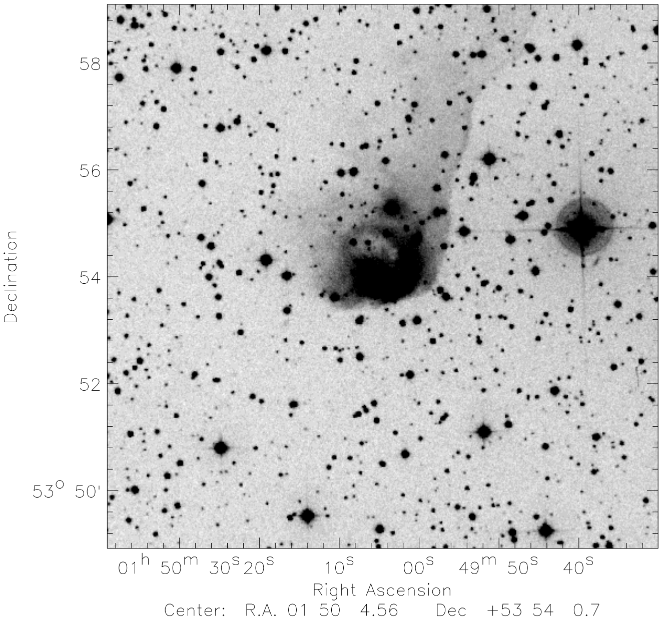

Figure 1.2: The $10' \times 10'$ optical image of the field containing LBN 131.54-08.16. The image is reproduced from the Digitized Sky Survey. The cometary nature of this cloud was identified in our search for such clouds using 100μm IRAS images. North is up and east is to the left.

Two alternative scenarios presented for the formation of the cometary morphology are:

- Relatively smaller dense cores distributed in a parent giant molecular cloud, exposed to the radiation and stellar winds from massive OB type stars in a newly born central OB association, can develop cometary head-tail morphology as the less dense core is shock-compressed to produce the head. The shocks can also trigger star formation in the CG head. If the cores subjected to the radiation are of low initial density (or low mass) then they may be completely evaporated (Reipurth 1983). During the evaporation process their radii will decrease, becoming undetectable at some stage of their evolution. *Tear drops* of Rosette nebulae are examples of CGs in the last stages of their life which could still survive the UV field for $10^3 - 10^4$ yr (Herbig 1974).

- Brand (1981) and Brand et al. (1983) argued that CGs are shocked clouds, formed when a supernova blast-wave sweep past an initially spherical cloud. The implosion produces a forward-moving shock and a reverse shock (a rarefaction wave) within the cloud. These together result in gravitationally unstable material in a dense clump (the head) and downstream-ejected cloud material (the tail) which is considerably denser than the intercloud medium. A single or group of stars may be formed in the head (e.g. association of Bernes 135 with CG 1).

Recent studies of meteorites confirm the presence of live Fe-60 in the early Solar System (Tachibana & Huss, 2003). No known mechanism could have formed this short-lived (half-life = 1.5 million years) radionuclide locally within the young Solar System. However, Fe-60 is produced in supernova explosions, along with Al-26, Ca-41, and other radioisotopes (Meyer & Clayton, 2000). Materials from nearby supernovae must have rapidly mixed with the material from which the meteorites formed. The implications of this is that the Sun did not form in a region like Taurus-Auriga. Rather, like most low-mass stars (Lada & Lada, 2003), the Sun formed in a high-mass star forming region where one or more stars went supernova. Understanding our origins means understanding the process of low-mass star formation in environments that are shaped by the presence of massive stars.

Massive stars with masses above $10 M_{\odot}$ (spectral type earlier to B2) profoundly affect their environment in several ways (Garay & Lizano 1999). Intense UV radiation emitted by O-type stars ionizes and heats the surrounding material and can affect the nearby cloud cores and the circumstellar material around YSOs by photoevaporation as is manifested by objects called *proplyds* in the Trapezium cluster (Bally et al. 1998). The powerful winds of massive stars deposit considerable amounts of momentum and kinetic energy into their surrounding medium. For example, a single O5 star is perfectly capable of dispersing a $10^4 M_{\odot}$ molecular cloud completely within only about 1 Myr (at the rate of $10^{-2\pm0.5} M_{\odot} yr^{-1}$, Yorke 1986). After a few Myr, the most massive stars end their life with supernova explosions. Each such explosion causes a strong shock wave that expands with initial velocities $\gtrsim 10000\ kms^{-1}$ and transfers typically some $10^{51} erg$ of kinetic energy in the ambient interstellar medium. Thus as soon as the first O-star ignites, it will terminate the star formation process in a steadily increasing volume around it. However, at larger distances, the slowed-down shock waves driven by the massive stellar winds and/or supernova explosions can provide the compression necessary to initiate cloud collapse and ***trigger*** star formation.

1.4 Triggered Star Formation

There is considerable evidence that star formation is often triggered. This may occur sequentially on both large (e.g., Preibisch & Zinnecker 1999) and small (Sugitani et al. 1995; Fukuda & Hanawa 2000) scales. Numerous examples of star formation in OB associations (Blaauw 1964) and other high pressure regions which are thought to be the result of triggered star formation are known. These observations are organized according to the proposed mechanisms of triggering into **small, intermediate,** and **large** scales in the following sense:

- *Small scale triggering:* direct squeezing of pre-existing clouds or globules by high pressure that nearly surrounds the whole cloud. This includes triggering in bright rims, proplyds, and small cometary globules.

- *Intermediate scale triggering:* compression of a nearby cloud from one side, leading to a dense ridge of moving gas that presumably collapses or recollects into denser cores in which star clusters eventually form.

- *Large scale triggering:* accumulation of gas into an expanding shell or ring partially surrounding the pressure source, with star formation in the shell or ring presumably triggered by gravitational collapse of swept-up gas.

For triggering on small and intermediate scales, the extent of triggering is probably limited to the pre-existing dense gas, i.e., to the molecular clouds in which the first generation of stars formed. For large scales, triggering apparently occurs in the ambient gas that was not previously part of the star forming cloud. However, whether the formation of first generation stars is also due to triggering is unknown. If 99% of all clouds and star formation is triggered, then there will be important implications for spiral structure of galaxies (Jungwiert & Palous 1994).

1.4.1 Small scale triggering - An Overview

Triggering mechanisms are usually related to high pressures. In one scenario, the pressures from ionized gas, stellar winds, or supernova explosions shape and compress pre-existing gas clouds, converting them from stable to unstable configurations while reshaping their periphery into cometary forms. Numerical simulations of the formation of bright rims and other peripheral structures are in Bedijn & Tenorio-Tangle (1984), Sandford, Whitaker, & Klein (1982, 1984), Klen, Sandford, & Whitaker (1983), Lefloch & Lazareff (1994), and Elmegreen, Kimura & Tosa (1995). Analytical work on the structure of embedded globules and cometary clouds is in many references, including Oort & Spitzer (1955), Kahn (1969), Dyson (1973), Brand (1981), Bertoldi (1989), and Bertoldi & McKee (1990).

In the simulations by Lefloch & Lazareff (1994), the effect of external radiation on a globule (or pre-existing clump) existing at the periphery of HII regions has been shown to lead to the Radiation Driven Implosion (RDI) of the globule, followed by the formation of a dense core extended along the globule's axis. This process occurs in two phases; an early collapse phase as the effect of the ionizing radiation compresses and ionises the globule, probably forming birght-rimmed clouds (BRCs), and a cometary phase in which the external ionised gas shields the tail from ionizing radiation and pressure confines the head, leading to a long-lived head-tail morphology as manifested by cometary globules. The collapse phase is rapid, lasting about 10% of the lifetime of the globule. It is possibly in this phase that star formation occurs.

The key observational diagnosis of RDI process is the ratio of external to internal pressure. As the surface of the globule becomes ionized due to the ionizing radiation from the external source, an ionized boundary layer (IBL) develops on the side facing it. If the pressure in this ionized boundary layer is greater or equal to the interior neutral cloud pressure, photoionization-induced shocks and a D-critical ionization front propagate into the cloud interior, compressing and heating the molecular gas (Bertoldi 1989; Lefloch & Lazareff 1994). On the other hand, if the globule is overpressured, the ionization front stalls at the cloud surface until the increasing recombination within the IBL raises the ionized gas pressure to equilibrium with the interior cloud pressure. Numerous observations of bright-rimmed clouds have been performed, at various wavelengths, mainly to study the structure of the molecular globules and their stellar content. Most of these observations show excellent agreement between the models and the observations with regard to the morphology of the globules and to their velocity field (Lefloch, Lazareff and Castets 1997; Sugitani et al. 1997; De Vries et al. 2002; Thompson et al. 2004).

The shock waves impacting molecular clouds and the subsequent collapse of the compressed cloud cores was studied by Vanhala & Cameron (1998). They found that shocks with velocities less than 45 kms^{-1} can cause the cores to collapse. The thermodynamics also plays a vital role in determining the collapse of the compressed core. The adiabatic exponent in the core material needs to fall below the stability value of 4/3 which in typical molecular cloud conditions occurs at a temperature $\sim 27K$. In their simulation study, about 1/3 of the original core mass collapses to form the stellar system, while the rest has been swept downstream. The fraction is larger for the massive cores, which are triggered into collapse rapidly, before most of the core material has been eroded by the shock flow. Thus the star formation efficiency estimated for triggered star formation is found to be $\sim$ 30% or even higher for more massive cores. Another interesting result obtained in their simulation is the triggered collapse resulting in the formation of multiple star system. These results, however, critically depend on the properties of the preimpact globule.

1.4.2 Small-scale sequential star formation

The photoionization of the cloud surface has been linked to induced star formation within the clouds (Elmegreen 1991; Sugitani et al. 1989, 1991). Signposts of star formation are often observed towards CGs and BRCs. Emission line stars and Herbig-Haro objects (HH) are detected in and around 28 of the 30 bright-rimmed clouds studied by Ogura et al. (2002). These objects are found to be concentrated near the tip of bright rims (i.e., in the head of the BRCs and just outside the rims) and often make loose aggregates similar to those of near-IR stars. These results support the hypothesis of **"small-scale sequential star formation"** in these clouds. Recent multi-wavelength study on cometary cloud L1616 (Alcala et al. 2004) revealed the presence of several X-ray sources, confirmed to be PMS stars, distributed spatially towards the east of the cloud head having a small age spread suggesting a quick and efficient star formation. Presence of numerous Hα emission line sources inside the cloud head and MIR source even further inside show sequential star formation in L1616. CG 30/31/38 in Gum Nebula (Kim et al. 2002) also show PMS stars outside and near its head presenting another example of small-scale sequential star formation in CGs.

1.5 Outline of the Thesis

The head-tail morphology of CGs suggest that they are subjected to some external influence and any star formation activity associated with them could likely be triggered. In this thesis, we will be presenting the results of a study of star-forming cometary globules and the young stellar objects formed in and near the CGs which will help in addressing the following key questions and lead to a better understanding of the effects of external trigger on the formation of stars in these clouds:

- What are the physical characteristics (distance, size, mass, magnetic field, morphology, etc) of the star-forming CGs.
- How are the YSOs distributed spatially inside and in the vicinity of the clouds ? Is there evidence for small-scale sequential star formation in CGs ?
- What is the mass of the most massive star formed and its relationship with the cloud mass ? What is the star formation efficiency ? How do they compare with that of the isolated clouds (with similar masses) which are isolated and located away from *HII* regions ?
- What is the evolutionary status of YSOs formed in CGs ?

CHAPTER 1

In chapter 1, we present a brief introduction to the current understanding of the formation of stars in Galactic star-forming regions. The important results obtained from the research carried out in the past on cometary globules and a brief introduction to the observational and theoretical/simulation studies carried out on cometary globules and on triggered star formation in general are also presented in this chapter. An updated list of CGs, prepared from the literature survey and from a search made by us using 100μm IRAS images to identify clouds with cometary morphology, from which we have chosen the objects for our current study is presented.

CHAPTER 2

Of the twelve CGs identified by Hawarden & Brand (1976) initially, two of them, CG 11 and CG 12 are outside the Gum nebula region. Hawarden & Brand (1976) themself had referred to CG 12 as *"noteworthy"* due to its Galactic position ($l = 316.5°, b = 21.2°$) and the orientation. In CG 12, the tail rather than head is pointing towards the Galactic plane. We have carried out an extensive study of CG 12 and results are presented in this chapter which is sub-divided into PART I, PART II, and PART III.

PART I

The relatively high-galactic latitude position ($b \simeq 21°$) of CG 12 could be due to two reasons. Either it is at a distance closer than $\sim$ 200 pc, adopting a scale height $\langle\ z\ \rangle$ of $\sim$ 60 pc above the Galactic midplane for the clouds in the solar vicinity (Magnani, Blitz & Mundy 1985; Keto & Myers 1986), or it is farther away and at a relatively large galactic height. The measurement of distance to an interstellar cloud is very important in order to determine several important physical properties like sizes, masses and densities (Clemens, Yun & Heyer 1991). Distances are also needed for obtaining luminosities of any embedded YSOs or protostars in these clouds (Yun & Clemens 1990). There exists a range (100-660 pc) of distances for CG 12 in the literature. In Part I of the chapter 2, we present a method for determining distances to dark clouds and Bok globules based on broad-band optical and near infrared photometry.In this method, intrinsic colour indices of stars projected towards the direction of a cloud are computed by dereddening the observed colour indices using various trial values of extinction A_V and a standard extinction law. The computed intrinsic colour indices for a star are then compared with the intrinsic colour indices of normal main-sequence stars and a spectral type is assigned to the star for which the computed colour indices best match with the standard intrinsic colour indices. Distances (d) to the stars are determined using the A_V and absolute magnitudes (M_V) corresponding to the spectral types thus obtained. A plot of A_V against d undergoes a sharp rise at a distance corresponding to the distance to the cloud. Using this method, we have determined a distance of 550 pc to the cometary globule CG 12.

PART II

It is generally well recognized that magnetic fields play an important role in the formation of interstellar clouds, controlling their morphology and the star formation process. However, our observational knowledge of the magnetic field and understanding of its role in the evolution of CGs is still rather limited. Earlier observations of CG 22 (Sridharan, Bhatt & Rajagopal 1996) and CG 30-31 complex (Bhatt 1999) showed that in CG 22, a majority of the stars seen projected within the cloud boundaries were found to be polarized (at a level $\sim 1\%$) with the electric vector oriented parallel to the CG tail. If the polarization is a result of non-spherical dust grains aligned by the magnetic field (Davis-Greenstein mechanism), then the results for CG 22 imply that the magnetic field in this CG is parallel to its tail. In the CG 30-31 complex, the field was found to be nearly perpendicular to the cometary tails and is more or less parallel to the bipolar molecular outflow from the YSO IRS 4 embedded in the head of CG 30. In part II of the chapter 2, we present results of optical linear polarization measurements of stars projected towards the region containing CG 12. A polarization map representing the geometry of the magnetic field in the cloud is produced. We find that in the lower-density outer parts of the cloud, the field is more or less parallel to the cometary tail, with position angle $\theta \sim 130°$. Other elongated structures, like the bipolar molecular outflow from near the infrared source IRAS 13547-3944 and the nebulosity around star 2 embedded in the cloud are also oriented in the same direction. Polarization vectors for the more highly reddened stars in the head region of the globule are found to be more or less parallel to the long axis of the elliptical, high-density C^{18}O core of the CG head, with position angle $\theta \sim 7°$. If the nebular contribution to the polarization of stars can be neglected, then a magnetic field in the high-density core oriented parallel to its long axis is indicated. It is suggested that the expanding supernova remnant that blew the lower density outer parts of the globule into a cometary tail is likely to have dragged the ambient magnetic field lines in the same direction. In the higher density inner parts of the globule head the original magnetic field remained unperturbed.

PART III

Williams et al. (1977) have speculated that CG 12 has been influenced by a high-galactic latitude supernova explosion resulting in the formation of a tail from the blown away low density outer parts of the globule. As shown and discussed in part II of the chapter 2, this most likely could have dragged the ambient magnetic field in the same direction of the tail, strengthening the supernova conjecture made by Williams et al. (1977). Any current star formation occurring in CG 12 could be thus possibly due to the external trigger. The distance of 550 pc to CG 12 determined in part I of the chapter 2 implies that it is at a height of $\sim$ 200 pc above the Galactic midplane. The simple structure and complete isolation of CG 12 provide us an opportunity to study the effects of triggered star formation at intermediate-to-high galactic latitude. In part III of the chapter 2, we present the results of our study of the structure and morphology of CG 12 using IRAS 60 & 100 μm images. The color temperature, optical depth and extinction maps of CG 12 are presented. The capability of an interstellar cloud to form stars depends on its initial physical conditions, which are subjected to the influence of the external conditions or medium. The spatial distribution of PMS stars is a key to understand the star formation process in general and, in particular, to describe the star formation history in a star-forming region. The identification of YSOs associated with CG 12 and study of their nature are carried out by combining our medium resolution optical spectroscopy and $BVRI$ photometric observations with ROSAT X-ray and 2MASS near-IR observations. In this study we find a number of ROSAT detected X-ray sources characteristics of weak-line T Tauri, stars thought to be as more evolved low-mass young stellar objects, distributed outside the head of CG 12. Inside the cloud boundary we find a number of near-IR excess continuum emission sources characteristics of classical T Tauri and emission line star $h4636N$ (northern component of the double star $h4636$ located in the head of CG 12 and illuminating the reflection nebula NGC 5367) considered to be relatively younger. The star $h4636N$ show spectroscopic signatures of the presence of a possible circumstellar shell or disk around it. Towards the north of the double star, *h*4636, we find an embedded near-IR excess emission source from 2MASS observations thought to be a Class I YSO. We, thus present a possible age sequence in YSOs associated with CG 12, from relatively more evolved YSOs outside of CG 12 to very young star found embedded inside CG 12. The location of the embedded star positionally coincides with the region of high optical depth and extinction found in the optical depth and extinction maps produced for CG 12 using IRAS 100μm and 60μm images. The estimated star formation efficiency in CG 12 is found to be $\gtrsim 16$ %. We also show the presence of a complete HI shell of $\sim 20^\circ$ angular diameter centred near $l = 315^\circ, b = 30^\circ$ as the evidence for the supernova theory responsible for the cometary morphology and star formation in CG 12.

CHAPTER 3

The investigations on the luminosity of protostars forming in molecular clouds as a function of the parental cloud mass by Dobashi et al. (2001) have shown that the protostars in clouds associated with HII regions are more luminous than those in clouds away from HII regions. In this chapter we present the results of a similar investigation carried out in cometary globules. We have estimated the luminosity of the IRAS sources found associated with CGs as a function of its cloud mass and then compared it with that of the IRAS sources found associated with the opacity class 6 clouds (isolated and relatively away from HII regions). We find that the luminosities of IRAS sources associated with CGs are larger than those for the opacity class 6 clouds. The mass of the most luminous star, estimated from its spectral type, associated with a cloud was found to correlate with the mass of the parent cloud (Larson 1982). We made spectroscopic observations of optically visible stars associated with star-forming CGs. We find that the masses of the most massive stars (estimated from their spectral types) associated with CGs are larger than that expected from their parental cloud mass. These results imply that the massive star environments have had influence on the star formation in clouds like CGs. The results of the spectroscopic study carried out on young stellar objects associated with CGs are also presented in this chapter.

CHAPTER 4

A significant fraction of the CGs are located at galactic latitude $|b| \gtrsim 10°$. The cometary globule CG 12, studied and discussed in great detail in chapter 2 lies at $b \sim 21°$. A more extensive survey of young stellar objects at high-galactic latitude would be valuable for a better understanding of star formation as a function of height above the Galactic plane. The Hα emission objects in the survey by Stephenson (1986) provide a magnitude limited sample of candidates for the YSOs at high-galactic latitude. In this chapter we present the results of spectroscopic observations of 52 objects from the list of Hα emission stars of Stephenson (1986). The study was aimed at identifying potential high galactic latitude YSO candidates among Stephenson objects on the basis of our spectroscopic observations, near-infrared excess form 2MASS observations and their detection in IRAS and/or ROSAT observations. We have confirmed the T Tauri nature of one star StHα 48, reported variability of StHa 40 in Hα which is also accompanied by variations in the underlying stellar absorption spectrum and photometric variability. No new Hα emitting YSOs are found in the present study of StHa objects. YSOs amongst StHa stars that are already known or confirmed as such in this study (StHα 48), and objects (StHα 52, 125 and 129) suggested in this study to be YSOs all belong to well known star-forming regions like Taurus, Orion and Ophiuchus. YSOs at high galactic latitudes in other parts of the sky are therefore rare.

CHAPTER 5

The double star $h4636$ in the head region of CG 12, a candidate Herbig Ae/Be star, was found to have its optical linear polarization position angle (161°) oriented roughly parallel to the molecular outflow position angle (148°) while the orientation of the binary component position angle (34°) was roughly perpendicular to both polarization and molecular outflow position angle. In this chapter, we present the results of an investigation carried out to understand the geometrical relationship between the distribution of circumstellar matter, observed optical linear polarization, outflows and binary orbital planes in Herbig Ae/Be stars which are YSOs with masses ranging between $2 - 8M_{\odot}$. Optical linear polarization measurements were carried out for a number of Herbig Ae/Be stars that are either known to be in binary systems and/or have bipolar jets. Available information on the position angles of polarization, outflows and binary companions for

Herbig Ae/Be stars is compiled and analyzed for any possible correlations. We found that out of 20 outflow sources, 17 sources (≈ 85%) have the outflow position angle within 30° of being either parallel or perpendicular to the polarization position angle. In 25 (≈ 81%) out of 31 sources, the direction of binary position angle is within 30° of being either parallel or perpendicular to the polarization position angle. In 10 (≈ 67%) out of 15 outflow sources, the binary position angle is within 30° of being perpendicular to the outflow position angle. These results indicate the presence of correlations between the position angles of polarization, outflows and binary companions for Herbig Ae/Be stars. These results are consistent with binary star formation scenarios in which the circumstellar disk planes are parallel to the binary orbital plane.

CHAPTER 6

We summarize the main results presented in the thesis and plan for the future research in this chapter.

Table 1.2: An updated list of CGs identified towards different locations of our Galaxy.

S No.	Object Id	$\alpha(J2000)$ $(^{h}\ ^{m}\ ^{s})$	$\delta(J2000)$ $(^{\circ}\ '\ '')$	$l(^{\circ})$	$b(^{\circ})$	Remarks	Ref.
1	CB 06	00 49 29	+50 44.6	122.62	-12.13		1
2	IC 59	00 57 42	+61 05 00	123.69	-1.78		2
3	IC 63	00 59 01	+60 53 18	123.85	-1.97		2
4	LBN 131-08	01 50 05	+53 53 54	131.48	-8.21	Nebulosity	†
5	RNO 6	02 16 30	+55 22 57	134.88	-5.50	Nebulosity, Em* source	3
6	CB 26	05 00 09	+52 04 54	156.06	+6.00		1
7	[OS98] 01	05 04 24	-06 12 12	206.00	-26.59		4
8	[OS98] 02	05 06 20	-03 56 00	204.02	-25.11		4
9	[OS98] 03	05 06 48	-03 23 00	203.54	-24.75	HH objects, Nebulosity, Em* sources	4
10	[OS98] 04	05 12 04	-01 55 36	202.83	-22.89		4
11	[OS98] 06	05 17 01	-07 44 36	209.09	-24.49		4
12	[OS98] 07	05 19 48	-05 52 05	207.60	-23.03	HH 240, Em* sources	4
13	[OS98] 10	05 20 50	-05 49 24	207.40	-22.94	Em* sources	4
14	[OS98] 12	05 22 11	-03 41 36	205.80	-21.50		4
15	Sim 130	05 22 55	+33 31 40	173.51	-01.58		5
16	Sim 129	05 23 09	+33 28 37	173.57	-01.57		5
17	[OS98] 16	05 26 54	-10 14 30	212.71	-23.38		4
18	[OS98] 17A	05 27 12	-10 28 42	212.98	-23.42		4
19	[OS98] 17B	05 27 01	-10 28 13	212.95	-23.45		4
20	[OS98] 25A	05 32 43	-02 55 42	206.39	-18.82		4
21	[OS98] 25B	05 32 29	-03 00 12	206.43	-18.91		4
22	[OS98] 29D	05 33 32	-01 36 18	205.25	-18.02		4
23	[OS98] 29K	05 34 40	-01 21.9	205.17	-17.66		4
24	[OS98] 29L	05 35 02	-01 15 48	205.12	-17.53		4
25	[OS98] 30	05 33 57	-03 41 42	207.26	-18.90		4
26	[OS98] 31	05 34 30	-02 58 15	206.65	-18.44		4
27	[OS98] 34	05 36 13	-04 00 42	207.83	-18.55		4
28	[OS98] 36	05 36 35	-04 01 12	207.88	-18.47		4
29	[OS98] 40A	05 38 05	-01 45 09	205.95	-17.09	HH 289	4
30	[OS98] 40B	05 37 54	-01 37 18	205.81	-17.07		4
31	[OS98] 40C	05 37 51	-01 35 36	205.77	-17.06		4
32	[OS98] 40D	05 37 52	-01 32 48	205.73	-17.04		4
33	[OS98] 41	05 38 26	-05 14 08	209.24	-18.61		4
34	[OS98] 42	05 38 51	-07 45 36	211.68	-19.65		4
35	[OS98] 45	05 39 42	-05 21 06	209.50	-18.38		4
36	[OS98] 46	05 40 18	-05 24 30	209.63	-18.28		4
37	[OS98] 47A	05 40 36	-05 25 00	209.67	-18.21		4
38	[OS98] 47B	05 40 58	-05 26 42	209.74	-18.14		4
39	[OS98] 55	05 41 08	-06 35 30	210.84	-18.62		4
40	[OS98] 56	05 41 37	-06 26 48	210.76	-18.45		4
41	[OS98] 59	05 43 07	-05 20 24	209.89	-17.62		4
42	[OS98] 60A	05 43 22	-05 01 00	209.62	-17.42		4
43	[OS98] 60B	05 43 52	-05 05 30	209.75	-17.34		4
44	[OS98] 61A	05 43 29	-03 35 30	208.31	-16.74		4
45	[OS98] 61B	05 43 32	-03 28 42	208.21	-16.68		4
46	[OS98] 62	05 47 24	+00 43 00	204.83	-13.87		4
47	LDN 1622	05 54 28	+01 48 12	204.70	-11.80	HH 122, Nebulosity, Em* sources	7
48	CG 1	07 19 22	-44 35 03	256.15	-14.07	Nebulosity, Em* source	6

continued on next page...

continued from previous page...

S No.	Object Id	$\alpha(J2000)$ $(h\ m\ s)$	$\delta(J2000)$ (o , , ,)	$l(^\circ)$	$b(^\circ)$	Remarks	Ref.
49	CG 2	07 16 01	-43 57 42	255.31	-14.36		7
50	CG 3	07 39 13	-47 52 33	260.72	-12.40		7
51	CG 4	07 34 13	-46 54 24	259.44	-12.72		7
52	CG 5	07 40 52	-43 49 12	257.18	-10.27		7
53	CG 6	07 30 31	-46 43 48	259.00	-13.21		7
54	CG 7	09 14 19	-42 29 23	266.04	+04.31		7
55	CG 8	07 42 42	-41 15 44	255.06	-08.76		7
56	CG 9	07 40 48	-41 27 07	255.06	-09.17		7
57	CG 10	07 42 35	-42 05 23	255.79	-09.18		7
58	CG 13	07 14 11	-48 28 32	259.48	-16.43	Nebulosity	7
59	CG 14	07 38 38	-49 51 24	262.49	-13.37		7
60	CG 15	07 32 20	-50 45 48	262.88	-14.67		7
61	CG 16	07 27 36	-51 04 44	262.86	-15.48		7
62	CG 17	08 52 30	-51 52 00	270.58	-04.69		7
63	CG 18	08 52 30	-50 40 00	269.66	-03.91		7
64	CG 22	08 28 46	-33 44 14	253.58	+02.96	Em* source	7
65	CG 23	07 36 06	-50 13 00	262.64	-13.89		7
66	CG 24	08 19 16	-42 54 27	260.02	-03.82		7
67	CG 25	07 37 22	-47 57 05	260.65	-12.71		7
68	CG 26	08 16 00	-33 50 10	252.15	+00.73		7
69	CG 27	08 12 25	-33 45 16	251.66	+00.15		7
70	CG 28	08 12 22	-33 55 36	251.80	+00.05		7
71	CG 29	08 12 24	-34 00 58	251.88	+00.01		7
72	CG 30	08 09 33	-36 05 00	253.29	-01.61	HH 120	7
73	CG 31A	08 09 03	-36 01 18	253.19	-01.66		7
74	CG 31B	08 08 48	-36 03 00	253.18	-01.72		7
75	CG 31C	08 08 33	-35 59 00	253.11	-01.73		7
76	CG 31D	08 08 17	-36 01 48	253.11	-01.80		7
77	CG 31E	08 08 13	-36 04 06	253.13	-01.83		7
78	CG 32	08 14 24	-34 30 19	252.52	+00.08		7
79	CG 33	08 15 30	-34 04 34	252.29	+00.51		7
80	CG 34	07 29 36	-41 10 00	253.82	-10.90		7
81	CG 36	08 37 18	-36 37 56	256.95	+02.65		7
82	CG 37	08 12 28	-33 05 36	251.12	+00.53		7
83	CG 38	08 09 39	-36 10 36	253.38	-01.65		7
84	CG 21	12 37 09	-69 59 54	301.70	-7.16		8
85	CG 20	12 40 48	-69 51 00	302.01	-7.00		8
86	CG 19	12 45 42	-55 25 00	302.11	+7.45		8
87	CG 12	13 57 42	-39 56 21	316.49	+21.18	Nebulosity, Em* source	9
88	BHR 136	16 54 32	-40 31 06	344.52	+1.95		10
89	CG 11	19 40 30	-34 46 00	4.87	-24.54		9
90	GM 1-27	20 20 13	+37 10 12	75.38	+00.44	Nebulosity, HH 214	11
91	CB 230	21 17 39	+68 17 32	105.17	+13.16	Nebulosity, sub-mm sources	1
92	Gal 096-15	22 34 30	+40 42 06	96.72	-15.10	Em* sources	12
93	Gal 110-13	23 37 39	+48 29 48	110.53	-12.59	Nebulosity	13

References:

(1) Launhardt et al. (1998); (2) Jansen et al. (1994); (3) Bachiller et al. (2002); (4) Ogura & Sugitani 1998, PASA, 15, 91; (5) Marco & Negueruela (2003) (6) Magakain (2003) (7) Sridharan (1992); (8) Zealey et al. 1983; (9) Hawarden & Brand (1976); (10) Bourke et al. (1995); (11) Neckel & Staude (1987); (12) Olano et al. (1994); (13) Odenwald et al. (1992)

† Identified in this work.

Bibliography

[1] Alcala, J. M., Silvotti, R., Grado, A., et al. 2004, A&A, 416, 677

[2] Bachiller, R., Fuente, A., Kumar, M. S. N, 2002, A&A, 381, 168

[3] Bally & Langer, 1982, ApJ, 255, 143

[4] Bally, John., Testi, Leonardo., Sargent, Anneila., Carlstrom, John., 1998, AJ, 116, 854

[5] Bate, Matthew R., 1998, ApJ, 508L, 95, 1998

[6] Bedijn & Tenorio-Tangle, 1984, A&A, 135, 81

[7] Bertoldi, Frank., 1989, ApJ, 346, 735

[8] Bertoldi & McKee, 1990, ApJ, 354, 529

[9] Bhatt, 1993, MNRAS, 262, 812

[10] Bhatt, 1999, MNRAS, 308, 40

[11] Blaauw, 1964, ARA&A, 2, 213

[12] Block, David L., Dyson, J. E., Madsen, Claus., 1992, ApJ, 390L, 13

[13] Bok and Reilly, 1947, ApJ, 105, 255

[14] Bourke, T. L., Hyland, A. R., Robinson, G., James, S. D., Wright, C. M., 1995, MNRAS, 276, 1052

[15] Bonnell, I. A., Bate, M. R., Clarke, C. J., Pringle, J. E., 1997, MNRAS, 285, 201

[16] Boss & Yorke, 1995, ApJ, 439L, 55

[17] Brand, 1981, MNRAS, 197, 217

[18] Brand, P. W. J. L., Harwarden, T. G., Longmore, A. J., et al. 1983, MNRAS, 203, 215

[19] Cernicharo, 1991, The Physics of Star Formation and Early Stellar Evolution, NATO Advanced Science Institutes (ASI) Series C, Vol. 342, held in Agia Pelagia, Crete, Greece, May 27th - June 8th, Dordrecht: Kluwer, 1991, edited by Charles J. Lada and Nikolaos D. Kylafis., p.287

[20] Clemens, Yun & Heyer, 1991, ApJS, 75, 877

[21] De Vries, Christopher H., Narayanan, Gopal., Snell, Ronald L., 2002, ApJ, 577, 798

[22] Dickman, 1975, ApJ, 202, 50

[23] Dobashi, Kazuhito., Yonekura, Yoshinori., Matsumoto, Tomoaki., 2001, PASJ, 53, 85

[24] Dyson, 1973, A&A, 27, 459

[25] Elliot, K. H., Goudis, C., Meaburn, J., 1976, MNRAS, 175, 605

[26] Elmegreen, 1991, in The Physics of Star Formation and Early Stellar Evolution, ed. C. J. Lada, & N. D. Kylafis (Dordrecht: KluWer), 35

[27] Elmegreen, Kimura & Tosa., 1995, ApJ, 451, 675

[28] Fukuda & Hanawa, 2000, ApJ, 533, 911

[29] Garay & Lizano, 1999, PASP, 111, 1049

[30] González-Alfonso, Cernicharo & Radford, 1995, A&A, 293, 493

[31] Gyulbudagyan, 1986, ASTROPHYSICS (TR. ASTROFIZIKA) V. 23, NO. 2, 533

[32] Harju, J., Sahu, M., Henkel, C., Wilson, T. L., et al. 1990, A&A, 233, 197

[33] Hartley, M., Tritton, S. B., Manchester, R. N., 1986,A&AS, 63, 27

[34] Hawarden & Brand, 1976, MNRAS, 175P, 19

[35] Herbig, 1974, PASP, 86, 604

[36] Jansen, David J., van Dishoeck, Ewine F., Black, John H., 1994, A&A, 282, 605

[37] Jungwiert & Palous, 1994, A&A, 287, 55

[38] Kahn, 1969, Physica, 41, 172

[39] Kane, B. D., Clemens, D. P., & Myers, 1994, ApJ, 433L, 49

[40] Kane, B. D., Clemens, D. P., 1997, AJ, 113, 1799

[41] Keto & Myers, 1986, ApJ, 304, 466

[42] Kim, J. Serena., Walter, F. M., Wolk, S. J., 2002, AAS, 20113605

[43] Klein, Sandford, & Whitaker, 1983, ApJ, 271L, 69

[44] Lada, 1988, BAAS, 20, 1030

[45] Lada, Elizabeth A., Strom, Karen M., Myers, Philip C., 1993, In: Protostars and planets III (A93-42937 17-90), p. 245-277

[46] Lada & Lada, 2003, ARA&A, 41, 57L

[47] Larson, 1969, MNRAS, 145, 271

[48] Larson, 1982, MNRAS, 200, 159

[49] Launhardt, Ralf., Evans, Neal J., II., Wang, Yangsheng., 1998, ApJS, 119, 59

[50] Lefloch & Lazareff, 1994, A&A, 289, 559

[51] Lefloch, Lazareff and Castets, 1997 A&A, 324, 249

[52] Leung, in: Protostars and planets II (A86-12626 03-90). Tucson, AZ, University of Arizona Press, 1985, p. 104-136. Research supported by the Research Corp.

[53] Magnani, Blitz & Mundy, 1985, ApJ, 295, 402

[54] Martin & Barrett, 1978, ApJS, 36, 1

[55] Marco, A., Negueruela, I., 2002, A&A, 393, 195

[56] Meyer & Clayton, in: From Dust to Terrestrial Planets. Proceedings of an ISSI Workshop, held February 15-19, 1999, in Bern, Switzerland. Space Sciences series of International Space Science Institute (ISSI). Edited by W. Benz, R. Kallenbach, and G. W. Lugmair. Published by Kluwer Academic Publishers, P. O. Box 17, 3300 AA Dordrecht, The Netherlands, ISBN 0-7923-6467-8, p.133

[57] Mouschovias, 1991, ApJ, 373, 169

[58] Myers & Benson, 1983, ApJ, 266, 309

[59] Nakano, Takenori., 1998, ApJ, 494, 587

[60] Neckel & Staude, 1987, ApJ, 320L, 145

[61] Odenwald, Sten., Fischer, Jacqueline., Lockman, Felix J., Stemwedel, Sally., 1992, ApJ, 397, 174

[62] Ogura & Sugitani, 1998, PASA, 15, 91

[63] Ogura, Katsuo., Sugitani, Koji., Pickles, Andrew., 2002, AJ, 123, 2597

[64] Olano, C. A., Walmsley, C. M., Wilson, T. L., 1994, A&A, 290, 235

[65] Oort & Spitzer, 1955, ApJ, 121, 6O

[66] Petr, Monika G., Coude Du Foresto, Vincent., Beckwith, Steven V. W., et al., 1998, ApJ, 500, 825

[67] Pettersson, 1984, A&A, 139, 135

[68] Preibisch & Zinnecker, 1999, AJ, 117, 2381

[69] Reipurth, 1983, A&A, 117, 183

[70] Sandford, Whitaker, & Klein, 1982, ApJ, 260, 183

[71] Sandford, Whitaker, & Klein, 1984, ApJ, 282, 178

[72] Sandqvist, 1976, MNRAS, 177, 69

[73] Santos, N. C., Yun, J. L., Santos, C. A., Marreiros, R. G., 1998, AJ, 116, 1376

[74] Schneps, Ho & Barret, 1980, ApJ, 240, 84

[75] Shu, Frank H., Adams, Fred C., Lizano, Susana., 1987, ARA&A, 25, 23

[76] Spitzer & Jenkins, 1975, ARA&A, 13, 133

[77] Sridharan, T. K., 1992, JApA, 13, 217

[78] Sridharan, T. K., Bhatt, H. C., Rajagopal, J., 1996, MNRAS, 279, 1191

[79] Stephenson, 1986, ApJ, 300, 779

[80] Sugitani et al. 1989, ApJ, 342L, 87

[81] Sugitani, Fukui, Yasuo., Ogura, Katsuo., 1991, ApJS, 77, 59

[82] Sugitani, Koji., Tamura, Motohide., Ogura, Katsuo., 1995, ApJ, 455L, 39

[83] Sugitani, Koji., Morita, Koh-Ichiro., Nakano, Makoto., et al. 1997, ApJ, 486L, 141

[84] Tachibana & Huss, 2003, ApJ, 588L, 41

[85] Thompson, M. A., Urquhart, J. S., White, G. J., 2004, A&A, 415, 627

[86] Vanhala & Cameron, 1998, ApJ, 508, 291

[87] Vilas-Boas, Myers & Fuller, 1994, ApJ, 433, 96

[88] White G. J., 1993, A&A, 274, L33

[89] Williams P. M., Brand P. W. J. L, Longmore A. J., Hawarden T. G., 1977, MNRAS, 181, 709

[90] Yorke, 1986, ARA&A, 24, 49

[91] Yun, Joao Lin., Clemens, Dan P., 1990, ApJ, 365L, 73

[92] Yun & Clemens, 1992, ApJ, 385L, 21

[93] Yun & Clemens, 1994, AJ, 108, 612

[94] Yun & Clemens, 1995, AJ, 109, 742

[95] Zealey, W. J., Ninkov, Z., Rice, E., Hartley, M., Tritton, S. B., 1983, ApL, 23, 119

Chapter 2

Cometary Globule - CG 12

2.1 Introduction

CG 12 is an isolated globule (Figure 2.1) at a relatively large galactic latitude ($l = 316.5°, b = 21.2°$) associated with the reflection nebula NGC 5367 surrounding the double star $h4636$ in its head. The double star system $h4636$ consists of two B type stars (B4 + B7) with the northern component (B4) has Hα line in emission (Williams et al. 1977). The head of CG 12 is $\sim 10'$ in diameter, and its nebular tail is more than 1° in length and is oriented nearly perpendicular to the galactic plane. Optical polarimetric observations of three stars towards CG 12 showed the magnetic field lines in this region to be roughly parallel to the cometary tail of the globule (Marraco & Forte, 1978). Santos et al. (1998) showed the presence of a couple of objects in their near-infrared images of a region around IRAS 13546-3941 in CG 12 with near-infrared colours characteristic of low-mass YSOs. CG 12 has been detected in CO (Otrupcek, Hartley, & Wang, 2000; Yonekura et al. 1999; White, 1993; Van till, Loren & Davis, 1975) and in dense (number density of H_2 molecules $n_{H_2} > 10^3\ cm^{-3}$) gas tracers like H_2CO (Goss et al. 1980) and NH_3 (Bourke et al. 1995) molecular line observations. The CO and IRAS study of CG 12 by White (1993) revealed the presence of a bipolar molecular outflow centred close to IRAS 13547-3944 source and the double star $h4636$. The well collimated outflow found by White (1993) is extended roughly along the major axis of cometary globule. These observations show that star formation is currently taking place in CG 12. CG 12 is thus an example of a high galactic latitude cloud undergoing current star formation. However, the cause of the cometary morphology and the ongoing star formation is unknown. The observed cometary shape and star formation in CG 12 has been suggested (Williams et al. 1977) to have been caused by a high galactic latitude supernova explosion at $l = 320°, b = 30°$.

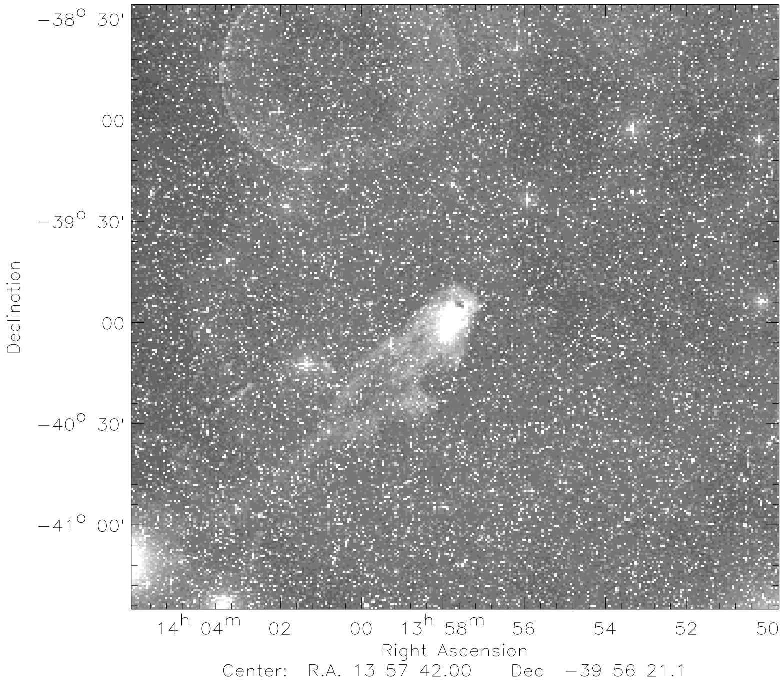

Figure 2.1: A images of the field (3° × 3°) containing CG 12 reproduced from Digitized Sky Survey (DSS) showing the isolated nature of the cloud. North is up and east is to the left.

The relatively high galactic latitude position ($b \simeq 21°$) of CG 12 could be due to two reasons. Either it is at a distance closer than $\sim$ 200 pc, adopting a scale height $\langle\ z\ \rangle$ of $\sim$ 60 pc above the galactic mid-plane for the clouds in the solar vicinity (Magnani, Blitz & Mundy, 1985; Keto & Myers 1986), or it is farther away and at a relatively large galactic height. Van till, Loren & Davis (1975), in order to estimate the mass of CG 12 from CO observations, assigned a distance of 300 pc assuming a value of 200 pc for the thickness of the galactic hydrogen gas layer in the solar vicinity and that CG 12 is at the upper limit of the range suggested by its galactic latitude. Using 300 pc as the distance, they estimated the mass of CG 12 as $\sim$ 30 $M_{\odot}$. Bourke et al. (1995) assigned a distance of 400 pc to CG 12 assuming it to be associated with cometary globules in Vela-Gum nebula region. Williams et al. (1977) from UBV photometry of 11 stars projected towards CG 12 which include stars associated with nebulosities within the cloud, determined a distance of 630 pc. Morraco and Forte (1978) estimated a distance of 660 pc based on observed β index and (β, M_V) calibration of a single star, star 2 (as numbered in Williams et al. 1977). Thus there exists a range (100-660 pc) of distances for CG 12 in the literature. The most favored distance to CG 12 is 630 pc estimated by Williams et al. (1977) since this distance estimate is based on stars of which some are associated with the cloud. The method assumes the stars to be on the zero age main sequence. However, the stars with nebulosities and infrared excesses are likely to be young and PMS objects. Thus absolute magnitudes, the character of reddening caused by the circumstellar dust around these stars and the distances derived should be considered uncertain. Uncertainty in the distance to the cloud leads to uncertainties in various derived physical parameters. For example the cloud mass derived from the measured gas column density scales as square of the distance. The star formation efficiency

$$SFE = \frac{M_{stars}}{(M_{stars} + M_{cloud})} \tag{2.1}$$

where M_{stars} and M_{cloud} are the total mass of the stars formed and the mass of the cloud respectively, will scale roughly inversely with the square of the distance if the stellar masses are derived from spectral types. The height of the cloud above the galactic plane scales linearly with distance. If CG 12 is a nearby cloud (say distance $<$ 200 pc), then this will be a low mass cloud with high SFE. On the other hand if it is as distant as $\sim$ 600 pc, then it is a massive cloud at a large ($\sim$ 200 pc) height above the galactic plane undergoing star formation with a lower SFE. In this case CG 12 would be one of those rare clouds forming early type stars at relatively large galactic heights [$\sim$ 200 pc as compared to the typical scale height of $\lesssim$ 65 pc for B type stars (Reed, 2000)]. Therefore, a determination of distance to CG 12 is important in order to find its true location in the Galaxy and study the process of star formation at high galactic latitudes. In PART I of this chapter, the distance to CG 12 is determined using optical and near-infrared broadband photometry.

Part I

Cometary Globule CG 12: Distance determination

2.2 Introduction

As for any astronomical object, the measurement of distance to an interstellar cloud is very important. Distances to interstellar clouds are needed in order to determine several important physical properties like sizes, masses and densities (Clemens, Yun & Heyer 1991). Distances are also needed for obtaining luminosities of any embedded YSOs or protostars in these clouds (Yun & Clemens 1990).

The traditional method of determining distances to interstellar clouds utilizes star counts (Bok & Bok 1941) or Wolf diagrams (Wolf 1923), which plot the number of stars versus apparent magnitude. However, the distance determination using these methods depends on questionable extrapolations of luminosity functions in order to work for small clouds. The other methods which have generally been used to determine the distance of interstellar clouds are: photometry (usually $UBVRI$ or Strömgren), distances of stars or fields associated with a cloud, kinematic distances from CO velocities, geometric distances from the galactic coordinates, using the empirical formula of Herbst & Sawyer (1981), D-line absorption spectra of NaI and polarised light from the background stars. An additional method of assigning distances to small dark clouds involves bracketing the cloud distance by using spectroscopic distances to stars close in front of and behind the cloud to infer the cloud distance (Hobbs, Blitz, & Magnani 1986). For a better estimate of distance to interstellar clouds, it is essential to have spectroscopic data for sufficient number of stars in front of and behind the cloud which is not only tedious but also requires lot of observing time. Using broad-band photometry and identifying unreddened M dwarfs in front of and reddened M dwarf stars behind the cloud from $(B-V)$ versus $(V-I)$ plots, one can bracket the cloud and determine its distance (Peterson & Clemens 1998). But finding M dwarfs both just in front of and behind the cloud is extremely difficult especially for small nearby clouds. In this chapter, we estimate the distance to

---

This chapter is based on the published work: Maheswar, G., Manoj, P., Bhatt, H. C., 2004, MNRAS, 355, 1272.

CG 12 using broad-band $VRIJHK$ photometry of stars in the field containing the cloud by using the method we present below.

2.3 The Method

The photometric (say in the V band) distance (d) to a star is given by

$$log\ d = \frac{(V - M_V + 5 - A_V)}{5} \tag{2.2}$$

where, V, M_V and A_V are apparent magnitude, absolute magnitude and extinction respectively. The distance can be determined if we know the absolute magnitude (M_V) and extinction (A_V). The absolute magnitude depends on the spectral type of the star. The spectral type also determines various colours $(V-R), (V-I), (V-J), (V-H), (V-K)$ *etc.* The observed colours are generally reddened due to interstellar extinction which is wavelength dependent. By assuming a value for A_V and the extinction law (considered here to be the mean interstellar extinction law and same for all the stars) one can estimate the various colour excesses and correct the observed colours to find the intrinsic colours of the stars. The computed intrinsic colours are then compared with the standard unreddened intrinsic colours of normal stars to determine the spectral type and hence M_V. Various trial values of A_V are used and a star is assigned a spectral type for which the computed colour indices best match (χ^2 minimum) with the standard intrinsic colour indices.

The method of determining distances to dark clouds involves five steps. First, measuring the observed $V, R, I, J, H, \& K$ magnitudes of the stars in the field containing the cloud. Second, finding the intrinsic colour indices $(V-R)_i, (V-I)_i, (V-J)_i, (V-H)_i, (V-K)_i$ of each star from the equations (2.3 - 2.7) obtained using the assumptions; (1) a normal interstellar extinction law (ratio of total-to-selective extinction, $R_V = 3.1$, Mathis 1990) (2) stars are in their main-sequence evolutionary stages. The equations relating the observed and dereddened colours are

$$(V-R)_i = (V-R)_o - 0.252A_V \tag{2.3}$$

$$(V-I)_i = (V-I)_o - 0.518A_V \tag{2.4}$$

$$(V-J)_i = (V-J)_o - 0.718A_V \tag{2.5}$$

$$(V-H)_i = (V-H)_o - 0.825A_V \tag{2.6}$$

$$(V-K)_i = (V-K)_o - 0.888A_V \tag{2.7}$$

where, $(V-R)_o, (V-I)_o, (V-J)_o, (V-H)_o, (V-K)_o$ are the observed colour indices and A_V is the interstellar extinction in the visual band, which is an unknown parameter in the above equations. Various trial values of A_V are used. For the illustrative case of CG 12, a set of A_Vs was used ranging from 0 to 6 in steps of 0.1 magnitude. These equations provide 60 sets of intrinsic colour indices for each star with each set corresponding to one value of A_V. Third, compare each of these 60 sets of intrinsic colour indices obtained for each star with the intrinsic colour indices for main-sequence stars of different spectral types. The main-sequence colour indices $(V-R)_{ms}$ & $(V-I)_{ms}$ are taken from Johnson (1966) and $(V-J)_{ms}, (V-H)_{ms}$ & $(V-K)_{ms}$ are taken from Koornneef (1983). One of the intrinsic colour indices among the 60 sets obtained for a star matches best with the intrinsic colour indices for main-sequence star of a particular spectral type giving a minimum value of χ^2 defined as

$$\chi^2 = \sum_{\lambda} \frac{[(V-\lambda)_i - (V-\lambda)_{ms}]^2}{(V-\lambda)^2_{ms}} \tag{2.8}$$

where $\lambda \equiv R, I, J, H \& K$.

This method not only provides spectral type for each star in the field but also the extinction towards it. Fourth, distance to each star can be obtained by using the equation 2.2, where values of M_V corresponding to the assigned spectral types are obtained from the absolute magnitude versus spectral type calibration (Schmidt-Kaler 1982). Fifth, the distance to the cloud is taken to be that value where, in a plot of extinction against distance to the star, the extinction increases steeply above the normal galactic extinction towards that direction. We nave used this method to obtain distance to the cometary globule CG 12 as described below.

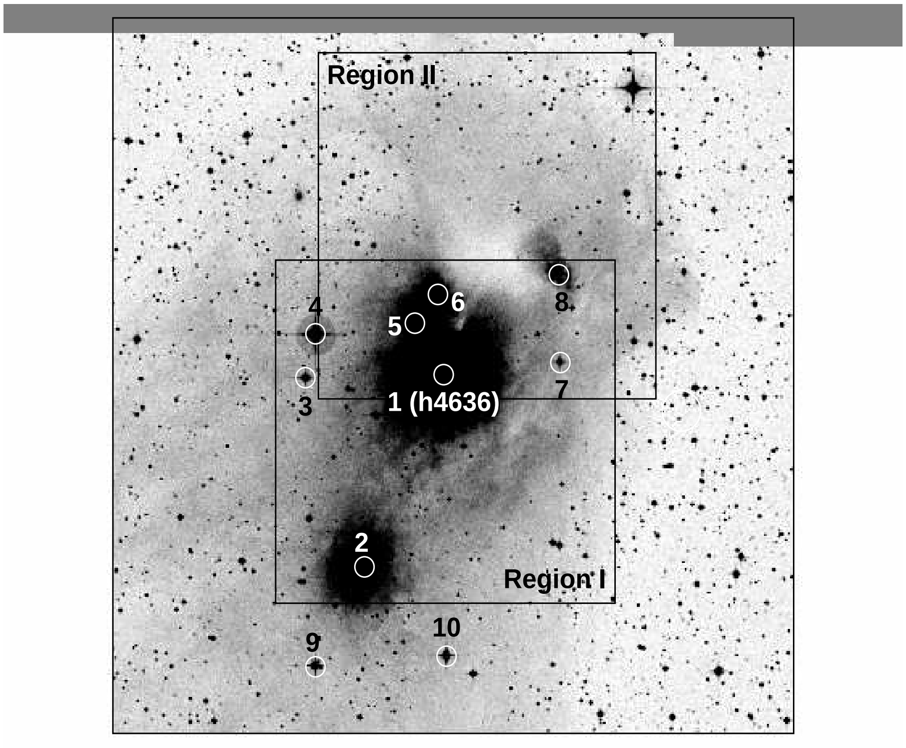

Figure 2.2: Regions, I & II, observed to measure photometric magnitudes of stars projected towards CG 12, are shown on this $20' \times 20'$ Digitized Sky Survey (DSS) image. North is up and east is to the left. Also numbered are stars studied by Williams et al (1977).

2.4 Observations and Data Analysis

Both photometric and spectroscopic observations of CG 12 were carried out with 2.34 m Vainu Bappu Telescope (VBT) at the Vainu Bappu Observatory, Kavalur (India).

2.4.1 Spectroscopy

Optical CCD spectra of 11 stars were obtained using the OMR (Optomechanics Research) spectrograph (Prabhu et al. 1998) on the VBT during the period 2001-2004. Photometric studies of these 11 stars which are projected towards the head region of CG 12 had earlier been carried out by Williams et al. (1977). All spectra were obtained with a slit of $2''$ width and spectral resolution $1.3 - 2.6$ $\AA\ pixel^{-1}$. All spectra were bias subtracted, flat-field corrected, extracted and wavelength calibrated in the standard manner using the

IRAF [1] reduction package. Spectral types were determined for the stars by comparing the observed spectrum with those in the atlas of Jacoby et al. (1984).

2.4.2 Optical Photometry

Images of CG 12 centred at two positions, $13^h57^m35^s - 39°54'19''$ (2000) (Region I) & $13^h57^m43^s - 40°00'54''$ (2000) (Region II) were carried out on 24 April, 2003 and 21 February, 2004 respectively at the prime focus (f/3.23) of VBT using Tektronix CCD chip of size $1024 \times 1024\, pixel^2$. The observed fields (each covering $10.75 \times 10.75\, arcmin^2$ of the sky) are shown in Figure 2.2 as Region I and Region II. Also marked in Figure 2.2 are stars studied by Williams et al. (1977) and numbered. Images were taken in $BVRI$ filters. Typical seeing during the observations was $\sim 2.5''$. During each observing run, twilight flats were acquired in all the filters. The bias frames were obtained at regular intervals. The bias frame closer to the observed image was used for bias subtraction. The flat frames were first bias-subtracted before stacking (using median) to obtain master flats for each filter. These master flats are used to flat-field the images. The star detection algorithm DAOFIND in IRAF was used to get the position of stars in the images. The aperture photometry was performed on the stars in the images using APPHOT in IRAF. The star 4 in Williams et al. (1977) was used to transform the observed fluxes to magnitudes. Observations of this star through B and V filters exist for three different epochs. The observed magnitudes in B and V filters are: 10.15 and 9.15 by Marraco and Forte (1978); 10.15 and 9.13 by Williams et al. (1977); 10.06 and 9.13 from Tycho-2 catalog. This shows that this star is not a photometric variable (within the observational errors) and can therefore be used to transform observed fluxes to magnitudes. The uncertainties in the derived magnitudes are generally $\sim$ 0.05 mag. The images taken through B filter were not deep enough and hence were not considered in further analysis. The processed CCD images of the fields containing CG 12 through V, R & I filters are shown in Figure 2.3. Figures 2.3 (a), 2.3 (b) & 2.3 (c) show CCD images of Region I through V, R & I filters respectively and Figures 2.3 (d), 2.3 (e) & 2.3 (f) show CCD images of Region II through V, R & I filters respectively.

---

[1] IRAF is distributed by National Optical Astronomy Observatories, USA.

2.4.3 2MASS Near-IR Measurements

Near-IR JHK_s magnitudes for the stars in both the frames were obtained from 2MASS [The Two Micron All Sky Survey, Cutri (2000)] catalogue. To ensure high-quality data, a maximum uncertainty of 0.1 mag was permitted in all the three bands. The JHK_s colours were transformed from 2MASS system to Koornneef system using the relations given by Carpenter (2001).

2.5 Results and Discussion

2.5.1 Distance to CG 12

A total of 143 stars from Region I and Region II are selected and the photometric results are presented in Tables 2.1 and 2.2 respectively. The eleven stars studied by Williams et al. (1977) (shown and identified in Figure 2.2) of which some are associated with nebulosities and have near-infrared excesses and hence could be PMS stars, are excluded from the current analysis. In both Table 2.1 and 2.2, columns 1, 2 and 3 are self-explanatory. Columns 4-9, give photometric magnitudes and corresponding errors in V, R, I filters from our observations. Columns 10-15 give photometric magnitudes and corresponding errors in J, H, K filters obtained from 2MASS observations. Columns 16-18 give A_V, χ^2 and spectral type obtained from the method described in section 2.3. Column 19 gives absolute magnitudes (M_V) for the corresponding spectral types and column 20 gives the estimated distances to the stars using equation (2.2). The estimated distance and A_V of stars projected towards CG 12 are plotted in Figure 2.4. Our stars for which $\chi^2 \lesssim 0.1$ are used in the plot. We have separated the stars observed into two groups depending on whether they are within or outside the cloud boundary [judged visually from Digitized Sky Survey (DSS) images]. In Figure 2.4, filled and unfilled circles represent stars found projected within and outside the cloud boundary respectively. In order to understand the global variation of extinction in the direction of CG 12, we have also considered other stars within a radius of 5° of CG 12 for which spectral information is known from the literature. B and V magnitudes of these stars were taken from Tycho-2 catalog (Hog et al. 2000). Distances and extinction for these

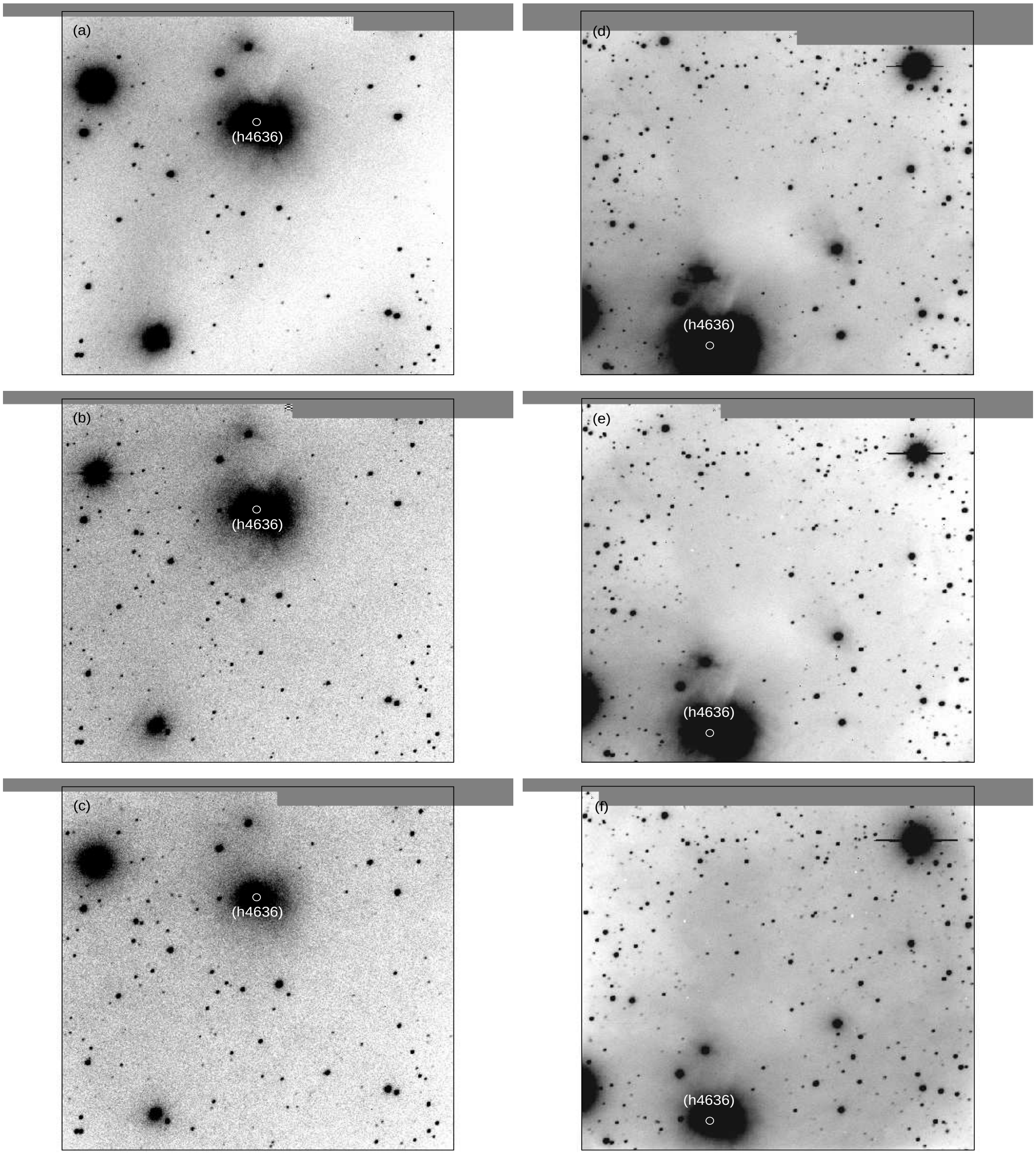

Figure 2.3: CCD images of the observed fields shown in Figure 2.2. North is up and east is to the left. Figures (a), (b) & (c) are CCD images of Region I in V, R & I filters respectively and Figures (d), (e) & (f) are CCD images of Region II in V, R & I filters respectively. All the CCD images cover a 10.75×10.75 $arcmin^2$ area each on the sky. The brightest star $h4636$ (star 1 in Williams et al. 1977), surrounded by nebulosity, is marked on each image.

stars were estimated and over plotted in Figure 2.4 represented by unfilled squares. The solid line represents the galactic obscuration as a function of distance (d) at a galactic latitude of 21° obtained from the expression given by Bahcall & Soneira (1980). They have assumed an exponential variation of the density of obscuring layer with height above the galactic plane.

Examination of Figure 2.2 shows that the reflecting material in CG 12 is not distributed uniformly and lacks sharp boundary unlike in some of the dark globules such as Barnard 68 (Bok 1977). Therefore the increase in A_V with distance, even for stars projected within the cloud boundary is not expected to take a step-like jump at the distance of CG 12. Extinction towards stars projected outside the cloud boundary is found to increase slowly with distance, but is generally $\lesssim 0.7$ mag even for distances as large as ~ 1 kpc. These stars represent the behaviour of extinction due to the general interstellar medium in the direction. It can be seen from Figure 2.4 that most of the stars that show extinction values much larger than expected due to the general interstellar medium are at distances $\gtrsim 550$ pc. This (550 pc) is also the distance at which a distinct jump in extinction appears, although a few stars at ~ 400 pc show unusually large values of extinction ($A_V \gtrsim 2$ mag). As discussed in section 2.5.2, for stars showing large values of A_V, the reddening law could be anomalous and their derived distances would be less reliable. We therefore disregard these stars and ascribe the sharp rise in extinction at ~ 550 pc to the presence of the cloud CG 12 at this distance. The star with $A_V \approx 1$ mag and distance ≈ 200 pc in Figure 2.2 shows an unusually large extinction for its derived distance. This star could be red giant behind the cloud. Its observed colours are equally well fit ($\chi^2 = 0.0590$ as compared with the $\chi^2 = 0.0602$ for a fit with main sequence K5 spectral type) by a reddened K4 giant with $A_V \sim 0.7$ mag at a distance of ~ 7 kpc. This and other possible errors and uncertainties in the distance determination using this method are discussed in section 2.5.2 .

Photometry in UBV for 11 stars projected towards the head region of CG 12 was performed by Williams et al. (1977). From the two-colour diagram they concluded that most of the stars are reddened variously. A colour-magnitude diagram from $(B-V)_o$ and V_o found by tracing the stars back along standard reddening vectors in two-colour diagram was drawn and a ZAMS with a distance modulus of 9 mag was fitted to the stars which are illuminating the nebulosity. From their study, stars 2, 7, 8 and both components of $h4636$ fall on ZAMS. They assumed star 5 and 6 to be pre-main-sequence, and star 4 an unreddened foreground star. Marraco and Forte, (1978) assigned a spectral type of B6V and an absolute magnitude M_V of + 0.2 to star 2 by means of observed β index and (β, M_V) calibration. They derived a distance of 660 pc to CG 12 assuming $R_V = 3$. We have estimated distances to these stars by determining their spectral types from the observed spectra.

Our spectroscopic results for the 11 stars studied by Williams et al. (1977) are given in Table 2.3. Column 1 gives star numbers as given by Williams et al. (1977). 1N and 1S represent northern and southern components of $h4636$ respectively. Columns 2 and 6 give observed magnitudes in V band and $(B-V)$ values taken from Williams et al. (1977) respectively. Column 3 gives spectral types determined by comparing the observed spectrum with those in the atlas of Jacoby et al. (1984). The spectral types determined by us and that estimated by Williams et al. (1977) from two-colour diagram are in good agreement with each other except for star 5. We have observed a spectral type of G9 for star 5 whereas they have assigned a spectral type of A4 to it. We note, however, that for star 5 if its spectral type were A4 as inferred by Williams et al. (1977) then its distance and extinction values would be 570 pc and $\sim$ 2.4 magnitude respectively. Columns 4 and 5 give corresponding intrinsic colour index and absolute magnitude respectively. Columns 7, 8 and 13 give estimated colour excess, A_V $(= 3.1 \times E(B-V))$ and distance to the stars. near-infrared colour indices (JHK magnitudes are from 2MASS) are given in columns 9 and 11 respectively with colour excesses in coloums 10 and 12 respectively.

The distances and A_V for the 11 stars are over plotted in Figure 2.4 represented by unfilled star symbols. Extinction towards stars 3, 4, 5 and 10 is $\lesssim 0.5$ and their distances are 501, 417, 204 and 427 respectively. Stars 2, 6, 8 and $h4636$ are clearly associated with CG 12 since there exist reflection nebulosities around them. Extinction values for these stars are $\gtrsim 0.7$ mag and they have a wide range of derived distances ($\sim$ 800-1200). Stars 7 and 9 also have extinction $\gtrsim 0.7$ mag and may be also associated with CG 12.

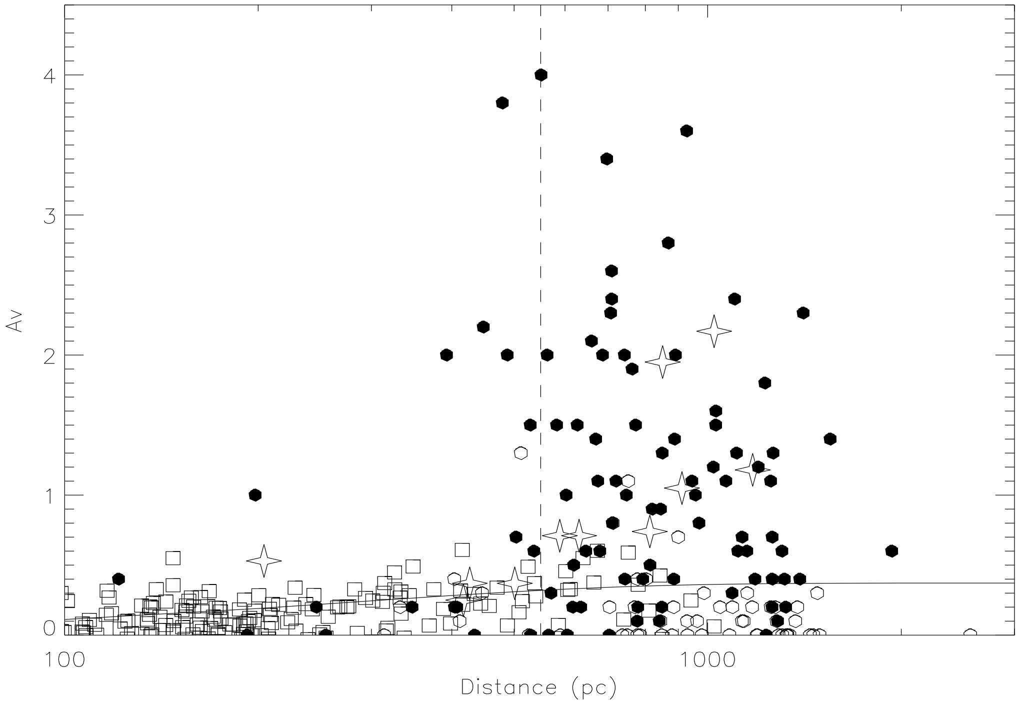

Figure 2.4: Distance-A_V plot for stars in regions I & II using the method described in § 2. In this figure, ***unfilled stars:*** stars studied by Williams et al. (1977); ***filled circles:*** stars found projected within the cloud boundary; ***unfilled circles:*** stars found projected outside the cloud boundary; ***unfilled squares:*** stars within a radius of 5° of CG 12 from literature. The ***solid line*** represents the galactic obscuration as a function of distance (d) at a galactic latitude of 21° obtained from the expression given by Bahcall & Soneira (1980). The ***vertical dash line*** is drawn at a distance of 550 pc (see § **2.5.1** for more explanations).

Thus for distances $\lesssim$ 600 pc the extinction is $\lesssim$ 0.5 but beyond $\sim$ 600 pc the extinction increases to $\gtrsim$ 0.7 mag, similar to that of star 2 which is associated with the cloud.

Based on this partial analysis of 11 stars, one would conclude that the cloud is at a distance of $\sim$ 600 pc. However, the derived distances to stars 2, 6, 8 and h4636 with nebulosities show a wide range. Their distances should be considered very uncertain for various causes discussed below.

2.5.2 Errors and Uncertainties

The main contribution to the errors in deriving distances to stars projected towards a cloud using the method described in § 2.3 comes from the following:

Table 2.1: Photometric results for stars in Region I.

S No (1)	RA (°) (2000) (2)	DEC (°) (2000) (3)	V (4)	ϵ_V (5)	R (6)	ϵ_R (7)	I (8)	ϵ_I (9)	J (10)	ϵ_J (11)	H (12)	ϵ_H (13)	K (14)	ϵ_K (15)	A_V (16)	χ^2 (17)	Sp (18)	M_V (19)	D (pc) (20)
1	209.335	-39.925	17.15	0.03	16.32	0.04	15.20	0.03	14.51	0.03	13.85	0.03	13.58	0.04	0.4	0.0846	K5	7.4	743
2	209.343	-40.005	19.06	0.07	17.75	0.06	16.95	0.05	15.49	0.07	14.71	0.07	14.33	0.08	1.6	0.0717	K5	7.4	1030
3	209.346	-40.055	17.30	0.04	16.26	0.03	15.08	0.03	14.22	0.03	13.63	0.03	13.39	0.04	1.0	0.0471	K5	7.4	603
4	209.350	-40.045	16.05	0.03	15.41	0.03	14.77	0.03	14.24	0.03	13.68	0.03	13.53	0.05	0.2	0.0454	K2	6.4	779
5	209.357	-40.034	15.55	0.02	14.87	0.02	14.32	0.02	13.81	0.03	13.21	0.02	13.08	0.03	0.2	0.0235	K2	6.4	617
6	209.363	-40.061	13.22	0.02	12.35	0.02	11.50	0.02	10.46	0.02	9.72	0.03	9.45	0.02	0.4	0.0966	K5	7.4	121
7	209.369	-40.084	17.85	0.04	16.55	0.04	15.02	0.03	13.75	0.03	13.10	0.02	12.79	0.03	2.2	0.0823	K5	7.4	448
8	209.376	-40.060	18.99	0.06	17.88	0.06	17.07	0.05	15.76	0.07	15.15	0.08	14.65	0.09	1.1	0.0766	K5	7.4	1253
9	209.376	-40.042	18.54	0.05	17.47	0.05	16.31	0.04	15.14	0.04	14.30	0.05	13.97	0.05	1.4	0.1041	K5	7.4	888
10	209.390	-40.093	18.16	0.05	17.08	0.04	16.46	0.04	15.52	0.05	14.86	0.07	14.85	0.13	0.4	0.0119	K5	7.4	1185
11	209.410	-40.069	18.43	0.05	17.61	0.05	17.12	0.06	16.24	0.11	15.70	0.15	15.64	0.22	0.6	0.0304	K2	6.4	1934
12	209.414	-40.021	17.16	0.03	16.14	0.03	15.14	0.03	14.38	0.03	13.70	0.02	13.61	0.04	0.6	0.0229	K5	7.4	680
13	209.415	-40.069	18.23	0.05	17.31	0.05	16.21	0.04	15.54	0.05	14.73	0.05	14.70	0.11	0.6	0.0544	K5	7.4	1114
14	209.417	-40.093	19.04	0.06	17.54	0.05	16.77	0.05	15.92	0.07	15.12	0.10	14.87	0.12	1.2	0.0209	K7	7.8	1020
15	209.417	-40.057	18.19	0.05	16.86	0.04	15.67	0.03	14.50	0.02	13.73	0.04	13.53	0.04	2.1	0.0226	K4	7.0	660
16	209.423	-40.086	18.35	0.05	17.09	0.04	16.09	0.04	15.84	0.07	15.29	0.10	14.98	0.15	0.1	0.0024	M0	8.8	777
17	209.444	-40.046	17.34	0.04	16.24	0.03	15.50	0.03	14.52	0.03	13.91	0.04	13.65	0.04	1.5	0.0114	K2	6.4	773
18	209.446	-40.016	16.86	0.03	16.00	0.03	15.27	0.03	14.49	0.04	13.91	0.03	13.79	0.05	0.9	0.0256	K2	6.4	820
19	209.451	-40.020	16.45	0.03	15.70	0.03	15.04	0.03	14.36	0.02	13.82	0.04	13.75	0.05	0.5	0.0330	K2	6.4	814
20	209.452	-40.038	19.20	0.07	17.89	0.06	16.97	0.05	16.01	0.08	15.10	0.09	15.08	0.14	1.3	0.0063	K5	7.4	1264
21	209.453	-40.067	17.02	0.03	15.80	0.03	15.02	0.03	14.04	0.03	13.29	0.02	13.11	0.03	1.5	0.0079	K3	6.7	582
22	209.454	-40.011	16.61	0.03	15.61	0.03	14.77	0.03	13.72	0.03	12.98	0.03	12.77	0.03	0.7	0.0537	K5	7.4	504
23	209.456	-40.027	16.93	0.03	16.12	0.03	15.36	0.03	14.54	0.03	13.97	0.04	13.75	0.05	0.9	0.0575	K2	6.4	845
24	209.460	-40.039	18.11	0.05	17.30	0.05	16.58	0.05	15.50	0.06	15.13	0.08	14.83	0.12	0.4	0.0799	K4	7.0	1391
25	209.462	-39.984	17.92	0.04	17.00	0.04	16.22	0.04	15.25	0.05	14.64	0.06	14.33	0.10	1.3	0.0593	K2	6.4	1109
26	209.464	-40.078	16.81	0.03	15.69	0.03	14.97	0.03	14.27	0.04	13.72	0.04	13.58	0.05	0.2	0.0027	K6	7.6	636
27	209.469	-40.093	17.49	0.04	16.54	0.04	15.85	0.04	15.17	0.05	14.63	0.05	14.30	0.09	0.3	0.0050	K4	7.0	1091
28	209.476	-40.002	13.32	0.02	12.85	0.02	12.50	0.02	12.26	0.02	11.88	0.02	11.87	0.02	0.0	0.0195	G2	4.7	531
29	209.485	-40.011	17.84	0.04	16.52	0.04	15.07	0.03	13.99	0.03	13.35	0.03	12.98	0.03	2.0	0.0439	K5	7.4	488
30	209.490	-39.963	17.99	0.04	16.98	0.04	16.27	0.04	15.50	0.06	14.84	0.06	14.64	0.10	1.2	0.0031	K2	6.4	1199
31	209.490	-39.990	16.23	0.03	15.53	0.03	14.56	0.03	14.22	0.04	13.61	0.04	13.33	0.05	0.0	0.0780	K4	7.0	703
32	209.493	-40.013	18.18	0.05	16.90	0.04	15.71	0.04	14.54	0.04	13.68	0.03	13.31	0.04	2.0	0.0473	K4	7.0	687
33	209.494	-39.998	16.08	0.03	15.24	0.03	14.52	0.03	13.66	0.03	13.05	0.03	12.82	0.03	0.3	0.0424	K4	7.0	571
34	209.500	-40.037	19.44	0.08	18.14	0.06	17.22	0.06	16.09	0.09	15.38	0.10	15.09	0.14	2.3	0.0109	K2	6.4	1408
35	209.501	-40.051	18.56	0.05	17.37	0.05	16.36	0.04	15.25	0.05	14.64	0.06	14.26	0.08	1.5	0.0254	K4	7.0	1029
36	209.502	-40.090	15.58	0.02	14.71	0.02	13.95	0.02	13.21	0.03	12.70	0.03	12.57	0.03	0.0	0.0181	K5	7.4	434
37	209.502	-40.021	15.23	0.02	14.32	0.02	13.69	0.02	13.08	0.03	12.46	0.03	12.32	0.03	0.2	0.0023	K4	7.0	404
38	209.502	-39.951	16.29	0.03	15.56	0.03	14.92	0.03	14.37	0.03	13.85	0.04	13.77	0.05	0.4	0.0251	K2	6.4	793
39	209.512	-39.981	17.30	0.04	16.33	0.04	15.68	0.03	14.87	0.03	14.45	0.06	14.11	0.06	1.0	0.0063	K2	6.4	957
40	209.518	-40.050	14.00	0.02	13.31	0.02	12.84	0.02	12.46	0.02	11.92	0.03	11.86	0.03	0.2	0.0055	K1	6.1	347
41	209.521	-40.040	17.99	0.04	16.99	0.04	16.28	0.04	15.63	0.06	15.21	0.08	14.81	0.12	0.4	0.0048	K4	7.0	1316
42	209.522	-39.979	18.60	0.06	17.63	0.05	16.44	0.04	15.84	0.08	15.17	0.09	15.00	0.13	0.7	0.0515	K5	7.4	1260
43	209.522	-40.073	15.85	0.02	15.09	0.03	14.42	0.03	13.74	0.02	13.33	0.03	13.10	0.03	0.5	0.0287	K2	6.4	619
44	209.524	-39.993	18.94	0.06	17.23	0.05	16.41	0.04	14.99	0.04	14.09	0.04	13.78	0.05	2.3	0.0542	K5	7.4	707
45	209.525	-40.004	18.08	0.05	16.63	0.04	15.59	0.03	14.63	0.04	13.98	0.04	13.80	0.06	1.5	0.0045	K6	7.6	627
46	209.527	-40.031	18.30	0.05	17.30	0.05	16.62	0.05	15.37	0.05	14.71	0.06	14.79	0.12	0.6	0.0667	K5	7.4	1151
47	209.529	-39.997	18.10	0.05	17.34	0.05	16.29	0.04	15.59	0.06	15.01	0.08	14.89	0.12	0.2	0.0890	K5	7.4	1260
48	209.533	-40.060	17.53	0.04	16.41	0.04	15.39	0.03	14.37	0.03	13.61	0.03	13.27	0.04	1.4	0.0379	K4	7.0	670
49	209.536	-40.085	18.18	0.05	16.93	0.04	15.63	0.03	15.03	0.04	14.47	0.05	14.01	0.06	1.1	0.0215	K7	7.8	720
50	209.537	-39.964	16.23	0.03	15.53	0.03	14.91	0.03	14.48	0.03	13.89	0.04	13.83	0.05	0.4	0.0219	K1	6.1	886
51	209.538	-40.066	18.33	0.05	17.28	0.05	16.02	0.04	15.44	0.05	14.71	0.07	14.44	0.08	0.8	0.0478	K6	7.6	970
52	209.541	-40.089	17.36	0.04	16.57	0.04	15.81	0.04	15.16	0.04	14.56	0.05	14.50	0.09	0.7	0.0338	K2	6.4	1131
53	209.320	-40.002	16.78	0.03	16.19	0.03	15.58	0.03	15.10	0.04	14.61	0.05	14.61	0.10	0.0	0.0496	K2	6.4	1192
54	209.321	-40.058	17.27	0.04	16.73	0.04	16.01	0.04	15.67	0.08	14.94	0.09	15.06	0.15	0.0	0.1022	K2	6.4	1494
55	209.324	-40.024	15.43	0.02	14.86	0.02	14.37	0.03	13.89	0.03	13.45	0.03	13.42	0.04	0.0	0.0388	K1	6.1	737
56	209.326	-40.040	16.13	0.03	15.48	0.03	14.95	0.03	14.37	0.03	13.81	0.04	13.71	0.05	0.1	0.0288	K2	6.4	845
57	209.339	-40.082	16.64	0.03	16.25	0.03	15.76	0.04	15.62	0.07	15.30	0.11	15.21	0.16	0.0	0.0741	G1	4.6	2562
58	209.342	-40.079	17.24	0.04	16.11	0.03	14.82	0.03	13.85	0.03	13.38	0.03	13.06	0.03	1.3	0.0533	K5	7.4	512
59	209.342	-40.038	17.78	0.04	17.04	0.04	16.36	0.04	15.58	0.06	14.81	0.06	14.80	0.10	0.1	0.0654	K4	7.0	1369
60	209.343	-40.057	17.87	0.04	16.88	0.04	15.79	0.04	15.04	0.05	14.35	0.05	14.22	0.07	0.7	0.0387	K5	7.4	900
61	209.347	-40.052	17.58	0.04	16.80	0.04	16.13	0.04	15.44	0.07	14.88	0.08	14.77	0.12	0.0	0.0240	K4	7.0	1307
62	209.377	-40.089	16.79	0.03	16.19	0.03	15.57	0.03	14.96	0.04	14.307	0.04	14.35	0.08	0.2	0.0808	K2	6.4	1093

Table 2.2: Photometric results for stars in Region II.

S No (1)	RA (°) (2000) (2)	DEC (°) (2000) (3)	V (4)	ϵ_V (5)	R (6)	ϵ_R (7)	I (8)	ϵ_I (9)	J (10)	ϵ_J (11)	H (12)	ϵ_H (13)	K (14)	ϵ_K (15)	A_V (16)	χ^2 (17)	Sp (18)	M_V (19)	D (pc) (20)
1	209.311	-39.975	19.00	0.03	17.66	0.02	15.98	0.01	14.82	0.04	14.17	0.04	14.01	0.07	2.4	0.0888	K5	7.4	709
2	209.315	-39.898	13.43	0.01	12.81	0.01	12.35	0.01	11.76	0.02	11.37	0.02	11.26	0.02	0.0	0.0337	K2	6.4	255
3	209.321	-39.953	17.47	0.02	16.32	0.02	15.19	0.01	14.01	0.03	13.19	0.02	12.87	0.03	1.5	0.0725	K5	7.4	530
4	209.333	-39.902	16.86	0.02	16.01	0.01	15.37	0.01	14.65	0.04	14.03	0.05	13.85	0.05	0.2	0.0165	K4	7.0	849
5	209.335	-39.925	17.40	0.02	16.36	0.02	15.36	0.01	14.51	0.03	13.85	0.03	13.58	0.04	0.8	0.0262	K5	7.4	711
6	209.335	-39.877	17.71	0.02	16.62	0.02	15.52	0.01	14.60	0.03	14.05	0.04	13.75	0.06	1.0	0.0311	K5	7.4	748
7	209.347	-39.905	17.47	0.02	16.79	0.02	16.12	0.01	15.33	0.05	14.88	0.06	14.53	0.09	0.0	0.0717	K4	7.0	1234
8	209.350	-39.952	14.89	0.01	14.31	0.01	13.88	0.01	13.40	0.03	12.96	0.02	12.86	0.03	0.0	0.0341	K1	6.1	566
9	209.350	-39.875	17.20	0.02	16.55	0.02	15.97	0.01	15.32	0.06	14.93	0.09	14.75	0.10	0.2	0.0405	K2	6.4	1323
10	209.360	-39.947	19.84	0.04	18.22	0.03	17.16	0.02	15.40	0.06	14.48	0.05	13.98	0.06	2.8	0.0940	K5	7.4	869
11	209.361	-39.911	18.25	0.02	17.31	0.02	16.51	0.02	15.53	0.07	14.87	0.06	14.56	0.10	0.4	0.0522	K5	7.4	1260
12	209.370	-39.883	17.07	0.02	16.30	0.02	15.63	0.02	15.57	0.06	14.89	0.07	14.75	0.10	0.6	0.0333	K0	5.9	1305
13	209.371	-39.884	17.05	0.02	16.21	0.02	15.44	0.01	14.99	0.04	14.48	0.06	14.22	0.07	1.4	0.0163	G2	4.7	1551
14	209.379	-39.966	19.26	0.03	17.96	0.03	16.93	0.02	15.89	0.08	14.93	0.07	14.72	0.10	1.8	0.0173	K4	7.0	1227
15	209.378	-39.926	20.05	0.04	18.23	0.03	16.33	0.02	14.52	0.04	13.96	0.04	13.57	0.05	4.0	0.0679	K5	7.4	551
16	209.384	-39.977	18.70	0.03	17.30	0.02	15.96	0.01	14.89	0.03	14.24	0.05	13.95	0.06	2.0	0.0173	K5	7.4	742
17	209.385	-39.906	15.31	0.01	14.69	0.01	14.23	0.01	13.70	0.03	13.15	0.03	13.12	0.03	0.0	0.0317	K2	6.4	605
18	209.394	-39.886	18.32	0.02	17.26	0.02	16.19	0.01	15.18	0.05	14.43	0.04	13.98	0.06	1.1	0.0629	K5	7.4	945
19	209.402	-39.956	18.29	0.02	17.12	0.02	15.89	0.01	14.95	0.04	14.45	0.06	14.10	0.07	1.3	0.0330	K5	7.4	850
20	209.400	-39.888	19.96	0.04	18.55	0.03	17.18	0.02	15.81	0.07	15.08	0.08	14.58	0.09	2.4	0.0547	K5	7.4	1102
21	209.408	-39.858	16.59	0.01	15.68	0.01	14.80	0.01	13.76	0.03	13.02	0.03	12.72	0.02	0.6	0.0856	K5	7.4	537
22	209.416	-39.901	18.10	0.02	16.85	0.03	15.45	0.01	14.19	0.03	13.56	0.03	13.28	0.04	2.0	0.0731	K5	7.4	563
23	209.421	-39.868	18.77	0.03	17.48	0.02	16.26	0.02	15.10	0.04	14.50	0.06	14.11	0.06	2.0	0.0307	K4	7.0	891
24	209.435	-39.864	18.66	0.03	17.40	0.02	15.98	0.01	14.93	0.03	14.26	0.06	13.95	0.06	1.9	0.0500	K5	7.4	763
25	209.450	-39.958	12.81	0.01	12.22	0.01	11.81	0.01	11.21	0.02	10.71	0.02	10.62	0.02	0.0	0.0501	K2	6.4	192
26	209.452	-39.872	17.00	0.02	16.01	0.01	15.11	0.01	14.29	0.04	13.55	0.04	13.39	0.04	0.6	0.0280	K5	7.4	647
27	209.458	-39.920	19.20	0.03	17.70	0.02	16.29	0.02	14.91	0.05	13.97	0.04	13.73	0.04	2.6	0.0418	K5	7.4	709
28	209.474	-39.959	20.78	0.06	18.99	0.04	17.29	0.02	15.77	0.08	15.04	0.07	14.63	0.10	3.6	0.0199	K5	7.4	928
29	209.476	-39.923	14.83	0.01	13.80	0.01	12.77	0.01	11.74	0.02	11.02	0.02	10.75	0.02	1.0	0.0602	K5	7.4	198
30	209.482	-39.990	19.55	0.04	17.78	0.02	15.90	0.01	14.33	0.03	13.53	0.03	13.20	0.04	3.8	0.0494	K5	7.4	480
31	209.487	-39.922	14.65	0.01	14.00	0.01	13.45	0.01	12.82	0.02	12.34	0.03	12.19	0.03	0.2	0.0381	K2	6.4	407
32	209.490	-39.990	16.14	0.01	15.26	0.01	14.42	0.01	14.22	0.04	13.61	0.04	13.33	0.05	1.1	0.0263	K0	5.9	675
33	209.490	-39.963	17.66	0.02	16.82	0.02	16.14	0.01	15.50	0.06	14.84	0.06	14.64	0.10	0.1	0.0161	K4	7.0	1285
34	209.493	-39.989	14.50	0.01	13.63	0.01	12.82	0.01	12.01	0.02	11.35	0.03	11.05	0.02	0.2	0.0433	K5	7.4	246
35	209.493	-39.946	19.96	0.04	18.34	0.03	16.59	0.02	15.05	0.04	14.24	0.04	13.93	0.06	3.4	0.0636	K5	7.4	697
36	209.492	-39.911	18.59	0.02	17.51	0.02	16.36	0.02	15.45	0.05	14.65	0.05	14.56	0.09	1.1	0.0441	K5	7.4	1068
37	209.500	-39.931	17.32	0.02	16.05	0.01	14.68	0.01	13.43	0.02	12.68	0.03	12.36	0.02	2.0	0.0687	K5	7.4	393
38	209.502	-39.951	16.12	0.01	15.49	0.01	14.87	0.01	14.37	0.03	13.85	0.04	13.77	0.05	0.1	0.0396	K2	6.4	841
39	209.282	-39.890	13.88	0.01	13.31	0.01	12.81	0.01	12.34	0.02	11.69	0.02	11.66	0.03	0.0	0.0568	K2	6.4	314
40	209.284	-39.877	14.33	0.01	13.84	0.01	13.45	0.01	13.09	0.03	12.63	0.03	12.62	0.03	0.2	0.0467	G2	4.7	770
41	209.288	-39.958	14.97	0.01	14.40	0.01	13.96	0.01	13.59	0.02	13.22	0.03	13.14	0.04	0.3	0.0124	G2	4.7	987
42	209.291	-39.970	15.85	0.01	15.20	0.01	14.70	0.01	14.16	0.03	13.61	0.03	13.54	0.04	0.0	0.0198	K2	6.4	778
43	209.291	-39.953	15.85	0.01	15.30	0.01	14.80	0.01	14.31	0.03	13.84	0.02	13.95	0.06	0.0	0.0550	K1	6.1	880
44	209.292	-39.862	16.34	0.01	15.67	0.01	15.16	0.01	14.60	0.03	13.96	0.03	13.89	0.05	0.1	0.0273	K2	6.4	929
45	209.294	-39.913	14.74	0.01	14.16	0.01	13.68	0.01	13.20	0.02	12.76	0.02	12.64	0.03	0.0	0.0360	K1	6.1	527
46	209.294	-39.889	14.71	0.01	14.24	0.01	13.86	0.01	13.52	0.03	13.12	0.03	13.10	0.03	0.1	0.0328	G2	4.7	963
47	209.297	-39.916	16.54	0.01	15.88	0.02	15.28	0.01	14.64	0.03	14.05	0.04	13.88	0.05	0.0	0.0515	K3	6.7	930
48	209.300	-39.969	14.94	0.01	14.23	0.01	13.65	0.01	13.02	0.02	12.43	0.02	12.32	0.02	0.3	0.0293	K2	6.4	446
49	209.300	-39.860	14.48	0.01	13.99	0.01	13.61	0.01	13.31	0.03	12.94	0.04	12.94	0.04	0.0	0.0162	G3	4.8	849
50	209.304	-39.983	15.30	0.01	14.74	0.01	14.32	0.01	13.94	0.03	13.49	0.03	13.44	0.04	0.3	0.0240	G2	4.7	1152
51	209.303	-39.940	17.74	0.02	16.94	0.02	16.20	0.01	15.50	0.05	14.91	0.06	14.74	0.10	0.2	0.0292	K4	7.0	1274
52	209.310	-39.967	13.55	0.01	13.08	0.01	12.72	0.01	12.47	0.03	12.06	0.02	12.01	0.02	0.0	0.0185	G2	4.7	590
53	209.314	-39.992	16.74	0.01	16.10	0.02	15.59	0.01	15.30	0.06	14.79	0.06	14.70	0.10	0.0	0.0111	K1	6.1	1327
54	209.313	-39.961	15.83	0.01	15.18	0.01	14.56	0.01	13.92	0.03	13.57	0.04	13.37	0.04	0.2	0.0411	K2	6.4	704
55	209.313	-39.833	15.50	0.01	14.92	0.01	14.46	0.01	14.04	0.03	13.54	0.03	13.48	0.04	0.0	0.0270	K1	6.1	750
56	209.313	-39.841	15.85	0.01	15.40	0.01	14.77	0.01	14.63	0.04	14.17	0.05	14.06	0.07	0.0	0.0872	G9	5.7	1081
57	209.314	-39.860	14.17	0.01	13.71	0.01	13.30	0.01	13.03	0.03	12.69	0.03	12.58	0.03	0.0	0.0233	G2	4.7	785
58	209.334	-39.846	16.68	0.01	16.10	0.02	15.67	0.01	15.25	0.05	14.57	0.05	14.66	0.09	0.0	0.0471	K1	6.1	1289
59	209.356	-39.850	16.69	0.01	15.99	0.02	15.45	0.01	14.82	0.04	14.19	0.05	14.15	0.07	0.2	0.0273	K2	6.4	1045
60	209.362	-39.857	17.03	0.02	16.36	0.02	15.81	0.01	15.38	0.06	14.85	0.08	14.67	0.10	0.1	0.0177	K2	6.4	1280
61	209.368	-39.827	17.19	0.02	16.59	0.02	16.07	0.01	15.70	0.06	15.11	0.07	14.86	0.10	0.0	0.0447	K2	6.4	1443
62	209.382	-39.842	17.71	0.02	16.85	0.02	16.19	0.01	15.43	0.05	14.71	0.07	14.71	0.10	0.2	0.0248	K4	7.0	1254
63	209.389	-39.836	16.78	0.02	16.18	0.02	15.71	0.01	15.19	0.04	14.67	0.05	14.56	0.10	0.0	0.0356	K2	6.4	1195
64	209.414	-39.848	17.03	0.02	16.42	0.02	15.91	0.01	15.28	0.05	14.94	0.07	14.65	0.10	0.0	0.0385	K2	6.4	1341
65	209.422	-39.847	17.83	0.02	16.76	0.02	15.58	0.01	14.74	0.03	13.98	0.03	13.82	0.05	1.1	0.0425	K5	7.4	753
66	209.428	-39.852	16.95	0.02	16.13	0.01	15.47	0.01	14.66	0.04	14.15	0.05	13.92	0.05	0.2	0.0284	K4	7.0	885
67	209.431	-39.853	17.41	0.02	16.44	0.02	15.55	0.01	14.43	0.03	13.65	0.02	13.36	0.04	0.8	0.0900	K5	7.4	712
68	209.431	-39.846	16.94	0.02	16.28	0.02	15.72	0.01	15.18	0.04	14.58	0.07	14.55	0.09	0.2	0.0286	K2	6.4	1172
69	209.442	-39.849	15.52	0.01	14.70	0.02	13.97	0.01	13.09	0.03	12.39	0.03	12.24	0.03	0.1	0.0555	K5	7.4	412
70	209.445	-39.847	17.02	0.02	16.37	0.02	15.73	0.01	15.37	0.05	14.87	0.06	14.73	0.10	0.2	0.0280	K1	6.1	1379
71	209.455	-39.835	13.13	0.01	12.55	0.01	12.13	0.01	11.75	0.03	11.29	0.03	11.16	0.02	0.4	0.0277	G2	4.7	404
72	209.463	-39.890	16.76	0.01	16.13	0.01	15.53	0.01	15.03	0.04	14.53	0.06	14.23	0.08	0.1	0.0424	K2	6.4	1130
73	209.466	-39.877	16.25	0.01	15.54	0.01	14.94	0.01	14.27	0.03	13.71	0.03	13.53	0.04	0.4	0.0377	K2	6.4	778
74	209.467	-39.837	15.52	0.01	15.03	0.01	14.65	0.01	14.43	0.04	13.99	0.03	13.95	0.06	0.0	0.0169	G2	4.7	1460
75	209.470	-39.879	17.02	0.02	16.42	0.02	15.84	0.01	15.28	0.05	14.86	0.06	14.67	0.10	0.0	0.0477	K2	6.4	1331
76	209.475	-39.852	17.40	0.02	16.59	0.02	15.92	0.01	15.20	0.05	14.51	0.05	14.32	0.07	0.1	0.0333	K4	7.0	1138
77	209.481	-39.889	16.74	0.02	16.12	0.01	15.60	0.01	15.24	0.06	14.79	0.06	14.71	0.10	0.0	0.0155	K1	6.1	1327
78	209.485	-39.901	15.15	0.01	14.30	0.01	13.58	0.01	12.67	0.02	11.90	0.03	11.75	0.03	0.2	0.0594	K5	7.4	332
79	209.491	-39.890	14.62	0.01	14.06	0.01	13.61	0.01	13.14	0.02	12.73	0.02	12.66	0.03	0.4	0.0431	G2	4.7	802
80	209.495	-39.894	16.08	0.01	15.52	0.01	15.05	0.01	14.55	0.03	14.22	0.04	14.03	0.07	0.0	0.0441	K1	6.1	980
81	209.498	-39.837	15.99	0.01	15.41	0.01	14.94	0.01	14.68	0.04	14.07	0.04	14.23	0.07	0.3	0.0308	G3	4.8	1480

Table 2.3: Spectroscopic results on 11 stars studied by Williams et al., (1977).

Obj. Id (1)	V (mag) (2)	Sp. Type (3)	$(B-V)_o$ (4)	M_V (5)	$(B-V)$ (6)	$E(B-V)$ (7)	A_V (8)	$(J-H)$ (9)	$E(J-K)$ (10)	$(H-K)$ (11)	$E(H-K)$ (12)	Distance (pc) (13)
1N*	10.70	B4	-0.19	-1.5	0.51	0.70	2.17	0.400	0.480	1.077	1.107	1024
1S*	10.26	B7	-0.14	-0.6	0.20	0.34	1.05	0.652	0.682	1.004	1.024	912
2*	10.08	B8	-0.11	-0.2	0.13	0.24	0.74	0.080	0.110	0.078	0.088	813
3	12.45	F6	0.47	3.6	0.59	0.12	0.37	0.371	0.171	-0.024	-0.084	501
4	9.13	G8III†	0.94	0.8	1.02	0.08	0.25	0.425	-0.045	0.215	0.095	417
5	12.77	G9	0.77	5.7	0.94	0.17	0.53	0.492	0.152	0.105	0.005	204
6*	13.30	A4	0.12	1.8	0.50	0.38	1.18	0.387	0.337	0.333	0.323	1175
7	13.31	F4	0.41	3.6	0.64	0.23	0.71	0.344	0.152	0.018	-0.032	631
8*	12.91	A2	0.05	1.3	0.68	0.63	1.95	0.447	0.417	0.261	0.251	851
9	11.96	A9	0.27	2.4	0.50	0.23	0.71	0.220	0.070	-0.004	-0.044	589
10	12.11	F4	0.41	3.6	0.53	0.12	0.37	0.286	0.096	0.030	-0.010	427

† Marraco & Forte (1978) classified star 4 as a G8III on the basis of $V-R$ and $V-I$ colours. * Stars associated with nebulosities.

2.5.2.1 Reddening Laws

The average value of R_V in our galaxy is found to be 3.1 However, there exist higher extinction regions where value of R_V departs from the average value of 3.1 to higher values (Kandori et al. 2003). Stars 2, 6, 8 and $h4636$ even though are associated with CG 12, have a larger range in their distances ($\sim$ 800-1200 pc). In the distance determination, we have used R_V as 3.1. Towards higher obscuration regions, R_V can be as high as 6.0 (Kandori et al. 2003; Whittet et al. 1987; Vrba & Rydgren 1984). Application of a fixed $R_V = 3.1$ can lead to large discrepancies between distances of stars which are clearly associated with the cloud (Thé et al. 1986). Knowing the spectral type of background stars of the clouds one can estimate R_V from colour excess ratios $R_V =$ 1.1 [E(V-K)/E(B-V)] (Whittet 2003). From Table 2.3, it can be noted that all the five stars have near-infrared excesses that could be due to heated dust in their vicinity. It is well known that infrared excess can lead to spuriously high estimates of R_V producing additional flux in the K-band which inflates the value of $E(B-V)$. But by assuming all these five stars to be located at a distance of 550 pc, R_V values independent of infrared excesses can be deduced. R_V values thus derived towards stars 2, 6, 8, $h4636N$ and $h4636S$ are 6.8, 7.4, 4.6, 5.0 and 6.4 respectively. This shows that the value of R_V in CG 12 is anomalous. The regions with $A_V > 2$ can have R_V which differ from that of non-star-forming regions (Kandori et al. 2003). Hence results obtained for stars with $A_V > 2$ from our distance method could have large errors and should be viewed cautiously.

2.5.2.2 Main-sequence intrinsic colours & binarity

The dereddened observed colours are fitted with the intrinsic colours of standard normal main-sequence stars. However, there can be a scatter in their ages within the main-sequence stage itself. This scatter can give errors in estimating the spectral types and hence in distance determination. If a star is in binary system, then the combined apparent magnitude of the star would be brighter than that of the individual components. This would bring the star closer than its true distance and can lead to considerable uncertainties at larger distances.

2.5.2.3 Evolved & pre-main sequence stars

Since most of the field stars are in main-sequence, we have assumed that the stars are all of luminosity class V and used the corresponding values of M_V. However, a few stars could be evolved objects that have moved away from the main-sequence. For example, as discussed in section 2.5.1 in Figure 2.4, the star with $A_V \approx$ 1 mag and at a distance of $\approx$ 200 pc is found to be consistent with a reddened ($A_V \sim 0.7$) K4 giant. This will place this star behind the cloud at a distance of $\sim$ 7 kpc. The presence of objects with near-infrared colours that are characteristic of low-mass YSOs (Santos et al. 1998) and the presence of a low luminosity molecular outflow (White 1993) give evidence for the continuing star formation at the present epoch. Hence there could be PMS stars in the regions of CG 12. Since giants and PMS stars have higher luminosities compared to dwarfs of similar spectral types, then, if they are wrongly classified as dwarfs, that can lead to the estimation of shorter distances with higher A_V.

2.6 Conclusions

We have determined the distance to CG 12 using a method which is based on broad-band optical and near-infrared photometry. In this method, we compute intrinsic colour indices of stars projected towards the direction of the cloud by dereddening the observed colour indices using various trial values of extinction A_V and a standard extinction law. These computed intrinsic colour indices for each star are then compared with the intrinsic colour indices of normal main-sequence stars and a spectral type is assigned to the star for which the computed colour indices best match with the standard intrinsic colour indices. Distances (d) to the stars are determined using the A_V and absolute magnitude (M_V) corresponding to the spectral types thus obtained. A distance versus extinction plot is made and the distance at which A_V undergoes a sharp rise is taken to be the distance to the cloud. We have derived a distance of $\sim$ 550 pc to the cometary globule CG 12 from this method which agrees more closely with the value derived by Williams et al. (1977) than with other estimates of its distance in the literature. The large distance to CG 12 makes this cloud an example of a site of intermediate-to-high mass star formation at relatively large height ($\sim$ 200 pc) above the Galactic plane. We have reevaluated the mass of the cloud as 100 $M_\odot$ for a distance of 550 pc.

Part II

Magnetic field geometry of Cometary Globule CG 12

2.7 Introduction

As mentioned earlier, the tail of CG 12 is $\sim 1^\circ$ in length and oriented roughly perpendicular to the galactic plane. In CGs, although the action of radiation and stellar wind from massive star(s) may account for the presence and the overall radial orientation of the tails, the fine structure and variety displayed by CGs is hard to explain. Does a magnetic field aligned along the CG tail help confine the gas which, for the observed velocity dispersions (Zealey et al. 1983, Sridharan 1992), would be expected to disperse perpendicular to the tail? What is the geometry of the magnetic field in CG 12?

Dust in a dark cloud causes extinction of light from background stars. Dust can also cause linear polarization if the dust grains are non-spherical and aligned. Polarization of starlight due to interstellar dust has been known since the first observations of interstellar polarization by Hall (1949) and Hiltner (1949). A physical mechanism for grain alignment was proposed by Davis and Greenstein (1951). In this mechanism elongated dust grains of paramagnetic material are aligned due to magnetic torques induced by the ambient magnetic field. The elongated grains are aligned with their short axes parallel to the magnetic field so that the starlight polarized due to dichroic extinction shows a polarization with the $\vec{E}$ vector parallel to the ambient magnetic field. Therefore, for stars whose light is extincted and polarized due to magnetically aligned dust grains in a dark cloud, the observed polarization vectors are parallel to the magnetic field in the cloud. A polarization map produced from observations of polarization of stars behind a dark cloud thus represents a map of the magnetic field in the cloud projected on the plane of the sky.

As part of a programme to map the magnetic fields in CGs by making optical polarization measurements of stars projected in the regions of these globules, cometary globules CG 22 (Sridharan, Bhatt & Rajagopal 1996) and the CG 30-31 complex (Bhatt 1999) had earlier been observed. In CG 22, a majority of the stars seen projected within

---

This chapter is based on the published work: Bhatt, H. C., Maheswar, G., Manoj, P., 2004, MNRAS, 348, 83.

the cloud boundaries were found to be polarized (at a level $\sim 1\%$) with the electric vector oriented parallel to the CG tail. If the polarization is a result of non-spherical dust grains aligned by the magnetic field (Davis-Greenstein mechanism), then the results for CG 22 imply that the magnetic field in this CG is parallel to its tail. In the CG 30-31 complex, the field was found to be nearly perpendicular to the cometary tails and is more or less parallel to the bipolar molecular outflow from the YSO IRS 4 embedded in the head of CG 30. Both CG 22 and the CG 30-31 complex are part of the system of CGs around the Vela OB2 association. In this chapter we present the results of polarization measurements of stars in the region of cometary globule CG 12.

2.8 Observations

Table 2.4: Polarimetric measurements for stars in the region of CG 12.

Star Identification	Mag	P (%)	ϵ_p (%)	θ ($^\circ$)	ϵ_θ ($^\circ$)
1 (h4636)	9.8	0.78	0.12	156	6
	$9.8^{\dagger}$	$0.83^{\dagger}$	$0.02^{\dagger}$	$161^{\dagger}$	$7^{\dagger}$
2 (CD-39 8583)	10.1	1.43	0.13	150	3
	$10.1^{\dagger}$	$1.25^{\dagger}$	$0.12^{\dagger}$	$146^{\dagger}$	$3^{\dagger}$
4 (CD-39 8586)	$9.2^{\dagger}$	$0.46^{\dagger}$	$0.09^{\dagger}$	$135^{\dagger}$	$6^{\dagger}$
5	12.8	1.03	0.40	7	13
8	12.9	0.82	0.39	15	17
9	11.9	0.57	0.30	95	11
11 (CD-39 8577)	9.6	0.13	0.11	120	11
12 (CD-39 8597)	10.1	0.49	0.19	46	7
13 (HD 121912)	7.9	0.19	0.08	93	6
14	11.0	0.61	0.21	109	9
15	10.4	0.81	0.19	117	7
16	11.0	0.51	0.22	29	14
17 (HD 121972)	8.0	0.48	0.09	130	7

† measurements by Marraco & Forte (1978)

Polarization measurements were carried out with a fast star-and-sky chopping polarimeter (Jain & Srinivasulu 1991) coupled at the $f/13$ Cassegrain focus of the 1-m telescope at the Vainu Bappu Observatory, Kavalur of the Indian Institute of Astrophysics. A dry-ice cooled R943-02 Hamamatsu photmultiplier tube was used as the detector. 13 stars brighter than ~ 13 *mag* were observed with integration times of 5 - 10 minutes. Two of the stars observed were in common with those observed earlier by Marraco & Forte (1978). All the measurements were made in the V band and an aperture of $15''$ was used. Observations were made on the nights of 01, 02, 03 March, 2000. The instrumental polarization was determined by observing unpolarized standard stars from Serkwoski (1974). It was found to be $\sim 0.1\%$, and has been subtracted vectorially from the observed polarization of the programme stars. The zero of the polarization position angle was determined by observing the polarized standards from Hsu & Breger (1982). A Digitized Sky Survey (DSS) image of the region of CG 12 observed is shown in Figure 2.5.

2.9 Results

The results of our polarimetric observations are presented in Table 5.3. Column 1 of Table 5.3 gives the identification number for the stars observed. We have followed the numbering system of Williams et al. (1977) as some of the stars observed here for polarization are identical to those studied photometrically by Williams et al. (1977). The measured values of polarization P (in %) and the probable error in polarization ϵ_P (in %) are given in Columns 3 and 4 respectively. The polarization position angle (of the $\mathbf{E}$ vector) θ (in $^\circ$) and the probable error in position angle ϵ_θ (in $^\circ$) are given in Columns 5 and 6. The position angles, in the equatorial coordinate system, are measured from the north, increasing eastward. As a rough guide to the brightness of the stars measured, Column 2 of Table 5.3 gives the magnitudes of the stars obtained from the mean intensity measured in our polarimetric observations. The probable errors in these magnitudes are $\sim$ 0.1 *mag*. We have included the polarization measurements for stars 1, 2 and 4 by Marraco & Forte (1978) in Table 5.3. For stars 1 and 2, our results agree with the observations of Marraco & Forte (1978) to within the probable errors of the measurements. In Figure 2.5, superposed on the optical image, we show a polarization map for CG 12. Centred on the stars observed, the polarization vectors have been drawn. The length of the polarization vector is proportional to the percentage polarization P and it is oriented parallel to the direction corresponding to the observed polarization position angle θ. For star 4, measurements by Marraco & Forte (1978) have been used.

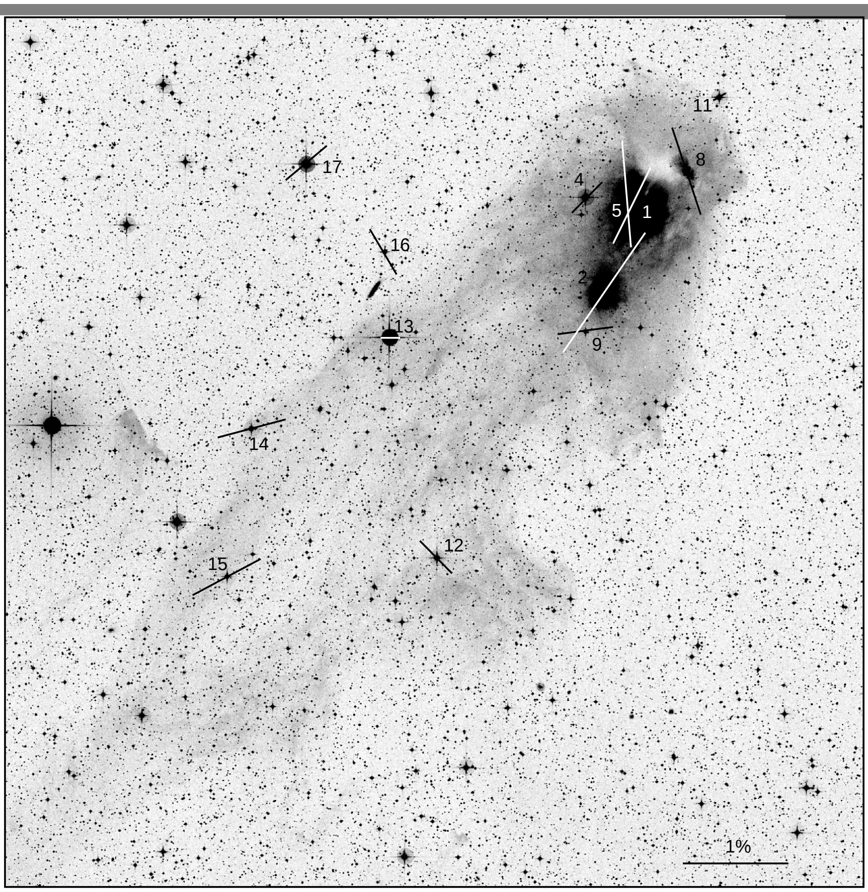

Figure 2.5: Polarization map for the region of CG 12. The polarization vectors have been drawn centred on the stars observed. The $1° \times 1°$ optical image (centred at $\alpha(2000) = 13^h58^m59^s, \delta(2000) = -40°15'22''$) has been reproduced from the Digitized Sky Survey. North is at the top, east to the left.

2.10 Discussion

The observed polarization of stars in the region of CG 12 ranges from ~ 0.1 to ~ 1.4 per cent. We notice, from Table 5.3, that fainter stars tend to show larger values of polarization. Although, the distances to individual stars are, in general, not known, it is likely that most of the fainter stars are in the background of the cloud and suffer larger extinction due to dust in the cloud, while most of the brighter stars are less extincted stars outside the cloud boundaries or nearby stars in the foreground of the cloud . For stars showing relatively larger values of polarization ($P \gtrsim 0.5\%$), the observed polarization is likely to be caused by the globule. CG 12 is an isolated cloud at a considerable galactic latitude ($l = 316.5°, b = 21.2°$), and interstellar polarization in this direction is expected to be relatively small. We have plotted in Figure 2.6, the polarization position angle against the percentage polarization for stars in the region of CG 12 as given in Table 5.3. Also plotted in Figure 2.6 are field stars in this direction, within $\sim 5°$ of the CG 12 head at $l = 316.5°, b = 21.2°$, for which polarization measurements are available in the stellar polarization catalogues (Heiles 2000). There are 11 such field stars, at angular distances from the CG head ranging from 2.01 to 5.20 degrees, plotted in Figure 2.6. Their polarizations range from ~ 0.02 to ~ 0.2 percent, while their distances (from the Sun) range from ~ 60 to ~ 400 pc as given in the *Hipparcos* catalogue.

The polarization position angles for a majority of the field stars (except two stars with position angles near 160° having large error bars) cluster around 50°. Stars in the region of CG 12 occupy a part in the $P - \theta$ diagram shown in Figure 2.6, that is distinct from that occupied by the field stars. Only two stars, numbered 12 and 16, have polarization position angles similar to the majority of the field stars. Distances to these stars are not known. Both show relatively lower values of polarization (0.49 ± 0.19 and 0.51 ± 0.22 % respectively). Star 16 is seen projected outside the cloud boundary. The observed polarization for this star is likely to be due to the general interstellar medium in this direction. Star 12, seen projected within the cloud boundary, may be a foreground star, although its distance is not known. Accurate distance measurement is available for only one star, ie. star 13, for which the *Hipparcos* catalogue gives: parallax $\pi = 7.84 \pm 0.92$ mas. Therefore, star 13, with a distance of 128 ± 15 pc is clearly in the foreground of CG 12 which is at a distance of ~ 550 pc (as determined in Part I). The relatively low value of the observed polarization ($P = 0.19 \pm 0.08$ %) for star 13 is consistent with its being a nearby star. The rest of the stars have polarization position angles that are quite different from the average value of 50° shown by the field stars. They are likely to be either stars involved in the cloud (eg. star $1 \equiv h4636$), or background stars whose light is being polarized by aligned dust grains in CG 12. For these stars θ ranges from $\sim 95°$ to $\sim 195°$ with the average $< \theta >= 139°$. The position angle shows a large dispersion in values, but it appears to vary somewhat systematically from an average $< \theta >= 118°$ for stars (numbered 4, 9, 11, 14, 17) with $P \lesssim 0.75$ %, most of which are in the tail region of CG 12, to an average $< \theta >= 161°$ for stars (numbered 1, 2, 5, 8, 15) with $P \gtrsim 0.75$ % which are all, except star 15, seen projected on the head of the cometary globule.

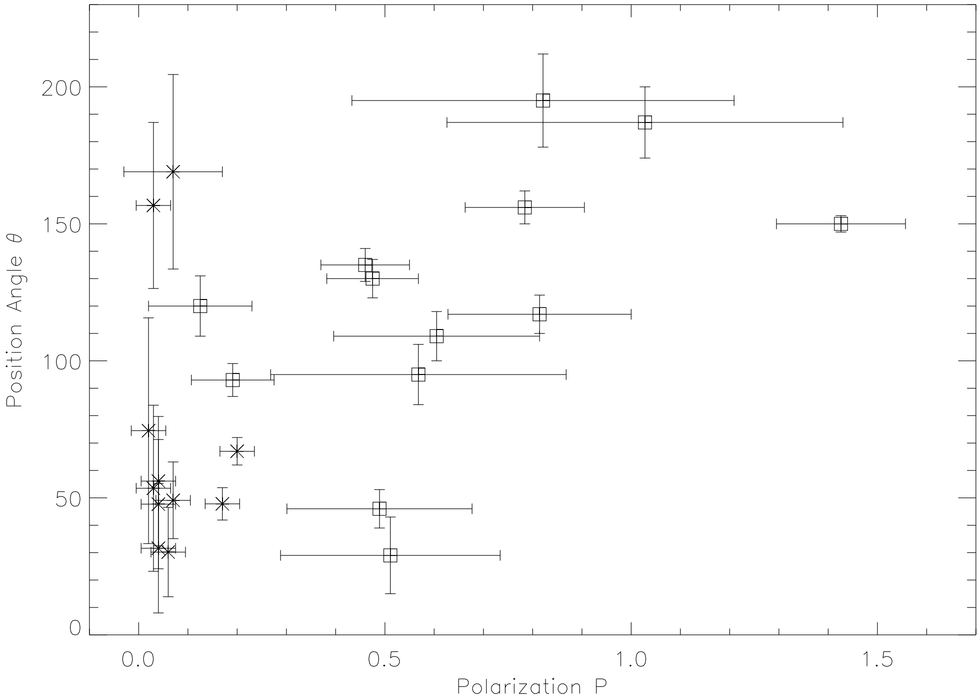

Figure 2.6: Polarization position angle (°) plotted against degree of polarization (%) for stars in the region of CG 12 (□) and for stars within ∼ 5° of CG 12 from the stellar polarization catalogues (Heiles, 2000) (∗).

Two other stars projected outside the cloud boundary are star 11 and star 17. Both show lower values of polarization, but the position angles are dissimilar from those for the field stars. Star 11 is just outside the CG head, as seen in the optical image in Figure 2.5. It is possible that it suffers a relatively low extinction and polarization due to a lower opacity envelope around the globule head as is commonly observed in molecular clouds. In fact, as discussed below (§ 2.10.1 and Figure 2.7), star 11 is seen projected within the cloud boundary as represented by IRAS 100μm emission. Star 17 is well outside the cloud boundary. Its position angle is difficult to explain. In the following we consider the polarization of stars 12, 13, 16 and 17 to be due to the general interstellar medium, while for the rest of the stars it is suggested to be due to the dust in the cometary globule.

2.10.1 Correction for the interstellar polarization

The polarization vectors for stars 1, 2, 4, 5, 8, 9, 11, 14 and 15 seem to follow, more or less, the elongated morphology of the cometary globule. For these stars, the average value of the polarization position angle $< \theta > = 140°$ with a dispersion $\sigma_\theta = 35°$. The position angle of the cometary tail of CG 12, as given in Hawarden & Brand (1976), is 135°. Although the polarization for the stars in or behind the globule may be dominated by the dust in the cloud, the observed polarization will be a superposition of an interstellar component due to interstellar dust in the foreground of the cloud, and another component due to the dust in the cloud. To evaluate the polarization caused only by the dust in the cloud, we need to subtract the foreground interstellar component from the observed polarization of the stars. As mentioned earlier, nearby field stars (with distances in the range from $\sim$ 60 to $\sim$ 400 *pc*) within $\sim 5°$ of CG 12 have polarizations in the range $\sim$ 0.02 to $\sim$ 0.2% with position angles clustered around 50°. An inspection of the Heiles (2000) and the *Hipparcos* catalogues shows that in the direction of CG 12, stars with $b \geq 15°$ and within $\sim 10°$ of the globule do not exceed $P \sim 0.2$ % even for distances larger than $\sim$ 500 *pc*. We therefore take the component of polarization caused by the general interstellar dust in the foreground of CG 12 to be represented by: $P_i = 0.20$ %, $\theta_i = 50°$. We then correct for the interstellar component by subtracting the corresponding Stokes parameters $U_i = P_i Sin 2\theta_i$ and $Q_i = P_i Cos 2\theta_i$ from those observed for the stars. The resulting P and θ, for stars 1, 2, 4, 5, 8, 9, 11, 14 and 15, representing the polarization caused by the dust in CG 12 are listed in Table 2.5 and shown pictorially in Figure 2.7. In the polarization map in Figure 2.7 we have superposed the $C^{18}O$ contours, representing the high-density head of CG 12, from Yonekura et al. (1999); and the IRAS 100μm contours representing the lower-density outer parts of CG 12 obtained from the Infrared Processing and Analysis Centre (IPAC). The IRAS 100μm contours (in MJy/ster) are at 2.6 (the outer most contour), 3.6, 4.6, 6.6, 8.6 and 12.6 (inner most contour). Contours with 100μm flux density larger than 12.6 MJy/ster are not shown in Figure 2.7 to avoid overlap with $C^{18}O$ contours in the CG head. Star 11 is seen projected within the cloud boundary as represented by IRAS 100μm emission.

Table 2.5: Percentage polarization and position angle for stars in the region of CG 12 after correcting for interstellar contributions.

Star Id.	P (%)	ϵ_p (%)	θ (°)	ϵ_θ (°)
1	0.96	0.12	153	6
2	1.62	0.13	149	3
4	0.66	0.09	137	6
5	1.03	0.40	1	13
8	0.78	0.39	8	17
9	0.60	0.30	105	11
11	0.31	0.11	132	11
14	0.72	0.21	116	9
15	0.96	0.19	121	7

2.10.2 Effects of nebulosity

The polarization map of Figure 2.7 can be considered to represent the geometry of the projected magnetic field in CG 12 if the polarization is caused by dust grains in the cloud aligned by the magnetic field (Davis-Greenstein mechanism), similar to the mechanism for interstellar polarization. It can be seen from Table 2.5 that the dust in the cloud causes polarization $P \sim 1\%$. Photometry for some of stars, observed here polarimetrically, near the CG 12 head by Williams et al. (1977) indicate that they suffer extinction $A_V \sim 1$ mag. Thus for these stars the ratio $P/A_V \sim 1$ $\%/mag$, similar to that for the general interstellar medium. However, it must be noted that CG 12 has an associated reflection nebulosity, that is brightest near star 1 ($h4636$) in the head region of the globule. The nebulosity may contribute polarized light over the aperture ($15''$ in diameter) used for the polarimetric observations. In a separate study to look for $H\alpha$ emission-line objects by CCD imaging, we have obtained $H\alpha$ and V band images ($10' \times 10'$ field centered at a point $\sim 2'$ south of $h4636$) in the head region of CG 12 that includes stars 1, 2, 4, 5 and 8. We have estimated the V band surface brightness of the nebulosity in this region. Over most of the CG head the nebulosity is fainter than $\sim 24 mag/arcsec^2$ except close to stars 1, 2, 5 and 8. In the tail region of the cloud, not covered in our CCD images, it is likely to be similar or fainter. Except for stars 1, 2, 5 and 8, over the aperture of $15''$ used for the polarimetric measurements, the nebulosity can contribute light equivalent to ~ 18.4 mag. Even if this light is 100% polarized, it can result in $\lesssim$ 0.1% polarization for stars of 11 mag, assuming no chopping. The star/sky chopping will remove much of the light due to the nebulosity; only surface brightness gradients over $2'$ angular scale (used

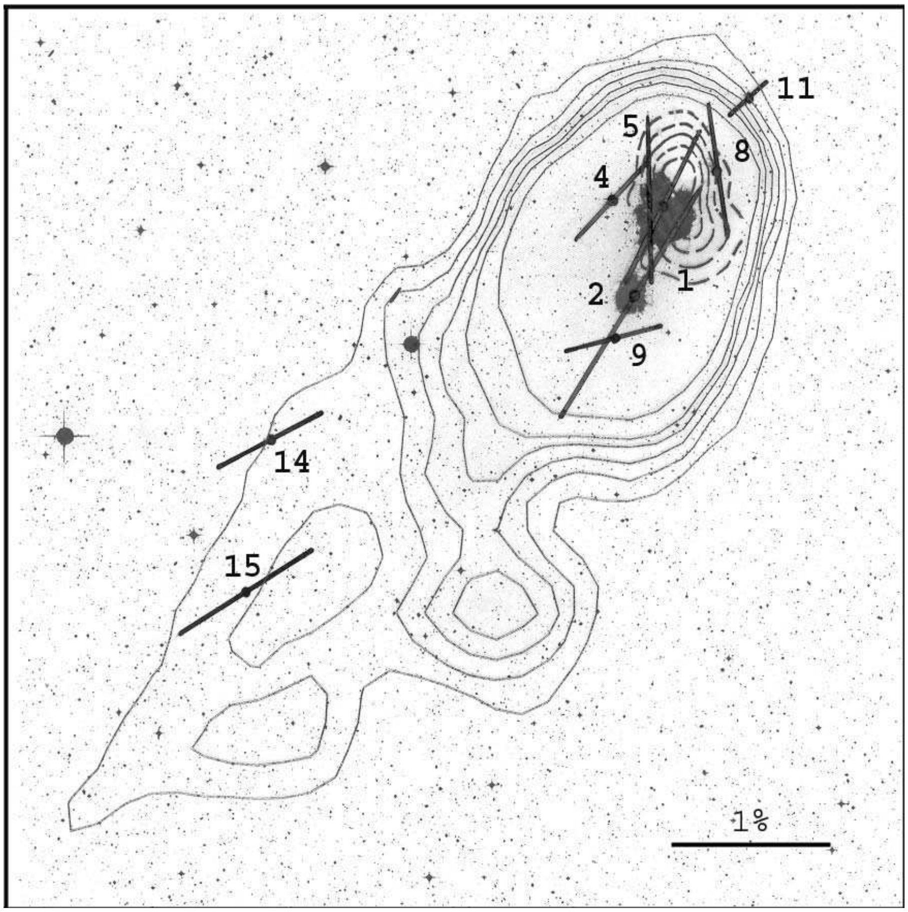

Figure 2.7: Polarization map for CG 12 after correcting for interstellar contributions. $C^{18}O$ contours (broken line) from Yonekura et al. (1999) representing high-density CG head, and IRAS 100μm contours representing the lower-density parts of the cloud, are overlayed on the DSS image. The image field is the same as in Figure 2.5.

for chopping in the polarimeter) will contribute. Thus the contribution of the nebulosity to the observed polarization will be negligible for the relatively bright stars 4, 11, 12, 13, 14, 15, 16 and 17. For star 9 ($V \sim 12$), a 24 $mag/arcsec^2$ nebulosity can contribute up to 0.25 % polarization, whereas the observed polarization is 0.57 %. Close to the stars, within a few seeing-disc ($\sim 3''$ in our observations) radii, it is difficult to measure the nebular brightness at a level below $\sim$ 1% of the stellar brightness. At an angular distance of $10''$ from stars 1, 2, 5 and 8, we estimate the nebular surface brightness to be about 18.6, 19.6, 21.0 and 21.6 $mag/arcsec^2$ respectively. In an aperture of $15''$ the nebulosity can contribute about 6, 3, 9, 6 % or more (since the nebular surface brightness is generally increasing towards the stars) light to the stellar brightness for these stars. If the nebular light is strongly polarized, this can result in large polarization values for the stars. However, since the nebulosities around the stars are more or less symmetric, the net polarization contributed by the nebular light can be much less. Calculations of the polarization and reddening produced by ellipsoidal circumstellar scattering envelopes by Shawl (1975) have shown that the maximum linear polarization, even for a circumstellar dust optical depth $\tau \sim 0.2$, is about 1.1%. Stars 1, 2, 5 and 8 show polarizations $\sim 1\%$, somewhat larger, but not greatly different from other stars polarized by the cloud dust. However, they show polarization position angles that are systematically larger (rotated eastward) than the other stars. This may be due to the nebular contributions to the observed polarization for stars associated with bright nebulosities in the CG head.

2.10.3 Magnetic field and cloud morphology

From the above discussion we conclude that the polarization in the light of stars 4, 9, 11, 14 and 15 seen projected within the boundaries of CG 12 is caused due to selective extinction by dust grains aligned by magnetic field in the cloud. The polarization vectors for these stars, as shown in Figure 2.7, can be considered to represent the geometry of the projected magnetic field in CG 12. The field is more or less parallel to the cometary tail of the globule. Two other features in CG 12, the bipolar molecular outflow centred close to the infrared source IRAS 13547-3944 discovered by White (1993) and the elongated structure in the nebulosity around star 2 noted by Marraco & Forte (1978), are also oriented nearly parallel to the CG tail. If circumstellar disks around the young stars 1 and 2 are the cause for these structures, then the disks must be perpendicular to the cloud magnetic field. This is consistent with current theories of star formation that suggest cloud collapse parallel to the magnetic field, leading to the formation of a flattened disk perpendicular to the field and a bipolar flow channelled parallel to the field.

As noted earlier, stars 1, 2, 5, 8 show polarization position angles that are systematically larger (rotated eastward) than the other stars, and this may be due to the nebular contributions to the observed polarization for these stars associated with relatively brighter nebulosities in the CG head. Alternatively, if the nebular contribution is negligible, polarization vectors for these stars also represent the direction of the projected magnetic field. Then, the position angles for these stars, in particular those for stars 5 and 8, suggest rotation of the field in the denser parts of the CG head. We notice from the CO maps for CG 12 by Van Till, Loren & Davis (1975) and Yonekura et al. (1999) that the CG head is elliptical with the long axis oriented more nearly in the north-south direction than the CG tail. In fact the highest density region of the CG head, that includes stars 5 and 8 in projection, most clearly seen in the $C^{18}O$ map by Yonekura et al. (1999), that has been superposed on the DSS image in Figure 2.7, is elongated and the position angle of its long axis is at $\sim 7°$, similar to the polarization position angle for stars 5 and 8.

The cometary shape of CG 12 and its orientation has been suggested by Williams et al. (1977) to have been caused by a high galactic latitude supernova explosion at $l = 320°, b = 30°$. The expanding supernova remnant that blew the lower density outer parts of the globule into a cometary tail is likely to have dragged the ambient magnetic field lines in the same direction. In the higher density inner parts of the globule head the original magnetic field may remain unperturbed. If the nebular contribution to the polarization of stars in the CG head is negligible, then the observed polarization position angles for stars 5 and 8 suggest that the original magnetic field in the cloud was parallel to the long axis of the elliptical core of the globule.

2.11 Conclusions

In this chapter we have presented the results of optical linear polarization measurements of stars in the region of the relatively isolated cometary globule CG 12. The dust in the cloud causes $\sim 1\%$ polarization in the light of the stars seen projected within the cloud boundaries. A polarization map representing the geometry of the magnetic field in the cloud is produced. Our results can be summarized as follows.

- In the lower-density outer parts of the cloud, the field is more or less parallel to the cometary tail, with position angle $\theta \sim 130°$. Other elongated structures, like the bipolar molecular outflow from near the infrared source IRAS 13547-3944 and the nebulosity around star 2 embedded in the cloud are also oriented in the same direction.

- Polarization vectors for the more highly reddened stars in the head region of the globule are found to be more or less parallel to the long axis of the elliptical, high-density $C^{18}O$ core of the CG head, with position angle $\theta \sim 7^\circ$. If the nebular contribution to the polarization of stars can be neglected, then a magnetic field in the high-density core oriented parallel to its long axis is indicated.

- It is suggested that the expanding supernova remnant that blew the lower density outer parts of the globule into a cometary tail is likely to have dragged the ambient magnetic field lines in the same direction. In the higher density inner parts of the globule head the original magnetic field remained unperturbed.

Part III

Multi-wavelength study of star formation in CG 12

2.12 Introduction

Williams et al. (1977) have speculated that CG 12 has been influenced by a high-galactic latitude supernova explosion resulting in the formation of a tail from the blown away low density outer parts of the globule. As shown and discussed in Part II of Chapter 2, this most likely could have dragged the ambient magnetic field in the same direction of the tail, strengthening the supernova conjecture made by Williams et al. (1977). Any current star formation occurring in CG 12 could be thus possibly due to this external trigger. The distance of 550 pc to CG 12 determined in Part I of Chapter 2 implies that the globule is at a height of $\sim$ 200 pc above the galactic midplane. The simple structure and complete isolation of CG 12 provide us with great opportunity to study the effects of triggered star formation at intermediate-to-high galactic latitude.

The spatial separation of subgroups of OB associations with different ages has led to the idea that star formation is triggered sequentially in molecular clouds by pressures from H II regions (Elmegreen & Lada 1977) and supernovae (van Till, Loren, & Davis 1975; Ögelman & Maran 1976; Herbst & Assousa 1977). Multi-wavelength observations of bright-rimmed globules have shown evidence for an age sequence for young objects which dependent on the location of the object with respect to the illuminating massive stars, i.e., older stars are located on the side of the cloud facing the OB stars and younger stars which are partially embedded, are located at a larger distances from the OB stars indicate waves of star formation running through the clouds (Sugitani et al. 1999; Ogura et al. 2002). Multi-wavelength study of a cometary globule, L1616, in Orion star forming region revealed the presence of 27 X-ray sources (Alcala et al. 2004). Of the 22 new PMS stars identified, 15 were X-ray detected, while the remaining 7 were identified from an unbiased lithium survey. Eleven additional stars are known to be PMS stars. The total PMS stars thus identified towards L1616 is 33. These stars are about 1-2 Myr old with a dispersion of about 1 Myr in their ages. The small dispersion in the ages of these stars was explained in terms of efficient and quick star formation. The millimeter-wave observations of L1616 revealed the presence of a tight group of dust continuum sources, the brightest of which was found to drive a powerful near-infrared (near-IR) H_2 jet (Stanke et al. 2002). This gives the evidence for at least two episodes of star formation in L1616:

the 1-2 Myr old sources representing first generation, while the millimeter-wave sources and other possible embedded sources representing the second generation. The estimated star formation efficiency in L1616 is $\sim 14\%$ (Ramesh 1995; Alcala et al. 2004). Alcala et al. (2004), on the basis of the spatial distribution of the PMS stars relative to the head and the embedded source, cometary shape of the cloud and high star formation efficiency, suggested that the star formation in L1616 was induced either due to the winds of the massive stars of the Orion OB association to the east of L1616 or due to a single supernova explosion. This could have triggered the formation of the 1-2 Myr old stars and the jets and winds of the newly formed stars might have triggered the formation of the embedded sources. From photometric and spectroscopic observations of the cometary complex CG 30/31/38, a total of 16 PMS stars were identified by Kim et al. (2002). Eight of the 13 X-ray sources detected towards the complex using ROSAT/ High Resolution Imager (HRI) were confirmed to be PMS stars. These spectroscopically confirmed stars are found to outline the CGs facing towards the ionizing source. From the spatial distribution of PMS stars, CG clouds, and ionizing sources (O stars and supernova remnants) Kim et al. (2002) suggested a triggered origin of star formation in CG 30/31/38 complex. The Herbig-Haro object found associated with the head of CG 30 indicates the signature of current star formation in the cloud (Reipurth 1983). Hence the sequential star formation found towards L1616 and CG 30/31/38 suggests that this could be a common feature of such cometary globules which are a result of external trigger. Observations of additional CGs are required to understand the star formation processes taking place in them.

We present in this chapter the results of a multi-wavelength study carried out to identify young stars towards CG 12 and look for any age sequence in them. For this purpose we have obtained spectroscopic observations, which was combined with IRAS, 2MASS and ROSAT X-ray data from archives. This chapter is organized in the following order. In section 2.13, we present the details regarding the observations and data reductions. The results and discussion are presented in sections 2.14, 2.15 and 2.16; and in section 2.17, we summarize the main results of this study.

2.13 Observations and data analysis

2.13.1 IRAS Data

IRAS images at 60 and 100 μm are obtained from Infrared Processing and Analysis Center (IPAC)[2]. The images are of $3^\circ \times 3^\circ$ size with a plate scale of 0.006 degree/pixel. IPAC has prepared a set of sky flux images called the IRAS Sky Survey Atlas (ISSA). The ISSA has had zodiacal light subtracted using a physical model of solar system dust and various imaging enhancements such as destriping. Even otherwise, the contribution of zodiacal light in the images of CG 12 would be minimum since it is away from the ecliptic plane ($\beta \gtrsim 25^\circ$). We have subtracted a background from all images in order to ensure that empty sky has zero surface brightness.

2.13.2 Spectroscopic observations

Williams et al. (1977) from UBV photometry of 11 stars projected towards CG 12, which include stars associated with nebulosities within the cloud, showed the presence of a sparse young cluster embedded in the head of CG 12. By fitting a ZAMS to the stars illuminating nebulosities in a colour-magnitude diagram, they suggested that, of these, some are potential PMS candidates. We made spectroscopic observations of all the 11 stars studied by William et al. (1977) to study the true nature of these stars. All spectra were obtained with a slit of $2''$ width and spectral resolution $1.3 - 2.6$ $\mathring{A}$ $pixel^{-1}$. All spectra were bias subtracted, flat-field corrected, extracted and wavelength calibrated in the standard manner using the IRAF reduction package. Spectral types were determined for the stars by comparing the observed spectrum with those in the atlas of Jacoby et al. (1984).

2.13.3 Near-IR 2MASS measurements

Near-IR JHK_s magnitudes for the stars were obtained from 2MASS (Cutri 2000) catalogue. The JHK_s colors were transformed from 2MASS system to Koornneef system

---

[2] IPAC is funded by NASA as part of the IRAS extended mission program under contract to JPL.

using the relations given by Carpenter (2001).

2.13.4 ROSAT X-ray data

X-ray data was obtained from the catalog "The WGACAT version of ROSAT sources (White et al. 2000)". WGACAT is a point source catalogue generated from all ROSAT PSPC (Position Sensitive Proportional Counter) pointed observations. The catalog was generated using an optimized sliding cell detect algorithm in XIMAGE (first developed for the EXOSAT project). The inner and outer parts of the images were run separately, to maximize the sensitivity to source detection. This method is very sensitive in finding point sources, but can also find spurious sources where there is extended emission. Visual inspection of each detection was made by the authors to remove the obvious spurious cases and they assigned a quality flag to each detection. Pointed observations of the field containing CG 12 was made on 14/08/1992. The image centre which corresponds roughly to the pointing position was at right ascension $13^h56^m50^s$ and declination $-39°52'40''$ (epoch 2000). There are a total of thirty seven ROSAT X-ray detections within a radius of 1° about the image centre. The quality flags for the sources in the catalog range from 0-12. Of these thirty seven X-ray detections, we have chosen sources with quality flags 12 and 11, which indicate a secure detection of a point source and a good detection but located near the inner detector support structure at $\sim 20'$ radius respectively, for the present analysis.

2.14 Dust colour temperature, optical depth and visual extinction

The thermal structure of the gas and the dust in a cloud depends on the presence of both internal (IR sources, newly formed stars) and the external (cosmic ray, UV photons) heating sources. We have estimated the dust colour temperature (T_d) at each pixel in IRAS 60 and 100 μm images containing the cloud, CG 12, by the following procedure. The ratios of flux densities (R) at 60 and 100 μm were calculated from the 60 and 100 μm IRAS images after matching their spatial resolutions. Here we assumed that the dust in a single beam can be characterized by one single temperature (T_d), and that the emission at 60 and 100 μm is due to blackbody radiation from dust grains at temperature T_d, modified by a power-law emissivity. Then a look-up table with the values of R calculated for a wide range of temperature T_d was constructed. For each pixel in the ratio image, T_d corresponding to R from the look-up table was replaced.

For optically thin dust grains, the flux density at wavelength λ is given by (e.g. Arce & Goodman 1999)

$$F_\lambda = B_\lambda(T_d) N_\lambda \tau_\lambda \Omega_\lambda \ \propto \ B_\lambda(T_d) N_\lambda \lambda^{-\beta} \Omega_\lambda \tag{2.9}$$

where B_λ is the plank function, N_λ is the column density of dust grains, τ_λ is the optical depth, Ω_λ is the solid angle at λ, and β is the power-law index of the dust emissivity. The ratios of flux densities (R) are then given by

$$R = F_{60}/F_{100} = 0.6^{-(5+\beta)}[(e^{226/T_d} - 1)/e^{(136/T_d} - 1)] \tag{2.10}$$

where we have assumed that $\Omega_{60} = \Omega_{100}$ for $\tau_\lambda \ll 1$ and the dust in the IRAS beam is at a single temperature. But this assumption of a single dust temperature in each pixel is not valid in clouds with embedded stars because such stars produce spatially unresolved temperature gradients. The temperature images are an emissivity, rather than a mass-weighted, temperature estimate. If a small amount of hot dust (by mass) is present in the same 100 μm beam as much colder dust, the emission will be dominated by the hot dust and we will overestimate the temperature of the dust because not much dust at this temperature is required to produce the 100 μm emission. Hence T_d in the vicinity of embedded stars will be unrealistic. There is a general agreement that the emissivity index depends on the grain size, composition, and physical structure (Weintraub et al. 1991), and the general consensus in recent years has been that β has a value most likely between 1 and 2; that in the general ISM β is closer to 2, and in denser regions with bigger grains β is closer to 1 (Beckwith & Sargent 1991; Mannings & Emerson 1994). We have computed the dust temperatures at each pixel corresponding to power-law index of the dust emissivity, $\beta = 1$. However, we have performed tests with $\beta = 2$ also and find that our results are not significantly affected.

T_d computed from the long-wavelength flux density ratio ($F_{60\mu m}/F_{100\mu m}$) in CG 12 vary from 21 to 35 K. Figure 2.8 presents the image of T_d of CG 12. The dust temperature is maximum near the double star $h4636$ (represented by filled black square in Figure 2.8). The dust temperature (35 K), obtained in our analysis, of the region near to $h4636$ (IRAS 13547-3944) matches well with that (32 K) estimated by White (1993) who found this location to coincide also with the main-brightness temperature of the CO $J = 2 - 1$ data. This suggest that the $h4636$ is the main source of heating for the dust and gas. The region north of $h4636$ shows a minimum value in T_d (21 K). This relatively colder region roughly coincides with the position of the denser region detected in C^{18}O (Yonekura et al. 1999) and an embedded near-IR excess source (Santos et al. 1998, see § 2.15.2) shown by a star symbol in Figure 2.8. The T_d of 21 K estimated towards this region is probably higher than that is expected from denser cloud cores. This could be because IRAS is more sensitive to hot dust, in this case, heated by $h4636$ which is only $\sim 3'$ away from this location.

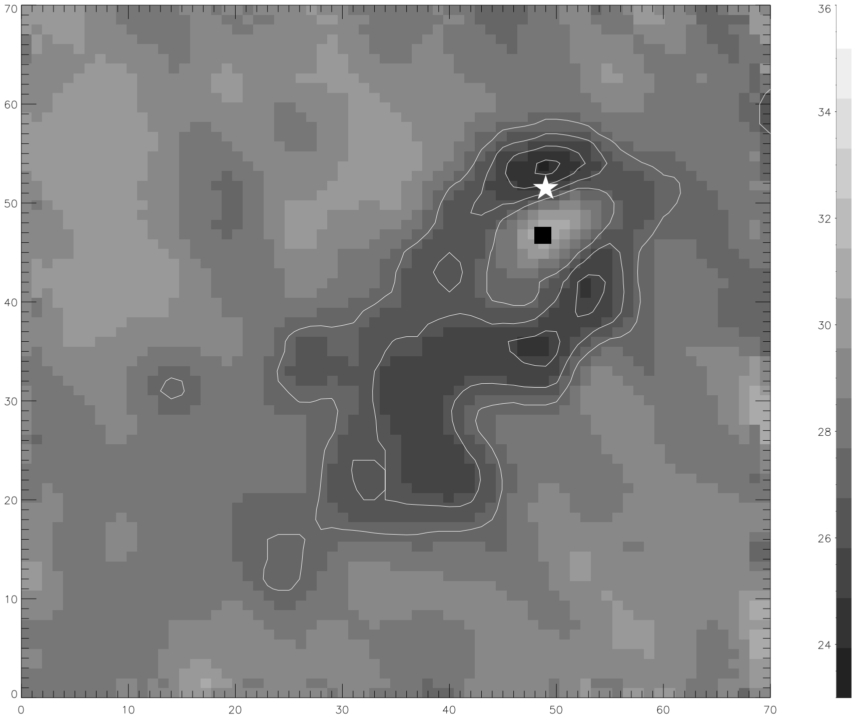

Figure 2.8: $T_{60/100}$ image obtained towards CG 12. The contours are plotted at 23 (inner most contour towards the north of $h4636$), 25, 26, 27, & 33 K. Positions of $h4636$ double star and the near-IR excess source (see § 2.15.2) are shown by filled square and star symbols respectively.

Towards the tail, the T_d is found to be roughly constant at $\sim 24 - 25K$. In order to understand the infrared emission from molecular clouds, the luminosity absorbed from

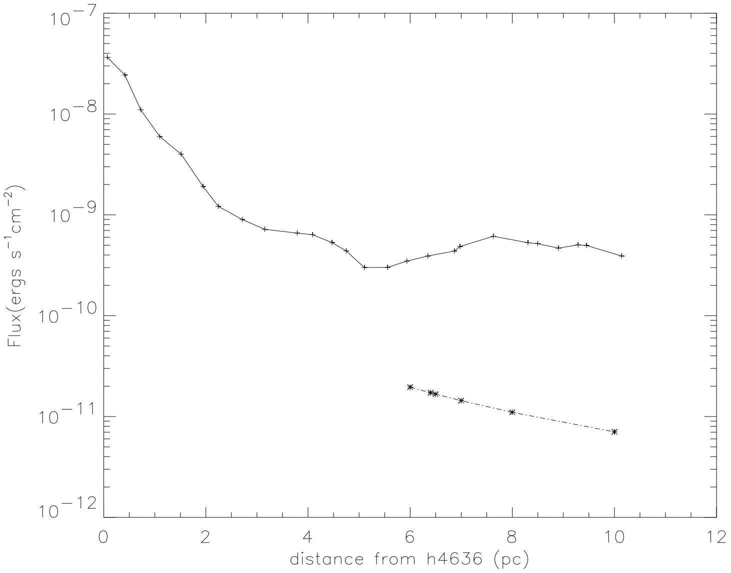

Figure 2.9: Total FIR flux measured at different locations of CG 12 from *h*4636 to down towards the tail within an aperture of 40$''$ is plotted w.r.t its distance from *h*4636 (solid line). Expected flux from different regions of the cloud, assuming *h*4636 to be the heating source of the dust in the tail of CG 12, is plotted w.r.t its distance from *h*4636 (broken line).

the ISRF (InterStellar Radiation Field) must be compared with the luminosity from the embedded stars. We have measured the total far-infrared (FIR) flux reaching us from different locations of CG 12, beginning from *h*4636 to down towards the tail (along a position angle $\sim 140°$) within an aperture of radius $\sim 40''$, to determine the illuminating source of the emission from the tail. Figure 2.9 shows the observed flux (solid line) from the locations plotted against the distance (pc) from *h*4636. The expected flux from different regions of the cloud, assuming *h*4636 to be the only heating source of the dust in CG 12 and the dust along the line of sight is characterized by a single temperature, was evaluated using the equation

$$F_{tot} = \frac{L_\star}{4\pi r^2}\,\frac{A}{4\pi d^2}\,\tau_v \tag{2.11}$$

where $L_\star$ is the luminosity of the most luminous northern component of *h*4636 estimated by assigning a B4 spectral type to it, r is the distance (pc) of different locations of CG 12 from *h*4636, d is the distance to CG 12 from the sun, A is the area of the aperture used and τ_v is the optical depth. But close to the local heating source(s), along the line of sight, dust can have a distribution in temperature and the measured flux value is a composite of emission from all the dust at various temperatures. Hence a direct comparison between the measured flux and that evaluated using the equation 2.11 can not be done. A complete analysis would require the knowledge of the nature and the distribution of the dust in the cloud. However, equation 2.11 is valid and a direct comparison can be made between the measured and expected flux from far way (from $h4636$) locations towards the tail of CG 12. We have evaluated the expected flux from the tail due to the heating of dust by the radiation from $h4636$ far away at 6 pc and beyond. The expected flux from different regions of CG 12, shown by broken line in Figure 2.9, is found to be negligible when compared to the observed flux implying that the radiation of $h4636$ is not the source of heating the dust towards the tail but most probably are heated by the interstellar radiation field. The average value of the total energy density of photons in the interstellar radiation field is $\approx 8 \times 10^{-14} J\ m^{-3}$ (Mathis 2000). Assuming a similar value for the interstellar radiation field for the region near CG 12, we have estimated the average flux that one would receive from the tail if it were heated by ISRF. We find that the estimated value ($\approx 3 \times 10^{-10} erg\ s^{-1}\ cm^{-2}$) is consistent with the observed values. However, due the proximity of CG 12 to Sco-Cen OB associations, the radiation field towards this region can be slightly higher than the average interstellar value.

The dust optical depth values from the dust colour temperatures at each pixel were estimated for an optically thin emission case using the expression

$$\tau_{100} = [F_{100}/B_{100}(T_d)] \tag{2.12}$$

where $B_{100}(T_d)$ is the Planck function and F_{100} is the 100 μm observed flux. The visual extinction (A_V) is then calculated from the optical depth using the expression

$$A_V = 15.078(1 - e^{-\tau_{100}/641.3}) \tag{2.13}$$

where τ_{100} is the optical depth given in units of 10^{-6} (Wood et al. 1994).

Figure 2.10 presents the image of dust optical depth towards CG 12. The derived 100μm optical depths typically range from $3 \times 10^{-6} - 50 \times 10^{-5}$ within CG 12. The maximum value of τ_{100} is found to coincide with the $C^{18}O$ core (Yonekura et al. 1999)

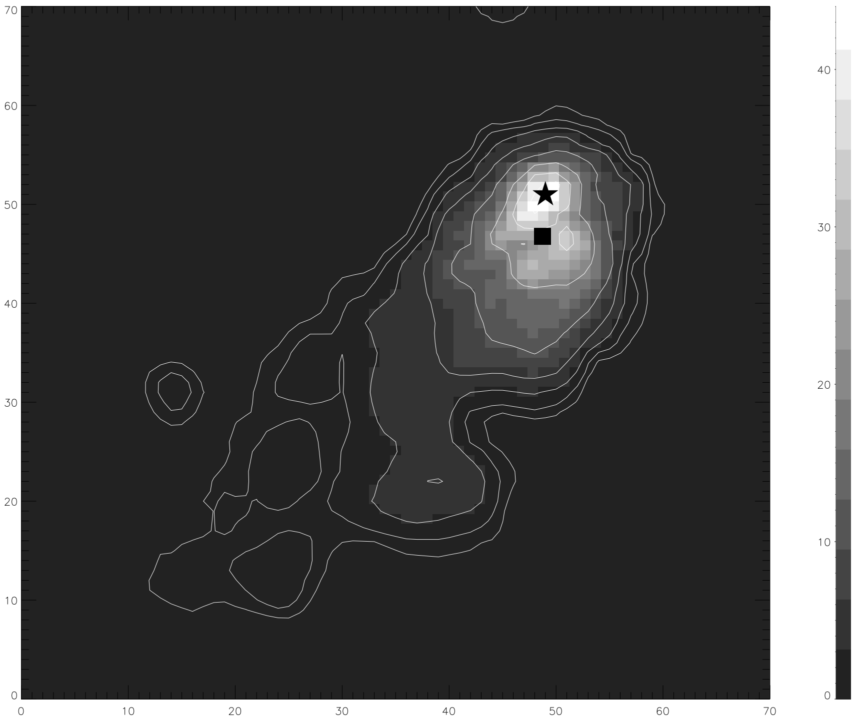

Figure 2.10: τ_{100} image obtained towards CG 12. The contours are plotted at 1.5, 2, 3, 5, 10, 20, 30, & 40×10^{-5}. Positions of *h*4636 double star and the near-IR excess source (see § 2.15.2) are shown by filled square and star symbols respectively.

and the near-IR excess embedded source (Santos et al. 1998, see § 2.15.2) towards the north of *h*4636 (indicated by a star symbol in Figure 2.10). Towards SW and very close to *h*4636, we find another peak in the optical depth image. This location positionally coincides with the $C^{18}O$ core and a bipolar molecular outflow detected by White (1993). In Figure 2.11, we present image of optical extinction towards CG 12. The extinction is found to range from 0.1 - 9 mag. The maximum extinction is also found towards the denser $C^{18}O$ core and at the position of the near-IR excess embedded source. We find that the orientation of the inner contours are more nearly in the north-south direction than the CG tail similar to the orientation of $C^{18}O$ detected by Yonekura et al. (1999). Even the magnetic field lines projected on to the CG 12 head (as discussed in Part II, § 2.10.3) are roughly oriented towards this direction.

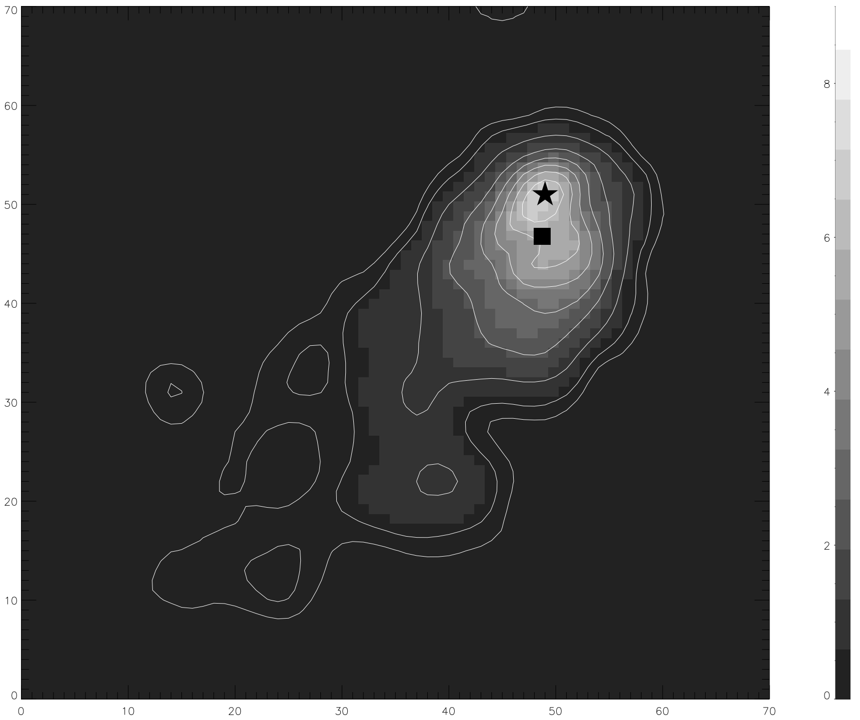

Figure 2.11: Extinction map obtained towards CG 12. The contours are ploteed at 0.3, 0.5, 1, 2, 3, 4, 5, 6, & 7 *mag*. Positions of *h*4636 double star and the near-IR excess source (see § 2.15.2) are shown by filled square and star symbols respectively.

2.15 Young stellar objects associated with CG 12

2.15.1 Stars associated with nebulosities

Our Spectroscopic and photometric results for 11 stars studied by Williams et al. (1977) are given in Table 2.6. Column 1 gives star numbers as given by Williams et al. (1977). 1N and 1S represent northern and southern components of *h*4636 respectively. Columns 2 and 6 give observed magnitudes in V band and $(B-V)$ values taken from Williams et al. (1977) respectively. Column 3 gives spectral types determined by comparing the observed spectrum with those in the atlas of Jacoby et al. (1984). Columns 4 and 5 give corresponding intrinsic colour indices and absolute magnitude respectively. Columns 7 and 8 give estimated colour excesses and A_V $(= 3.1 \times E(B-V))$ of the stars. Near-IR colour indices (JHK magnitudes are from 2MASS) are given in columns 9 and 11 respectively with colour excesses in columns 10 and 12 respectively. The read flag given for sources in 2MASS point source catalogue (Cutri et al. 2003) indicates the source of *JHK* "default" magnitudes. For $h4636N$ the read flag is set to 1 for J which implies that the source was detected in J and the default magnitude was derived from aperture photometry. The read flag is set to 6 for $H\&K$ bands which implies that the default magnitudes were the 95% confidence upper limit derived from a $4''$ radius aperture measurement taken at the position of the source on the Atlas Image. The sky background was estimated in an annular region with inner radius of $14''$ and outer radius of $20''$. This procedure is adopted for doing photometry in a band for pairs of sources which are detected and resolved in another band, but are detected and not resolved in this band. This differs from a read flag set to 0 for a band because then there is no detection of the source in the band. This indicates that $h4636N$ was detected but not resolved in $H\&K$ bands.

Table 2.6: Spectrophotometric results on 11 stars studied by Williams et al. (1977).

Obj. Id (1)	V (mag) (2)	Sp. Type (3)	$(B-V)_o$ (4)	M_V (5)	$(B-V)$ (6)	$E(B-V)$ (7)	A_V (8)	$(J-H)$ (9)	$E(J-H)$ (10)	$(H-K)$ (11)	$E(H-K)$ (12)
1N*	10.70	B4	-0.19	-1.5	0.51	0.70	2.17	0.400‡	0.480	1.077‡	1.107
1S*	10.26	B7	-0.14	-0.6	0.20	0.34	1.05	0.652	0.682	1.004	1.024
2*	10.08	B8	-0.11	-0.2	0.13	0.24	0.74	0.080	0.110	0.078	0.088
3	12.45	F6	0.47	3.6	0.59	0.12	0.37	0.371	0.171	-0.024	-0.084
4	9.13	G8 III†	0.94	0.8	1.02	0.08	0.25	0.425	-0.045	0.215	0.095
5	12.77	G9	0.77	5.7	0.94	0.17	0.53	0.492	0.152	0.105	0.005
6*	13.30	A4	0.12	1.8	0.50	0.38	1.18	0.387	0.337	0.333	0.323
7	13.31	F4	0.41	3.6	0.64	0.23	0.71	0.344	0.152	0.018	-0.032
8*	12.91	A2	0.05	1.3	0.68	0.63	1.95	0.447	0.417	0.261	0.251
9	11.96	A9	0.27	2.4	0.50	0.23	0.71	0.220	0.070	-0.004	-0.044
10	12.11	F4	0.41	3.6	0.53	0.12	0.37	0.286	0.096	0.030	-0.010

† Marraco & Forte (1978) classified star 4 as a G8 III on the basis of $V-R$ and $V-I$ colours. ⋆ Stars associated with nebulosities. ‡magnitudes are upper limits, object was detected but not resolved in that band due to the presence of a visual companion.

The presence of nebulosity in the vicinity of a star is one amongst various pointers for it being young. Towards CG 12, star 1, 2, 6, and 8 are clearly associated with nebulosities. Star 1 ($h4636$), a visual binary with angular separation of the components $\sim 4''$ (Reipurth & Zinnecker 1993), is located in the head region of CG 12 illuminating the reflection nebula NGC 5367. Spectra of northern (h4636N) and southern ($h4636S$) components of $h4636$ in the range 4500-6700Å and 7500-9000Å are shown in the Figure 2.13 (a) and (b) respectively. The presence of He I ($\lambda6678$) in absorption in $h4636N$ and $h4636S$ indicates that both are early type hot stars. Based on the relative strength of He I ($\lambda6678$) in $h4636N$ and $h4636S$ and comparing the spectra with those in the atlas of Jacoby et al. (1984), we have determined a B4 and B7 spectral type to $h4636N$ and $h4636S$ respectively. The spectrum of $h4636N$ shows Hα (λ6563) and Hβ (λ4861) Balmer lines in emission in the spectral range 4500-6700Å. The Ca II triplet lines $\lambda\lambda$8498, 8542, 8662, O I λ8446 and Paschen lines are found to be in emission in the range 7500-9000Å with O I λ7774 line in absorption. The spectrum of $h4636S$ shows no emission features.

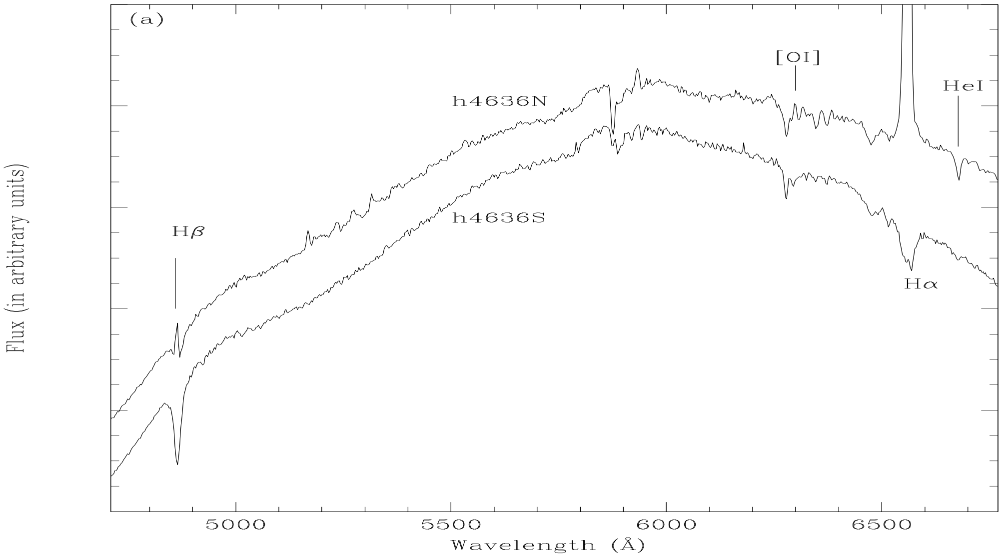

Figure 2.12: Spectra in the range 4500-6700Å of northern and southern components of the visual binary $h4636$.

The medium resolution (R $\sim$ 2500) spectrum of $h4636N$, presented in Figure 2.14 shows Hα in emission with a double-peaked line profile. The strength of the secondary peak is found to be more than half the strength of the primary and hence the line profile can be classified as type II according to the definition given by Reipurth et al. (1996). Spectrum of $h4636N$ also shows the presence of forbidden lines [O I] (λ6300 and λ6364) in emission. In a recent study on 131 Herbig AeBe stars which includes $h4636N$, Vieira et al. (2003) classified the line profile of Hα line of $h4636N$ as type III. Sources with the strength of the secondary peak less than half the strength of the primary are classified as type III. This suggests a possible variability in the Hα line profile of $h4636N$. They also noted the presence of [O I] (λ6300 and λ6364) in emission in $h4636N$. In order to look for a correlation between the circumstellar environment and

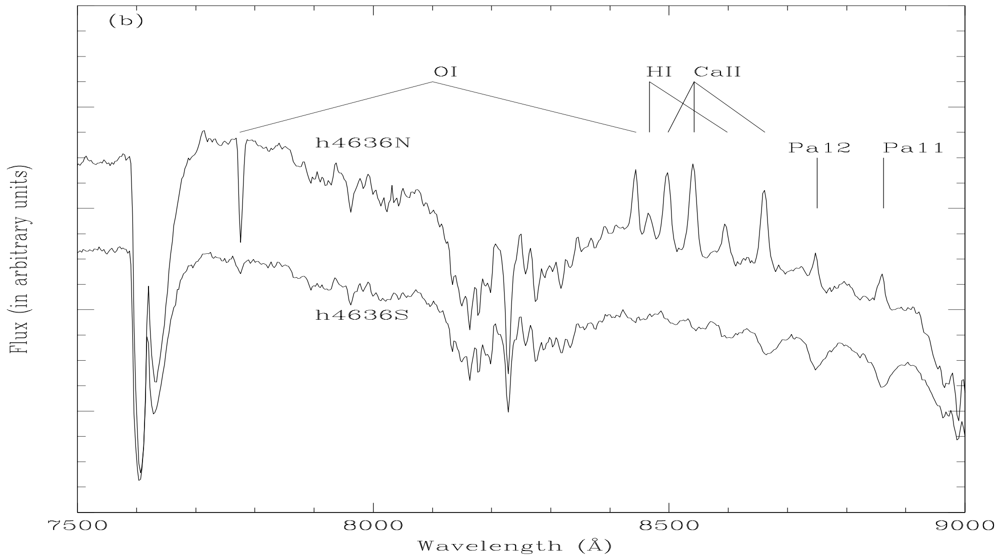

Figure 2.13: Spectra in the range 7500-9000Å of northern and southern components of the visual binary *h*4636.

the Balmer line profiles and also the presence of forbidden lines, Vieira et al. (2003) conducted a study on 62 Herbig AeBe stars. They found that the Hα line profiles of type II and III and the forbidden lines are concentrated in those objects which have significant circumstellar contribution inferred from the calculated SEDs of these objects. Corcoran & Ray (1997) suggested an evolutionary sequence for Herbig AeBe stars based on their study of forbidden lines in these stars. According to them, stars with strong blueshifted [O I] λ6300 emission are less evolved (catagory I), stars with lower blueshifted velocities and a reduced frequency of outflow activity (catagory II) are older than catagory I, stars with low velocity redshifted emission and no association with jet or molecular outflow activity (catagory III) are considered as more evolved compared to catagory I and II, and category IV stars showing symmetric and unshifted [OI] emission and which are not generally believed to power outflow phenomena are considered as most evolved. No shift in the central wavelength is apparent for the forbidden lines in $h4636N$ at the resolution of the spectrum. These spectral features indicate that $h4636N$ is relatively evolved Herbig Be star.

The equivalent width (W_λ) of Hα, Hβ, O I λ8446, and Ca II triplet lines $\lambda\lambda$8498, 8542, 8662 emission lines in the spectrum of $h4636N$ are 47.2, 1.4, 2.3, 3.8, 5.0 and 4.5

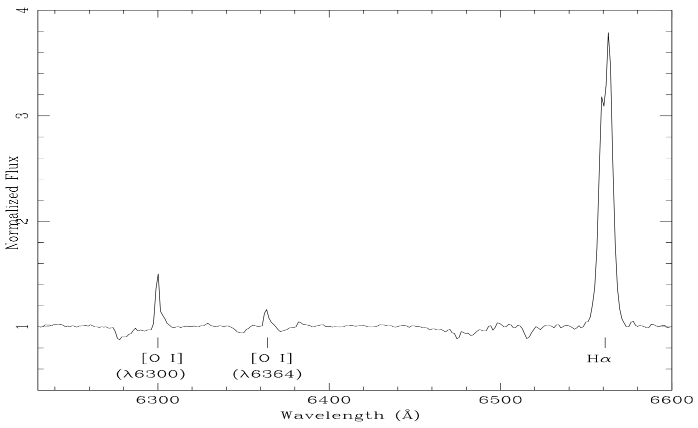

Figure 2.14: Medium-resolution spectrum of h4636N showing a double-peaked Hα line and forbidden [O I] (λ6300 and λ6364) lines.

Å respectively. As found in T Tauri stars and Herbig AeBe stars, the relative strengths of the Ca II triplet lines in h4636 are closer to unity than to the 1:9:5 ratio of their gf-values. This implies optically thick and saturated emission (Hamann & Persson 1992). The gas near the photosphere of h4636N (spectral type B4) will be ionized even at higher densities. This requires more extended high-density regions to explain the Ca II emission, probably also associated with a circumstellar disk, forming just above and below extended evaporating disk, due to the intense thermal and radiative pressures exerted by the star (Hamann & Simon 1986,1988). Equivalent width of O I λ7774 absorption line in h4636 is 2.3 Å. For stars near the main sequence (luminosity class III-V), the O I absorptions do not exceed $W_\lambda \sim 1.0$ Å and are greatest in the early A type stars (Keenan & Hynek 1950). In four Herbig AeBe stars namely, KK Oph, VV Ser, LkHα 234, and LkHα 215, the equivalent widths of O I line are 2.6, 4.8, 2.4, and 2.8 Å respectively (Hamann & Persson 1992). They pointed out that these are too strong for any spectral type and require large envelope contribution. The same can be concluded for h4636N, where a rotating disk or highly turbulent envelope could be responsible for the observed absorption of O I line.

From the infrared photometry in $JHKL$ of the combined light from h4636 and scanner spectroscopic observations made on the individual components of the double star, Williams et al. (1977) suggested the presence of a circumstellar shell around one component producing Balmer line emission and thermal re-radiation by grains. From Table 2.6, we find that both $h4636N$ and $h4636S$ have relatively large near-IR excess. This indicate the presence of dust surrounding both the components which are re-radiating at near-IR wavelengths. The optical extinction estimated towards $h4636N$ and $h4636S$ are found to be $A_v = 2.17$ and $A_v = 1.05$ respectively. The separation between the two components is $\sim$ 2200 AU at the derived distance of 550 pc. The variation in the observed extinction (also noted by Williams et al. 1977) towards the two components within such a small scale is hard to explain unless the observed extinction is arising from a circumstellar shell or disk around $h4636N$. Combining both spectroscopic and photometric evidences, we conclude that both $h4636N$ and $h4636S$ have significant amounts of circumstellar material probably in a shell geometry. The presence of an additional disk around $h4636N$ is highly likely through which the star is still accreting matter. The observed degree of polarization and position angle of the combined optical light (V band) from $h4636$ after correcting for interstellar contribution are 0.96±0.12 % and 156±6° respectively. The polarization position angle of 156±6° is found to be roughly perpendicular to the binary position angle of 34°.

Stars 2, 6, and 8 are also associated with nebulosities. We have determined a B8, A4 and A2 spectral types for stars 2, 6, and 8 respectively. The spectrum of these stars show no emission features which are characteristics of PMS stars. These stars must have evolved and already reached the main sequence. The visual extinction found towards stars 2, 6, and 8 are 0.74, 1.18 and 1.95 respectively. Relatively large visual extinction towards these stars and the presence of near-IR color excess (given in Table 2.6) indicate that they are partially embedded and have significant amounts of circumstellar dust in their environments. The nature of stars 2, 6, and 8 is more like the non-emission line stars found associated with the Orion star forming region (Manoj et al. 2002) showing the presence of dust even after the cessation of accretion activity in them.

The remaining stars, stars 3, 4, 5, 7, 9 and 10, also show no emission features in their spectrum. We find that stars 3, 4 and 10 are more likely to be foreground since the extinction towards them (0.37, 0.25 and 0.37 respectively) are relatively low and consistent with the interstellar extinction at their corresponding distances. We have determined a F6, G8, G9, F4, A9 and F4 spectral types for stars 3, 4, 5, 7, 9 and 10 respectively. Our spectral type determinations are in good agreement with those inferred by Williams et al. (1977) except for star 5. We have observed a spectral type of G9 for star 5, whereas Williams et al. (1977) (from two-colour diagram) have inferred a spectral type of A4 to it. The early spectral type (A4) of star 5 would imply that it is at a distance of $\sim$ 570 pc with a relatively large extinction ($\sim$ 2.4 magnitude) placing it just behind the cloud.

2.15.2 NIR-excess sources from 2MASS

The near-IR photometry derived from 2MASS survey allows us to study via colour-colour diagram (c-c) and colour-magnitude (c-m) diagrams, the combined effects of both the intrinsic properties of the sources and the overlying extinction. Near-IR photometry allows us to penetrate deeper into the molecular clouds, observe embedded population and learn about the global properties of the star formation region and its individual sources. Useful information concerning the nature of YSOs can be inferred from observed JHK colours of groups of stars when such data are displayed in the form of a c-c diagram. The reason for this is that observations at wavelengths between 1 and 2 μm probe the environments close to the surface of a YSO and are sensitive to the presence and the structure of any circumstellar material there. Also, the temperature regime probed by observations at such wavelengths corresponds to that where interstellar dust, a major source of opacity for circumstellar material, is thermally destroyed. Protostars, classical T Tauri stars (cTTS), weak-line T Tauri stars (wTTS), Herbig AeBe stars, and classical Be stars tend to occupy different regions of c-c space, although overlap of various types of objects also occur.

In Figure 2.15, we present $(J-H)$, $(H-K)$ c-c diagram for sources from within an area of radius $15'$ about h4636 which are represented by open circles. The JHK_s magnitudes of the sources are obtained from 2MASS observations (Cutri et al. 2000). Only sources with errors in JHK_s magnitudes $\lesssim 0.1$ are chosen and plotted in Figure 2.15. We assume that the Rieke & Lebofsky (1985) reddening law can be applied to the CG 12 cloud and represents a reasonable approximation of the NIR extinction caused by the associated molecular cloud. Also plotted as solid lines in Figure 2.15, are the locations of both unreddened main-sequence and giant stars (Koornneef 1983). From the

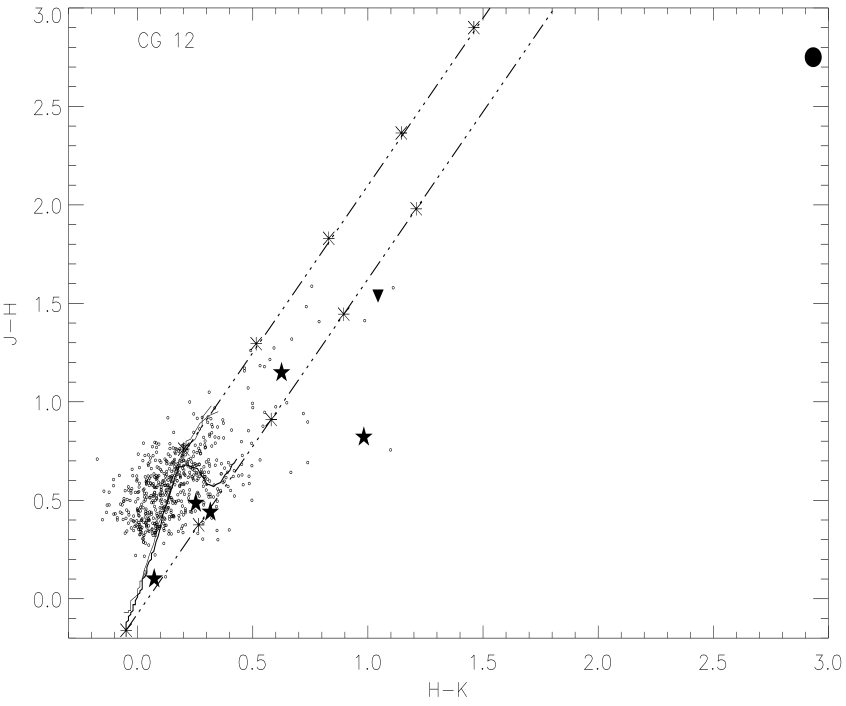

Figure 2.15: $J - H, H - K$ colour-colour diagram of objects found within $15'$ radius circular area around CG 12. The objects with errors in JHK magnitudes $\lesssim 0.1$ are plotted using open circles. Superimposed are two dashed lines parallel to the interstellar reddening vector. The region bounded by these lines can be occupied by reddened main-sequence dwarfs and giants. Points marked with asterisk on the dashed lines are at an interval of $A_v = 5\ mag$. The thick line represents main-sequence dwarfs and giants (Koornneef 1983). Filled star symbol represents stars associated with nebulosities. Visual companion to star 8 is also shown ($J - H = 1.15$ & $H - K = 0.63$). Two near-IR sources detected by Santos et al. (1998) are shown by filled circle and inverted triangle symbols.

extreme points of these curves we have plotted two dashed lines parallel to the Rieke & Lebofsky (1985) interstellar reddening vector. Points marked with asterisk on the dashed lines are at an interval of $A_v = 5\ mag$. The area between these lines corresponds to the reddening zone for normal stars. A reference field far away ($\sim 1°$) from the cloud is chosen and JHK_s magnitudes of the sources within an area of $15'$ in radius and with errors in magnitudes $\lesssim 0.1$ are obtained from 2MASS observations. The $(J - H)$, $(H - K)$ c-c diagram of sources from the reference field is shown in Figure 2.16. From Figure 2.15 it is clear that a significant fraction of the objects observed towards CG 12 are located between the two reddening vectors and is consistent with reddened background stars seen through the cloud since such objects are clearly absent in the Figure 2.16 which represents

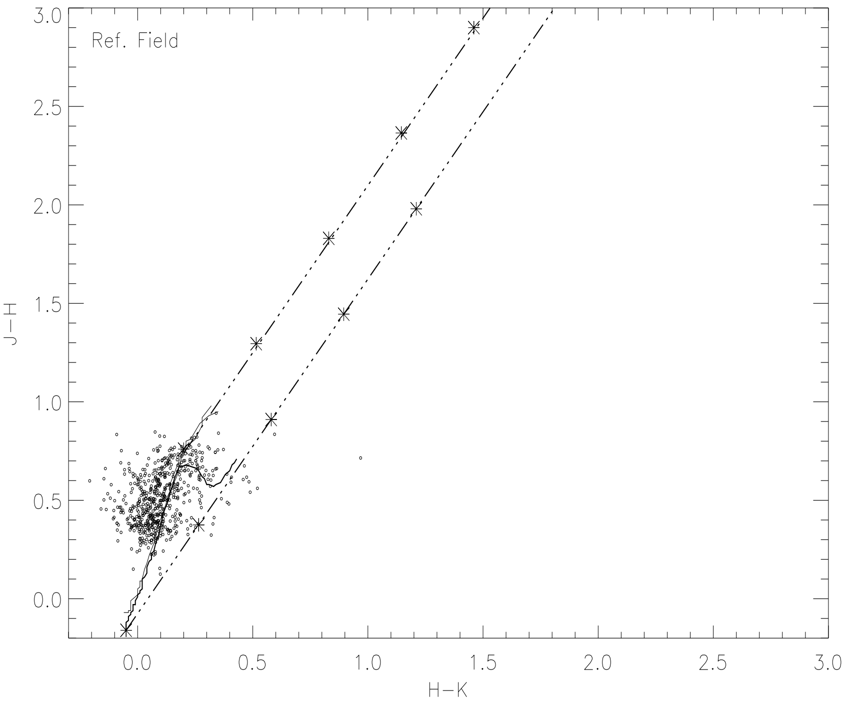

Figure 2.16: $J-H, H-K$ colour-colour diagram of objects found within $15'$ radius circular area around a reference region $\sim 1^\circ$ away from CG 12. The objects with errors in JHK magnitudes $\lesssim 0.1$ are plotted using open circles. Other plotted points have same meaning as in the Figure 2.15.

the objects observed towards the reference field. The region to the right of the reddening band is known as the infrared excess region (Lada & Adams 1992) and corresponds to the location of PMS stars. We find twice the number of objects (30) occupying this region (Figure 2.15) as compared to that (15) in the reference region (Figure 2.16). However, naked-T Tauri stars, post-T Tauri stars and some class I sources do not show any near-IR excess, and will be found between the two reddening vectors in such a diagram [e.g., sources found in ρ Ophiuchus by Wilking & Lada (1983)]. The objects occupying the region located between the two reddening vectors are spread along this band indicating that the extinction caused by the cloud or the circumstellar material can reach values upto 10-15 magnitudes of visual extinction. This is consistent with the extinction values obtained for CG 12 from the colour temperature. We have also plotted, in Figure 2.15, the stars associated with nebulosities and discussed in the previous section. Star 8 is found to have a visual companion with $J-H$ & $H-K$ values as 1.15 & 0.63 respectively is also shown in Figure 2.15. This source is either a low-mass PMS star with near-IR excess emission or a heavily extincted background star.

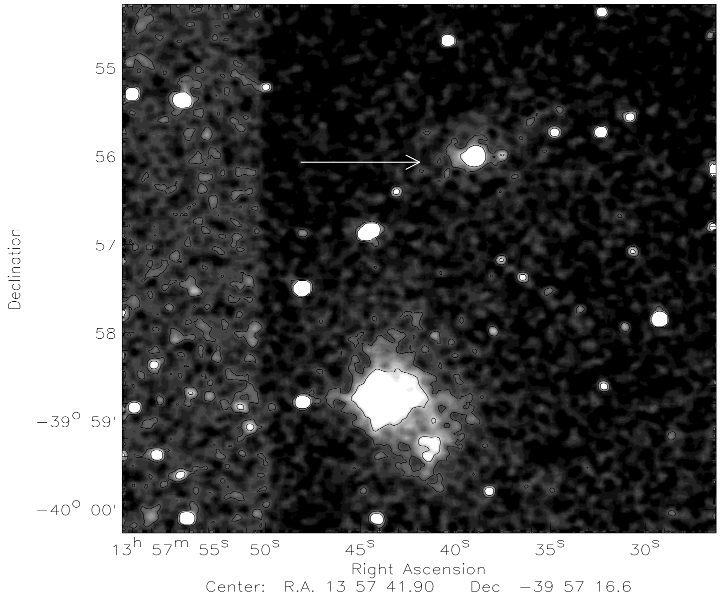

Figure 2.17: 2MASS K-band image of a field containing the head region of CG 12. The near-IR excess embedded source detected by Santos et al. (1998) positionally coincides with a source which is showing a faint nebulosity as indicated by an arrow. North is up and east is to the left.

Two objects showing near-IR excess emission and detected in near-IR observations of Santos et al. (1998) are shown with a filled circle and with an inverted filled triangle in Figure 2.15 respectively. Based on its near-IR colours, Santos et al. (1998) have classified this source as a class I young stellar object (YSO). The image of the field containing this source, from 2MASS observations, is presented in Figure 2.17. The presence of a faint nebulosity (indicated by an arrow) around this source, as evident from the Figure, indicates that it is associated with CG 12. The J, H, K magnitudes of this source (2MASS observations) are $15.230{\pm}0.068, 12.464{\pm}0.077, 10.109{\pm}0.112$. The position of this source in JHK c-c diagram (represented by a filled circle in Figure 2.15) is consistent with its classification as a class I YSO by Santos et al. (1998). It has large near-IR excess ($H - K = 2.93$) and is probably embedded deep ($J - H = 2.75$) inside the cloud. The binary component of this source is detected in K band of 2MASS observations also. Within the error ellipse of IRAS 13546-3941, Santos et al. (1998) have detected a faint source and classified it as a class II YSO based on its near-IR colors, but did not rule out the possibility of it being a background main-sequence star. The 2MASS J, H, K

magnitudes of this source are given as $16.428 \pm 0.117, 14.899 \pm 0.062, 14.045 \pm 0.058$. The position of this source in JHK c-c diagram (JHK from 2MASS) shown using an inverted filled triangle in Figure 2.15 indicates the presence of near-IR excess and hence this source is more likely to be a class II YSO and not a background main sequence star. The positions of both these sources coincide with the maximum extinction value we have obtained towards CG 12 (see § 2.14). The $C^{18}O$ emission also peaks at the same position (Yonekura et al. 1999) suggesting that this region is the site of current star formation in CG 12.

The K versus $J-K$ colour-magnitude (c-m) diagram for all the objects found within $15'$ radius about $h4636$ is plotted in Figure 2.18. In this diagram, main sequence loci are plotted for the distance (550 pc) of CG 12 (the solid line). Positions of the main sequence stars with various spectral types are marked on the solid line. A representative Rieke & Lebofsky (1985) reddening vector ($A_V = 5mag$) is plotted as an arrow.

With the K=14.7 (within 10% error), we would observe unreddened and unextincted main sequence stars down to spectral type M0 at 550 pc. This corresponds to a stellar mass of $\sim 0.6\ M_\odot$ obtained using the mass-M_K relation for main sequence stars shown in Zinnecker et al. (1993). However, PMS stars are over-luminous for their mass which would lower the effective PMS mass detection limit significantly. Zinnecker & McCaughrean (1991) derived age dependent mass-luminosity function over the age range 2×10^5 years to 2×10^6 years from homogeneous tracks calculated by I.Mazzitelli. They suggested that over this age range, 0.08 $M_\odot$ PMS objects would show a relatively small change in M_K from 4.9 to 5.3. This corresponds to a K magnitude range of 13.6-14.0 for stars in CG 12. But these values do not take into account the extinction due to the presence of the molecular cloud. At K the effect of the extinction is however minimal and the range of A_V values roughly between 0-15 magnitudes (as implied by near-IR c-c diagram) could lead the embedded population to become $\sim$ 1.5 magnitudes fainter than the values quoted above. This would suggest that 0.08 $M_\odot$ PMS stars would have K = 15.1-15.5. This is certainly below the currently chosen limit of 14.7. Hence with the K=14.7, we can detect PMS stars with masses above 0.2 $M_\odot$ towards CG 12.

In Figure 2.18 (c-m diagram), we show objects with near-IR excess from c-c diagram (Figure 2.15) represented by open star symbols. Thirty sources are found to have near-

IR excess towards the direction of CG 12. We also show the locations of stars with nebulosities which are clearly associated with CG 12, represented by filled star symbols. The J magnitude of star 6 (associated with nebulosity) is an upper limit. The read flag for this star is set to 6 in J band. Hence the star was detected in J band but could not resolve due to the presence of a visual companion. In Figure 2.18, we also show the visual companion to star 8, identified as 8a. Except for the stars with nebulosities and the near-IR embedded source (not shown in the figure due to its large $(J - K)$ value) found by Santos et al. (1998), all other sources with near-IR excess towards CG 12 are found to be fainter than $K \sim 12$ magnitude. The locations of stars with nebulosities in c-c and c-m diagrams indicate that they have not yet reached the main sequence even thought they show no spectroscopic features of a PMS star. The solid lines shown in green, blue and red are isochrones of low mass stars form 0.075 to 1 $M_\odot$ (Baraffe et al. 1998) of 2 Myr, 6 Myr and 5 Gyr drawn for 550 pc respectively. The six sources with near-IR excess emission and brighter than $K \sim 14$ magnitude are positionally distinct (in Figure 2.18) from other near-IR excess sources found towards CG 12. The companion to star 8, identified as 8a, is also located at similar regions occupied by these six stars. Based on their locations in c-c and c-m diagrams, we infer that these objects are low-mass PMS star candidates, having near-IR excess and very large extinction either due to the presence of cloud or circumstellar material or both.

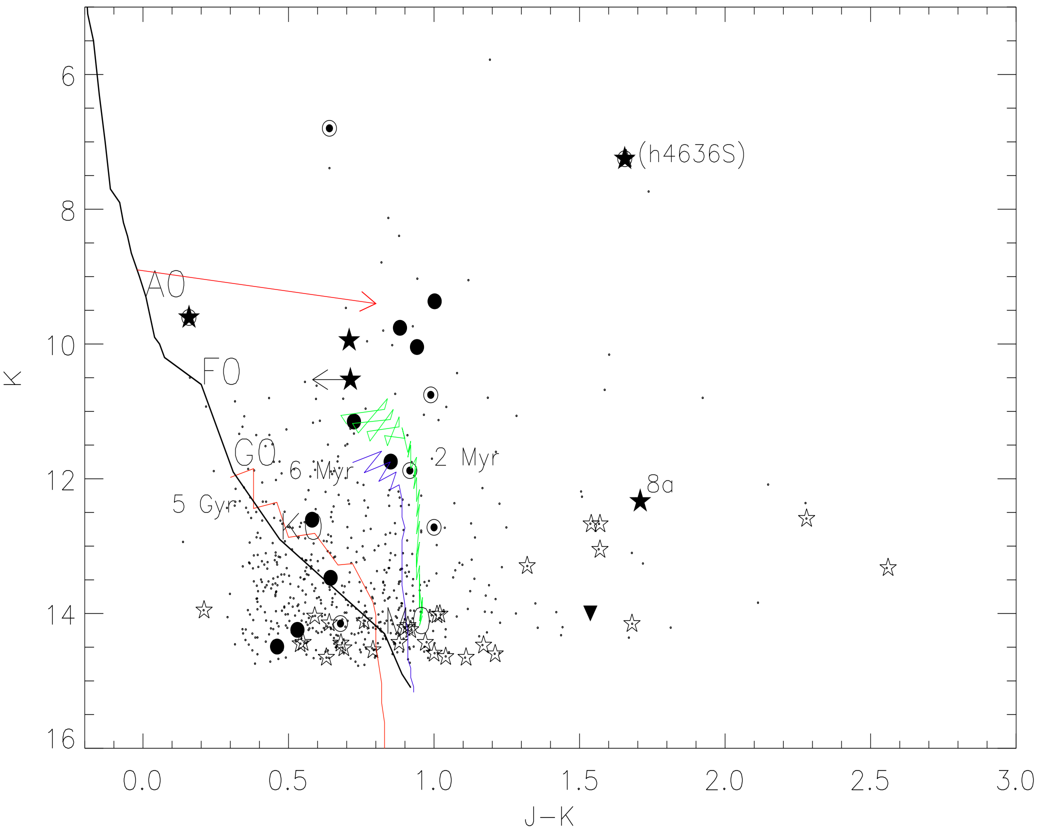

Figure 2.18: The $K, (J-K)$ colour magnitude diagram (CMD) of the sources found towards CG 12. **Solid line** represents main sequence loci plotted for the distance (550 pc) of CG 12. **Arrow** represents the reddening vector corresponding to an $A_V = 5$ mag. **Filled dots:** Sources found within a circular area of $15'$ radius around CG 12 about $h4636$, **Filled stars:** Stars associated with nebulosities, **Open stars:** Sources with near-IR excess emission found within the circular area of $15'$ radius, **Filled circles with halo:** X-ray sources detected within the cloud boundaries towards CG 12, **Filled circles:** X-ray sources detected outside the cloud boundaries towards CG 12, **Inverted triangle:** Near-IR source detected by Santos et al. (1998) which lies within the error ellipse of IRAS 13546-3941. The **green**, **blue**, and **red solid lines** are isochrones (Baraffe et al. 1998) of 2 Myr, 6 Mys and 2 Gyr for 550 pc distance respectively.

2.15.3 X-ray sources from ROSAT

The results of the study on 25 X-ray sources found towards CG 12 are given in Table 2.7. The eight sources found within the cloud boundaries and seventeen sources found outside the cloud boundaries are distinguished in Table 2.7. In Table 2.7, column 1 gives (1) serial number, column (2) gives radial distance of the detection from the position of the double star $h4636$ in *degree*, column (3) gives source identification as in the catalog, columns (4)and (5) give right ascension and declination of sources (epoch 2000) respectively, column (6) and (7) give background subtracted count rate accumulated in 0.24-2.0 keV and mean error on counts respectively. In columns (8) and (9) we give hardness ratios, i.e., X-ray colors, which are defined as follows (Neuhäuser et al. 2000): If $Z_{s,h1,h2}$ are the count rates in the bands soft (0.1-0.4keV), hard 1 (0.4-0.9keV), hard 2 (0.9-2.0keV), respectively, then

$$HR1 = \frac{Z_{h1} + Z_{h2} - Z_s}{Z_{h1} + Z_{h2} + Z_s} \quad \& \quad HR2 = \frac{Z_{h2} - Z_{h1}}{Z_{h2} + Z_{h1}} \tag{2.14}$$

The X-ray flux, given in column (10) are estimated using the equation

$$f_X = ECF.(count\ rate) \quad erg\ cm^{-2}\ s^{-1} \tag{2.15}$$

where ECF is the energy conversion factor. The conversion from the measured count rate to an energy flux requires some assumptions for the intrinsic source spectrum. Models for T Tauri X-ray emission assume a thermal spectrum with $k.T_X = 1keV$ (e.g., Feigelson & Decampli 1981) with Boltzmann's constant k and X-ray emission temperature T_X. The X-ray extinction is dominated by hydrogen and helium up to photon energies of about 0.5 keV (Morrison & McCammon 1983), and is mostly due to metals at higher energies. It is relatively insensitive to the state of hydrogen (molecular or atomic) or to the coalescence of dust grains. There will, however, be a dependence on the relative abundances. To determine the appropriate X-ray extinction from the optical extinction, it is necessary to assume a gas-to-dust ratio. In particular, the gas-to-dust ratio may be significantly lower in molecular clouds, owing to the suppression of the grain destruction mechanisms. This has two possible implications, firstly, trapping the metals in grains can slightly increase the X-ray opacity (Morrison & McCammon 1983) and secondly,

Table 2.7: X-ray sources detected by ROSAT towards the direction of CG 12.

S. no: (1)	r (°) (2)	Catalog source name (3)	α(J2000) (°) (4)	δ(J2000) (°) (5)	count rate (ct/s) (6)	ϵ_{count} (ct/s) (7)	HR1 (8)	HR2 (9)	log f_X (10)	log L_X (11)
X-ray sources projected inside the cloud boundaries										
1[†]	0.002	J1357.7-3958	209.430	-39.982	0.00253	0.00071	0.67	0.44	-13.523	30.011
2[*]	0.047	J1357.6-3956	209.409	-39.936	0.00343	0.00076	0.70	0.86	-13.385	30.149
3	0.057	J1357.8-3955	209.470	-39.931	0.00307	0.00078	0.70	0.29	-13.434	30.100
4[†]	0.061	J1358.0-3958	209.510	-39.970	0.00256	0.00079	0.37	-0.14	-13.581	29.953
5	0.067	J1357.3-3957	209.346	-39.965	0.00182	0.00062	0.67	0.00	-13.666	29.868
6[†]	0.103	J1357.9-4004	209.476	-40.077	0.00699	0.00120	0.76	0.31	-13.064	30.470
7	0.140	J1357.3-3951	209.349	-39.855	0.00218	0.00064	0.50	0.67	-13.622	29.912
8	0.152	J1357.9-3950	209.499	-39.837	0.00891	0.00120	0.62	0.29	-12.985	30.549
X-ray sources projected outside the cloud boundaries										
9	0.122	J1357.0-3958	209.272	-39.977	0.00188	0.00062	0.55	0.41	-13.677	29.857
10	0.123	J1357.1-4002	209.296	-40.047	0.00594	0.00100	0.70	0.09	-13.146	30.388
11	0.150	J1357.0-4003	209.270	-40.065	0.00251	0.00075	0.45	0.43	-13.572	29.962
12	0.185	J1357.7-3947	209.440	-39.795	0.00377	0.00086	0.44	0.15	-13.396	30.138
13	0.189	J1358.4-3951	209.621	-39.859	0.01430	0.00160	0.32	-0.12	-12.843	30.691
14	0.191	J1356.7-4000	209.183	-40.003	0.00336	0.00076	0.44	0.08	-13.446	30.088
15	0.194	J1356.7-3955	209.190	-39.921	0.00324	0.00074	0.43	-0.12	-13.465	30.069
16	0.282	J1356.3-3953	209.081	-39.894	0.00205	0.00067	0.23	0.00	-13.709	29.825
17	0.290	J1356.7-3945	209.199	-39.752	0.01710	0.00160	0.44	0.01	-12.739	30.795
18	0.330	J1356.6-4014	209.165	-40.240	0.01930	0.00190	0.64	0.26	-12.647	30.887
19	0.424	J1356.2-3939	209.072	-39.658	0.01570	0.00180	0.29	-0.05	-12.810	30.724
20	0.437	J1356.7-4022	209.197	-40.378	0.01330	0.00210	-0.02	-0.13	-12.963	30.571
21	0.516	J1400.2-4009	210.066	-40.154	0.02220	0.00320	-0.00	-0.20	-12.735	30.799
22	0.538	J1354.9-3953	208.739	-39.897	0.00785	0.00150	-0.06	-0.49	-13.202	30.331
23	0.544	J1354.8-3959	208.721	-39.995	0.00548	0.00150	0.09	-0.36	-13.317	30.217
24	0.783	J1359.2-3915	209.803	-39.251	0.04840	0.00470	0.16	-0.16	-12.354	31.180
25	0.847	J1353.7-3936	208.439	-39.610	0.02720	0.00350	-0.11	-0.36	-12.678	30.856

[†] Stars studied by Williams et al. (1977). S no: 1, 4, & 6 correspond to *h*4636, star 4, & star 2 respectively. [*] Embedded near-IR source.

the extinction due to dust measured by photometry would be higher compared to the true hydrogen column density which would then lead to an overestimate of the X-ray extinction. For a Raymond-Smith spectrum (Raymond & Smith 1977) the ROSAT PSPC energy conversion factor (ECF) varies only slightly when varying N_H between $10^{18} cm^{-2}$ and $10^{22} cm^{-2}$ and $k.T_X$ between 0.4 keV and 2 keV (Neuhäuser et al. 1995). Schmitt et al. (1995) have derived an expression for the conversion factor as a function of hardness ratio HR 1, assuming the X-ray extinction to be negligible, for their study of low-mass stars in the solar neighbourhood which is given as

$$ECF = (5.30.HR1 + 8.31).10^{-12} erg\ cm^{-2}\ cts^{-1} \tag{2.16}$$

The estimated luminosity of the X-ray sources, assuming a distance of 550 pc to CG 12, are given in column (11).

We present in Figure 2.19, the HR 1 and HR 2 X-ray c-c diagram for the 25 X-ray sources found towards CG 12. Sources found within and outside the cloud boundaries

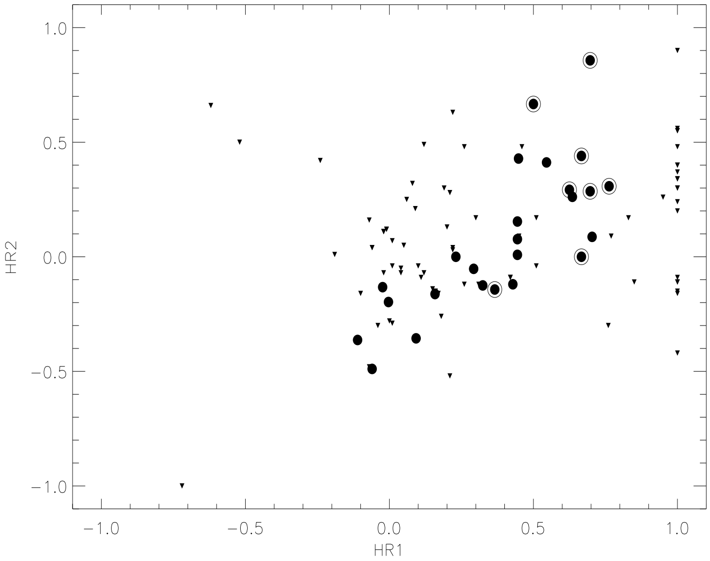

Figure 2.19: Positions of X-ray sources found towards CG 12 are shown in HR 1 versus HR 2 diagram. Filled circles with and without halo represent X-ray sources found inside and outside the cloud boundaries respectively. Positions of wTTS (Alcala et al. 1997) are shown using inverted triangles.

are represented by filled circles with and without halo respectively. We also plot in Figure 2.19, X-ray sources identified with weak-line T Tauri stars towards Chamaeleon star forming region (Alcala et al. 1997). The distribution of X-ray sources detected towards CG 12 plotted in Figure 2.19 are similar to those identified with weak-line T Tauri stars towards Chamaeleon star forming region suggesting that these sources are most likely wTTS. In most parts of the parameter space populated by T Tauri stars in X-ray c-c diagram, the HR 1 and N_H as well as HR 2 and T_X are found to correlate (Neuhäuser 1995). The HR 2 values of wTTS and cTTS span a wide range and, hence, X-ray emission temperatures. While HR 1 values of wTTS range from $\sim$ 0 to 1, majority of cTTS have HR1 values 1 or close to 1. The separation of cTTS and wTTS in the hardness plot is mainly due to different amounts of material along the line-of-sight absorbing X-ray photons, particularly soft X-ray emission, so that highly absorbed TTS cannot be detected in ROSAT's soft energy band, hence HR=1. Neuhäuser et al. (1995) have discussed various possible sources (like ISM in front of star forming region, intercloud gas within star forming region, and circumstellar material) which are responsible for the absorption of X-ray photons. From the observational studies of various star forming regions, it was

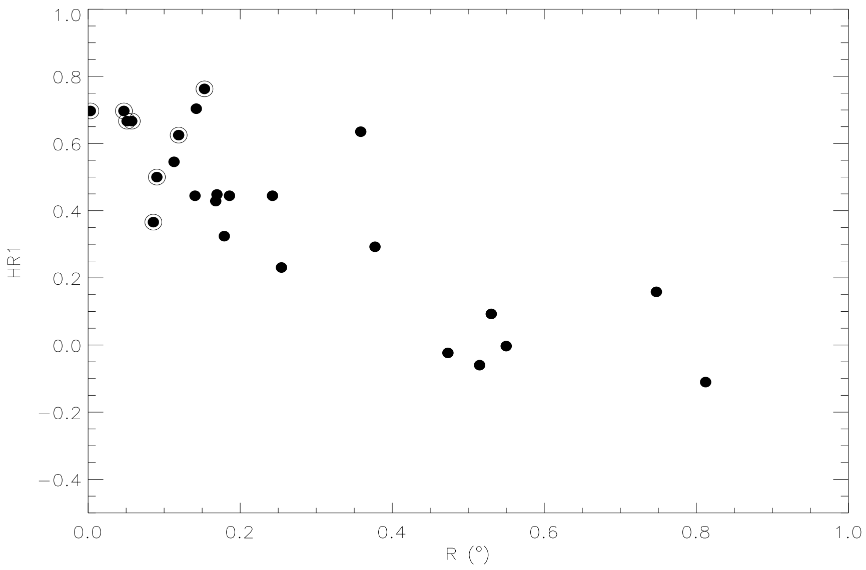

Figure 2.20: The HR 1 values of X-ray sources found within (filled circles with halo around) and outside the cloud boundaries (filled circles) plotted against the angular distance (°) of the sources w.r.t to the densest part in CG 12.

concluded that the different hardness ratios of cTTS and wTTS are caused mainly by different absorption in circumstellar material (Neuhäuser 1995). Towards CG 12, HR1 values of X-ray sources found within the cloud boundaries are in the range 0.5-0.8. In Figure 2.20, we plot HR 1 values of the X-ray sources against their projected angular distances from the densest part of the cloud (position where extinction values from our extinction map of CG 12 and $C^{18}O$ emission (Yonekura et al. 1999) peaks). As shown in Figure 2.19, HR 1 values are found to decrease with their projected angular distances from the dense region in the head. Sources found within the cloud boundaries show harder colours compared with that detected outside the cloud. This shows that the soft X-ray photons from the sources located inside the cloud boundaries are absorbed more. Most probably, the sources which are located inside the cloud boundary are relatively young and have significant amount of circumstellar material to absorb the soft X-ray photons.

In order to identify 2MASS counterparts to the X-ray sources found towards CG 12, we have made a search for the brightest source detected within 40″ radius (typical positional error of ROSAT detections) about X-ray detections in 2MASS observations. This is because, the PMS stars are brighter in K compared to their main sequence

Table 2.8: X-ray sources detected by ROSAT towards the direction of CG 12.

S No: (1)	r ($arcsec$) (2)	α(J2000) (°) (3)	δ(J2000) (°) (4)	J (5)	ϵ_J (6)	H (7)	ϵ_H (8)	K$_s$ (9)	ϵ_{K_s} (10)	B (11)	log (f_X/f_B) (12)
X-ray sources projected inside the cloud boundaries											
1	0.038	209.433127	-39.979763	8.865	0.021	8.069	0.088	7.264	0.065	11.21	-4.48
2	3.720	209.412178	-39.932983	15.230	0.068	12.464	0.077	10.109	0.112	-	-
3	8.684	209.476428	-39.922794	11.697	0.023	10.988	0.024	10.745	0.023	14.91	-2.91
4	0.766	209.514383	-39.963993	7.389	0.021	6.967	0.049	6.776	0.023	9.62	-5.18
5	20.22	209.346744	-39.963860	13.675	0.024	12.952	0.021	12.712	0.030	17.80	-1.99
6	6.989	209.483403	-40.072014	9.709	0.023	9.650	0.024	9.566	0.025	11.08	-4.07
7	7.179	209.355850	-39.850319	14.778	0.043	14.196	0.049	14.128	0.070	16.61	-2.42
8	16.63	209.500838	-39.834583	12.748	0.026	12.090	0.024	11.866	0.027	16.27	-1.92
X-ray sources projected outside the cloud boundaries											
9	37.390	209.267675	-39.962864	14.065	0.030	13.593	0.022	13.448	0.038	16.15	-2.66
10	13.618	209.297206	-40.042927	11.826	0.023	11.253	0.024	11.131	0.021	14.52	-2.78
12	11.970	209.447119	-39.791817	12.548	0.027	11.902	0.025	11.730	0.024	15.62	-2.59
14	36.166	209.194303	-40.005592	14.722	0.040	14.353	0.043	14.216	0.074	16.19	-2.41
15	25.240	209.192933	-39.921947	10.595	0.023	9.926	0.021	9.746	0.019	13.97	-3.32
16	24.003	209.077232	-39.886204	14.900	0.039	14.572	0.057	14.462	0.082	16.03	-2.74
17	16.194	209.199299	-39.748764	10.322	0.028	9.673	0.031	9.357	0.021	14.81	-2.26
18	34.780	209.161315	-40.227097	13.138	0.028	12.664	0.026	12.583	0.030	14.83	-2.16
19	15.621	209.073521	-39.655048	10.939	0.023	10.277	0.022	10.033	0.021	15.80	-1.93

counterparts and hence the brightest source within 40″ could most probably be the source of X-ray emission and PMS as well. All the eight X-ray detections found inside the cloud boundaries have 2MASS counterparts within 40″ radius. Of the seventeen X-ray detections found outside the cloud boundaries nine are found to have 2MASS counterpart within 40″ positional offset. The results are presented in Table 2.8. Column 1 gives serial number same as given in Table 2.7. Columns 2 & 3 give right ascension and declination of selected 2MASS sources (epoch 2000) respectively. Columns 4, 6, & 8 give JHK magnitudes with corresponding errors given in column 5, 7, & 9 respectively. JHK magnitudes with errors $\lesssim$ 0.1 are considered here. The X-ray c-c diagram for different objects such as stars, AGNs, cataclysmic variables, white dwarfs and X-ray binaries shows that except for white dwarfs (soft sources) and X-ray binaries (hard sources), other sources have similar X-ray colours (Motch et al. 1998). It is thus important to see if any of the X-ray detections towards CG 12 are of extragalactic in origin. The most informative diagrams are those involving optical information, basically in the form of the f_X/f_{opt} ratio. Although stars and extragalactic sources have similar X-ray colours, their mean X-ray to optical ratios are quite different, because extragalactic X-ray sources are optically faint but X-ray bright, and thus the two populations are well separated in the HR 1/2, f_X/f_{opt} diagram (Motch et al. 1998). Since V magnitudes for all X-ray sources found inside and outside the cloud boundaries are not available, we obtained

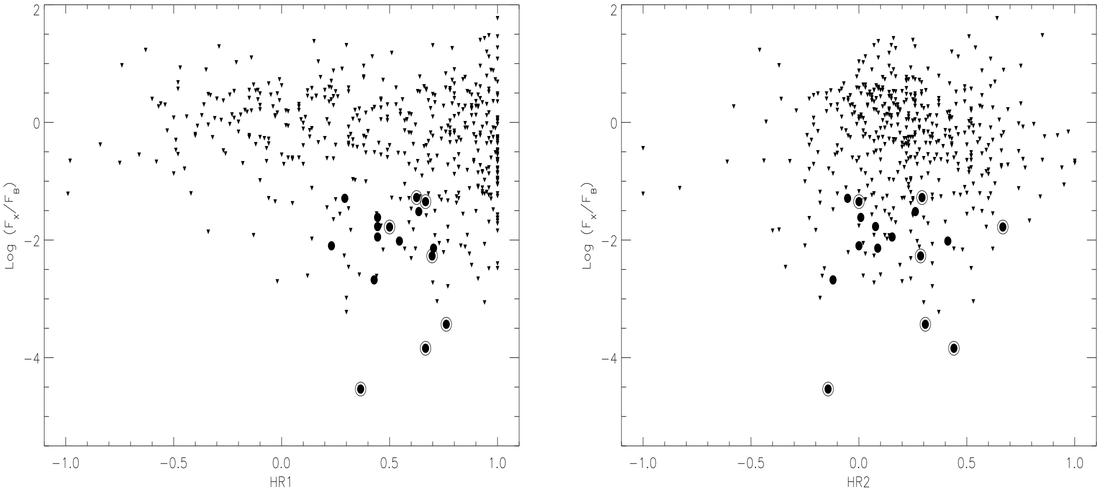

Figure 2.21: Left: Positions of X-ray sources in log (f_X/f_B) versus HR 1 plot is presented. Filled circles with and without halo represent X-ray sources found within and outside the cloud boundaries. Also presented are X-ray sources identified with extragalactic counterparts (Zimmermann et al. 2001) represented by inverted triangles . Right: Sources plotted in Left plot are given in log (f_X/f_B) versus HR 2 plot (all the symbols have same meaning).

B magnitudes for all the 2MASS counterparts to X-ray sources from the USNO-B1.0 Catalog (Monet et al. 2003). These values (B magnitudes) are presented in column 10 of Table 2.8. All the 2MASS sources have USNO detections with positional offsets $\lesssim 1-2''$. In column 11, we give log (f_X/f_B) ratios for all the X-ray detections. For calculating f_B, we used $f_B = 6.3\times10^{-6}.10^{-0.4m_B}$, where m_B is the B magnitude of the sources from USNO. In Figure 2.21, we plot log (f_X/f_B) versus HR 1 and HR 2. Filled circles with and without halo represent X-ray sources found within and outside the cloud boundaries. In a correlation study of the ROSAT All-Sky Survey Bright Source Catalogue with the Catalogue of Principal Galaxies, X-ray sources with possible extragalactic counterparts within a search radius of $100''$ are found (Zimmermann et al. 2001). We have obtained HR 1, HR2, f_X and B magnitude for sources identified by them as galaxies. The log (f_X/f_B) for these sources are plotted against HR 1 and HR 2 in Figure 2.21. It is clear from the Figure 2.21 that the distribution of X-ray sources are quite different from that of the galaxies implying that the X-ray detections found towards CG 12 are most probably stellar than extragalactic in origin.

The double star $h4636$, star 2, star 4 and the embedded near-IR source, discussed in previous sections, are among the eight sources, located within the cloud boundaries,

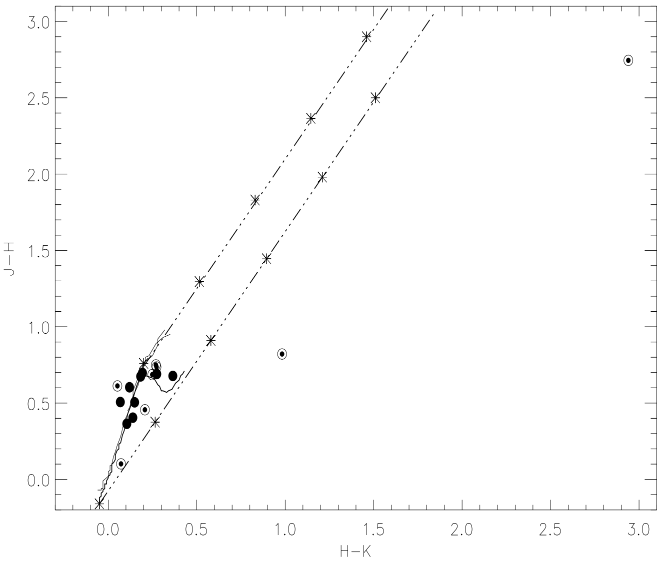

Figure 2.22: Positions of X-ray sources in $J - H, H - K$ colour-colour diagram are shown. Symbols used in this plot are same as in HR 1 versus HR 2 diagram.

showing X-ray emission. The northern component $h4636N$, showing the characteristics of a Herbig Be star, could possibly be the source of X-ray emission among the double star $h4636$. Herbig AeBe stars have been detected as X-ray sources with their X-ray luminosity found to correlate not to $v_{rot} sin\ i$ but to mass-loss rate (Zinnecker & Preibisch 1994). This implies that X-ray emission of Herbig AeBe stars is not caused by the magnetic activities, mechanism responsible for X-ray emission from low-mass star, but is originating from shock heated regions in the radiation driven winds. The presence of forbidden line [O I] (λ6300 Å) in emission in $h4636N$, which is an indicator of stellar wind (Böhm & Catala 1994; Böhm & Hirth 1997), strengthens the argument. The spectrum of star 2 is consistent with a B8 type main sequence star. Main sequence stars in the intermediate-mass range (2 - 10 $M_\odot$) or spectral range (A4 - B2) exhibit no significant X-ray activity (Rosner et al. 1985; Berghöfer et al. 1997), because of the absence of X-ray producing mechanisms (neither the strong UV fields to accelerate high-speed stellar winds working in high-mass stars nor the surface convection responsible for magnetic activity in low-mass stars). But the log (L_X/L_{bol}) ratio of star 2 is ~ -5.1 which is higher than the typical values for B type main sequence stars of -8 to -9 (Cassinelli et al. 1994). The position of star 2 in the c-m diagram (Figure 2.18) indicates that this star has not yet arrived on the main sequence. However, the X-ray emission from a low-mass companion to star 2 is highly likely. The spectrum of star 4 is more consistent with that of a late type giant (G8 III). The f_X/f_V estimated for this source is $\sim 2.5 \times 10^{-5}$ is which is consistent with the typical f_X/f_V values ($\sim 2.5 \times 10^{-5}$ to $\lesssim 7 \times 10^{-7}$ found for G giants (Maggio et al. 1990). The embedded near-IR excess source, discussed in section 2.15.2, is also found to be a source of X-ray emission. The HR 1 value of this star is found to be 0.70 which is somewhat lower than that of a typical cTTS and higher than that of a wTTS. This source, thus, must be representing an intermediated stage between cTTS and wTTS. The positions of the rest of the four X-ray sources (J1357.8-3955, J1357.3-3957, J1357.3-3951, and J1357.9-3950) found within the cloud boundaries and not identified with any of the previously known sources are shown in Figure 2.18 using filled circles with halo. Of these four, three sources (J1357.8-3955, J1357.3-3957, and J1357.9-3950) are brighter in K ($\lesssim 13$) and found to occupy positions above the main sequence in $(K, J-K)$ c-m diagram. These sources show a slight near-IR excess emission in $J-H, H-K$ c-c diagram given in Figure 2.22. The presence of a slight near-IR excess in wTTS, probably due to a remnant of circumstellar matter, was shown by Chavarria et al. (2000) from their study on wTTS in Taurus-Auriga, Orion and Scorpius OB2-2 star forming regions. The positions of these three sources (J1357.8-3955, J1357.3-3957, and J1357.9-3950) in $K, J-K$ colour magnitude and $J-H, H-K$ c-c diagrams suggest that they are the probable wTTS candidates. We have inferred an age of $\sim 1-2$ Myr for these three sources by comparing their positions w.r.t the isochrones of low mass PMS stars (Baraffe et al. 1998) in Figure 2.18.

The positions of the X-ray sources found outside the cloud boundaries are represented by filled circles in Figure 2.18. Of the nine X-ray sources (for which we found 2MASS counterparts within $40''$ radius), five sources (J1357.1-4002, J1357.7-3947, J1356.7-3955, J1356.7-3945 and J1356.2-3939) occupy positions above main sequence. Three of them (J1356.7-3955, J1356.7-3945, and J1356.2-3939) which are brighter than $K = 11$ magnitude could be late A - late F type PMS star candidates and two sources (J1357.1-4002 and J1357.7-3947) with K brighter than 12 but fainter than 11 magnitude could be low-mass PMS star candidates. All these five sources show near-IR excess similar to the normal main sequence stars (Figure 2.22). We identify the two sources (J1357.1-4002 and J1357.7-3947) which are fainter than $K = 11$ magnitudes with weak-line T Tauri stars based on their locations in c-m and c-c diagrams and estimate an age of $\sim$ 6 - 7 Mys by isochrone fitting. However, spectroscopic observations of all the identified PMS star candidates are needed to confirm their true nature.

2.16 Star formation at high galactic latitudes

From the multi-wavelength study of star forming region CG 12, we have identified the probable PMS candidates towards the direction of the cloud. The spatial distribution of PMS stars is a key to understand the star formation process in general and, in particular, to describe the star formation history in a star-forming region. In Figure 2.23 we show the distribution of all the PMS star candidates identified towards CG 12. The five X-ray sources detected outside the cloud boundaries are shown using red stars. These sources are distributed towards the north-west part of the head. The four X-ray sources which are detected inside the cloud boundaries but are not identified with any of the previously known sources are represented by dark blue stars. The near-IR excess sources identified from $J - H$, $H - K$ c-c diagram, which are brighter than $K = 14$ magnitude, and not identified with any of the previously known objects are shown using light blue stars in Figure 2.23. Stars with nebulosities are represented by filled yellow circles. The embedded near-IR excess source identified by Santos et al. (1998) are shown using green star. The location where the bipolar molecular outflow was detected by White (1993) is shown using filled blue circle. We have superposed the 100 μm contours on the Digitized Sky Survey (DSS) image in Figure 2.23. We notice in Figure 2.23 that majority of the identified PMS star candidates are lying within and in the vicinity of highest density regions of the CG head. This shows that the star formation is active towards the north and north-west parts of $h4636$. In Figure 2.23, it is clear that the distribution of the identified PMS candidates are also oriented roughly in the direction of the tail and the magnetic field lines. This indicates a common mechanism which is responsible for the cometary morphology, observed magnetic field orientation and star formation in CG 12.

Williams et al. (1977) suggested that a high galactic latitude supernova explosion at $l \simeq 320°, b \simeq 30°$ could be the cause of cometary morphology and triggering of star formation. The presence of a shell or loop of HI centred near $l = 320°, b = 30°$ in the radiophotograph by Heiles (1976) was proposed as evidence for this. Only a part of this loop is seen in the HI map of Heiles (1976) as their HI observations did not entirely cover the region containing CG 12 due to its southern declination. The HI maps in Cleary, Haslam & Heiles (1979) and Dickey & Lockman (1990) that combine both northern and southern sky surveys in HI do show the presence of a complete HI shell of $\sim 20°$ angular diameter centred near $l = 315°, b = 30°$. In Figure 2.24, we show the HI map (resolution $\sim 1°$) of the region. CG 12, as seen in projection, is positioned close to the shell boundary and its cometary tail points away from the centre of the HI shell. The supernova theory for the cometary morphology and star formation in CG 12 is therefore plausible. However, it is not clear whether this dense globule was formed as a result of the supernova remnant expanding into the ambient interstellar gas or it was a pre-existing cloud. The IRAS 100μm image, centred at $RA(J2000) = 13^h40^m24^s$ and $DEC(J2000) = -31°41'00''$, of the region containing CG 12 is shown in Figure 2.25. We have identified the positions of CG 12 and a dark cloud, DCld 318.7+16.9. A image of the field containing the dark cloud, DCld 318.7+16.9, reproduced from Digitized Sky Survey is shown in Figure 2.26. The arrow indicates the direction towards the shell centre. The sharp edges of the cloud is evident from the Figure 2.26 which shows that shock waves from the supernova explosion, responsible for the cometary morphology and triggering of star formation in CG 12, might have influenced the dark cloud DCld 318.7+16.9 also.

A lower limit to the total mass of recently formed stars in the cloud can be computed by summing up the masses (corresponding to the main sequence spectral types) of the stars 1 (h4636, B4+B7), 2 (B8), 6 (A4) and 8 (A2) that are associated with nebulosities involved in the cloud and show characteristics of YSOs. Using stellar mass values (from Schmidt-Kaler) of 6.4, 4.5, 3.8, 2.4 and 2.1 $M_\odot$ for the spectral types B4, B7, B8, A2 and A4 respectively, the total mass $M_\star$ of the young stars formed in the cloud is $\gtrsim 19\ M_\odot$. Therefore the star formation efficiency (SFE = $M_\star/(M_\star+M_{gas})$, where M_{gas} ($\sim 100\ M_\odot$) is the mass of the cloud in gas form) is $\gtrsim 16$ %. The cloud is also forming stars with masses lower than that of star 6 (2.1 $M_\odot$), the least massive of the optically visible YSOs. In addition to CO outflow and infrared sources detected by White (1993) and Santo et al. (1998) there could be other as yet undiscovered lower mass YSOs in CG 12. If the star formation process in CG 12 produces young stars with a mass function similar to the Salpeter initial mass function ($dn_\star/dm_\star \propto m_\star^{-2.35}$, where $dn_\star$ is the number of stars in the mass range $m_\star + dm_\star$), as also found in many embedded star clusters like Trapezium and IC 348 (Lada & Lada 2003), and stars as low in mass as 0.6 $M_\odot$ (below which the initial mass function seems to flatten and then decline beyond $\sim$ 0.1 $M_\odot$), then, by integrating the mass function over the range 0.6 $M_\odot$ to 6.4 $M_\odot$, the total mass of stars formed (or to be formed) in CG 12 is found to be $\sim$ 50 $M_\odot$ (not counting any star in the mass range 0.6 - 0.1 $M_\odot$ that may also form). The SFE will then be $\sim$ 33 %.

By estimating the age of the supernova shell, Williams et al. (1977) have suggested that the shell has been expanding for about 7 to 19 Myr. As discussed above, we find the X-ray sources with ages $\sim 6 - 7$ Myr lying outside the CG head in the direction towards the shell centre ($l = 315°, b = 30°$) and younger YSOs with ages $\sim 10^5$ yr $\sim$ 1 Myr are found embedded within the CG head. This is consistent with a star formation episode triggered by supernova explosion $\sim$ 10 Myr ago and still in progress in the CG head.

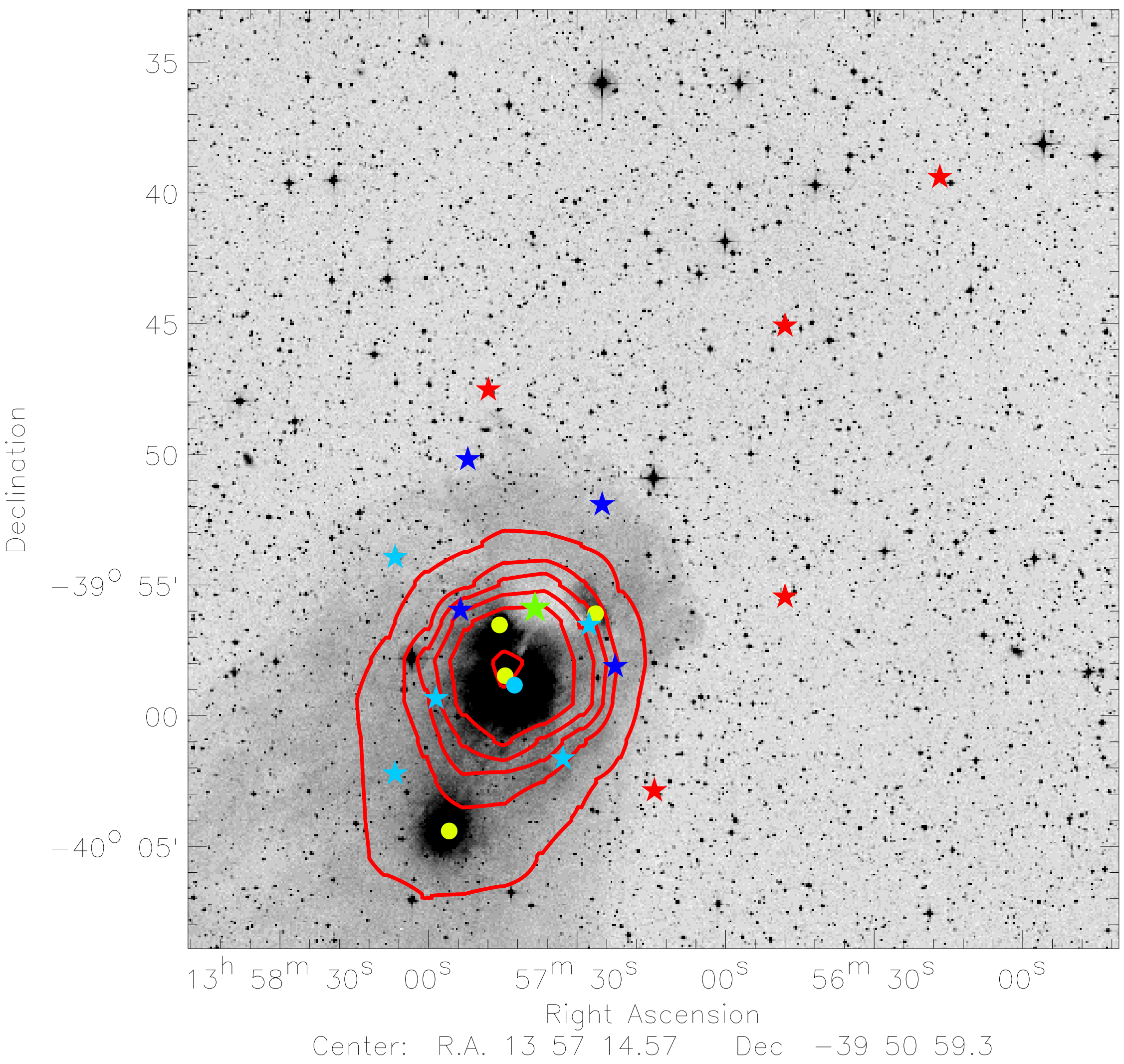

Figure 2.23: Distribution of YSOs associated with CG 12 are presented. Objects represented by symbols: **red star**: X-ray sources located outside the cloud boundaries and identified with wTTS candidates; **dark blue**: X-ray sources located inside the cloud boundaries and identified with wTTS candidates; **light blue**: near-IR excess sources brighter than $K = 14$ magnitudes; **filled yellow circle**: sources associated with nebulosities; **green star**: embedded near-IR source identified by Santos et al. (1998); **filled blue circle**: bipolar molecular outflow source detected by White (1993). Overplotted are the 100 μm contours with levels at 30, 50, 60, 80, 100 & 150 $MJy\ sr^{-1}$ (innermost contour).

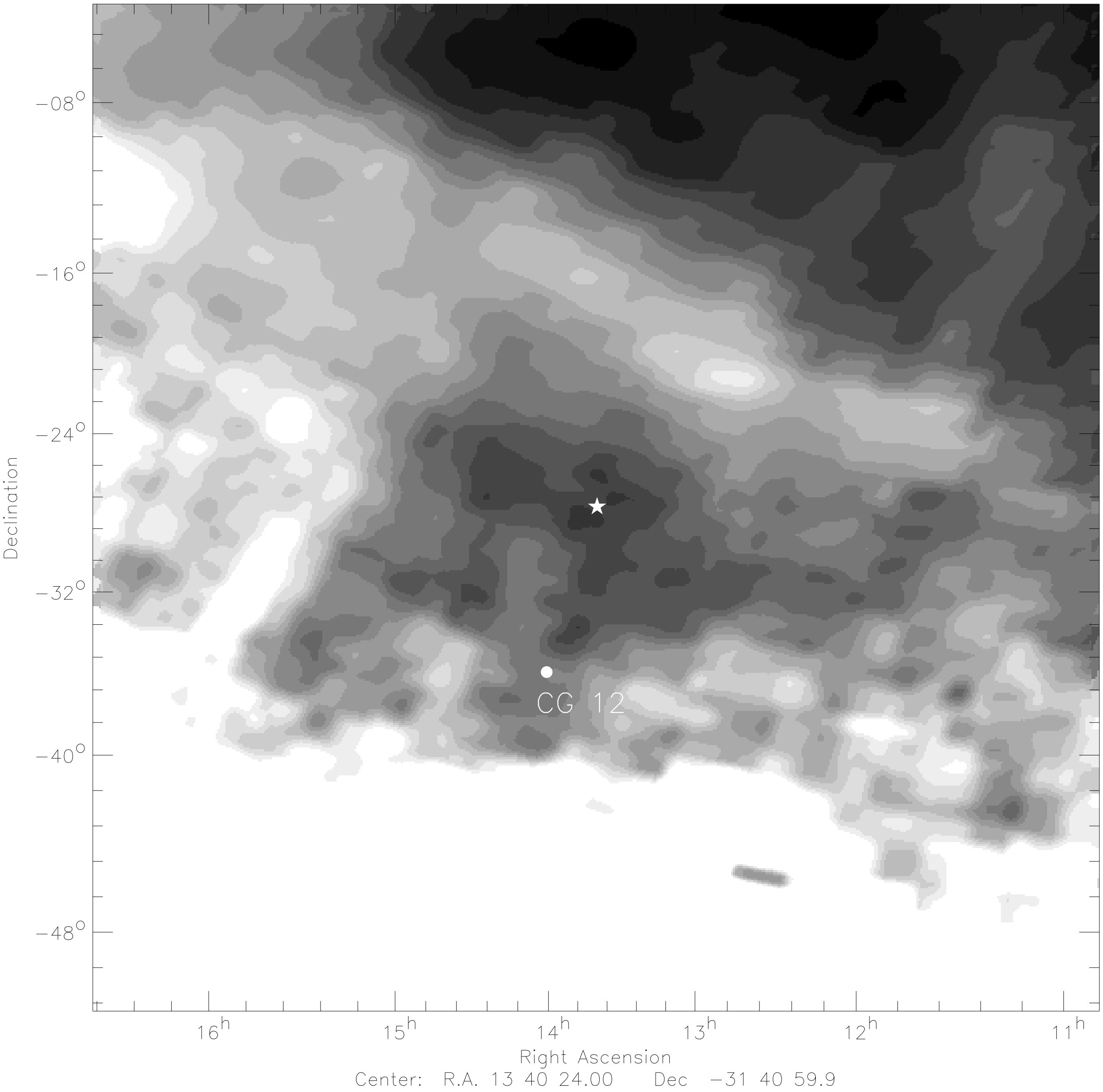

Figure 2.24: The HI map (resolution ~ 1°) of 50° × 50° field containing CG 12. CG 12, as seen in projection, is positioned close to the shell boundaries and its cometary tail points away from the centre of the H I shell. North is up and east is to the left. The H I image is obtained from the SkyView (a Virtual Observatory on the Net generating images of any part of the sky at wavelengths in all regimes from Radio to Gamma-Ray).

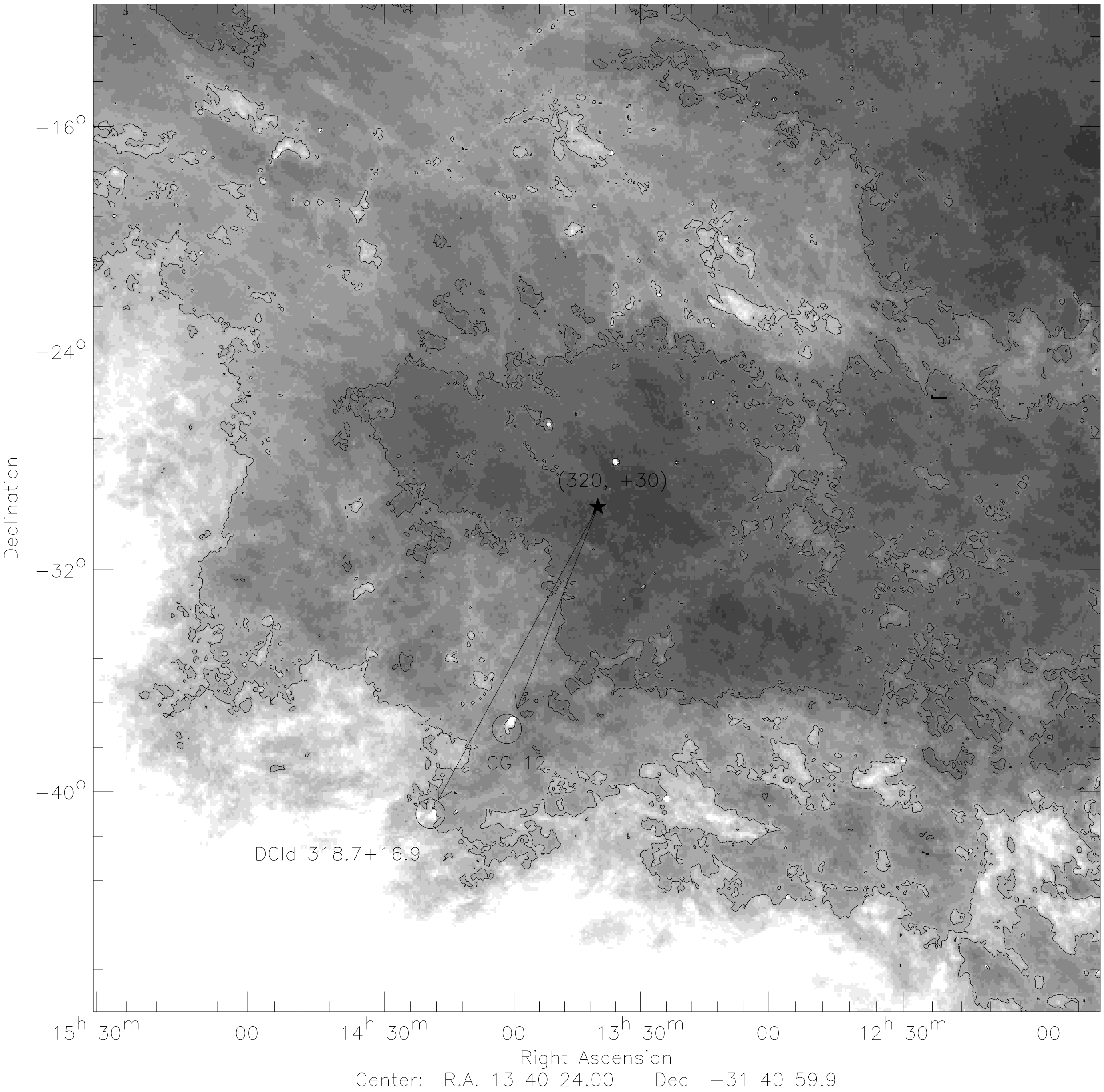

Figure 2.25: We show the IRAS 100 μm image of the field containing CG 12. Contours are plotted at 6.5 and 9.5 $MJy\ sr^{-1}$. The centre of the shell shown in Figure 2.24 is mark. A circle is drawn about this centre with its radius ∼ 10°. The locations of CG 12 and the dark cloud, DCld 318.7+16.9, shown in Figure 2.26 are also marked and labelled. North is up and east is to the left.

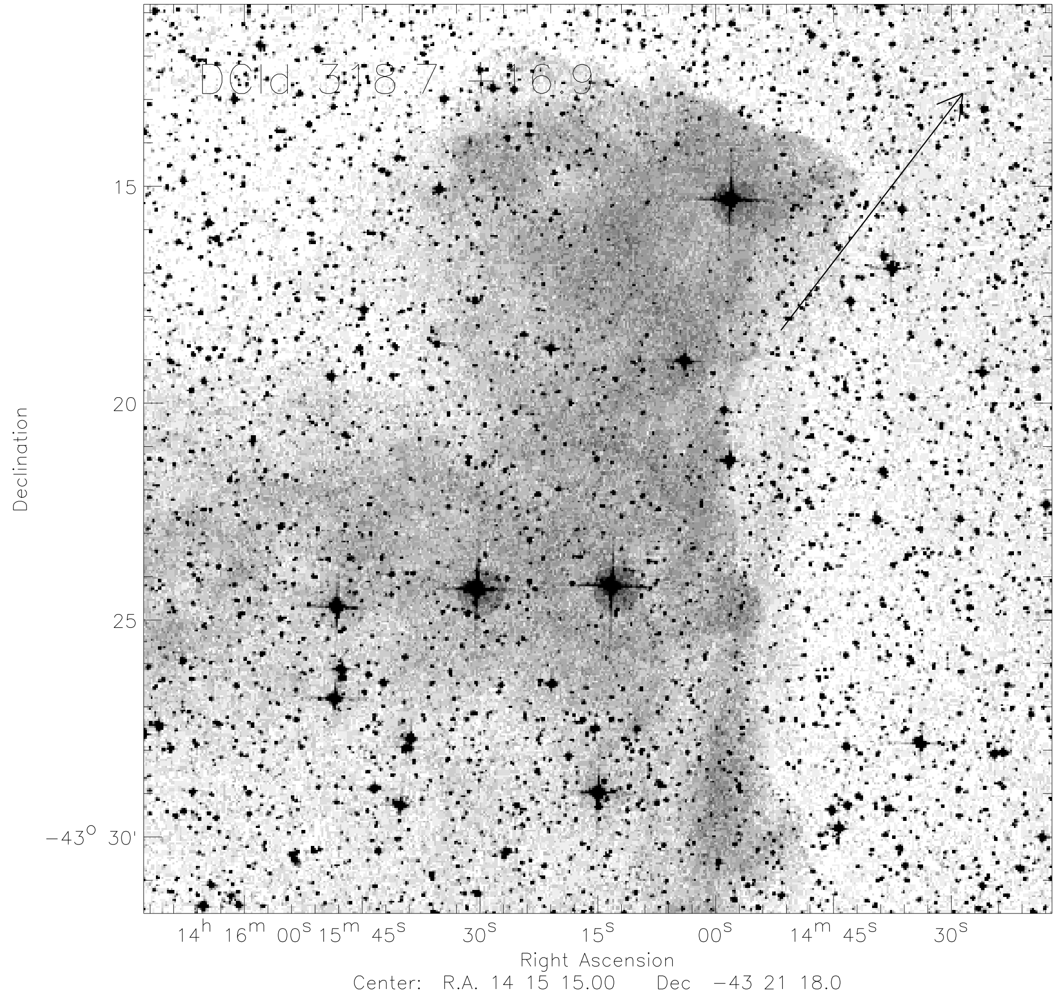

Figure 2.26: We show the image of the field containing DCld 318.7+16.9. The arrow indicates the direction of the H I shell centre. This image is reproduced from Digitized Sky Survey (DSS). North is up and east is to the left.

2.17 Conclusions

In this chapter we have presented the results of a multi-wavelength study of star forming region CG 12. Our results can be summarized as follows.

- The dust colour temperature, optical depth and extinction maps of CG 12 are produced. The dust colour temperature computed from the long-wavelength flux density ratio ($F_{60\mu m}/F_{100\mu m}$) in CG 12 vary from 21 to 33 K. The dust colour temperature is found to peak at the position of $h4636$. The minimum value of the dust colour temperature is found towards the north of $h4636$ which coincides with the peak emission of $C^{18}O$. The inner contours of extinction map is oriented nearly north-ward w.r.t the orientations of the tail much similar to the orientation of high-density $C^{18}O$ contours.

- Of the four stars associated with nebulosities, only northern component of the double star $h4636$ show emission features in its spectrum. We find a B4 and B7 spectral types for the northern and southern components of the double star $h4636$. The northern component, $h4636N$ shows Hα and Hβ Balmer lines in emission whereas, these lines are in absorption in the southern component, $h4636S$. Spectroscopic signatures for the presence of a shell and/or a disk around $h4636N$ is presented. Spectrum of other three nebulous stars are consistent with them to be main sequence stars.

- A total of 30 near-IR excess objects are identified towards the direction of CG 12 on the basis of their positions in $J-H, H-K$ c-c diagram and $K, J-K$ colour magnitude diagram. Of these, seven sources which are brighter than $K = 14$ magnitude could be low-mass PMS star candidates. The near-IR embedded source found by Santos et al. (1998) show a faint nebulosity (in K band) in 2MASS observations which indicates its association with the cloud. The position of this source in c-c diagram suggests it to be a class I YSO with large near-IR excess emission ($H - K = 2.93$) and is probably embedded ($J - H = 2.75$) deep inside the cloud .

- Of the 25 X-ray sources detected towards CG 12, we find eight sources within the cloud boundaries and seventeen sources outside the cloud boundaries. Sources found inside show harder X-ray colours compared to those found outside. The hardness of the sources (indicated by HR 1 ratio) decrease with their projected distances from the densest part of the cloud (position where extinction and $C^{18}O$ emission peaks in CG 12). Of the eight sources found inside the cloud boundaries, four are identified (positionally) with previously known sources (h4636 double star, embedded near-IR source, star 2 and star 4). We find 2MASS counterparts for all the eight X-ray detections found within the cloud boundaries and for nine (out of seventeen) X-ray detections outside the cloud boundaries. From their locations in $K, J-K$ colour magnitude diagram, and by comparing with the isochrones of low-mass PMS stars, we identify 3 X-ray sources which are found inside the cloud boundaries and not identified with previously known sources and 5 X-ray sources located outside the cloud boundaries as the probable YSO candidates with their ages in the range 1 - 7 Mys.

- The efficiency of star formation in the cloud is estimated to be relatively high ($\gtrsim 16$ % to as large as ~ 33 %).

- More recent radio maps confirm the existence of an HI shell centred at $l = 315°, b = 30°$, with CG 12 near its boundary and its tail pointing away from the centre of the shell. Based on the spatial distribution of PMS stars relative to the head of the cloud and the embedded sources, as well as the cometary shape of the cloud and its high star formation efficiency, we believe that the star formation in CG 12 was induced by the supernova explosion which took place about $\sim$ 10 Myr ago somewhere near $l = 315°, b = 30°$. This could have triggered the formation of the 6 - 7 Myr old X-ray sources found outside and towards the NW part of the CG head. The same event must have triggered star formation further inside the cloud forming X-ray sources of $\sim 1-2$ Myr found within the cloud boundaries, near-IR excess sources, and the binary system h4636. The deeply embedded near-IR excess source and molecular outflow source, which are roughly of the ages $\lesssim 10^5$ yr, are the youngest of the PMS stars currently forming in CG 12.

Bibliography

[1] Alcala, J. M., Krautter, J., Covino, E., et al., 1997, A&A, 319, 184

[2] Alcala, J. M., Wachter, S., Covino, E., 2004, A&A, 416, 677

[3] Arce, Hctor G., Goodman, Alyssa A., 1999, ApJ, 517, 264

[4] Bahcall, J. N., Soneira, R. M., 1980, ApJS, 44, 73

[5] Baraffe, I., Chabrier, G., Allard, F., et al., 1998, A&A, 337, 403

[6] Beckwith, Steven V. W., Sargent, Anneila I., 1991, ApJ, 381, 250

[7] Berghöefer, T. W., Schmitt, J. H. M. M., Danner, R., et al., 1997, A&A, 322, 167

[8] Bhatt, H. C., 1999, MNRAS, 308, 40

[9] Böhm & Catala, 1994, A&A, 290, 167

[10] Böhm, T., Hirth, G. A., 1997, A&A, 324, 177

[11] Bok, B. J., Bok, P. F., 1941, The Milky Way (Cambridge: Harvard Univ. Press)

[12] Bok, Bart J., 1977, PASP, 89, 597

[13] Bourke, T. L., Hyland, A. R., Robinson, G., 1995, MNRAS, 276, 1052

[14] Carpenter, J. M. 2001, AJ, 121, 2851

[15] Cassinelli, J. P., Cohen, D. H., Macfarlane, J. J., 1994, ApJ, 421, 705

[16] Chavarra-K, C., Terranegra, L., Moreno-Corral, M. A., et al., 2000, A&AS, 145, 187

[17] Cleary, M. N., Haslam, C. G. T., Heiles, C., 1979, A&AS, 36, 95

[18] Clemens, Dan P., Yun, Joao Lin., Heyer, Mark H., 1991, ApJS, 75, 877

[19] Corcoran, M.; Ray, T. P., 1997, A&A, 321, 189

[20] Cutri R.M., Skrutskie M.F., Van Dyk S., et al., 2000, 2MASS All-Sky Catalog of Point Sources

[21] Davis and Greenstein, 1951, ApJ, 114, 206

[22] Dickey, John M., Lockman, Felix J., 1990, ARA&A, 28, 215

[23] Elmegreen, B. G., Lada, C. J., 1977, ApJ, 214, 725

[24] Feigelson, E. D., Decampli, W. M., 1981, ApJ, 243L, 89

[25] Goss, W. M.; Manchester, R. N., Brooks, J. W., Sinclair, M. W., Manefield, G. A., Danziger, I. J., 1980, MNRAS, 191, 533

[26] Hall, 1949, Science, 109, 166

[27] Hamann, Fred, Persson, S. E., 1992, ApJS, 82, 285

[28] Hamann, F., Simon, M., 1986, ApJ, 311, 909

[29] Hamann, F., Simon, M., 1988, ApJ, 327, 876

[30] Hawarden T. G., Brand P. W. J. L., 1976, MNRAS, 175, 19

[31] Heiles, C., 1976, ApJ, 208, L137

[32] Heiles C., 2000, AJ, 119, 923

[33] Herbst, W., Assousa, G. E., 1977, ApJ, 217, 473

[34] Herbst, W., Sawyer, D. L., 1981, ApJ, 243

[35] Hiltner, 1949, ApJ, 109, 471

[36] Hobbs, L. M., Blitz, L., Magnani, L., 1986, ApJ, 306, L109

[37] Hog et al., 2000, The Tycho-2 Catalogue, I/259

[38] Hsu J. C., Breger M., 1982, ApJ, 262, 732

[39] Jacoby, G. H., Hunter, D. A., Christian, C. A., 1984, ApJS, 56, 257

[40] Jain S. K., Srinivasulu G., 1991, Opt. Eng., 30 1415

[41] Johnson, Harold L., 1966, ARA&A, 4, 193

[42] Kandori, Ryo; Dobashi, Kazuhito., Uehara, Hayato., Sato, Fumio., Yanagisawa, Kenshi., 2003, AJ, 126, 1888

[43] Keenan, P. C., Hynek, J. A., 1950, ApJ, 111, 1

[44] Keto, E. R., Myers, P. C., 1986, ApJ, 304, 466

[45] Kim, J. Serena., Walter, F. M., Wolk, S. J., 2002, AAS, 20113605

[46] Koornneef, J., 1983, A&AS, 51, 489

[47] Lada, Charles J., Adams, Fred C., 1992, ApJ, 393, 278

[48] Lada, Charles J., Lada, Elizabeth A., 2003, ARA&A, 41, 57

[49] Maggio, A., Vaiana, G. S., Haisch, B. M., et al. 1990, ApJ, 348, 253

[50] Magnani, L., Blitz, L., Mundy, L., 1985, ApJ, 295, 402

[51] Manoj, P., Maheswar, G., Bhatt, H. C., 2002, MNRAS, 334, 419

[52] Mannings, Vincent, Emerson, James P., 1994, MNRAS.267, 361

[53] Marraco & Forte, 1978, ApJ, 224, 473

[54] Mathis, John S., 1990, ARA&A, 28, 37

[55] Mathis, John S., 2000, JGR, 10510269

[56] Monet, David G., Levine, Stephen E., Canzian, Blaise., et al., 2003, AJ, .125, 984

[57] Morrison, R., McCammon, D., 1983, ApJ, 270, 119

[58] Motch, C., Guillout, P., Haberl, F., 1998, A&AS, 132, 341

[59] Neuhäuser, R., Sterzik, M. F., Schmitt, J. H. M. M., et al., 1995, A&A, 297, 391

[60] Neuhäuser, R., Walter, F. M., Covino, E., 2000, A&AS, 146, 323

[61] Ögelman, H. B., Maran, S. P., 1976, ApJ, 209, 124

[62] Ogura, Katsuo., Sugitani, Koji., Pickles, Andrew., 2002, AJ, 123, 2597

[63] Otrupcek, R. E., Hartley, M., Wang, J.-S., 2000, PASA, 17, 92

[64] Peterson, Dawn E., Clemens, Dan P., 1998, AJ, 116, 881

[65] Prabhu, T. P., Anupama, G. C., Surendiranath, R., 1998, BASI, 26, 383

[66] Ramesh, B., 1995, MNRAS, 276, 923

[67] Raymond, J. C., Smith, B. W., 1977, ApJS, 35, 419

[68] Reed, B. Cameron., 2000, AJ, 120, 314

[69] Reipurth, B., 1983, A&A, 117, 183

[70] Reipurth, B., Pedrosa, A., Lago, M. T. V. T., 1996, A&AS, 120, 229

[71] Reipurth, Bo, Zinnecker, Hans., 1993, A&A, 278, 81

[72] Rieke, G. H., Lebofsky, M. J.,1985, ApJ, 288, 618

[73] Rosner, R., Golub, L., Vaiana, G. S., 1985, ARA&A, 23, 413

[74] Santos N. C., Yun J. L., Santos C. A., Marreiros R. G., 1998, AJ, 116, 1376

[75] Schmidt-Kaler, Th. 1982, Landolt-Brnstein, Numerical data and Functional Relationships in Science and Technology, New Series, Group VI, vol. 2(b), ed. K.

[76] Schmitt, Juergen H. M. M., Fleming, Thomas A., Giampapa, Mark S., 1995, ApJ, 450, 392

[77] Serkwoski K., 1974, in Gehrels T., ed., Planets, Stars and Nebulae studied with Photopolarimetry, Univ. of Arizona Press, Tucson, p. 135

[78] Shawl S.J., 1975, AJ, 80, 602

[79] Sridharan, T. K., 1992, JApA, 13, 217

[80] Sridharan, T. K., Bhatt, H. C., Rajagopal, J., 1996, MNRAS, 279, 1191

[81] Stanke, T., Smith, M. D., Gredel, R., Szokoly, G., 2002, A&A, 393, 251

[82] Sugitani, K., Tamura, M., Ogura, K., 1999, sf99.proc, 358

[83] Thé, P. S., Tjin, H. R. E., Steenman, H., Wesselius, P. R., 1986, A&A, 155, 347

[84] Van Till H., Loren R., Davis J., 1975, ApJ, 198, 235

[85] Vieira, S. L. A., Corradi, W. J. B., Alencar, S. H. P., 2003, AJ, 126, 2971

[86] Vrba, F. J., Rydgren, A. E., 1984, ApJ, 283, 123

[87] Weintraub, David A., Sandell, Goran., Duncan, William D., 1991, ApJ, 382, 270

[88] White, G. J., 1993, A&A, 274, L33

[89] White N.E., Giommi P., Angelini L., 2000, The WGACAT version of the ROSAT PSPC Catalogue (IX/31, CDS Catalogues)

[90] Whittet, D, C, B., 2003, *Dust in the galactic environment* (second edition), Institute of Physics Publishing

[91] Wilking, B. A., Lada, C. J., 1983, ApJ, 274, 698

[92] Williams P. M., Brand P. W. J. L, Longmore A. J., Hawarden T. G., 1977, MNRAS, 181, 709

[93] Wolf, M., 1923, Astron. Nachr., 219, 109

[94] Wood, Douglas O. S., Myers, Philip C., Daugherty, Debra A., 1994, ApJS, 95, 457

[95] Yonekura Y., Hayakawa T., Mizuno N., Mine Y., Mizuno A., Ogawa H., Fukui Y., 1999, PASJ, 51, 837

[96] Yun, Joao Lin., Clemens, Dan P., 1990, ApJ, 365, 73

[97] Zealey, W. J., Ninkov, Z., Rice, E., Hartley, M., Tritton, S. B., 1983, ApL, 23, 119

[98] Zimmermann, H.-U., Boller, Th., Dbereiner, S., Pietsch, W., 2001, A&A, 378, 30

[99] Zinnecker, Hans., McCaughrean, Mark J., Wilking, Bruce A., 1993, in: Protostars and planets III (A93-42937 17-90), p. 429-495.

[100] Zinnecker, Hans., McCaughrean, Mark., 1991, (Vulcano Workshop on Young Star Clusters and Early Stellar Evolution, Vulcano, Italy, Sept. 16-20, 1991, Proceedings. A92-42951 17-90) Societa Astronomica Italiana, Memorie (ISSN 0037-8720), vol. 62, no. 4, 1991, p. 761-766.

[101] Zinnecker, H., Preibisch, Th., 1994, A&A, 292, 152

Chapter 3

Other star forming cometary globules

3.1 Introduction

The capability of an interstellar cloud to form stars depends on its initial physical conditions, which are subjected to the influence of the external medium (nearby massive stars, ionization fronts, density waves, etc; Myers 1990). The cometary morphology of CG suggests that they are subjected to the influence of some external forces. Observations of these CGs show that the external forces have influenced and modified their internal properties also. For example, cometary globules, as a group, are detected more frequently in ammonia than the other Bok globules (75% compared to only 38%, Bourke et al. 1995) and the kinetic temperatures estimated for some of the CGs like CG 1 ($T_K \sim 15K$, Harju et al. 1990), CG 4 and CG 6 ($T_K \sim 15K$, Gonz$\acute{a}$Lez-Alfonso, Cernicharo & Radford 1995), CG 12 ($T_K \lesssim 20K$, White 1993), CG 30 and CG 31A ($T_K \sim 13K$, Bourke et al. 1995) and Orig-I-2 ($T_K \sim 25K$, Cernicharo 1991) are found to be slightly higher than that estimated for darker globules ($T_K \sim 8 - 10K$) (Dickman 1975; Martin & Barrett 1978; Myers & Benson 1983; Clemens et al. 1991; Bourke et al. 1995).

Studies on bright-rimmed clouds (Sugitani et al. 1989; Sugitani, Fukui, & Ogura 1991 and Sugitani & Ogura 1994) have shown that the ratios of the derived luminosities of IRAS point sources associated with bright-rimmed clouds and the mass of the parent clouds , i.e., L_{IR} to M_{cloud} ratios, are higher for bright-rimmed clouds than those for the isolated dark globules. The results from their studies show that the calculated L_{IR}/M_{cloud} values for bright rimmed clouds range between ~ 0.01 and 10^2 and the corresponding values for isolated dark globules range between ~ 0.03 and 0.3. They adopted a relationship between stellar luminosity and mass of $L \propto M^{3-4}$, and suggested that the difference of about two orders of magnitude could be explained by the formation of 3-4 times more massive stars in the bright-rimmed clouds. Dobashi, Barnard and Fukui (1996), based on a study of clouds with larger mass range (~ 10 to $\sim 1\times10^4$), suggested that for the clouds with masses $\lesssim$100 $\mathrm{M}_\odot$, the IRAS sources in the clouds associated with HII regions are systematically more luminous than those belonging to isolated clouds. For clouds with $M_{cloud} < 100 M_\odot$, the ratio L_{IR}/M_{cloud} was distributed from 1 to 10. The value for clouds away from the HII regions was found to be 0.1 on average, significantly lower. The difference between the IRAS luminosities in clouds located inside and outside HII regions is unclear in the clouds with masses $\gtrsim$100 $\mathrm{M}_\odot$. Based on a study conducted on clouds from various locations of the Galaxy, which includes the bright rimmed clouds studied by Sugitani et al. (1989, 1991) and Sugitani & Ogura (1994), Dobashi et al. (2001) have shown the presence of an upper and a lower limit to the luminosity distribution and suggested that the observed upper envelope might be limited by the star-formation efficiency (SFE).

In this chapter we study the properties of young stellar objects associated with CGs to address some of the questions like: How do the properties of young stellar objects associated with CGs compare with those of isolated dark clouds? Is there any influence of external forces on to the star formation process in CGs? Already from the study of CG 12 (Chapter 2), we have seen that the estimated star formation efficiency is $\gtrsim$ 16%, implying that the external forces have affected the star formation in CG 12.

3.2 Observations and Data Analysis

Optical CCD spectra of sources found towards the direction of cometary globules were obtained using the OMR spectrograph on the VBT (Vainu Bappu Telescope) at Kavalur and HFOSC (Hanle Faint Object Spectrograph Camera) on HCT (Himalayan Chandra Telescope) at Hanle during the period 2001-2005. Instrumental setup used for obtaining spectra of stars are given in Table A.1 of the Appendix. All spectra were bias subtracted, flat-field corrected, extracted and wavelength calibrated in the standard manner using the IRAF.

3.3 IRAS sources associated with CGs

From the study of IRAS point sources found in Taurus-Auriga, Myers et al. (1987) have shown that the stars in cores (higher density regions of molecular clouds, see Table 1.1 of Chapter 1) probably become visible T Tauri stars in less than 1×10^5 yr after they become detectable by IRAS, i.e., after they attain luminosity greater than $\sim 0.1 L_\odot$. This implies that they are extremely young and may still be accreting. Hence IRAS point sources with spectral energy distributions (SED) characteristic of young stellar or protostellar objects are primarily predecessors of T Tauri stars. Radiation Driven Implosion (RDI), the mechanism thought to be responsible for the formation of cometary globules is shown to be a two-stage process (Lefloch & Lazareff 1994): (a) collapse phase: it occurs over a short time-scale (typically 10^5 yr). Maximum compression, possibly leading to star formation, occurs in the early stages of the collapse. (b) cometary phase: the globule is in a quasi-hydrostatic equilibrium. The lifetime of this stage is of the order of a few 10^5 yr to a few Myr. Hence IRAS sources with SEDs characteristic of young stellar or protostellar objects associated with cometary globules may have probably formed due to the influence of the external trigger.

The IRAS sources associated with 45 CGs are given in Table 3.1. Column 1 gives cloud identifications and column 2 gives IRAS source identifications [as given in the catalog "IRAS catalog of Point Sources, Version 2.0 (IPAC 1986)"] which are found associated with the CGs. Column 3 gives the offset of IRAS sources from the cloud coordinates (coordinates quoted in literature are in general correspond to the densest region of CGs). Columns 4, 5, 6 and 7 give IRAS flux densities (in Jansky) in 12, 25, 60 and 100μm wavelength bands respectively. We have selected those IRAS point sources which show an increase in flux towards the longer-wavelengths, a characteristic feature of YSOs. Column 8 gives the flux quality in each band. Columns 9 & 10 give the distance (D) of the globules from the Sun in *parsec* and the corresponding references respectively. Distances are not available for two CGs (LBN 131.54-08.16 & Sim 129) in the literature. We have carried out spectroscopy of stars associated with nebulosities in these two CGs and obtained distances from their spectroscopic parallaxes. Cometary globules appear to be composed of a dense head region and a less dense tail. Star formation is found to occur in the dense head part of the globules. We made a rough estimate of the radius of the head region of the globule by assuming a round shape with radius $R = w/2$ where w is the width of the head region. This procedure was adopted by Sugitani et al. (1991) to estimate the radii of type C (comet shaped) clouds. The optical angular area calculated using the estimated radius of the globules are given in column 11. The mass of the globule head is estimated using the equation

$$M_{cl} = \Omega D^2 \mu m_H N_H \tag{3.1}$$

where Ω and D are the angular area and distance to the globule respectively, μ is the mean molecular mass, m_H is the mass of a hydrogen atom and N_H is the number column density of hydrogen. Standard conversion formulae (e.g. Jenkins & Savage 1974) can be used to give the number column density from the opacity (S) of the clouds as, $N_H = 2.5 \times 10^{21}\ S$. Opacity is the extinction of the cloud in magnitudes. On expressing equation **??** in suitable units, the globule mass M in solar units is given as

$$M_{cl} = 6.25 \times 10^{-3}.\Omega.A_V.D^2 \quad M_\odot \tag{3.2}$$

where Ω is measured in square degrees, A_V in magnitudes and D in parsecs. Cometary globules are generally found to be optically opaque and dense. From Figure 2.11, it is evident that the extinction towards most parts of the head of CG 12 (obtained from FIR color temperature) is in the range 2 - 7 magnitudes except for the most dense region where the extinction can be higher that 10 magnitude. Observations of some of the cometary clouds, for example, CG 4 & CG 6 (Gonnälez-Alfonso et al. 1995), CG 30/31 complex (Knude & Nielsen 2000) show that the extinction in these CGs ranges between 1-10 magnitudes. For the estimation of the mass of the head region of CGs, we have taken a fixed A_V of 5 magnitude for all the CGs. The mass estimates using this procedure could result in an underestimation of the mass of some of the CGs due to the distribution of material in their tails (e.g., CG 1, Harju 1990). We have derived the far-infrared luminosity of the IRAS sources using the equation

$$L_{IR} = 4\ \pi\ D^2\ F_{IR} \tag{3.3}$$

where F_{IR} is the total far-infrared flux estimated using (Cox, 2000)

$$F_{IR} = (20.65\ S_{12} + 7.53\ S_{25} + 4.578\ S_{60} + 1.762\ S_{100}) \times 10^{-11}\ erg\ s^{-1}\ cm^{-2} \qquad (3.4)$$

We then derived the normalized IRAS luminosities per unit cloud mass, i.e., L_{IR} to M_{cl} ratios which are given in column 12 of Table 3.1. In the case of CGs with more than one IRAS source found, we have selected the one which is the most luminous.

In Table 3.2 we present the properties of IRAS sources found within the cloud boundaries of 29 Lynds opacity class 6 clouds obtained from Parker (1988). Of the 1802 optically selected dark clouds cataloged by Lynds (Lynds 1962), 147 clouds are classified as class 6. Estimates of opacity of the Lynds clouds were made on a scale of 1 to 6, with the class 6 clouds being the most opaque with $A_V \gtrsim 5$ mag. These visual estimates were based on a comparison of the cloud with the neighbouring fields for the particular Palomar photograph on which the cloud appeared. These clouds are generally more compact than low opacity clouds and have more easily discernible boundaries. For this reason, the cloud properties and the properties of YSOs found associated with cometary globules can be compared with those of Lynds opacity class 6 clouds. Parker (1988) has cataloged IRAS sources found lying within the boundaries of Lynds opacity class 6 clouds. Out of 147 opacity class 6 clouds, 73 clouds were found to contain IRAS sources which have $S_{100} > S_{25}$, where S_{100} and S_{25} are the 100 and 25 μm flux densities (Parker 1988). We have selected, from Parker's catalog, those IRAS sources which show an increase in flux densities with increasing wavelength. Column 1 of Table 3.2 gives cloud identifications, column 2 gives IRAS source identifications from the catalog, columns 3, 4, 5 & 6 give flux densities (in Jansky) in 12, 25, 60 & 100 μm respectively and column 4 gives flux quality in each band. Distance to the clouds and their references are given in columns 5 & 6 respectively. We have assigned a distance of 225 pc to L111 because it is located close ($\sim 30'$) to L100 which is known to be at a distance of 225 ± 25 pc from the Sun (Reipurth & Gee 1986). The V_{lsr} velocity of L216 (10.4 $km\ s^{-1}$) & L219 (10.5 $km\ s^{-1}$) are found to be similar to that of L226 (10.5 $km\ s^{-1}$) (Clemens & Barvainis 1988) which is located at distance of 160 pc (Launhardt & Henning 1997). Hence same distance is assumed for L216 and L219. Because of the close proximity ($\sim 30'$) of L676 to L673 and L677, which are estimated to be at a distance of 300 pc (Hilton & Lahulla 1995; Lee & Myers

Table 3.1: Properties of IRAS sources associated with CGs.

Object Id. (1)	IRAS name (2)	r ($'$) (3)	S_{12} (Jy) (4)	S_{25} (Jy) (5)	S_{60} (Jy) (6)	S_{100} (Jy) (7)	Qly (8)	D (pc) (9)	Ref. (10)	Ω $(')^2$ (11)	L_{IR}/M_{cl} $(L_\odot/M_\odot)$ (12)
CB 6	00465+5028	0.654	2.50e-01	1.01e+00	3.96e+00	8.96e+00	1333	800	1	9.13	0.15
IC 59	00547+6052	3.671	3.21e-01	6.09e-01	3.44e+00	6.62e+01	3312	230	2	12.64	0.33
IC 63	00560+6037	0.403	1.93e+00	2.52e+00	4.31e+01	7.43e+01	3333	230	2	3.16	4.01
LBN131	01467+5339	0.807	1.61e+00	1.94e+00	2.45e+01	7.17e+01	3333	2000	†	5.80	1.62
CB 26	04559+5200	2.563	2.70e-01	3.19e-01	4.88e+00	1.11e+01	1133	300	1	16.00	0.09
RNO6	02130+5509	0.154	2.57e+00	3.19e+00	3.32e+01	9.64e+01	3333	2000	3	12.64	1.03
Sim 129	05198+3325	0.064	8.32e+00	2.62e+01	1.46e+02	1.63e+02	3333	3400	‡	1.50	28.90
[*OS*98]01	05018-0616	1.558	2.72e-01	3.54e-01	5.79e-01	2.22e+00	1133	460	4	1.55	0.14
[*OS*98]02	05038-0400	0.553	2.50e-01	2.50e-01	8.18e-01	1.64e+01	1113	460	4	23.00	0.04
[*OS*98]03	05044-0325	1.078	1.31e+01	3.86e+01	2.32e+02	3.82e+02	3333	460	4	113.76	0.66
[*OS*98]04	05095-0159	0.480	2.50e-01	2.50e-01	1.55e+00	1.31e+01	1132	460	4	9.13	0.11
[*OS*98]06	05146-0747	0.126	2.50e-01	2.50e-01	1.97e+00	1.56e+01	1133	460	4	4.94	0.24
[*OS*98]07	05173-0555	0.010	2.50e-01	3.02e+00	2.71e+01	6.13e+01	1332	460	4	79.00	0.11
[*OS*98]10	05185-0552	0.591	2.50e-01	2.50e-01	1.59e+00	2.66e+01	1133	460	4	64.00	0.03
[*OS*98]16	05245-1017	0.824	2.50e-01	2.50e-01	6.62e-01	6.19e+00	1123	460	4	1.14	0.40
[*OS*98]25*B*	05299-0302	0.464	2.50e-01	2.61e-01	4.00e+00	3.39e+01	1231	460	4	6.64	0.10
[*OS*98]29*D*	05310-0138	0.701	3.26e-01	2.84e-01	3.93e+00	1.75e+01	1233	460	4	7.11	0.23
[*OS*98]29*L*	05324-0117	0.843	2.50e-01	2.63e-01	3.94e+00	1.28e+01	1123	460	4	3.16	0.42
[*OS*98]31	05320-0300	0.007	2.50e-01	3.50e-01	7.21e+00	2.50e+01	1323	460	4	10.82	0.24
[*OS*98]40*A*	05355-0146	0.004	3.84e-01	1.40e+00	1.33e+01	4.21e+01	3333	460	4	6.19	0.81
[*OS*98]41	05359-0515	0.012	1.44e+00	1.95e+00	1.89e+01	9.76e+01	3321	460	4	5.34	0.80
[*OS*98]45	05372-0522	0.283	4.13e-01	3.41e-01	7.89e+00	3.78e+01	1123	460	4	2.85	1.18
[*OS*98]59	05407-0522	1.565	2.95e-01	4.60e-01	7.95e+00	4.28e+01	1321	460	4	3.48	0.37
[*OS*98]60*B*	05414-0507	0.555	2.50e-01	3.33e-01	4.80e+00	3.54e+01	1312	460	4	1.34	1.58
L1622	05516+0142	6.674	5.97e-01	1.34e+00	2.10e+00	4.21e+01	3311	450	5	316.00	0.002
CG 1	07178-4429	0.772	6.68e+00	7.60e+00	1.31e+01	3.36e+01	3333	450	6	3.16	3.25
CG 2	07144-4352	0.370	2.50e-01	3.73e-01	4.41e-01	8.88e+00	1123	450	6	3.16	0.18
CG 3	07378-4745	0.834	2.50e-01	2.50e-01	1.79e+00	1.31e+01	1133	450	6	3.55	0.29
CG 4	07329-4647	2.724	2.50e-01	3.79e-01	1.34e+00	5.82e+00	1331	450	6	3.16	0.09
CG 5	07391-4342	1.616	2.50e-01	2.50e-01	9.37e-01	4.80e+00	1133	450	6	0.40	1.04
CG 8	07408-4108	1.469	2.50e-01	2.50e-01	1.65e+00	8.44e+00	1133	450	6	0.79	0.93
CG 9	07389-4119	1.813	2.50e-01	2.50e-01	1.55e+00	5.97e+00	1133	450	6	0.80	0.72
CG 14	07372-4945	1.002	2.50e-01	2.50e-01	6.13e-01	8.92e+00	1123	450	6	2.37	0.26
CG 22	08267-3336	1.086	3.95e-01	1.09e+00	3.20e+00	1.43e+01	3333	450	6	11.85	0.16
CG 25	07358-4750	1.106	2.50e-01	2.50e-01	4.35e-01	3.88e+00	1113	450	6	0.20	1.12
CG 26	08140-3340	0.225	2.50e-01	2.50e-01	4.00e-01	3.31e+00	1113	450	6	2.00	0.10
CG 27	08105-3335	0.926	2.50e-01	2.50e-01	4.00e-01	4.08e+00	1113	450	6	2.00	0.12
CG 28	08103-3346	0.833	2.50e-01	2.50e-01	6.43e-01	5.43e+00	1113	450	6	0.79	0.40
CG 30	08076-3556	0.008	6.30e-01	3.73e+00	1.82e+01	4.75e+01	3332	450	6	4.74	1.44
CG 32	08124-3422	1.473	2.50e-01	2.96e-01	1.19e+01	4.05e+01	1333	450	6	3.56	1.18
CG 19	12427-5508	0.759	2.50e-01	2.50e-01	2.23e+00	1.22e+01	1133	300	7	2.21	0.47
CG 12	13547-3944	2.382	7.81e+00	8.94e+00	6.75e+01	2.02e+02	3333	550		79.0	0.37
BHR 136	16510-4026	0.647	9.62e-01	1.68e+00	1.59e+01	5.68e+01	3221	145	8	0.79	4.36
GM1-27	20183+3700	0.126	5.58e-01	2.27e+00	9.32e+00	2.72e+01	3333	1000	9	0.79	4.94
CB 230	21169+6804	0.004	2.50e-01	6.83e-01	1.18e+01	3.35e+01	1333	450	1	17.70	0.22

References:

(1) Launhardt & Henning 1997; (2) Jansen et al. (1994); (3) Bachiller et al. (2002); (4) Ogura & Sugitani (1998); (5) Knude et al. (2002); (6) Sridharan (1992); (7) Bourke et al. (1995); (8) Vilas-Boas, Myers & Fuller (2000); (9) Neckel & Staude (1987); (10) Olano, Walmsley, & Wilson (1994)

1999) respectively, we have assigned 300 pc to L676 also. The optical angular areas of the clouds (in $arcmin^2$) are given in column 7. The area of the clouds are estimated from the semi-major and semi-minor axes of the clouds given by Parker (1988). The mass of the clouds and luminosity of the IRAS sources are calculated using the equations **??** and 3.3 respectively. For the estimation of the mass of opacity class 6 clouds, we have taken a fixed A_V of 5 magnitude for all the clouds. The clouds in which there are more than one IRAS sources present, we have selected the one which is the most luminous. The L_{IR} to M_{cl} ratios for opacity class 6 clouds are given in column 11 of Table 3.2.

Table 3.2: Properties of IRAS sources associated with Lynds opacity class 6 clouds.

Object (1)	IRAS name (2)	S_{12} (Jy) (3)	S_{25} (Jy) (4)	S_{60} (Jy) (5)	S_{100} (Jy) (6)	Qly (7)	D (pc) (8)	Ref. (9)	Ω $(')^2$ (10)	L_{IR}/M_{cl} $(L_\odot/M_\odot)$ (11)
L43	16316-1540	1.50e+00	6.05e+00	3.53e+01	6.44e+01	3333	160	HL	84.97	0.14
L111	17119-2027	2.50e-01	3.31e-01	4.00e-01	7.14e+00	1113	225	1	9.67	0.04
L158	16445-1352	2.68e-01	3.34e-01	2.22e+00	3.26e+01	1132	160	HL	89.68	0.03
L162	16459-1411	1.41e+00	1.90e+00	2.33e+00	6.47e+00	3313	160	HL	225.08	0.01
L204	16444-1201	2.50e-01	3.53e-01	8.91e-01	1.18e+01	1133	170	HL	342.89	0.002
L216	17347-1938	5.58e-01	4.76e-01	6.41e-01	6.49e+00	1113	160	2	29.01	0.01
L219	17364-1946	2.55e-01	1.25e+00	1.02e+01	1.74e+01	1333	160	2	191.04	0.02
L260	16442-0930	5.71e-01	3.31e+00	7.83e+00	7.54e+00	3333	160	HL	77.93	0.04
L323	18126-1820	1.95e+00	4.15e+00	2.44e+01	3.78e+02	1311	200	HL	38.68	0.03
L462	18046-0444	2.50e-01	3.84e-01	5.35e-01	6.32e+00	1113	200	CM	83.27	0.004
L483	18148-0440	2.50e-01	6.91e+00	8.91e+01	1.66e+02	1333	200	HL	58.78	0.43
L530	18474-0454	8.34e-01	1.17e+00	2.41e+00	5.82e+01	1131	350	HL	314.75	0.001
L531	19037-0659	2.50e-01	4.98e-01	9.81e-01	9.84e+00	1332	400	HL	34.54	0.02
L581	19051-0403	2.60e-01	3.40e-01	5.46e-01	6.15e+00	1113	200	CM	71.03	0.01
L588	18331-0035	2.50e-01	6.06e-01	1.48e+01	3.49e+01	1333	200	CM	84.97	0.05
L663	19345+0727	2.50e-01	2.50e-01	8.30e+00	4.20e+01	1133	250	HL	7.60	0.49
L673	19184+1055	3.74e+00	5.46e+00	3.69e+00	9.69e+00	3312	300	HL	284.01	0.02
L676	19187+1127	7.63e-01	8.66e-01	6.61e+00	9.67e+01	3311	300	3	15.20	0.05
L677	19197+1126	5.85e-01	1.57e+00	5.70e+00	7.51e+01	1331	300	CM	9.67	0.13
L769	19219+2300	2.50e-01	2.50e-01	2.77e+00	1.25e+01	1133	200	CM	142.71	0.01
L1148	20395+6714	2.50e-01	2.50e-01	4.00e-01	2.82e+00	1113	350	HL	193.11	0.001
L1246	23228+6320	2.62e-01	7.38e-01	2.06e+00	7.98e+00	2332	700	LH	9.67	0.12
L1262	23238+7401	2.50e-01	7.76e-01	9.60e+00	1.52e+01	1333	200	HL	58.91	0.04
L1535	04325+2402	2.50e-01	2.10e+00	1.29e+01	2.24e+01	1333	140	HL	108.99	0.04
L1544	05013+2505	2.53e-01	3.87e-01	4.00e-01	3.33e+00	1113	140	HL	46.28	0.004
L1551	04287+1801	1.00e+01	1.06e+02	3.73e+02	4.58e+02	3333	160	HL	110.21	1.07
L1686	16235-2416	3.51e+01	2.65e+02	2.20e+03	4.64e+03	2333	160	HL	83.27	8.41
L1709	16285-2356	3.07e-01	4.23e-01	1.01e+00	6.09e+01	1113	160	HL	268.47	0.01
L1782	16394-1941	2.70e-01	5.09e-01	1.13e+00	1.28e+01	1132	160	CM	39.56	0.02

References:

HL- Hilton & Lahulla (1995); LH - Launhardt & Henning (1997); CM - Lee & Myers (1999); 1 - L111 is located close ($\sim 30'$) to L100 which is at a distance of 225 pc (Reipurth & Gee 1986); 2 - The V_{lsr} velocity of L216 (10.4) & L219 (10.5) are similar to that of L226 (10.5) (Clemens & Barvainis 1988) which is located at distance of 160 pc (Launhardt & Henning 1997); 3 - L676 is located close ($\sim 30'$) to L673 and L677.

The luminosity of IRAS sources found towards CGs and opacity class 6 clouds are plotted against their parent cloud mass in Figure 3.1. Open and filled circles represent CGs and opacity class 6 clouds respectively. The luminosity of IRAS sources found towards CGs are in the range ~0.3 - 4 × 10^3 $L_\odot$ and that of opacity class 6 clouds are in the range ~0.03 - 2 × $10^2 L_\odot$. In Figure 3.1, we find that the maximum luminosity of the IRAS sources increases along with the parent cloud mass in the cloud mass range $\sim 1 - 10^3 M_\odot$. This shows that the parent cloud mass is a decisive parameter influencing the population of massive stars. Besides, the maximum luminosity of the IRAS sources found associated with CGs are systematically more luminous (roughly by one order of magnitude) than those found towards the opacity class 6 clouds for a range of parent cloud masses (~ 4 - 300 $M_\odot$). This indicate that brighter and more massive stars can form in clouds which are influenced by external forces. This effect of high pressure was already pointed out first by Sugitani et al. (1989) in the case of bright rimmed clouds and and later by Dobashi et al. (2001) in the case of bright rimmed clouds and clouds associated with HII regions. In order to eliminate the uncertainties in the determination of L_{IR} and M_{cl} due to uncertainties in the distance estimation, we have calculated normalized IRAS luminosity per unit cloud mass, L_{IR}/M_{cl}, for both CGs and opacity class 6 clouds. Both L_{IR} and M_{cl} being proportional to ($distance^2$), the ratio L_{IR}/M_{cl} is independent of distance. For the comparison of L_{IR}/M_{cl} of bright-rimmed clouds with that of isolated dark clouds, Sugitani et al. (1989) have estimated L_{IR}/M_{cl} for four dark globules L43, L663, L1221 & L1262. Of these, three clouds L43, L663, & L1262, are in common with our list of 29 opacity class 6 clouds. The L_{IR}/M_{cl} values estimated by them for these three clouds (0.10, 0.25, & 0.03) are found to be similar to those of our estimates (0.14, 0.49, & 0.04). We note that Sugitani et al. (1989) have used CO column densities for mass estimate whereas we have used a fixed A_V (5 magnitude). In Figure 3.2 we present the distribution of the L_{IR}/M_{cl} values for CGs (unshaded histograms) and that for opacity class 6 clouds (shaded histograms). The average value of L_{IR}/M_{cl} for 46 CGs is 1.43 $L_\odot/M_\odot$. The average value of L_{IR}/M_{cl} for 29 opacity class 6 clouds, 0.38 $L_\odot/M_\odot$, is found to be significantly lower. In terms of the total stellar mass, the star formation in CGs is likely to produce more massive stars than that in the opacity class 6 clouds by a factor of ~ 2 on the assumption that the IRAS luminosity is related to the stellar mass through $(L/L_\odot) = (M/M_\odot)^{3.45}$, the relation for main sequence stars (Allen 1973). However, because of the assumption of constant extinction value (5 magnitude) for all the clouds (both for CGs and opacity class 6 clouds) and the estimation of angular area of

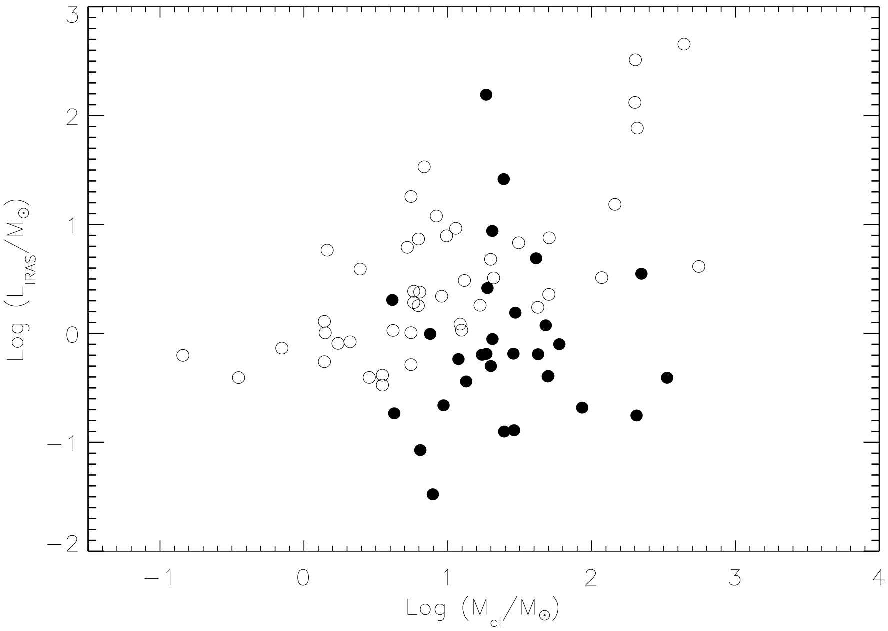

Figure 3.1: IRAS point-source luminosity vs. parent cloud mass. Open circles and closed circles denote IRAS sources associated with CGs and opacity class 6 clouds respectively (Parker 1988).

CGs from the width of the head, the masses of the clouds are to be considered uncertain by a factor of a few. Nevertheless, since the differences are very large, about more than an order of magnitude, we consider that the luminosity-to-mass ratios are systematically larger in the cometary globules.

3.4 Optical sources associated with CGs

The various evidences of current star formation (presence of nebulosity, Hα sources, Herbig-Haro objects, etc.) are found towards a number of CGs as given in Table 1.2. Of the 93 CGs listed in Table 1.2, 14 show association of nebulosities and/or Hα emission sources. In a study conducted by Larson (1981, 1982) to understand the initial mass function of stars, he found a correlation between the maximum stellar mass and the mass of the molecular cloud with which the star is associated. Similar correlation was obtained

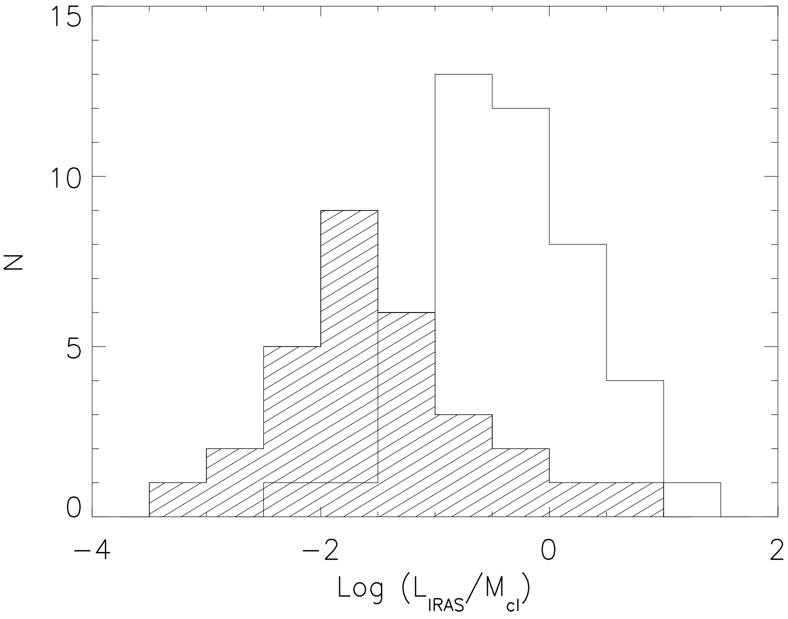

Figure 3.2: Distribution of IRAS luminosity to parent cloud mass ratios of CGs (unshaded histograms) and opacity class 6 clouds (shaded histograms).

by Ho et al. (1981) between the maximum stellar masses and the mass of the molecular cloud cores. The mass of the most luminous stars and the mass of the parent clouds are related by (Larson 1982)

$$M_{max-star} = 0.33 M_{cloud}^{0.43} \tag{3.5}$$

This result implies that the mass of the most massive star formed is related to the mass of the cloud with which it is associated. While the low-mass stars can form in clouds of all sizes, massive stars form only in massive clouds, together with large numbers of less massive stars.

In this section we present the results of a study carried out by us to look for a relation between the mass of the most massive star currently associated with CGs and the mass of the parent cloud. In order to identify the most massive star associated with CGs, we have made spectroscopic observations of stars associated with nine CGs. Discussions on individual CGs are presented below.

3.4.1 Spectral types and cloud masses

LBN 131.54-08.16

The cometary nature of this cloud is identified for the first time in this work. The Galactic coordinates of this cloud are $l = 131.59$ and $b = -7.98$. The image of the field containing LBN 131.54-08.16 is shown in Figure 3.3. The image is reproduced from Digitized Sky Survey. The head is $\sim 3'$ in width with its tail extending $\sim 8'$ in length. The cause of the cometary nature of this cloud is unclear. Also marked in Figure 3.3 are two stars (star 1 & star 2) which are found associated with nebulosities. The star 1 is identified with GSC 03684-01833. We made spectroscopic observations of star 1 and star 2. The spectra of both these stars are shown in Figure A.1 (Appendix A). The presence of He I (λ6678Å) in the spectrum of star 1 shows that it is an early type hot star. We have determined a B4 spectral type for this star. The spectrum of star 1 shows no emission features which are characteristics of pre-main sequence stars. The B and

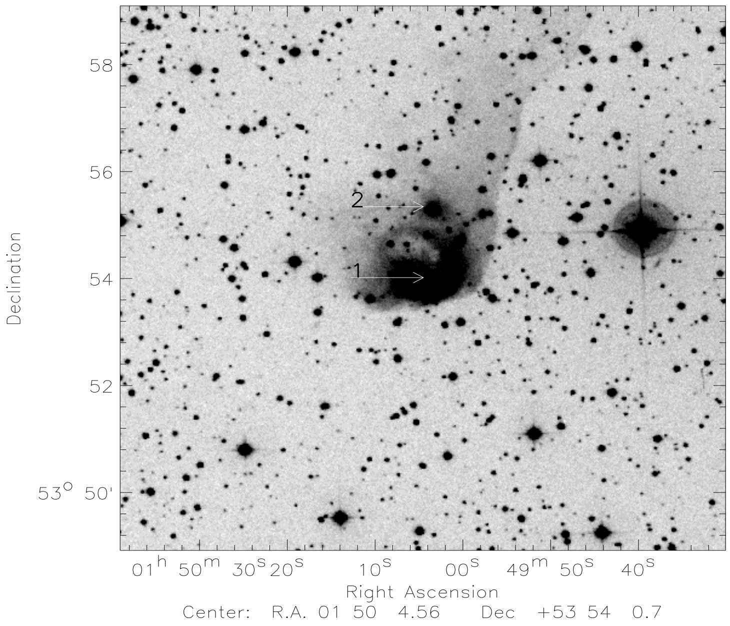

Figure 3.3: We present a $10' \times 10'$ image (reproduced from Digitized Sky Survey) of the field containing LBN 131.54-08.16. The sources for which we have spectroscopic observations are marked. North is up and east is to the left.

V magnitudes of star 1 from the Tycho-2 Catalog (Hog et al. 2000) are 10.68 ± 0.04 & 10.74 ± 0.05 respectively. The estimated spectroscopic parallax corresponds to star 1 is $\sim$ 2000 pc. The presence of a number of stars projected on to the cloud supports the estimated larger distance for the cloud. The star 2, located north of star 1, also shows no emission features in its spectrum. We find a A5 spectral type for star 2. The IRAS 01467+5339, found towards the direction of LBN 131.54-08.16, is about ($50''$) away from both star 1 and star 2. The association of IRAS point source with an embedded source can not be ruled out. The far infrared luminosity of the IRAS point source is estimated to be $\sim 325 L_{\odot}$. For the current analysis we have assumed that star 1 is the most massive source associated with the cloud. The estimated mass of the head region of the cloud (using equation **??** and taking a fixed A_V of 5 magnitude) is $\sim$ 200 $M_{\odot}$.

RNO 6

Red Nebulous Object 6 (RNO 6, Cohen 1980) is a rather bright nebulosity of $\sim 1'$ size lying at the eastern border of an optical extinction patch of $\sim 2'$ and placed ~ 5 ° below the galactic plane in the Perseus constellation. The object was first catalogued as GM 4 by Gyulbudagyan & Magakyan (1977). The cometary structure of RNO 6 is believed to be created by the UV radiation from numerous OB stars lying 1.5° to the north. Such OB stars are associated with the double cluster h and χ Persei, and are probably members of the PerOB1 association (Bachiller et al. 2002). RNO 6 contains a B star (HBC 334) with Hα emission (Cohen 1980) which thus fulfills all the criteria that define Herbig Ae/Be stars as a class, namely (i) its spectral type is A or earlier with emission lines in the spectrum, (ii) its location is in an obscured region, and (iii) it is illuminating a nebulosity. This star has been hence included in some standard lists of HAeBe stars (e.g. Th$\acute{e}$ et al. 1994). The estimated mass of RNO 6 is $\sim 190 M_{\odot}$ (Bachiller et al. 2002).

The spectrum of HBC 334 is presented in Figure A.2 (Appendix A). We have determined a B1 spectral type to this source. No emission features are seen in the spectrum. Hα line is neither in emission nor in absorption. This nature of Hα line was previously been noted by Weintraub (1990). Most luminous IRAS source is positionally associated with RNO 6 implying that this is the most massive source associated with RNO 6.

L1616

L1616 is a cometary cloud east of the Orion A giant molecular cloud. L1616 extends over about 40' (5.2 pc at a distance of 450 pc) roughly in east-west direction. The estimated mass of L1616 is $\sim 180 M_\odot$ (Ramesh 1995). Its head, pointing towards the east, in the general direction of the Orion OB associations, harbours the NGC 1788 reflection nebula, which is illuminated by a small cluster of low-to-intermediate mass stars. Observations in 1.2 mm continuum and in near- and mid-IR images of the cometary cloud L1616 have shown a tight group of dust continuum sources, the brightest of which is seen to drive a powerful near-infrared H2 jet, apparently a very young protostar of Class 0 type. The location of the newly discovered protostar with respect to the older cluster and the direction towards the OB association suggests an age sequence due to a wave of star formation driven through the cloud and triggered by the impact of the nearby OB association: the older generation of stars is located on the side of the cloud directly facing the OB association, whereas a new generation of star formation takes place deeper within the cloud.

We have carried out a spectroscopic study of stars found within the small cluster located in the head region of L1616. In Figure 3.4 we identify eight sources for which we have made spectroscopic observations. The spectrum of star 1, identified with HD 293815, show no emission features (Figure A.3). We estimate a B9 spectral type for HD 293815. Star 2 is in a visual binary system with a separation of $\sim 7''$ and oriented in EW direction. We have marked (Figure 3.4) the eastern and western components as 2b and 2a respectively. Spectrum of star 2a and 2b are shown in Figure A.4 and A.5 respectively. Star 2a and 2b both shows Hα in emission. The presence of Li (λ6707) line in absorption is an indication of these sources to be low-mass T Tauri stars. We determine a K8 and K3 spectral types for stars 2a and 2b respectively. Spectrum of star 3, identified with NSV 1831, is presented in Figure A.6. This star shows Hα and O I (λ8445) line in clear emission. The presence of He I (λ6678) in absorption indicates that this star is an early type hot star. We have determined a B3 spectral type for

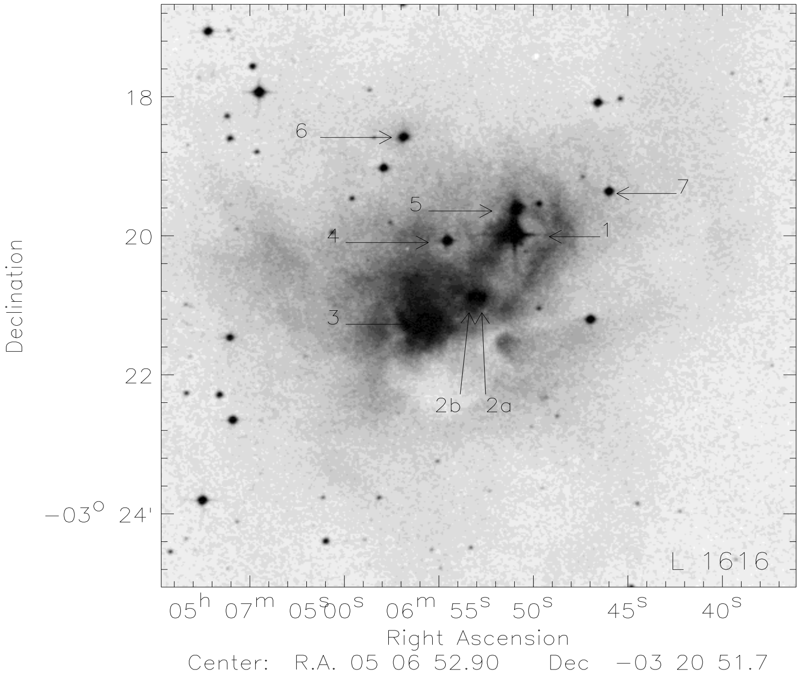

Figure 3.4: We show an $8' \times 8'$ image of the field containing L 1616. The image is reproduced from Digitized Sky Survey. We have marked sources for which we have made spectroscopic observations. North is up and east is to the left.

star 3. Our spectral type determination is consistent with that estimated by Vieira et al. (2003). The IRAS low resolution spectrum of star 3 [obtained from the catalog "IRAS Low Resolution Spectra (IRAS team, 1987)"] which cover the wavelength range between 8 and 22 shows 9.7 μm silicate dust feature in absorption. Emission features corresponding to the stretching and bending vibrational modes at 9.7 μm arise when silicate dust is heated to temperatures of a few hundred Kelvin or more. This commonly occurs in the envelopes of luminous young stars embedded in their parent molecular clouds and in the extended atmospheres of cool, evolved stars with O-rich circumtellar shells. However, the circumstellar emission by warm dust and foreground absorption by cold dust may be superposed in the same line of sight towards an embedded star (Whittet 2003). The 9.7 μm feature seen in absorption in the spectrum of star 3 implies that this star is deeply embedded and the cold optically thick dust in its environment is absorbing the radiation. The visual extinction estimated towards star 3, from $(J - H)$ colour and assuming that the Rieke & Lebofsky (1985) reddening law can be applied to L1616 cloud, is ~ 8 magnitudes. The positional association of the most luminous IRAS with star 3 indicate that this star is the most massive star in L1616. Spectra of stars 4, 5, 6 and 7 are shown in Figure A.7, A.8, A.9 and A.10 respectively. All of these four stars show Hα in emission. The T Tauri nature of these stars is recognized from the presence of Li (λ6707) line in absorption. We assign a K6, M0, M1 and M0 spectral type to star 4, 5, 6 and 7 respectively. Alcala et al. (2004) have made spectroscopic observations of a larger number of stars towards the direction of L1616. The spectral types determined for stars studied by us and those which are in common with Alcala et al. (2004) are generally in good agreement except for star 3. They have assigned a K3 spectral type, estimated not from its spectrum but from its SED, to this star. We find eight pre-main sequence stars within an area of $\sim 0.2\,pc^2$. The stellar density (number/pc^2) in this cluster is thus found to be ~ 40. This value is much higher than that found in Taurus (0.3) and comparable to that found in ρ Oph core (50) (Lada et al. 1993).

Sim 129

Campbell, Persson & Matthews (1989) (CPM) have identified luminous YSOs from a sample of bright IRAS point sources within ±5° of the Galactic plane, with mid- to far-infrared energy distributions similar to YSOs. CPM 16 is associated with a bright emission cometary nebulae Sim 129 (Marco & Negueruela, 2003). This cloud is situated at the north-eastern edge of the *HII* region IC 410. There is another bright emission cometary nebulae Sim 130 towards NW of Sim 129. The head of Sim 129 is $\sim 1.3'$ wide with its tail extending to $\sim 6'$ and directed away from the center of IC 410. Marco & Negueruela (2003), from a search for emission line pre-main sequence (PMS) stars in the area of the star-forming young open cluster NGC 1893 by means of slit-less spectroscopy, found that all the PMS stars are confined to two small regions: the outer rim of the molecular cloud associated with the *HII* region IC 410 and in the vicinity of the bright emission cometary nebulae Sim 129 and Sim 130. From the overall spatial distribution of PMS stars, they suggested that present day star formation in NGC 1893 is triggered by the O-type stars in the cluster. The cometary morphology of the cloud also supports

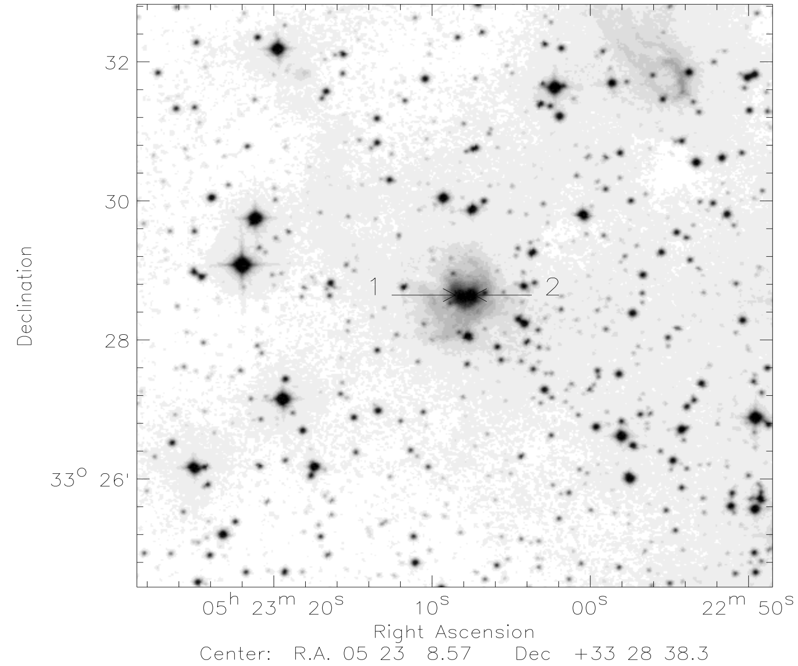

Figure 3.5: We show an $8' \times 8'$ image of the field containing Sim 129. The image is reproduced from Digitized Sky Survey. We have marked two sources for which spectroscopic observations were carried out. North is up and east is to the left.

this argument. The distance to Sim 129 is assumed to be same as that of IC 410 which is estimated at a distance of 3.4 kpc (Sugitani et al. 1991). The estimated mass of the head region of Sim 129 (using equation **??** and adopting a fixed value for A_V as 5 magnitude) is found to be $\sim$ 130 $M_\odot$.

In Figure 3.5 we show a image of the field containing Sim 129 (reproduced form Digitized Sky Survey). There are two sources in the head region of this cloud which are identified as 1 and 2 in Figure 3.5. They form a visual binary with a separation of about $9''$ which corresponds to 0.15 pc at 3400 pc. They are oriented in EW direction and almost parallel to the direction of the tail. We made spectroscopic observations of both the sources 1 and 2. The spectra of sources 1 and 2 are shown in Figure A.11 and A.12 respectively. Star 1 shows Hα, O I λ7774, O I λ8446, Ca II triplet lines $\lambda\lambda$8498, 8542, 8662, and Paschen lines in emission. No emission lines are seen in the spectrum of star 2. We find B1 and B3 spectral types for both star 1 and star 2 respectively. The bright

IRAS point source, IRAS 05198+3325, which was identified as to be a luminous YSO by Campbell, Persson & Matthews (1989) is positionally coinciding with star 1 indicating that star 1 is the most massive source in Sim 129.

L1622

The bright-rimmed cloud called Orion East by Herbig and Rao (1972) is associated with L1621 and L1622. The head region of L1622 harbours a reflection nebula VDB 62 (Magakain 2003) which is probably illuminated by a T Tauri star HD 288313. The distance estimate, 400-500 pc (see the compilation of LDN distances by Hilton & Lahulla 1995), is based on an assumed proximity to the early type stars ionizing its edges facing the Orion OB 1b association ≈450 pc.

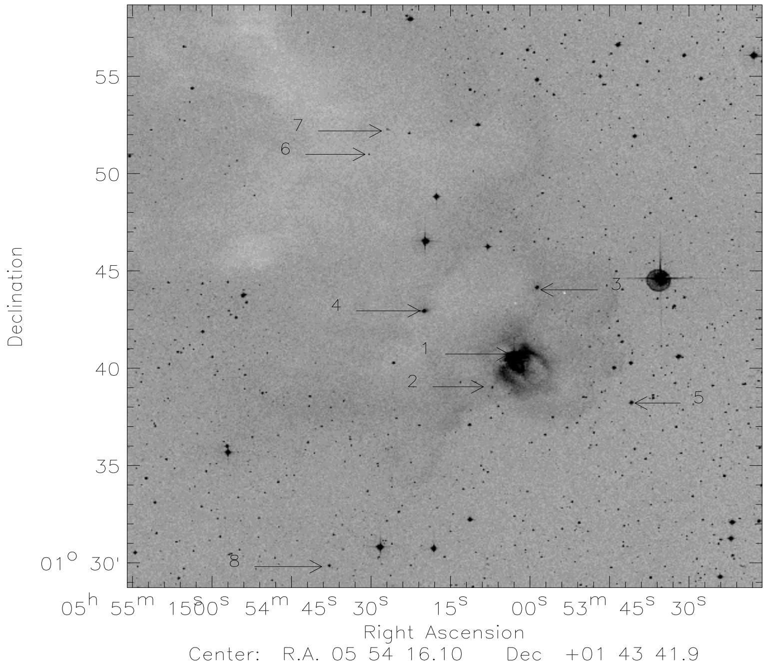

Figure 3.6: We present a $30' \times 30'$ DSS image of the filed containing L 1622 with sources for which we made spectroscopic observations are marked. North is up and east is to the left.

In Figure 3.6, we mark all the Hα sources found within and two sources outside the cloud boundaries for which we have made spectroscopic observations. The spectrum of star 1 which is identified with HD 288313, a known T Tauri star (Herbig & Bell 1988), is given in Figure A.13. The spectrum is devoid of any emission lines. The T Tauri nature of this star is recognized by the detection of Li (λ6707) line in absorption. We find a K1 spectral type for star 1. From an objective prism survey conducted for Hα emission stars of T Tauri type by using Kiso Schmidt telescope, Ogura & Hasegawa (1983) have shown that it is not the star 1 but a faint source to the north-west and $\sim 30''$ away from star 1 is the source of Hα emission. Because of the presence of nebulosity, we could not obtain spectrum for the Hα source separately. However, we made slit-less spectroscopy of the region by combining grism (R$\sim$2000) and R - filter. In Figure A.26 we present the image showing spectra of stars present in the field (roughly $10' \times 10'$) containing L1622. Spectra of stars showing Hα in emission are marked. The source identifications are same as in Figure 3.6. The Hα source detected in Hα survey of Ogura & Hasegawa (1983) is shown with an arrow adjacent to star 1. The spectra of this star was extracted from the image using standard IRAF packages and wavelength calibrated. In Figure A.14 we present the spectrum of this star. We determine a M3 spectral type for this star. Star 1 is thus the most luminous source illuminating the nebulosity. The most luminous IRAS source is positionally associated near star 1. The spectrum of star 2 (Kiso A-0905 5), 3 (Lk Hα 335), 4 (RJ Hα 33), 5 (LkHα 334) and 8 (Lk Hα 337) are shown in Figure A.15, A.16, A.17, A.18 and A.19. We have determined M1, K3, K4, K0 and M2 spectral types for stars 2, 3, 4, 5 and 8 respectively. The presence of Li (λ6707) in all of them except star 2 shows that they are low-mass T Tauri stars. Among the YSOs found within the cloud boundaries of L1622, star 1 is the most luminous source.

CG 1

Cometary globule 1 is a typical example of a cometary globule, with a dense pointed head which is $\sim 2'$ wide, covered by luminous bright rims, and a thin luminous tail $\sim 25'$ long (Figure 1.1, Chapter 1). From the molecular line observations of CG 1, it was noted that most of the molecular mass is concentrated in the tail (Harju et al. 1990). The total molecular mass of CG 1 is estimated to be 20-45 $M_\odot$ (Harju et al. 1990). For our analysis we have taken an average value of $\sim$ 30 M$_\odot$ for CG 1. Very close to the tip of the head is seen a star, Bernes 135 (NX Pup), which is classified as a Herbig Ae/Be (Reipurth, 1983; Thé et al. 1994).

In Figure A.20 we present our spectrum of NX Pup. The spectrum shows Hα and [O I] (λ6300 and λ6364) lines in emission. We have determined a spectral type of A2 for NX Pup. Reipurth (1983) have suggested that this star is earlier to F3-F4 spectral types based on the presence of photospheric absorption features. A range (A0 - F2) of spectral types assigned to NX Pup are available in the literature (Molster & Thé 1994; Thé et al. 1994). The photometric variability of NX Pup has been studied extensively by Bibo & Thé (1991). The binary nature of NX Pup was first noted by Bernacca et al. (1993). Using simultaneous optical and near-infrared high angular resolution observations of NX Pup, Schöller et al. (1996) have shown that the secondary component is of spectral type F7-G4 (1.6-1.9 M$_\odot$). This shows that NX Pup is the most massive star among the binary components currently associated with CG 1 .

Gal 96-15

This cloud is located at the very edge of Lac OB1 association. The head of this cloud complex points towards the center of the Lac OB1 younger subgroup, in which lies the bright star 10 Lac, of spectral type O9 V. This younger group of stars is inside a HI void, which also contains the optical HII region S126, bordered by the LBN 437 (Gal 96-15 coincides with bright nebula LBN 437, as cataloged by Lynds (1965)). It contains a group of faint Hα emission stars, among them LkHα 233 whose spectral type is about A7V (Herbig 1960; Thé et al. 1994). LkHα 233 is the central star of the reflection nebula of dimensions 1'$\times$ 3', Bernes 35 (1976) ,classified morphologically as a bipolar nebula by Calvet & Cohen (1978) (see also Aspin et al. 1985). The other three faint Hα emission stars, LkHα 230, 231 and 232 lie near the center of a small dark cloud, 3' northwest of LkHα 233. This region was observed in molecular lines of CO, NH_3 and H_2CO (Olano et al. 1994) . The mass of the cloud as estimated from H_2CO and CO lines is 130-300 M$_\odot$. For our study, we adopt an average mass of $\sim$ 210 M$_\odot$ for Gal 96-15.

In Figure A.21, A.22, A.23 and A.24 we present the spectra of LkHα 233, LkHα 230, LkHα 231, and LkHα 232 respectively. We have determined a A7 spectral type for LkHα 233. This star shows Hα line strongly in emission. The spectra of LkHα 230, LkHα 231, and LkHα 232 shows emission line features typical of low-mass pre-main sequence stars. We have determined K9 spectral type for LkHα 230 and a K0 spectral type for both LkHα 231, and LkHα 232. Both LkHα 230 and LkHα 232 show strong Hα, Ca II triplet lines $\lambda\lambda$8498, 8542, 8662, He I λ5875 and Na DI line λ5896 lines in emission. Hα and Ca II triplet lines are relatively weaker in LkHα 231. No other Hα sources or sources associated with nebulosities are identified towards Gal 96-15. Therefore LkHα 233 is the most massive star in this cloud.

Gal 110-13

Odenwald (1988) found that this cloud has a striking, highly elongated, comet-like shape at far-IR wavelengths. Odenwald et al. (1992) presented IRAS, radio continuum and 21 centimeter and CO data towards this region. Gal 110-13 is not connected to other areas of diffuse far-IR emission in this region of the sky. The aspect ratio of the cloud is 10:1 and its southern end terminates in a bright knot which is identified as the head. The tail extends $\approx 1^\circ.5$ northeast of the head before changing the direction northward, twisted into a kink or loop like structure. The tail is not an uniform filament, but contains three clumpy structures separated by $\approx 16'$. The major axis of the cloud ($PA \approx 45^\circ$) is oriented towards a small cluster of late, B-type stars identified as NGC 7801 located 4° northeast of the Head. The estimated mass of Gal 110-13 is found to be M $\approx 85\mathrm{M}_\odot$ Odenwald et al. (1992). Scenarios involving "champagne" outflows, or interactions with supernova remnants and ionization fronts, seem unable to account for the structure and local environment of the cloud since the pre-requisite O-type stars, ionization fronts, or SNRs are not present.

Two B-type stars, BD +47°4220 (Sao 53209) and BD +47°4214 are clearly embedded within the cloud as both are associated with nebulosities. In Figure A.25 we present the spectrum of BD +47°4220. No emission features are seen in the spectrum. We have determined a B8 spectral type for this star. Aveni & Hunder (1969) have carried out a spectroscopic study of 24 stars towards the direction of Gal 110-13. From their study

Aveni & Hunder (1969) have assigned a B9.5 and B9 spectral types to BD +47°4220 and BD +47°4214 respectively. No other sources (both optically visible and embedded) are present towards the region which are hotter than those of BD +47°4220 and BD +47°4214. The most luminous IRAS point source IRAS 23353+481 is found associated with BD +47°4220 because of which we have chosen BD +47°4220 for our study.

3.4.2 Maximum stellar masses in CGs

In Table 3.3, we present the properties of the most massive stars and the parent clouds. Columns 1 and 2 give the object identifications and the CGs to which the star is associated with, respectively. Column 3 gives the spectral types of the most massive star associated with CG. Column 4 gives the mass of the stars corresponding to the main-sequence spectral types (Schmidt-Kaler 1982). In column 5 and 6 we give mass of the CGs and references respectively. For six clouds, the mass estimates from molecular line observations are available in the literature. In the case of three clouds, LBN 131.54-08.16, Sim 129 and L1622, we have used the cloud masses estimated using the procedure discussed in section 3.3. In Figure 3.7 we plot the mass of the most massive star associated with the CGs against the parent cloud mass. The dashed line represents the relation for the mass of the most luminous star and the mass of the parent cloud (equation 3.5) given by Larson (1982). It should be noted here that the Larson's relation given in equation 3.5 is based on samples from different locations and from different environments. In Figure 3.7 we find that in the case of 7 CGs, the mass of the most massive star formed is significantly higher than that represented by Larson's relation. This implies that stars formed in CGs are relatively more massive than those formed in isolated clouds of similar mass. If the star formation process in CGs produce young stars with a mass function similar to the Salpeter initial mass function, the increase in maximum stellar mass in CGs imply that the total number of stars formed in these CGs are also higher. This will increase the star formation efficiency in these clouds. In two CGs, L1622 and Gal 96-15, the mass of the most massive star formed is found to be much lower when compared to other CGs. This could be because of two reasons: either the most massive star currently associated with these CGs might have formed before the influence of the external trigger or the

Table 3.3: Properties of the most massive star associated with CGs and those of the parent clouds.

Object (1)	Globule Identification (2)	Sp. Type (3)	$M_{\star-max}$ ($M_{\odot}$) (4)	M_{cl} ($M_{\odot}$) (5)	Ref. (6)
GSC 03684-01833	LBN 131.54-08.16	B4	6.4	200	†
HBC 334	RNO 6	B1	13.9	190	Ba
NSV 1832	L1616	B3	7.6	180	Ra
CPM 16	Sim 129	B1	13.9	130	†
HD 288313	L1622	K1	0.8	550	†
NX Pup	CG 1	A2	2.4	32	Ha
h 4636	CG 12	B4	6.4	100	Wh‡
LkHa233	Gal 96-15	A7	1.8	215	Ol
Sao 53209	Gal 110-13	B8	3.8	85	Od

Reference:

Ra- Ramesh (1995); Ha- Harju et al. (1990); Wh- White (1993); Ol- Olano et al. (1994); Od- Odenwald et al. (1992); Ba- Bachiller et al. (2002); Ne- Neckel & Staude (1987)

† Mass estimated using equation **??** assuming $A_V = 5$ mag.

‡ Re-evaluated mass of CG 12 for the distance of 550 pc estimated in Chapter 2 (Part I).

most massive star is yet to form in these CGs. From the calibration of the Michigan class V stars in the range from A0 to G5 in terms of intrinsic Tycho-2 color $(B_{\mathrm{T}} - V_{\mathrm{T}})_0$ and absolute magnitude $M_{V_{\mathrm{T}}}$, Knude et al. (2002) have studied the extinction in the direction L1622. They suggested the existence of molecular material even at a distance as close as 160 pc. But whether L1622 is at 160 pc is still unclear. It is however noteworthy the remark made by Bally (2001) in his discussion of the ISM structure in the Orion/Eridanus bubble just mentioning that the near side of this expanding bubble could be as close as 180 pc. The different radial velocities ~1 km s^{-1} and ~10 km s^{-1} measured for L 1622 and L 1617 cloud (similar to Orion B cloud) respectively (Bally 2001) might suggest that they belong to the near and far part of the expanding Orion bubble. If the distance of L 1622 becomes ~ 160 pc,i.e., reduced by a factor of ~ 3, then the mass of L 1622 (which was estimated using equation **??**) will reduce by a factor of ~ 9. But still the mass of the most massive star formed in L 1622 is found to be lower.

3.5 Conclusions

In this chapter we have investigated the maximum luminosity of young stellar objects as a function of the parent cloud mass in CGs and compared them with that in isolated

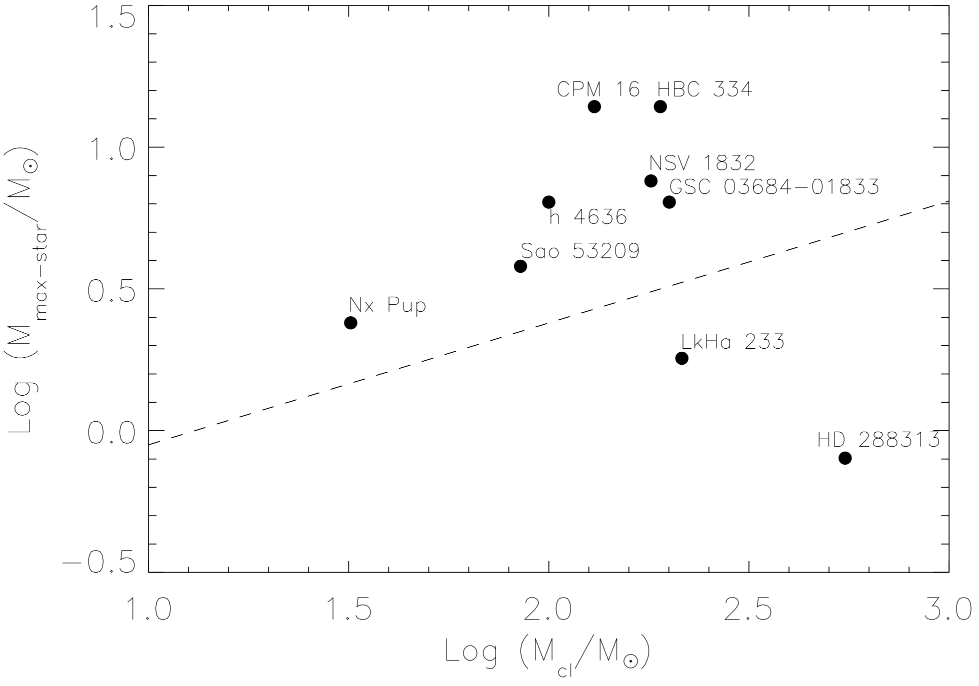

Figure 3.7: The mass of the most massive star associated with CGs are plotted against parent cloud mass. The dashed line represents the relation for the mass of the most luminous star and the mass of the cloud (equation 3.5) given by Larson (1982).

dark cloud (opacity class 6 cloud). The main findings of this work are summarized as following:

- The maximum luminosity of young stellar objects associated with clouds (CGs & opacity class 6 clouds) increases with the increase in the parent cloud masses showing that the cloud mass is apparently one of the most important parameters to characterize star formation.

- Protostars (IRAS sources) forming in CGs are apparently more luminous than those in opacity class 6 clouds which are relatively more isolated and away from the influences of any external forces. This suggest that the external forces which are responsible for the cometary morphology have influenced the internal properties as well as the star formation of CGs.

- The masses of the most massive stars (estimated from their spectral types) associated with CGs are larger than that expected from their parental cloud masses.

Bibliography

[1] Alcala, J. M., Wachter, S., Covino, E., 2004, A&A, 416, 677

[2] Allen, 1973, Allen's astrophysical quantities, p.489

[3] Aspin, C., McCaughrean, M. J., McLean, I. S., 1985, A&A, 144, 220

[4] Aveni, A. F., Hunter, J. H., 1969, AJ, 74, 1021

[5] Bachiller, R., Fuente, A., Kumar, M. S. N., 2002, A&A, 381, 168

[6] Bally, J., 2001, Tetons 4: Galactic Structure, Stars and the Interstellar Medium, ASP Conference Series, Vol. 231. Edited by Charles E. Woodward, Michael D. Bicay, and J. Michael Shull. San Francisco: Astronomical Society of the Pacific. ISBN: 1-58381-064-1, p.204

[7] Bernacca, P. L., Lattanizi, M. G., Bucciarelli, B., et al., 1993, A&A, 278L, 47

[8] Bibo, E. A., The, P. S., 1991, A&AS, 89, 319

[9] Bourke, T. L., Hyland, A. R., Robinson, G., 1995, MNRAS, 276, 1052

[10] Burton, W. B., 1974, IAUS, 60, 551

[11] Calvet, N., Cohen, M., 1978, MNRAS, 182, 687

[12] Campbell, Bel., Persson, S. E., Matthews, K., 1989, AJ, 98, 643

[13] Cernicharo, 1991, The Physics of Star Formation and Early Stellar Evolution, NATO Advanced Science Institutes

[14] Clemens, Dan P., Barvainis, Richard., 1988, ApJS, 68, 257

[15] Clemens, Dan P., Yun, Joao Lin., Heyer, Mark H., 1991, ApJS, 75, 877

[16] Cohen, M., 1980, AJ, 85, 29

[17] Cox, Arthur N., 2000, Allen's astrophysical quantities, 4th ed. Publisher: New York: AIP Press; Springer, 2000. Editedy by Arthur N. Cox. ISBN: 0387987460

[18] Dickman, R. L., 1975, ApJ, 202, 50

[19] Dobashi, Kazuhito., Bernard, Jean-Philippe., Fukui, Yasuo., 1996, ApJ, 466, 282

[20] Dobashi, Kazuhito., Yonekura, Yoshinori., Matsumoto, Tomoaki., 2001, PASJ, 53, 85

[21] González-Alfonso, Cernicharo & Radford, 1995, A&A, 293, 493

[22] Gyulbudagyan, A. L., Magakyan, T. Yu., 1977, PAZh, 3, 113

[23] Harju, J., Sahu, M., Henkel, C., Wilson, T. L., et al., 1990, A&A, 233, 197

[24] Herbig, George H., 1960, ApJS, 4, 337

[25] Herbig, G. H., Kameswara Rao, N., 1972, ApJ, 174, 401

[26] Herbig, G. H., Bell, K. Robbin., Lick Observatory Bulletin, Santa Cruz: Lick Observatory, c1988

[27] Hilton, J., Lahulla, J. F., 1995, A&AS, 113, 325

[28] Ho, P. T. P., Martin, R. N., Barrett, A. H., 1981, ApJ, 246, 761

[29] Hog et al., 2000, The Tycho-2 Catalogue, I/259

[30] Jansen, David J., van Dishoeck, Ewine F., Black, John H., 1994, A&A, 282, 605

[31] Jenkins, E. B., Savage, B. D., 1974, ApJ, 187, 243

[32] Knude, J., Nielsen, A. S., 2000, A&A, 362, 1138

[33] Knude, J., Fabricius, C., Hog, E., Makarov, V., 2002, A&A, 392, 1069

[34] Lada, Elizabeth A., Strom, Karen M., Myers, Philip C., 1993, In: Protostars and planets III

[35] Lada, Charles J., Lada, Elizabeth A., 2003, ARA&A, 41, 57

[36] Larson, R. B., 1981, MNRAS.194, 809

[37] Larson, R. B., 1982, MNRAS, 200, 159

[38] Launhardt, R., Henning, T., 1997, A&A, 326, 329

[39] Lee, Chang Won., Myers, Philip C., 1999, ApJS, 123, 233

[40] Lefloch & Lazareff, 1994, A&A, 289, 559

[41] Lynds, Beverly T., 1962, ApJS, 7, 1

[42] Lynds, Beverly T., 1965, ApJS, 12, 163

[43] Magakian, T. Yu., 2003, A&A, 399, 141

[44] Marco, A., Negueruela, I., 2003, A&A, 406, 119

[45] Martin & Barrett, 1978, ApJS, 36, 1

[46] Molster, F. J., Thé, P. S., 1994, ASPC, 62, 199

[47] Myers, P. C., Fuller, Gary A., Mathieu, R. D., 1987, ApJ, 319, 340

[48] Myers, P. C., Benson, P. J., 1983, RMxAA, 7, 238

[49] Myers, P. C., Molecular Astrophysics, a Volume honoring Alex Dalgarno. Edited by. T.W. Hartquist. Cambridge, UK: Camb ridge University Press, 1990., p.328

[50] Neckel & Staude, 1987, ApJ, 320L, 145

[51] Odenwald, Sten F., 1988, ApJ, 325, 320

[52] Odenwald, Sten F., Fischer, Jacqueline., Lockman, Felix J., Stemwedel, Sally., 1992, ApJ, 397, 174

[53] Ogura, K., Hasegawa, T., 1983, PASJ, 35, 299

[54] Ogura & Sugitani, 1998, PASA, 15, 91

[55] Olano, Walmsley, & Wilson, 1994, A&A, 290, 235

[56] Parker, N. D., 1988, MNRAS, 235, 139

[57] Ramesh, B., 1995, MNRAS, 276, 923

[58] Reipurth, 1983, A&A, 117, 183

[59] Reipurth, Bo., Gee, Graham., 1986, A&A, 166, 148

[60] Rieke, G. H., Lebofsky, M. J.,1985, ApJ, 288, 618

[61] Scarrott, S. M., Brosch, N., Ward-Thompson, D., 1986, MNRAS, 223, 505

[62] Schmidt-Kaler, Th. 1982, Landolt-Brnstein, Numerical data and Functional Relationships in Science and Technology, New Series, Group VI, vol. 2(b), ed. K.

[63] Schoeller, M., Brandner, W., Lehmann, T., 1996, A&A, 315, 445

[64] Sridharan, T. K., 1992, JApA, 13, 217

[65] Sugitani et al., 1989, ApJ, 342L, 87

[66] Sugitani, Fukui, Yasuo., Ogura, Katsuo., 1991, ApJS, 77, 59

[67] Sugitani, Koji., Ogura, Katsuo., 1994, ApJS, 92, 163

[68] Th$\acute{e}$, P. S., de Winter, D., Perez, M. R., 1994, A&AS, 104, 315

[69] Vieira, S. L. A., Corradi, W. J. B., Alencar, S. H. P., 2003, AJ, 126, 2971

[70] Vilas-Boas, J. W. S., Myers, P. C., Fuller, G. A., 2000, ApJ, 532, 1038

[71] Weintraub, David A., 1990, ApJS, 74, 575

[72] White G. J., 1993, A&A, 274, L33

[73] Whittet, D, C, B., 2003, *Dust in the galactic environment* (second edition), Institute of Physics Publishing

Chapter 4

Star formation at high galactic latitudes: A multi-wavelength study of Stephenson Hα objects

4.1 Introduction

Currently star formation in the Milky Way is generally confined to relatively thin layer in the Galactic disk. The scale height for the vertical distribution of the massive early type (O-B stars) is only $\sim$ 70 pc (Reed 2000). For lower mass YSOs, their distribution and vertical scale height is not very well known due to their lower brightness and uncertainty in the distances. In Chapter 2 we have presented a detailed study of CG 12 which is shown to be a site of low to intermediate star formation at a relatively large height ($\sim$ 200 pc) above the Galactic plane. A more extensive survey of young stellar objects at high-galactic latitude would be valuable for a better understanding of star formation as a function of height above the Galactic plane. The Hα emission objects in the survey by Stephenson (1986) provide a magnitude limited sample of candidates for the YSOs at high-galactic latitude. This chapter presents results of such a study that we have carried out.

A survey of the northern sky ($\delta > -25°$) for Hα - emission stars at relatively high galactic latitudes ($|b| \geq 10°$), based on red-sensitive objective prism plates taken with

---

This chapter is based on the published work: Maheswar, G., Manoj, P., Bhatt, H. C., 2003, A&A, 402, 963.

the Burrell Schmidt telescope of the Warner and Swasey Observatory, was reported by Stephenson (1986). The spectral dispersion was about 1000 Å mm^{-1} at Hα and the limiting magnitude was ≈ 13. The survey resulted in a catalogue of 206 Hα- emission stars (hereafter designated as StHa stars). The sky distribution of these new emission-line stars is different from that of those already known at lower galactic latitudes, large numbers of which lie in Orion, Taurus and other star forming regions. The StHa stars, except for a conspicuous concentration in Orion, are more uniformly distributed in galactic longitude. Of the 206 stars, only 41 had known spectral types then, mostly of type M. Understanding of the physical nature of the StHa objects would require follow-up studies.

The first follow-up spectroscopic observations of StHa stars were reported by Downes & Keyes (1988) who observed 105 StHa objects, at spectral resolutions $\sim 11.5 - 13$ $\mathring{A}$, along with 6 objects from the list of low-latitude Hα emission stars of Stephenson & Sanduleak (1977). Of the 105 stars observed, 24 were found to be T Tauri stars, 1 Ke star, 5 Me stars, 3 cataclysmic variables, 6 symbiotic stars, 1 BQ[ ]star, 1 carbon star, 16 Be stars and 1 Seyfert galaxy. The rest (47 objects) failed to show Hα in emission. Of these non-emission objects, 11 were listed in Stephenson (1986) as having weak emission, and therefore, the report of emission for these objects could possibly have been spurious (Downes & Keyes 1988). The spectral types determined for the remaining 36 non-emission stars, listed earlier by Stephenson (1986) as having moderate-strength Hα emission, were typically of the type G - K, indicating that these objects could be T Tauri stars with variable emission. Further monitoring of these objects is necessary to confirm if they are indeed T Tauri stars. Are there more T Tauri and other young stellar objects (YSOs), like Herbig Ae/Be stars, in the StHa list? Due to their relatively high galactic latitudes ($|b| \geq 10°$) the StHa objects are potential candidates for being high-latitude YSOs. Three of the StHa stars (16, 17, 18) have in fact been now recognized (see eg. Luhman 2001) as members of the young association around the high-latitude molecular cloud MBM 12 (Magnani, Blitz & Mundy 1985). A study of the StHa objects, in particular those that have not been followed up so far, would be important for confirming their classification as emission-line objects and looking for additional YSO candidates at high galactic latitudes.

In this chapter we present the results of optical spectroscopic observations, at $\sim 2.6 - 5.3$ Å resolution in the wavelength range $5300 - 7500$ Å, of 52 stars from Stephenson (1986), 22 of which are common with those observed by Downes & Keyes (1988) at $\sim 11.5 - 13$ Å resolution, and 30 are new. Since YSOs are generally characterised by excess infrared emission and low-mass YSOs are often bright in X-rays, we also cross-correlate StHa objects with sources in the 2MASS, IRAS and ROSAT catalogues. For stars in common with those in Downes & Keyes (1988), the results of our spectroscopic observations are compared and variabilities noted. Spectral types are estimated for 28 new stars. The behaviour of StHa stars at X-ray and infrared wavelengths is discussed with particular reference to the known YSOs and YSO candidates. Comments are also made on the statistics of objects of different classes in the StHa catalogue.

4.2 Observations

Optical CCD spectra of StHa stars were obtained using the OMR (Optomechanics Research) spectrograph (Prabhu et al. 1998) on the 2.34 m VBT at Vainu Bappu Observatory during the period 1999-2002. StHa 57 was observed on 03 January 2003. All spectra were obtained with a slit of $2''$ width and spectral resolution $1.3 - 2.6$ Å $pixel^{-1}$. All raw spectra were bias subtracted, flat-field corrected, extracted and wavelength calibrated in the standard manner using the IRAF reduction package.

Searches in 2MASS, IRAS and ROSAT catalogues were performed to find detections of StHa stars by 2MASS, IRAS and ROSAT surveys.

4.3 Results and Discussion

4.3.1 Spectroscopic Results

We observed 52 StHa objects spectroscopically. Table 4.1 gives the results of the spectroscopic observations of StHa stars. Column (1) gives object identification, column (2) indicates whether Hα is in emission, columns (3) & (4) give equivalent widths (negative values indicating emission in the line) of Hα emission line and Li I $\lambda 6708$ Å absorption line respectively when detected, column (5) gives spectral type determined by comparing the observed spectrum with those in the atlas of Jacoby et al. (1984), column (6) gives spectral types obtained from literature, column (7) gives the reference for the spectral type from literature, column (8) & (9) give the class of the object and reference respectively.

Downes & Keyes (1988) found that the Stephenson (1986) catalogue contains objects that belong to a number of physically different classes. In the following, we present the results of our spectroscopic study for the various groups of objects and discuss some individual objects in greater detail.

4.3.1.1 Emission-line objects

Of the 52 objects observed by us, 12 show Hα line clearly in emission. In one object, StHa 40, Hα varied from being in absorption to emission over a period of two years. There are several categories of objects showing Hα in emission.

(1) *T Tauri stars:* StHa 16, 17, 18, 19 , 48 and 127 show Hα in emission with equivalent widths given in column (3) of Table 4.1. StHa 16,17, 18, 19 and 127 are known to be T Tauri stars (Appenzellar et al. 1983; Downes & Keyes 1988, Fernandez et al. 1995). The large Hα emission line equivalent widths ($W_{H\alpha} \sim 10$ Å - 60 Å) observed here are consistent with their classification as T Tauri stars. A comparison with the description of spectra in Downes & Keyes (1988) shows that Hα line strengths have undergone variations. For example, following the system of "emission-line class" based on the relative strength of the emission lines as defined in Herbig (1962), Downes & Keyes (1988) assign an emission-line class of 5 to StHa 17 and class 2 to StHa 18, whereas our measurements give $W_{H\alpha}$ values of 10 Å and 56 Å respectively for these two stars.

StHa 48 was identified as an emission-line star in the survey observations (spectral observations using objective prism at a resolution of 600-700 Å/mm) performed by Wiramihardja et al. (1989) towards the Orion region. Our observations of StHa 48 confirm that this object is a T Tauri star. Figure 4.1 shows our spectrum for StHa 48. It shows Hα and H$_\beta$ in emission. Li I λ6708 absorption line is also found to be present in this star. It is very close to the star forming region IC 423 (CB 31; Clemens & Barvainis 1988). As

Table 4.1: Results from spectroscopic observations on StHa stars.

Object	Hα in emission	$W_{H\alpha}$ (Å)	W_{Li} (Å)	Sp.Type (this work)	Sp. Type (literature)	Reference for Sp. Type	Class of object	Reference for Object class
StHa 05	no	-	-	A3	-	-	-	-
StHa 07	yes	-4.7	-	K4	-	-	Ke	3
StHa 12 *	yes	-11.4	-	B	B	1	Be	1
StHa 15	no	-	-	A5	-	-	-	-
StHa 16 *	yes	-26.0	-	K9	M0	2	T Tau	2
StHa 17 *	yes	-10.4	0.35	K0	K5	2	T Tau	2
StHa 18 *	yes	-56	-	M0	early M	2	T Tau	2
StHa 19 *	yes	-25.8	0.41	G9	G8	2	T Tau	2
StHa 21	no	-		G7	-	-	-	-
StHa 35 *	no	-	-	G0	mid K	1	-	-
StHa 40 *	variable	-14.5†	0.33†	G2/K0	late F/early G	1	T Tau	1
StHa 44 *	no	-	-	F7	mid F	1	-	-
StHa 46	no	-	-	G6	-	-	-	-
StHa 48	yes	-16.8	0.70	K4	-	1	T Tau	3
StHa 56	no	-	-	G2	-	-	-	-
StHa 57	no	-	-	M5	M3	4	-	-
StHa 58	no	-	-	F0	-	-	-	-
StHa 61	no	-	-	G9	-	-	-	-
StHa 62 *	yes	-156	-	BQ[ ]	-	1	BQ[ ]	1
StHa 64 *	no	-	-	K4	late type absorption	1	-	-
StHa 65	no	-	-	F7	F8	5	-	-
StHa 71 *	no	-	-	G1	absorption	1	-	-
StHa 72	no	-	-	G2	-	-	-	-
StHa 75	no	-	-	A7	-	-	-	-
StHa 77	no	-	-	G2	-	-	-	-
StHa 79	no	-	-	F7	-	-	-	-
StHa 80	no	-	-	K0	-	-	-	-
StHa 81	no	-	-	G2	-	-	-	-
StHa 82 *	no	-	-	G6	Me‡	1	-	-
StHa 83 *	no	-	-	K4	early-mid K	1	-	-
StHa 84	no	-	-	A7	A5	5	-	-
StHa 85	yes	-98	-	-	NGC 4051 (galaxy)	6	Galaxy	6
StHa 86	yes	-124	-	-	NGC 1494 (galaxy)	7	Galaxy	7
StHa 87	no	-	-	G6	-	-	-	-
StHa 88 *	no	-	-	M5	M	1	-	-
StHa 89 *	no	-	-	F7	mid F	1	-	-
StHa 90	no	-	-	K4	-	-	-	-
StHa 91 *	no	-	-	G6	G	1	-	-
StHa 92 *	no	-	-	K0	K	1	-	-
StHa 93 *	no	-	-	A7	early F	1	-	-
StHa 95 *	no	-	-	G6	G	1	-	-
StHa 96 *	no	-	-	G6	G	1	-	-
StHa 99 *	no	-	-	G2	early-mid F	1	-	-
StHa 107	no	-	-	F3	G5	5	-	-
StHa 108	no	-	-	G0	-	-	-	-
StHa 109	no	-	-	F7	-	-	-	-
StHa 110	no	-	-	G2	-	-	-	-
StHa 127	yes	-62	0.85	K4	K6,7	2	T Tau	2
StHa 134	no	-	-	A1	F0	5	-	-
StHa 139	no	-	-	A2	A2	5	-	-
StHa 160 *	yes	-16.3	-	B	B	1	Be	1
StHa 163	no	-	-	M5	M1	5	-	-

* stars which are in common with those of Downes & Keyes (1988).

† These values correspond to the October 2002 spectrum. Hα is in absorption in the February 2000 spectrum and $W_{Li} = 0.13$ Å then.

‡ Possibly misidentified. See text.

References

(1) Downes & Keyes (1988); (2) Herbig-Bell Catalog (1988): (3) This work; (4) Stephenson (1986); (5) Catalogue of Positions & Proper motions (1988); (6) Lewis (1972); (7) Allen (1976)

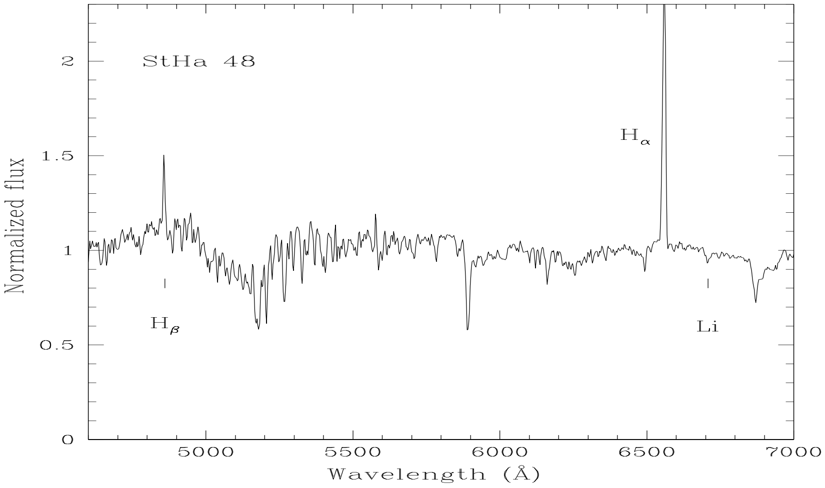

Figure 4.1: Spectrum of StHa 48.

discussed later this star is a ROSAT X-ray source and its 2MASS measurements (Table 4.2) seem to show near infrared excesses characteristic of T Tauri stars.

StHa 40 has shown remarkable variability in its Hα activity. Figure 4.2 shows spectra of StHa 40 obtained by us in February 2000 and October 2002. In February 2000, the object shows Hα in absorption while the October 2002 spectrum shows Hα clearly in emission ($W_{H\alpha} = 14.5\ \AA$). Not only is there a drastic change of Hα from absorption to emission, but also there are significant changes in the underlying photospheric absorption spectrum. The February 2000 spectrum closely matches a G2 type stellar spectrum, while in the October 2002 spectrum absorption features characteristic of a cooler spectral type (K0) are seen. Spectroscopic observations of Downes & Keyes (1988) had shown StHa 40 to have Hα in emission on a late F/ early G spectral type for the stellar spectrum. Earlier Mac Connell (1982) had also listed StHa 40 as a star with Hα in emission. Torres et al. (1995) found the star to have Hα in emission ($W_{H\alpha} = 9\ \AA$) with variation in profile. They also found the Li $\lambda6708\ \AA$ line in absorption ($W_{Li} = 0.13\ \AA$) and the radial velocity variations indicating that the star could be a spectroscopic binary.

Our spectroscopic observations also suggest that StHa 40 varied photometrically during the period February 2000 - October 2002. Comparison with spectrophotometric standards observed on the same nights (HD 117880 on 16 February 2000 and Feige 15 on 04 October 2002) gives photometric magnitudes $V = 12.5, R = 12.2$ in February 2000 and $V = 10.9, R = 10.5$ in October 2002.

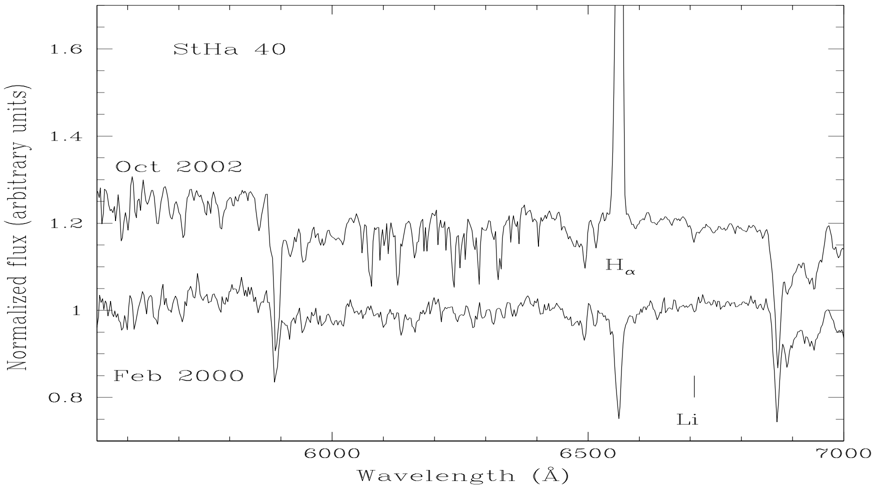

Figure 4.2: Spectrum of StHa 40.

StHa 40 was thus fainter by ~ 1.6 *mag* in the V band in February 2000 when it had Hα in absorption, as compared with its brightness in October 2002 when it showed Hα in emission. Its $V - R$ colour, however, varied only marginally ($V - R = 0.3 - 0.4$). Our measurements can also be compared with those reported in Gregorio-Hetem (2002) who give for StHa 40: spectral type G5, $V = 10.96$ and $V - R = 0.45$ based on observations of Torres et al. (1995). The observed spectrophotometric variability of StHa 40 may, in part, be related to the possibility of its being a close binary (Torres et al. 1995). Further monitoring of the object would help clarify its nature.

(2) *Other emission-line stars*: StHa 12 and 160 were classified by Downes & Keyes (1988) as Be stars. Our spectra for these objects show Hα with modest equivalent widths of 11 $\AA$ and 16 $\AA$ respectively. The spectrum of StHa 07 shows only Hα in emission ($W_{H\alpha} = 4.8\AA$). It is a bright ($m_v = 10.5$, Stephenson 1986), high galactic latitude ($b = -36°.6$) object. We derive a spectral type K4 for this object. It is found to be associated with an X-ray source identified in the ROSAT Bright Survey (Schwope et al. 2000). It is possibly a nearby Ke star.

(3) *Post AGB star:* The spectrum of StHa 62 in Downes & Keyes (1988) showed Balmer lines of hydrogen and [N II] $\lambda6584$ in emission superposed on a featureless continuum. It is now recognized as a post-AGB star (Fujii et al. 2002). We present the

spectrum of StHa 62, at a resolution higher than that used in the observations of Downes & Keyes (1988) in Figure 4.3. It shows strong Hα and other permitted and forbidden lines characteristic of BQ[ ] type spectra.

(4) *Emission line galaxies:* StHa 85 is known to be a Seyfert I galaxy (Lewis 1972). Spectrum of StHa 85 shows H I, He I, [O III] $\lambda\lambda$4959, 5007, [N II] $\lambda\lambda$6548, 6583 and [S II] $\lambda\lambda$6716, 6731 lines in emission. StHa 86 is known to be an emission line galaxy (Allen 1976). Our spectrum of StHa 86 shows H I, [N II] $\lambda\lambda$6548, 6583 and [S II] $\lambda\lambda$6716, 6731 lines in emission.

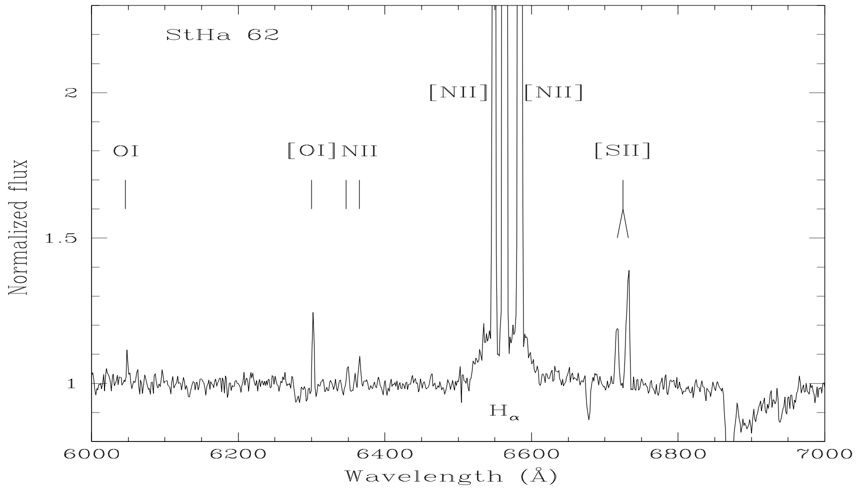

Figure 4.3: Spectrum of StHa 62.

4.3.1.2 Objects with no line emission

Out of 52 StHa objects observed by us, 39 did not show Hα in emission. In one object (StHa 40, discussed above) the Hα line varied from being in absorption, in February 2000, to emission in October 2002. Of these objects with no emission in Hα, 15 are in common with those observed by Downes & Keyes (1988). The present results, regarding the behaviour of Hα (absence of emission) and the derived spectral type, are in general agreement with the results of Downes & Keyes (1988) except for StHa 35, 40 (discussed below in detail) and 82. For StHa 35 our observations agree with those of Downes & Keyes (1988) in finding Hα to be in absorption, but the spectral type determined by us (G0) differs by more than a spectral class from that (Mid K) given in Downes &

Keyes (1988). Our spectrum for StHa 82 gives a spectral type G6 with Hα in absorption, whereas Downes & Keyes (1988) listed this object as an Me star. It is possible that Downes & Keyes (1988) have observed the M3 type flare star CW UMa which is $\sim 1'.5$ north-west of StHa 82 (Stephenson 1986).

A majority of the objects observed in the present study do not show Hα in emission. Twenty five of the thirty newly observed (not common with Downes & Keyes 1988) StHa objects are non-emission line stars. Stephenson (1986) listed 14 of these objects as having weak emission. It is possible that they were spurious detections. The remaining 11 objects were listed by Stephenson (1986) as having moderate-strength (10 objects) or strong (1 object) emission. If the emissions were real, then the present non-emission character of these objects implies spectral variability. We do find spectral variability in StHa 40 which showed Hα change from being in absorption to emission over a period of two years as compared with the observations of Downes & Keyes (1988) who listed this object as Hα emitting T Tauri star.

4.3.2 2MASS, IRAS and ROSAT results

A significant fraction (26 of 105) of StHa objects had turned out to be T Tauri stars in the study by Downes & Keyes (1988). There were also emission-line objects of other types, like 3 cataclysmic variables, 6 symbiotic stars, 17 Be stars, 5 Me stars, two BQ[ ] stars, two emission-line galaxies, one planetary nebula, and one carbon star. T Tauri stars are YSOs that, in addition to Hα emission, are generally characterised by excess infrared emission. These low mass YSOs are often bright in X-rays. Emission line objects of other classes (eg., Be stars, symbiotic stars) are also known to show excess infrared emission due to circumstellar matter. We therefore cross-correlate all StHa objects with sources in 2MASS, IRAS, ROSAT catalogues to confirm the nature of known classes of StHa objects and to look for additional candidate YSOs among them.

Table 4.2 gives the results of searches made in 2MASS, IRAS and ROSAT catalogues for StHa stars. Of the 206 stars in StHa list, 112 have 2MASS observations. In Table 4.2, column (1) gives object identification, column (2) gives radial distance ($arcmin$) from StHa star to the 2MASS detection, columns (3, 5 & 7) give J, H & K_s magnitudes respectively, columns (4, 6 & 8) give estimates of all the possible random errors that contribute to the photometric uncertainties in J, H & K_s bands respectively, columns (9, 10) give $J-H$ and $H-K_s$ colours evaluated from the observed magnitudes. Column (11) gives spectral types of StHa stars. These include spectral types determined by us and those available in literature. The reference for the listed spectral type is given in parentheses. A search was made around StHa stars for IRAS (IPAC, 1986; Moshir 1989) and ROSAT (ROSAT, 2000) sources associated with it within 1 *arcmin* radius. The IRAS and ROSAT data points were superimposed on DSS image of the corresponding StHa star and the nearest detection was selected. Columns (12, 13) indicate whether the StHa stars were detected by IRAS satellite and ROSAT respectively. Values given in parentheses of columns 12 and 13 are the radial distances (in *arcmin*) of IRAS and ROSAT detections from StHa stars respectively. Column 14 gives the class of StHa stars and relevant references. Stars which failed in showing emission lines in spectroscopic observations (this work and Downes & Keyes 1988) are marked with 'No-emission' in this column.

IRAS detections are available for 58 StHa objects. Of these 20 are T Tauri stars, one (StHa 49) associated with condensations in the Herbig - Haro outflow HH 1-2 (eg. Molinari, S & Noriega-Crespo, 2002), 1 B 1.5 type star, 4 Be stars, 1 BQ[ ] star, 1 B9 type star, 1 carbon star, 3 M giants, 1 Mira variable, 2 semi-regular pulsating stars, 3 symbiotic stars, 12 M type stars, 2 Me stars, 3 galaxies, 2 planetary nebule, and one object (StHa 69) for which the spectral type and object class is as yet uncertain.

The M and Me type stars all have IRAS flux densities decreasing with wavelength ($F_{25\mu m} < F_{12\mu m}$) except StHa 23 and StHa 125 for which $F_{25\mu m} \simeq$ or $> F_{12\mu m}$ which is more characteristic of T Tauri stars. Stephenson (1986) lists StHa 23 as an atypically red M0r star. No spectrum for StHa 23 is available in the literature. StHa 125 was listed by Stephenson (1986) as an atypically red star with a strong Hα emission. Downes & Keyes (1988) found the star to have an M type spectrum with Hα in emission. StHa 125 is in the neighbourhood of several other known T Tauri stars (StHa 122, 123, 124, 127, 128 and 130) in the region of Ophiuchus star forming cloud. The observed flux density distribution suggests that StHa 125 is also likely to be a T Tauri star.

ROSAT detections are found for 24 objects. Of these 14 are T Tauri stars, 1 (StHa

49) associated with the Herbig - Haro outflow HH 1-2, 2 Ke stars, 1 Me star, 1 M5 type star, 2 cataclysmic variables, 1 galaxy, 1 B 1.5 type star and 1 object (StHa 129) for which the spectral type and object class is as yet unknown. StHa 129 is also near the Ophiuchus star forming cloud. Three other StHa objects (StHa 127, 128 and 130) within $\sim 1°$ of StHa 129 that are also ROSAT sources are known T Tauri stars. StHa 129 may also be a T Tauri star related to the same star forming region.

Of the 13 StHa objects with both IRAS and ROSAT detections, 10 are T Tauri stars, 1 associated with the Herbig - Haro outflow HH 1-2, 1 galaxy and 1 B 1.5 type star. The B1.5 star (StHa 52) as discussed below is likely a Herbig Be type YSO.

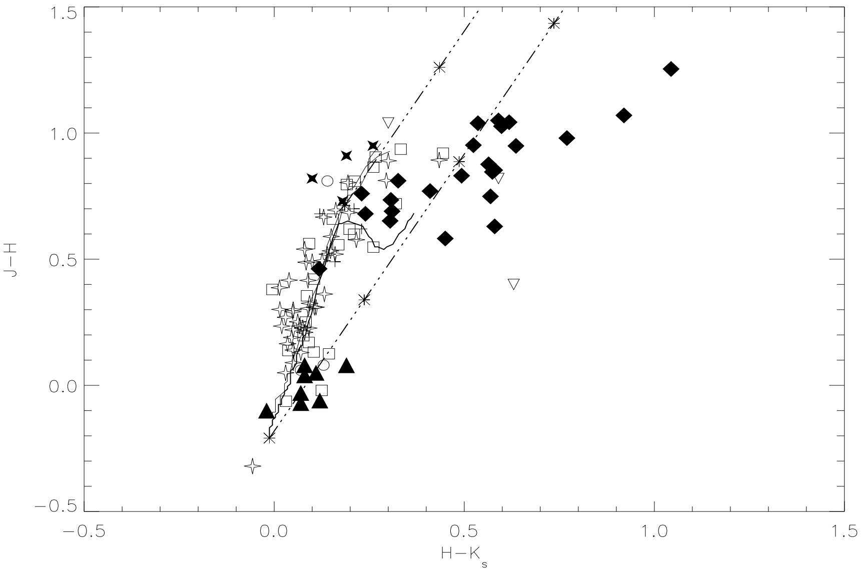

Figure 4.4: Color-colour plot for StHa stars. Symbols represent, **diamonds**: Known T Tauris, **squares**: Stars with unknown spectral type, **filled triangles**: Be stars, **open stars**: Non-emission stars, **filled stars**: Symbiotic stars, **inverted triangles**: NGC 1495, BQ[ ] and mira variables, **open circles**: cataclysmic variables, and **plus signs**: Ke and Me type stars.

Figure 4.4 gives the $(J - H)$, $(H - K_s)$ colour-colour diagram, based on 2MASS measurements, for all the 112 StHa stars with 2MASS observations. Superimposed are two dashed lines parallel to the interstellar reddening vector. The region bounded by these lines can be occupied by reddened main-sequence dwarfs and giants. Points marked with $*$ on the dashed lines are at an interval of $A_v = 5\ mag$. The thick line represents main-sequence dwarfs and giants (Koornneef 1983) and transformed to 2MASS photometric system using the relations in Carpenter (2001). It can be noted that different types of objects occupy different regions of the plot. It can be seen from Table 4.2, that StHa 52 has J-H=-0.02 and H-K_s=0.13 and it occupies the position normally occupied by Be stars in the plot. StHa 52 is detected by both IRAS and ROSAT and is associated with the reflection nebula NGC 2023 in the Orion star forming region. Stephenson listed this star as having weak emission. This star could be a Herbig Be type star that are characterized by infrared excesses and association with nebulosity (eg. Hillenbrand et al. 1992).

In Figure 4.4, a majority of the non-emission stars fall in the region occupied by main-sequence stars. Of the 206 StHa objects, 72 are identified as having no emission (Downes & Keyes 1988 and this work). Of these, 28 are listed as having weak emission objects by Stephenson (1986). It is possible that they were spurious detections. Remaining 44 are listed as moderate (41 objects) and strong emission (3 objects). Objects listed as having moderate and strong emission, failing to show emission, could be due to variability. Active stars like YSOs (eg. StHa 40) can show such variability. From Tables 4.1 and 4.2 it can be seen that a majority of the emission-line objects, including T Tauri stars, have IRAS and/or ROSAT detections. However, only two non-emission stars (StHa 162 and 165) have IRAS detections and only one non-emission star (StHa 88) has ROSAT detection. Stephenson (1986) listed StHa 162 and 165 as having strong emission. Both these stars were studied by Downes & Keyes (1988) , who suggested that there exists a strong bandhead near Hα in the case of StHa 162 which might have been identified as Hα emission, and StHa 165 was found to have a M type absorption spectrum. StHa 165 shows very red near-infrared colours (J-H=0.89, H-K_s=0.43). From 2MASS and IRAS measurements we find that its colour K_s-[12] = 0.39, with the 12μm magnitude $[12] = -2.5\ logS_{12}(Jy) + 4.03$ where S_{12} is the flux density in the IRAS 12μm band, is consistent with photospheric emission of a cool M giant (Kenyon et al. 1988). So, StHa 165 is perhaps a reddened M giant. StHa 88 was studied by Downes & Keyes (1988) who suggested that it could be the TiO band structure which peaks at around the location of Hα and made it appear to be an emission line object in low dispersion spectrum of Stephenson (1986).

T Tauri stars clearly occupy a distinct region of the (J-H), (H-K_s) colour-colour plot (Figure 4.4). StHa 48, an Hα emission line star (Wiramihardja et al. 1989) found to have Li I λ6708 $\mathring{A}$ absorption line in our observations presented here, also falls in the region occupied by known T Tauri stars. Stars of unknown status showing near-infrared excess with IRAS and/or ROSAT detections occupying the same region as by T Tauri stars in the plot, could be potential YSO candidates. Two such objects are: StHa 69 (J-H=0.92, H-K_s=0.44) and StHa 165 (J-H=0.89, H-K_s=0.43). Both are IRAS sources detected only in the 12μm band with $F_{12\mu m} > F_{25\mu m}$, the latter being an upper limit. Gigoyan et al. (1998) have listed StHa 69 in their list of late-type M and C stars found on plates of the first Byurakan Spectral Sky Survey. Kazarovets (1998) listed it as suspected variable star. For StHa 69 the colour K_s-[12] = 0.67, similar to the colour of an M giant (Kenyon et al. 1988). Thus both StHa 69 and 165 (discussed above) are likely to be reddened M giants.

4.4 Conclusions

We have observed spectroscopically 52 objects from the list of Hα emission stars of Stephenson (1986). The results of our study can be summarized as follows:

(a) Six objects are known T Tauri stars. Five of them show Hα in emission and one star, StHa 40, showed variability in Hα. The variability of StHa 40 in Hα is also accompanied by variations in the underlying stellar absorption spectrum and photometric variability.

(b) We confirm the T Tauri nature of StHa 48 on the basis of the presence of Hα and H_β in emission and Li I λ6708 in absorption. It is in the vicinity of the star forming region IC 423 (CB 31), showing near-infrared excesses and is a ROSAT X-ray source.

(c) From 2MASS, IRAS and ROSAT observations we suggest that StHa 52 is a Herbig Be type YSO while StHa 125 and StHa 129 are T Tauri stars in the Orion and Ophiuchus star forming clouds.

(d) There are six other emission line objects which include one Ke star, two Be stars, two galaxies and one post-AGB star (StHa 62). A higher-resolution spectrum of StHa 62 is presented. It shows permitted and forbidden emission lines typical of BQ[ ] stars.

(e) Thirty nine stars are non-emission line stars. Of these 14 objects are in common with Downes & Keyes (1988) who had also listed them as non-emission stars. Stephenson (1986) listed 17 of them as having weak emission. It is possible that they were spurious detections. Objects listed in Stephenson (1986) as having moderate and strong emission failing to show emission in the present study could be variables.

(f) No new Hα emitting YSOs are found in the present study of StHa objects. YSOs amongst StHa stars that are already known or confirmed as such in this study (StHa 48), and objects (StHa 52, 125 and 129) suggested here to be YSOs all belong to well known star forming regions like Taurus, Orion and Ophiuchus. YSOs at high galactic latitudes in other parts of the sky are therefore rare.

Table 4.2: 2MASS, IRAS and ROSAT results of Stephenson stars.

object (1)	r (') (2)	J (3)	ϵ_J (4)	H (5)	ϵ_H (6)	K (7)	ϵ_K (8)	J-H (9)	H-K_s (10)	Spec. Type(Ref) (11)	IRAS (12)	ROSAT (13)	Class of obj. (Ref) (14)
StHa 05	0.003	8.31	0.04	8.26	0.03	8.23	0.03	0.05	0.03	A3(1)	-	-	No-emission(1)
StHa 07	-	-	-	-	-	-	-	-	-	K2e(1)	-	√(0.133)	Ke star(1)
StHa 08	0.204	8.05	0.03	7.49	0.04	7.32	0.04	0.56	0.17	-	-	-	-
StHa 09	0.450	11.83	0.04	11.47	0.04	11.33	0.04	0.36	0.13	mid K(2)	-	-	No-emission(2)
StHa 10	-	-	-	-	-	-	-	-		Me(2)	-	√(0.130)	-
StHa 12	0.002	10.32	0.03	10.27	0.03	10.16	0.03	0.05	0.11	Be(2)	-	-	-
StHa 13	0.001	9.98	0.03	10.05	0.03	9.98	0.03	-0.07	0.07	Be(2)	-	-	-
StHa 14	0.015	10.98	0.03	10.92	0.03	10.85	0.03	0.06	0.07	B(3)	-	√(0.045)	Cataclysmic(2)
StHa 16	0.006	11.28	0.03	10.26	0.03	9.66	0.03	1.03	0.60	M0(4)	√(0.036)	√(0.116)	T Tau(4)
StHa 17	0.023	10.23	0.03	9.40	0.03	8.90	0.03	0.83	0.49	K5(4)	√(0.290)	√(0.098)	T Tau(4)
StHa 18	0.084	10.70	0.04	9.88	0.03	9.56	0.04	0.81	0.33	early M(4)	-	-	T Tau(4)
StHa 19	0.021	9.49	0.04	8.75	0.03	8.45	0.04	0.73	0.31	G8(4)	-	√(0.708)	T Tau(4)
StHa 21	0.154	10.98	0.03	10.59	0.03	10.58	0.03	0.39	0.01	G7(1)	-	-	No emission(1)
StHa 22	0.269	11.558	0.04	11.480	0.03	11.40	0.03	0.08	0.08	Be(2)	-	-	-
StHa 23	-	-	-	-	-	-	-	-		M0(3)	√(0.110)	-	-
StHa 25	0.013	9.22	0.03	8.52	0.02	8.30	0.03	0.70	0.21	Me(2)	-	√(0.174)	T Tau(4)
StHa 26	0.014	10.12	0.03	9.08	0.03	8.54	0.03	1.04	0.54	-	√(0.408)	-	T Tau(4)
StHa 27	0.011	9.76	0.03	8.88	0.03	8.31	0.04	0.88	0.56	M0(4)	√(0.261)	√(0.122)	T Tau(4)
StHa 28	0.011	9.43	0.04	8.38	0.03	7.76	0.04	1.04	0.62	M0(4)	√(0.105)	-	T Tau (4)
StHa 29	0.022	9.34	0.03	8.38	0.03	7.86	0.03	0.95	0.52	K6(4)	√(0.162)	√(0.174)	T Tau(4)
StHa 30	0.038	9.03	0.04	8.08	0.03	7.44	0.03	0.95	0.64	K7(4)	√(0.151)	√(0.067)	T Tau(4)
StHa 31	0.011	10.71	0.04	9.46	0.04	8.41	0.04	1.25	1.04	K/M(4)	√(0.103)	-	T Tau(4)
StHa 32	0.004	10.20	0.03	9.47	0.03	9.29	0.03	0.73	0.18	-	-	-	Symbiotic(2)
StHa 33	0.001	7.20	0.05	6.51	0.03	6.20	0.03	0.69	0.31	G/K(5)	-	-	T Tau(5)
StHa 34	0.162	10.71	0.04	10.06	0.03	9.75	0.03	0.65	0.30	early K(2)	-	-	T Tau(2)
StHa 36	0.204	9.47	0.03	9.01	0.03	8.89	0.03	0.46	0.12	mid K(2)	-	-	T Tau(2)
StHa 37	0.043	10.04	0.03	9.41	0.04	8.83	0.03	0.63	0.58	-	√(0.047)	-	T Tau(4)
StHa 38	0.056	11.04	0.03	10.19	0.04	9.62	0.03	0.85	0.57	-	-	-	T Tau(2)
StHa 39	0.152	9.54	0.02	8.69	0.04	8.11	0.03	0.85	0.58	mid K(2)	√(0.241)	√(0.286)	T Tau(2)
StHa 40	-	-	-	-	-	-	-	-	-	G2/K0(1)	√(0.008)	√(0.500)	T Tau(2)
StHa 41	0.002	9.02	0.03	8.44	0.07	7.99	0.05	0.58	0.45	late F(2)	√(0.046)	-	T Tau(2)
StHa 42	0.011	10.81	0.03	10.06	0.04	9.50	0.03	0.75	0.57	K5(4)	-	-	T Tau(4)
StHa 44	0.133	10.05	0.04	9.82	0.03	9.75	0.04	0.23	0.07	F7(1)	-	-	No-emission(1)
StHa 45	0.000	9.70	0.04	9.50	0.04	9.42	0.03	0.20	0.08	F7(3)	-	-	
StHa 46	0.104	8.66	0.04	8.14	0.06	8.00	0.04	0.52	0.14	G6(1)	-	-	No-emission(1)
StHa 47	-	-	-	-	-	-	-	-	-	mid K(2)	√(0.346)	-	T Tau(2)
StHa 48	0.044	10.23	0.02	9.51	0.04	9.18	0.03	0.72	0.32	K4(1)	-	√(0.029)	T Tau(1)
StHa 49	0.226	15.67	0.09	15.24	0.12	14.79	0.00	0.42	0.45	-	√(0.802)	√(0.777)	HH(6)
StHa 52	0.004	7.40	0.03	7.42	0.06	7.29	0.03	-0.02	0.12	B1.5(3)	√(0.352)	√(0.756)	Herbig Be(1)
StHa 54	0.074	10.24	0.03	9.17	0.03	8.25	0.05	1.07	0.92	-	√(0.055)	-	T Tau(7)
StHa 55	-	-	-	-	-	-	-	-	-	-	√(0.055)	-	Carbon Star(2)
StHa 56	0.016	7.76	0.04	7.16	0.03	7.01	0.03	0.59	0.15	G2(1)	-	-	No-emission(1)
StHa 57	0.051	8.17	0.04	7.36	0.03	7.07	0.04	0.81	0.29	M3(1)	-	-	No-emission(1)
StHa 58	0.001	8.56	0.03	8.43	0.03	8.38	0.04	0.14	0.05	F0(1)	-	-	No-emission(1)
StHa 59	0.001	10.08	0.03	9.89	0.03	9.84	0.04	0.19	0.05	mid F(2)	-	-	No-emission(2)
StHa 60	-	-	-	-	-	-	-	-	-	M3(3)	√(0.161)	-	-
StHa 61	0.056	9.57	0.04	9.05	0.04	8.90	0.03	0.52	0.16	G9(1)	-	-	No-emission(1)
StHa 62	0.133	12.82	0.02	12.42	0.03	11.79	0.04	0.40	0.63	BQ[ ](2)	√(0.092)	-	BQ[ ](2)
StHa 63	0.020	10.68	0.03	9.87	0.03	9.66	0.03	0.81	0.21	-	-	-	-
StHa 64	0.208	11.21	0.04	10.72	0.04	10.64	0.04	0.49	0.08	K4(1)	-	-	No-emission(1)
StHa 65	0.006	8.25	0.04	8.02	0.02	7.98	0.03	0.22	0.05	F7(1)	-	-	No-emission(1)
StHa 66	0.002	8.21	0.03	7.64	0.03	7.55	0.04	0.56	0.09	K2(3)	-	-	-
StHa 67	0.113	9.49	0.03	8.82	0.03	8.69	0.03	0.68	0.12	Ke(2)	-	√(0.163)	-
StHa 68	0.135	9.94	0.03	9.58	0.03	9.50	0.04	0.35	0.09	-	-	-	
StHa 69	0.044	7.78	0.03	6.86	0.06	6.41	0.05	0.92	0.44	late M/C(8)	√(0.354)	-	M Giant(1)
StHa 71	0.138	11.35	0.03	11.04	0.04	11.03	0.04	0.30	0.02	G1(1)	-	-	No-emission(1)
StHa 73	0.362	14.59	0.04	14.04	0.04	13.78	0.06	0.55	0.26	-	-	-	-
StHa 75	0.027	11.11	0.04	10.81	0.04	10.76	0.03	0.30	0.05	A7(1)	-	-	No-emission(1)
StHa 76	-	-	-	-	-	-	-	-	-	M3(9)	√(0.152)	-	-
StHa 77	0.152	10.77	0.03	10.55	0.04	10.47	0.02	0.21	0.08	G2(1)	-	-	No-emission(1)
StHa 82	0.333	10.37	0.04	9.88	0.05	9.72	0.04	0.49	0.16	G6(1)	-	-	No-emission(1)
StHa 83	0.255	9.99	0.03	9.29	0.03	9.13	0.03	0.69	0.16	K4(1)	-	-	No-emission(1)
StHa 85	-	-	-	-	-	-	-	-	-	galaxy	√(0.068)	-	Seyfert I (10)
StHa 86	0.074	12.14	0.04	11.31	0.06	10.72	0.05	0.82	0.59	galaxy	√(0.174)	√(0.532)	NGC 1494 (11)
StHa 87	0.048	11.37	0.04	11.24	0.03	11.17	0.03	0.13	0.07	G6(1)	-	-	No-emission(1)
StHa 88	-	-	-	-	-	-	-	-	-	M5(1)	-	√(0.750)	No-emission(1)
StHa 91	0.084	11.62	0.03	11.21	0.04	11.17	0.04	0.42	0.04	G6(1)	-	-	No-emission(1)
StHa 94	0.245	12.44	0.08	12.76	0.03	12.82	0.05	-0.32	-0.06	G (2)	-	-	No-emission(2)

continued on next page

continued from previous page

object (1)	r (') (2)	J (3)	ϵ_J (4)	H (5)	ϵ_H (6)	K (7)	ϵ_K (8)	J-H (9)	H-K$_s$ (10)	Spec. Type(Ref) (11)	IRAS (12)	ROSAT (13)	Class of obj. (Ref) (14)
StHa 95	0.001	8.65	0.03	8.16	0.03	8.03	0.03	0.49	0.13	G6(1)	-	-	No-emission(1)
StHa 97	0.092	11.24	0.03	11.01	0.03	10.94	0.03	0.23	0.07	early F(2)	-	-	No-emission(2)
StHa 99	0.202	11.04	0.03	10.88	0.03	10.84	0.03	0.17	0.03	G2(1)	-	-	No-emission(1)
StHa 100	0.090	11.56	0.03	11.31	0.03	11.25	0.04	0.25	0.06	-	-	-	No-emission(2)
StHa 101	0.353	11.12	0.03	10.71	0.03	10.62	0.03	0.42	0.09	mid G(2)	-	-	No-emission(2)
StHa 104	-	-	-		-	-	-	-	-	M3(9)	✓(0.421)	-	-
StHa 105	0.013	10.96	0.03	10.54	0.04	10.43	0.04	0.42	0.10	-	-	-	-
StHa 106	0.075	8.89	0.03	8.27	0.03	8.07	0.05	0.62	0.20	-	-	-	-
StHa 107	0.003	8.50	0.03	8.23	0.03	8.20	0.04	0.27	0.03	F3(1)	-	-	No-emission(1)
StHa 108	0.002	8.02	0.03	7.53	0.03	7.44	0.03	0.49	0.10	G0(1)	-	-	No-emission(1)
StHa 110	0.119	10.69	0.03	10.38	0.03	10.27	0.03	0.31	0.11	G2(1)	-	-	No-emission(1)
StHa 112	0.304	9.25	0.03	8.95	0.04	8.86	0.03	0.30	0.09	early G(2)	-	-	No-emission(2)
StHa 113	0.167	11.45	0.03	11.14	0.03	11.04	0.03	0.31	0.11	early G(2)	-	-	No-emission(2)
StHa 114	0.002	9.15	0.03	9.01	0.03	8.97	0.03	0.14	0.04	-	-	-	-
StHa 116	0.165	7.02	0.02	6.22	0.02	6.03	0.04	0.80	0.19	M0(9)	✓(0.158)	-	-
StHa 117	-	-	-		-	-	-	-	-	M3(9)	✓(0.140)	-	-
StHa 118	-	-	-		-	-	-	-	-	G6(2)	✓(0.033)	✓(0.157)	T Tau(2)
StHa 119	-	-	-		-	-	-	-	-	M3(9)	✓(0.199)	-	-
StHa 120	0.165	11.50	0.03	11.27	0.04	11.18	0.03	0.23	0.09	G(2)	-	-	No-emission(2)
StHa 121	0.145	10.72	0.03	10.39	0.04	10.30	0.02	0.33	0.09	G(2)	-	-	No-emission(2)
StHa 122	0.102	9.98	0.03	9.22	0.03	8.99	0.03	0.76	0.23	mid K(2)	✓(0.190)	-	T Tau(2)
StHa 124	0.319	9.66	0.03	8.98	0.04	8.74	0.03	0.68	0.24	late K(2)	-	-	T Tau(2)
StHa 125	-	-	-	-	-	-	-	-		Me(2)	✓(0.004)	-	T Tau(1)
StHa 127	-	-	-	-	-	-	-	-		K4(1)	✓(0.052)	✓(0.127)	T Tau(4)
StHa 128	0.035	9.76	0.03	8.70	0.06	8.11	0.04	1.05	0.59	late K(4)	-	✓(0.054)	T Tau(4)
StHa 129	-	-	-	-	-	-	-	-	-	-	-	✓(0.511)	T Tau(1)
StHa 130	0.020	9.14	0.03	8.38	0.05	7.96	0.04	0.77	0.41	M1.5(4)	✓(0.124)	✓(0.048)	T Tau(4)
StHa 131	0.060	10.51	0.02	10.26	0.03	10.18	0.03	0.25	0.08	-	-	-	-
StHa 132	0.210	11.01	0.03	10.72	0.03	10.67	0.03	0.29	0.05	G(2)	-	-	No-emission(2)
StHa 133	0.001	9.26	0.03	9.18	0.03	8.99	0.03	0.08	0.19	Be(2)	✓(0.830)	-	-
StHa 134	0.002	9.08	0.03	8.98	0.04	8.93	0.03	0.09	0.05	A1(1)	-	-	No-emission(1)
StHa 135	-	-	-	-	-	-	-	-		M1(9)	✓(0.521)	-	PulsV*†(9)
StHa 138	-	-	-	-	-	-	-	-		late K(4)	✓(0.270)	-	T Tau(4)
StHa 140	0.028	9.91	0.04	9.34	0.06	9.12	0.04	0.58	0.22	mid K(2)	-	-	No-emission(2)
StHa 141	0.265	9.66	0.03	8.62	0.07	8.34	0.03	1.04	0.30	-	-	-	Mira variable(9)
StHa 143	0.133	11.76	0.03	11.72	0.03	11.64	0.04	0.04	0.08	Be(2)	-	-	-
StHa 144	-	-	-	-	-	-	-	-	-	M4(9)	✓(0.506)	-	Mira variable(9)
StHa 145	-	-	-	-	-	-	-	-	-	Be(2)	✓(0.060)	-	-
StHa 146	-	-	-	-	-	-	-	-	-	M4(9)	✓(0.012)	-	PulsV*†(9)
StHa 147	-	-	-	-	-	-	-	-	-	B1III(3)	✓(0.024)	-	P Ne‡(12)
StHa 148	0.127	9.85	0.03	9.17	0.03	8.97	0.02	0.68	0.20	K(2)	-	-	No-emission(2)
StHa 149	0.264	8.01	0.04	7.06	0.03	6.80	0.03	0.95	0.26	M2(9)	✓(0.687)	-	Symbiotic(2)
StHa 150	0.001	11.62	0.03	11.72	0.03	11.73	0.02	-0.10	-0.02	Be(2)	✓(0.668)	-	-
StHa 151	0.102	9.09	0.03	8.23	0.03	7.97	0.04	0.87	0.26	M0(9)	-	-	-
StHa 152	0.005	10.39	0.04	10.26	0.03	10.15	0.04	0.13	0.10	B3III(13)	-	-	-
StHa 153	0.052	9.41	0.03	8.61	0.03	8.41	0.04	0.80	0.19	late K(2)	-	-	No-emission(2)
StHa 154	-	-	-	-	-	-	-	-	-	M2(9)	✓(0.024)	-	Symbiotic(14)
StHa 155	-	-	-	-	-	-	-	-	-	M7(9)	✓(0.148)	-	Giant(15)
StHa 156	0.155	11.67	0.02	11.14	0.03	10.99	0.03	0.53	0.15	K(2)	-	-	No-emission(2)
StHa 157	0.184	7.23	0.03	6.29	0.03	5.96	0.03	0.94	0.33	M2(9)	✓(0.201)	-	-
StHa 161	0.001	11.01	0.03	10.88	0.03	10.74	0.04	0.12	0.14	B(3)	✓(0.079)	-	P Ne‡(16)
StHa 162	-	-	-	-	-	-	-	-	-	mid M(2)	✓(0.411)	-	No-emission(2)
StHa 163	0.087	8.76	0.03	7.87	0.07	7.57	0.04	0.89	0.30	M5(1)	-	-	No-emission(1)
StHa 165	0.197	7.07	0.03	6.17	0.02	5.74	0.03	0.89	0.43	mid M(2)	✓(0.632)	-	M Giant(1)
StHa 166	0.154	12.01	0.03	12.04	0.03	11.96	0.03	-0.03	0.07	Be(2)	-	-	-
StHa 170	0.201	10.45	0.03	9.79	0.03	9.63	0.03	0.66	0.15	-	-	-	-
StHa 171	0.094	10.49	0.03	10.11	0.03	10.11	0.03	0.38	-0.01	-	-	-	-
StHa 172	0.001	8.32	0.03	8.15	0.05	8.06	0.04	0.17	0.09	A0(3)	-	-	-
StHa 173	-	-	-	-	-	-	-	-	-	M7(9)	✓(0.086)	-	Giant(15)
StHa 174	-	-	-	-	-	-	-	-	-	M5(9)	✓(0.256)	-	-
StHa 176	0.006	10.00	0.03	9.19	0.03	9.05	0.03	0.81	0.14	-	-	-	Catacysmic(17)
StHa 177	-	-	-	-	-	-	-	-	-	M7(3)	✓(0.163)	-	Giant(15)
StHa 179	0.001	10.46	0.03	9.63	0.04	9.54	0.04	0.82	0.10	G(3)	-	-	Symbiotic(14)
StHa 180	0.285	9.60	0.03	8.69	0.04	8.51	0.03	0.91	0.19	-	-	-	Symbiotic(18)
StHa 182	0.052	8.66	0.04	8.05	0.03	7.82	0.04	0.62	0.23	M2(9)	-	-	-
StHa 184	0.158	11.07	0.03	11.13	0.03	11.01	0.03	-0.06	0.12	Be(2)	✓(0.433)	-	-
StHa 185	-	-	-	-	-	-	-	-	-	Me(2)	✓(0.213)	-	-
StHa 186	0.071	7.97	0.03	7.06	0.05	6.80	0.04	0.91	0.27	M4(9)	-	-	-
StHa 188	0.385	10.21	0.03	9.55	0.03	9.42	0.03	0.67	0.13	mid K(2)	-	-	No-emission(2)

continued on next page

continued from previous page

object (1)	r (') (2)	J (3)	ϵ_J (4)	H (5)	ϵ_H (6)	K (7)	ϵ_K (8)	J-H (9)	H-K_s (10)	Spec. Type(Ref) (11)	IRAS (12)	ROSAT (13)	Class of obj. (Ref) (14)
StHa 189	0.003	7.77	0.06	7.17	0.03	6.96	0.03	0.60	0.21	B8(3)	-	-	-
StHa 190	-	-	-	-	-	-	-	-	-	-	√(0.116)	-	Symbiotic(14)
StHa 193	0.007	11.70	0.05	11.62	0.05	11.49	0.05	0.08	0.13	-	-	√(0.067)	Catacysmic(17)
StHa 195	-	-	-	-	-	-	-	-	-	M2(9)	√(0.101)	-	-
StHa 200	-	-	-	-	-	-	-	-	-	galaxy	√(0.144)	-	Seyfert I(2)
StHa 202	0.213	9.23	0.03	8.25	0.04	7.48	0.05	0.98	0.77	mid F(2)	√(0.010)	-	T Tau(2)
StHa 203	0.220	11.23	0.03	11.00	0.03	10.98	0.03	0.24	0.02	mid F(2)	-	-	No-emission(2)
StHa 204	0.002	8.70	0.03	8.76	0.03	8.73	0.03	-0.06	0.03	A0(9)	-	-	-
StHa 205	-	-	-	-	-	-	-	-	-	B9(9)	√(0.263)	-	-

† semi-regular pulsating variable star

‡ Planetary nebula

Reference

(1) This work; (2) Downes & Keyes (1988); (3) SIMBAD Astronomical Database; (4) Herbig Bell Catalogue (1988); (5) Weaver & Hobson (1988); (6) Molinari, S & Noriega-Crespo (2002) ; (7) Torres et al. (1995); (8) Gigoyan et al. (1998); (9) Stephenson (1986); (10) Lewis (1972); (11) Allen (1976); (12) Arkhipova et al. (1999); (13) Vijapurkar (1993); (14) Munari (2002); (15) Sharples et al. (1995); (16) van de Steene & Pottasch (1995); (17) Downes et al. (1997); (18) Belczynski et al. (2000).

Bibliography

[1] Allen, D.A., 1976, ApJ, 207, 367

[2] Appenzeller, I., Krautter, J., Jankovics, I., 1983, A&AS, 53, 291

[3] Arkhipova, V. P., Ikonnikova, N. P., Noskova, R. I., Sokol, G. V., Esipov, V. F., Klochkova, V. G., 1999, AstL, 25, 25

[4] Belczynski,K., Mikolajewska, J., Munari, U., Ivison, R. J., Friedjung, M., 2000, A&AS, 146, 407

[5] Carpenter, J. M. 2001, AJ, 121, 2851

[6] Clemens, Dan P., Barvainis, Richard., 1988, ApJS, 68, 25

[7] Downes, Ronald A., Keyes, Charles D., 1988, AJ, 96, 777

[8] Downes, Ronald., Webbink, Ronald F., Shara, Michael M., 1997, PASP, 109, 345

[9] Fernandez, M., Ortiz, E., Eiroa, C., Miranda, L. F., 1995, A&AS, 114, 439

[10] Fujii, T., Nakada, Y., Parthasarathy, M., 2002, A&A, 385, 884

[11] Gigoyan, K. S., Hambaryan, V. V., Azzopardi, M., 1998, Ap, 41,356

[12] Gregorio-Hetem, J., Hetem, A., 2002, MNRAS, 336, 19

[13] Herbig, G. H., 1962, Trans. IAU, 11A, 275

[14] Herbig, G. H., Bell, K. Robbin., 1988, V/73A

[15] Hillenbrand, Lynne A., Strom, Stephen E.; Vrba, Frederick J., Keene, Jocelyn., 1992, ApJ, 397, 613

[16] IRAS catalogue of Point Sources, Version 2.0 (IPAC 1986)

[17] IRAS Faint Source Catalog, $\mid b \mid > 10^\circ$, Version 2.0 (Moshir 1989)

[18] Jacoby G.H., Hunter D.A., Christian C.A., ApJS, 1984, 56,257

[19] Kazarovets, V., Samus, N. N., Durlevich, O. V., 1998, IBVS, 4655,1

[20] Kenyon, Scott J., Fernandez-Castro, T., Stencel, R. E., 1988, AJ, 95, 1817

[21] Koornneef, J., 1983, A&A, 128, 84

[22] Lewis, B.M., 1972, IAUS, 44, 267

[23] Luhman, K. L. 2001, ApJ, 560, 287

[24] Mc Connell, D, J., 1982, A&AS, 48, 305

[25] Magnani, Blitz, & Mundy (1985) Astrophys. J., 295, 402-421

[26] Molinari, Sergio., Noriega-Crespo, Alberto., 2002, AJ, 123, 2010

[27] Munari, U., Zwitter, T., 2002, A&A, 383, 188

[28] Prabhu, T., Anupama, G, C., Surendiranath, R., BASI, 1998, 26, 383

[29] Schwope, A. D., Hasinger, G., Lehmann, I., et al., 2000, Astron. Nachr., 321, 1-52

[30] Second ROSAT PSPC Catalog (ROSAT, 2000)

[31] Sharples, R. M., Whitelock, P. A., Feast, M. W., 1995, MNRAS, 272, 139

[32] SIMBAD Astronomical Database, Strasbourg, France

[33] Stephenson, C. B., 1986, ApJ, 300, 779

[34] Stephenson, C. B., and Sanduleak, N., 1977, ApJS, 33, 459

[35] The 2MASS database (IPAC/UMass, 2000)

[36] Torres, C. A. O., Quast, G., de La Reza, R., Gregorio-Hetem, J., Lepine, J. R. D., 1995, AJ, 109, 2146

[37] van de Steene, G. C., Pottasch, S. R., 1995, A&A, 299, 238

[38] Vijapurkar, Jyotsna., Drilling, John S., 1993, ApJS, 89, 293

[39] Weaver, Wm. Bruce., Hobson, Stewart W., 1988, PASP, 100, 1443

[40] Wiramihardja, Suhardja D., Kogure, Tomokazu., Yoshida, Shigeomi., Ogura, Katsuo., Nakano, Makotom., 1989, PASJ, 41, 155,

Chapter 5

Circumstellar disks around young stellar objects: polarization, outflows and binary orbits of Herbig AeBe stars

5.1 Introduction

In Chapter 2 - 4, we have presented results of our study of some of the individual star forming clouds and a search for YSOs at high galactic latitudes. As discussed in Chapter 1 star formation in molecular cloud produces YSOs that go through different evolutionary stages and the character of this circumstellar environment changes with time. Observations of circumstellar disks around YSOs provide important constrains on the theoretical models for star formation in molecular clouds. In this chapter we study the polarization, bipolar outflows and binary orbits of Herbig AeBe stars which represents YSOs of intermediate masses (2 - 8 $M_\odot$).

Herbig AeBe stars are PMS objects of intermediate mass ($2 \leq M/M_\odot \leq 8$). In the original survey (Herbig 1960) these objects were defined as A and B stars, located in regions of known star formation, with emission in the Balmer lines of hydrogen and

---

This chapter is based on the published work: Maheswar, G., Manoj, P., Bhatt, H. C., 2002, A&A, 387, 1003.

associated with optical reflection or emission nebulosity. Herbig (1960) listed 26 objects belonging to this class. The catalogue was later expanded by Finkenzeller & Mundt (1984) to include 57 stars. The most recent catalogue by Thé et al. (1994), adopting a more extended definition, lists 109 Herbig AeBe stars and a number of candidates that include stars with later spectral types (G0 or earlier) and those found relatively isolated from star forming clouds. The PMS nature of Herbig AeBe stars is now well established, based on their position in the HR diagram and comparison with theoretical evolutionary tracks (Strom et al. 1972; Cohen & Kuhi 1979; van den Ancker et al. 1998; Palla & Stahler 1991). Infrared, submillimetre and millimetre measurements have shown that Herbig Ae/Be stars are associated with significant amounts of circumstellar dust emitting excess radiation, over that produced by stellar photosphere, at these wavelengths (eg., Rydgren et al. 1976; Cohen & Kuhi 1979; Bertout et al. 1988; Strom et al. 1988; Beckwith et al. 1990; Weintraub Sadnell & Duncan 1989; Adams et al. (1990); Hillenbrand et al. 1992). The existence of circumstellar dust is also supported by the relatively large values of intrinsic polarization observed for these objects (eg., Breger 1974; Garrison & Anderson 1978; Vrba et al. 1979; Jain et al. 1990; Jain & Bhatt 1995; Yudin & Evans 1998) which is generally ascribed to the presence of circumstellar dust grains (eg., Bastien 1987).

While the existence of circumstellar dust around Herbig AeBe stars is well established, the geometrical distribution of the dust is not yet fully clear. Hillenbrand et al. (1992), from an analysis of the spectral energy distributions (SED) of 47 Herbig AeBe stars, classified these objects into three groups. The infrared SED of the Group I objects ($\lambda F_\lambda \sim \lambda^{-4/3}$) could be explained by invoking a geometrically thin, optically thick circumstellar accretion disk with an optically thin inner region to account for the observed inflections in their near-infrared spectra. Group II objects, with flat or rising infrared spectra, consist of a star or star/disk system surrounded by gas and dust that is not confined to a disk. Group III objects have small or no infrared excess, similar to classical Be stars, and the small excesses can be ascribed to free-free emission in a gaseous envelope. Berrilli et al. (1992), on the other hand, produced models with spherically symmetric dust envelopes. Natta et al. (1993) proposed models with at least three components that contribute to the observed infrared emission: the central star, a circumstellar disk, and an extended, almost spherically symmetric, envelope. Models with symmetrical envelopes generally lead to much higher visual extinctions toward the central star than are observed.

Polarimetric measurements provide an important tool to study the nature and geometry of the circumstellar material. The integrated light from a Herbig AeBe object can have intrinsic polarization (in addition to the interstellar component) only if the distribution of the scattering material in its circumstellar regions is not spherically symmetric. Circumstellar dust distributed in a disk can cause relatively large polarization, the degree of polarization depending on the amount of scattering dust, degree of flattening of the disk and its orientation with respect to the observer's line of sight to the star. If the disk optical depth is small ($\tau \leq 0.3$) and polarization is produced by single scattering, then the position angle of the E vector of the linearly polarized light is perpendicular to the disk, while for optically thick disks the observed polarization may be dominated by optically thin scattering dust distributed perpendicularly to the disk (for example in bipolar jets and outflows) resulting in a polarization position angle that is parallel to the disk plane (eg., Brown & McLean 1977; Elsasser & Staude 1978). Polarization vectors perpendicular to the disk plane can also be obtained for scattering off the surface of optically thick disks, while polarization vectors parallel to the disk plane require the addition of an extensive circumstellar envelope (see eg., Whitney & Hartmann 1992, 1993). Some Herbig AeBe stars, similarly to their lower mass counterparts, the T Tauri stars, have also been found to exhibit bipolar optical jets and molecular outflows (eg., Canto et al. 1984; Strom et al. 1986; Corcoran & Ray 1998) which are believed to be directed perpendicular to the circumstellar disks (eg. Konigl, 1982). One may therefore expect a correlation between the position angle of polarization and the direction of the jets and outflows from the Herbig AeBe stars. In a sample of 23 T Tauri stars and other YSOs, including 8 Herbig AeBe stars, Bastien (1987) found that for about 50 to 60 % of the sources the directions of the outflow and of the polarization are within 30° of being perpendicular to each other. If only the 8 Herbig AeBe stars in their sample are considered, then the correlation is not clear. In recent years more extensive polarization measurements and observations of jets and outflows from more Herbig AeBe stars have become available. A study of the correlation between the polarization and outflow directions can now be performed on a larger sample of Herbig AeBe stars.

A relatively large fraction (as compared with that for the main-sequence field stars) of Herbig AeBe stars have been found to have binary companions (eg., Leinert et al. 1997). Are the circumstellar (or circumbinary) disks in the binary Herbig AeBe systems coplanar with the binary orbital plane? Their relative orientations may depend on the binary formation process. For example, fragmentation of rotating protostellar clouds during collapse (eg. Boss 1988) to form binary systems will favour the formation of disks that are coplanar with the orbital plane. On the other hand, formation of the binary system by capture of independent young stellar or protostellar objects (eg., Larson 1990) will not favour any such alignment. An observational study of the relative orientations of the polarization position angles, bipolar outflows and binary orbital planes may therefore be useful in discriminating between the different models for the origin of binary systems.

In this chapter we present the results of our measurements of optical linear polarization for a number of Herbig AeBe stars that are either known to be in binary systems and/or have bipolar jets. Available information on the position angles of polarization, outflows and binary companions for Herbig AeBe stars is compiled and analysed for any possible correlations. Our polarimetric observations are presented in Section 5.2. Data from the literature is compiled in Section 5.3. Various correlations are presented in section 5.4 and discussed in Section 5.5. Conclusions are summarized in Section 5.6.

5.2 Observations

Table 5.1: Polarization of the observed Herbig AeBe stars.

Object	Date of observation	P (%)	θ_p (°)	ϵ_p (%)	ϵ_θ (°)
HD 35187	03 Mar 00	0.18	128	0.07	8
GU CMa	10 Mar 99	1.19	28	0.07	2
NX Pup	02 Mar 00	1.23	38	0.23	6
Her 4636	01 Mar 00	0.77	157	0.12	6
HD 141569	29 Apr 00	0.79	82	0.05	1
HD 144432	30 Apr 00	0.47	20	0.06	4

Optical linear polarization measurements of 6 Herbig AeBe stars were made with a fast star and sky chopping polarimeter (Jain & Srinivasulu 1991) coupled at the $f/13$ Cassegrain focus of the $1m$ telescope at Vainu Bappu Observatory, Kavalur of the Indian Institute of Astrophysics. A dry-ice cooled R943-02 Hamamatsu photomultiplier tube was used as the detector. All measurements were made in the V band with an aperture of $15''$. Observations were made during the period of 1999-2000. The instrumental polarization was determined by observing unpolarized standard stars from Serkowski (1974). It was found to be $\sim 0.1\%$, and has been subtracted vectorially from the observed polarization of the programme stars. The zero of the polarization position angle was determined by observing polarized standard stars from Hsu & Breger (1982). The position angle is measured from the celestial north, increasing eastward. The Herbig AeBe stars selected for observations were taken from the Thé et al. (1994) catalogue. HD 35187 (Dunkin et al. 1998) and Her 4636 (Williams et al. 1977) satisfy all the criteria of being Herbig AeBe stars and hence we have made polarimetric observations of these objects and included them in our sample. The selected objects are either known to have outflows and/or are in binary systems. Results of our polarimetric measurements are given in Table 5.1. Columns in Table 5.1 give respectively, (1) identification of the star, (2) date of observation, (3) degree of polarization, (4) polarization position angle, (5-6) 1σ probable errors in measurements of polarization and the position angle.

5.3 Data on polarization, outflows and binary companions of Herbig Ae/Be stars

In recent years several studies on polarization, outflows and binarity of Herbig AeBe stars have become available in the literature. In Table 5.2 we list position angle of the binary companion and outflow taken from the literature. The columns give, respectively, (1) object identification, (2-3) distance and spectral type taken from the literature, (4) secondary component position angle with respect to primary measured from celestial north, (5) angular separation (*arcsec*) of the secondary from the primary star, (6) derived projected linear separation (AU) of the secondary component from the primary star, (7) the mode of detection, (8) outflow position angle, (9) references. In Table 5.3 we list polarization data on Herbig AeBe stars. The column 1 gives object identification, columns 2 and 3 give observed degree of polarization and position angle. For most of the stars measurements at multiple epochs are available. Average values are given here. Columns 4 and 6 give estimated contribution of interstellar polarization and its position angle. Contributions to the observed polarization in YSOs are primarily due to the scattering of stellar light by dust distributed in the cicumstellar environment and that due to the interstellar medium. For most of the Herbig AeBe stars being considered here, the observed polarization is dominated by the circumstellar component. The interstellar contribution becomes relatively more important for stars which have smaller circumstellar polarization either due to smaller quantities of scattering dust or due to unfavourable orientation, especially for more distant objects. We estimate the interstellar contribution to the polarization of the Herbig AeBe stars by considering the observed polarization of normal stars, at different distances in the direction of the object, from the catalogue Stellar polarization catalogs agglomeration by Heiles (2000). Around each Herbig AeBe star, a search is made for normal stars in circles of increasing angular radii. Minimum of 10 stars are used to estimate the interstellar contribution to each target star. Circles of radius 1°, 2°, 3°, 5° and 7° are used to choose the stars. If less than 10 stars are found in 7°, those stars are used. Stoke's parameters U (=P$sin2\theta$) and Q (=P$cos2\theta$) are evaluated from the degree of polarization (P) and position angle (θ) for each star. U and Q parameters thus evaluated are plotted against the distance to the respective stars. Stoke's parameters U_{ism} and Q_{ism} representing interstellar polarization at the target star's distance are estimated by making a least-square fit. The interstellar polarization value P_{ism} and position angle θ_{ism} are calculated as

$$P_{ism} = \sqrt{(U_{ism})^2 + (Q_{ism})^2} \tag{5.1}$$

$$\theta_{ism} = (1/2)tan^{-1}(U_{ism}/Q_{ism}) \tag{5.2}$$

P_{ism} and θ_{ism}, and probable errors $\epsilon_{p_{ism}}$ and $\epsilon_{\theta_{ism}}$ in their estimation, are given in columns 4, 6 and 5, 7 of Table 5.3 respectively. Stoke's parameters $U_\star$ and $Q_\star$ representing the observed polarization for the target stars are evaluated from the observed degree of polarization and position angle measured at each epoch. The Stoke's parameter U_i and

Q_i representing the intrinsic (circumstellar polarization of the target star) polarization are estimated as

$$U_i = U_\star - U_{ism} \tag{5.3}$$

$$Q_i = Q_\star - Q_{ism} \tag{5.4}$$

The intrinsic polarization P_i and position angle θ_i are then evaluated as

$$P_i = \sqrt{(U_i)^2 + (Q_i)^2} \tag{5.5}$$

$$\theta_i = (1/2)tan^{-1}(U_i/Q_i) \tag{5.6}$$

In the case of V892 Tau, HD 150193 and Par 21 not many stars are available to determine the interstellar polarization and position angle. However, we note that they have relatively high observed polarization and are at relatively smaller distances. With relatively small intrinsic interstellar contribution, the observed polarization for the stars is considered to represent their intrinsic polarization in this study. Columns 8 and 9 give average values of intrinsic degree of polarization and position angle for Herbig AeBe stars corrected for the estimated interstellar contribution. Column 10 gives number of multiple epoch observations used for each star. Columns 11 and 12 give the probable errors in the polarization and position angle values inclusive of the dispersions in the individual measurements at different epochs. The median value of dispersion in position angle is ≈ 8°. Only for some stars namely, T Ori, HD 144432, AS 477 and MWC 1080, the dispersion in position angles is found to be more than or equal to 30°. Column 13 gives various apertures used in the polarimetric measurements and column 14 gives the references.

5.4 Relationship between polarization angles, outflow directions and binary orbital planes

Various alignments between the linear polarization vector and other phenomena have earlier been looked for by several authors. The polarization vector is found to be perpendicular to the optical jets or CO molecular outflows for most sources (Mundt and

Table 5.2: Data on binarity and outflows in Herbig AeBe stars.

Object	Dis. (pc)	Sp.typ	θ_b (°)	Angular Separation ($arcsec$)	Linear Separation (AU)	Mode of detection	θ_o (°)	Ref
V633 Cas	600	A5	3	5.5	3300	Near Infrared (NIR)	160	1,11
V376 Cas	600	F0	-	-	-	-	120	3
XY Per	160	B6	255	1.2	192	NIR	-	2
V892 Tau	140	A6	23	4.1	570	NIR	-	1
UX Ori	460	A2	257	0.02	10	Optical	-	3
HD 35187	150	A2	185	1.3	195	Optical	-	10
CO Ori	460	F8	280	2.0	920	Optical	-	3
HK Ori	460	A5	42	0.3	138	NIR	160	1,12
T Ori	460	B9	73	7.7	3540	NIR	-	1
V380 Ori	460	B9	204	0.15	71	NIR	56,149	1,11
LkHα 208	1000	B7	114	0.12	120	NIR	0	1,13
GGD 18	1600	B2	254	5.8	9280	NIR	150	22,23
R Mon	800	B0	331	0.7	560	NIR	0	4,11
Gu CMa	1150	B1	189	0.7	800	Optical	-	5
Z CMa	1150	B5	123	0.1	115	NIR	60	1,14
HD 53367	240	B0	298	0.7	167	Optical	-	5
NX Pup	500	A0	62	0.13	65	NIR	-	6
HD 76534	400	B3	304	2.0	800	Optical	-	5
Her 4636	600	B2	34	3.3	1980	Optical	148	9,20
HD 141569	100	A0	312	6.8	680	NIR	-	2
HD 144432	250	A7	354	1.2	300	Optical	-	5
HR 5999	200	A0	115	1.4	280	NIR	-	1
HD 150193	150	A2	236	1.1	165	NIR	-	2
KK Oph	160	A6	247	1.5	240	NIR	-	1
HD 163296	120	A0	-	-	-	-	8	15
AS 310	2500	B0	153	4.2	11000	NIR	55	7,12
R CrA	130	F0	-	-	-	-	130	13
T CrA	130	F5	275	0.14	18	Optical	133	8,13
Par 21	400	A5	-	-	-	-	155	21
V1685 Cyg	1000	B2	23	0.14	141	Optical	-	5
MWC 349	1200	B[e]	280	2.4	2880	Optical	10	25
LkHα 234	1000	B3	315	2.7	2700	NIR	226,252	1,18,21
PV Cep	600	A5	-	-	-	-	348	16
HD 200775	400	B2	164	2.3	900	NIR	70	2,17
AS 477	900	A0	43	4.2	3762	NIR	112	2,12
LkHα 233	800	A5	-	-	-	-	50,90	13
HD 216629	725	B2	147	7.0	5046	NIR	-	1
MWC 1080	2500	B0	86	4.7	11725	NIR	60	1,19

Notes:

V380 Ori and LkHα233 have two outflow components.

LkHα234 shows an inner infrared jet at position angle 226° *and an outer optical jet at a position angle* 252° *(Cabrit et al. 1997).*

MWC 1080 is a triple systems consisting of a close unresolved spectroscopic binary and a tertiary star. Position angle of the tertiary is given here.

References:

(1) Leinert et al. 1997; (2)Pirzkal et al. 1997; (3) Bertout et al. 1999; (4) Close 1997; (5) Dommanget 1994; (6) Brandner et al. 1995; (7) Ageorges et al. 1997; (8) Bailey J. 1998; (9) Chelli et al. 1995; (10) Dunkin et al. 1998; (11) Strom et al. 1986; (12) Goodrich 1993; (13) Bastien 1987; (14) Poetzel et al. 1989; (15) Devine et al. 2000; (16) Reipurth et al. 1997; (17) Watt 1986; (18) Ray et al. 1990; (19) Poetzel et al. 1992; (20) White 1993; (21) Cabrit et al. 1997; (22) Lenzen et al. 1984; (23) Lada and Gautier 1982; (24) Meyer et al. 2001; (25) White and Becker 1985.

Table 5.3: Data on polarization in Herbig AeBe stars.

Object (1)	$\langle P_\star \rangle$ (%) (2)	$\langle \theta_\star \rangle$ (°) (3)	P_{ism} (%) (4)	$\epsilon_{P_{ism}}$ (%) (5)	θ_{ism} (°) (6)	$\epsilon_{\theta_{ism}}$ (°) (7)	$\langle P_i \rangle$ (%) (8)	$\langle \theta_i \rangle$ (°) (9)	n (10)	σ_P (%) (11)	σ_θ (°) (12)	Aperture (*arcsec*) (13)	Ref (14)
V633 Cas	1.67	25	1.24	0.26	72	6	2.30	9	3	0.26	10	10,15,8.3	1,2
V376 Cas	22.0	26	1.22	0.26	71	6	23.5	24	7	1.65	3	10,15,8.3	1,2
XY Per	1.58	126	0.15	0.39	140	52	1.45	124	7	0.07	3	10,15	3,4
V892 Tau	4.72	3	-	-	-	-	4.72	3	1	0.29	2	12	5
UX Ori	1.22	99	0.26	0.12	123	13	1.07	94	10	0.21	7	20,10	6,4
HD 35187	0.18	128	0.51	0.29	61	17	0.65	145	1	0.07	8	15	15
CO Ori	2.28	164	0.17	0.39	97	52	2.39	165	9	0.28	9	4.3,10	10,4
HK Ori	1.10	159	0.08	0.35	89	52	1.17	161	5	0.18	6	10,15,-,13	1,3,7,8,9
T Ori	0.32	94	0.15	0.16	148	32	0.28	100	11	0.10	40	10,-,13	3,7,8,9,4
V380 Ori	0.92	88	0.16	0.19	72	35	0.80	91	6	0.29	7	15,-,14.3,20	3,7,8,11,6
LkHα 208	2.28	6	1.46	0.38	172	8	1.24	25	4	0.49	11	10,15,13,-	1,9,7,8
GGD 18	3.60	81	-	-	-	-	3.60	81	1	0.50	2		24
R Mon	13.0	92	0.70	0.34	167	14	13.5	91	10	1.96	8	26,8,13,15,10	12,1,8
Gu CMa	1.25	21	0.47	0.36	146	22	1.46	29	4	0.07	4	10,15	13,14,3,15
Z CMa	0.80	125	0.36	0.32	135	26	0.67	173	5	0.26	23	10,-,20,15	3,7,8,16
HD 53367	0.53	36	0.14	0.28	152	52	0.62	41	2	0.04	1	10,15	3,8
NX Pup	1.10	47	0.28	0.13	38	13	0.82	50	2	0.21	10	20,10	15,16
HD 76534	0.61	126	0.15	0.38	88	52	0.59	133	1	0.29	11	15	3
Her 4636	0.80	159	0.12	0.06	86	14	0.90	162	2	0.05	1	-,15	22,15
HD 141569	0.57	88	1.00	0.71	86	20	0.43	175	10	0.71	20	15	4,15
HD 144432	0.30	30	0.24	2.38	36	52	0.19	172	5	2.39	52	15	4,15
HR 5999	0.52	177	0.96	0.62	17	19	0.68	121	2	0.62	19	-	29
HD 150193	4.91	59	-	-	-	-	4.91	59	6	0.51	9	15,12,20	3,4,5
KK Oph	5.10	180	0.13	0.26	179	52	4.92	180	10	1.33	8	20,10	16,4
HD 163296	0.21	59	0.70	0.45	162	19	0.76	70	13	0.45	19	15,13,27	3,17,18
R CrA	7.6	189	0.02	0.09	31	52	7.6	9	1	0.50	5	5	21
T CrA	4.59	181	0.02	0.09	31	52	4.58	1	3	2.86	11	10,15,5	1,8,21
Par 21	7.60	75	-	-	-	-	7.60	75	1	1.50	6	7	23
V1685 Cyg	1.18	14	0.16	0.46	12	52	1.02	15	6	0.08	4	15	8,3,4
MWC 349	7.70	167	3.6	0.50	100	20	10.4	174	11	1.55	4	-	25,26
	0.53	107	0.87	0.65	43	21	1.16	149	11	0.65	21	10,15,13	1,9,8,4
PV Cep	14.2	77	0.99	0.50	141	15	14.8	76	1	0.41	1		19
HD 200775	0.94	93	0.69	0.52	141	21	1.23	76	4	0.50	21	10,15	1,7,8
AS 477	1.10	35	0.49	0.58	35	34	0.84	44	5	0.41	42	10,15,13,-	1,9,3,7,20
LkHα 233	11.1	156	0.60	0.78	85	37	11.6	157	2	0.40	2	10,15	1,8
HD 216629	4.72	105	1.29	0.67	80	15	4.03	112	1	0.20	1		27
MWC 1080	2.00	75	2.18	1.00	72	13	0.42	150	10	1.00	30	10,15,13,8.3	1,9,8,28

Notes:

GGD 18: Combined K-band degree of polarization and position angle are given here.

MWC 349: The interstellar degree of polarization and position angle values are taken from Yudin (1996) and are used to remove the interstellar contribution from observed polarization values of this star.

References

(1) Hillenbrand et al. 1992; (2) Asselin, Manard and Bastien 1991; (3) Jain et al. 1995; (4) Oudmaijer et al. 2001; (5) Whittet et al. 1992; (6) Hutchinson et al. 1994; (7) Breger 1974; (8) Vrba et al. 1979; (9) Garrison and Anderson 1978; (10) Bastien 1982; (11) Bastien 1982; (12) Scarrott 1989; (13) Hall 1958; (14) Serkowski et al. 1975; (15) This work (16) Yudin and Evans 1998; (17) Barbier and Swings 1992; (18) Gnedin et al. 1992; (19) Menard and Bastien 1992; (20) Vrba 1975; (21) Ward-Thompson et al. 1985; (22) Marrco and Forte 1978 (23) Draper et al. 1985; (24) Sato et al. 1985; (25) Yudin 1994; (26) Meyer et al. 2001; (27) Heiles 2000; (28) Manset and Bastien 2001; (29) Bessell and Eggen 1972.

Fried, 1983; Nagata, Sato and Kobayashi, 1983; Hodapp, 1984; Bastien, 1987). Bastien (1987) compiled a list of 23 young outflow sources for which the central source has been found and measured its linear polarization. The list included 8 TTS, 8 HAeBe, 1FUOR, 4 YSO, and 2 objects with unknown status. The distribution of the difference of the outflow position angle, θ_{jet}, and the linear polarization position angle, θ_*, was studied and it was found that in 61% of the sources these two directions are perpendicular to each other to within 30°. This was done to distinguish between two models of the origin of polarization namely oblate configuration as in a circumstellar disk around the star and prolate configuration as in two oppositely directed jets. Both the models have the same sin^2i dependence, and hence it is difficult to distinguish between elongated and flat models. However, the polarization is usually perpendicular to the scattering plane. One expects the polarization vector to be along the axis for flat models and perpendicular to it for the elongated distribution. Thus for an outflow source, the polarization vector and the outflow position angle would be roughly parallel to each other in a flat model and perpendicular to each other for an elongated model. Also, if the source is in a binary system and if the disk as well as the orbital plane are coplanar, the polarization position angle would be roughly perpendicular to the binary position angle in a flat model and parallel to the binary position angle in an elongated model (for favoured orientations). In the following we present a study of correlation between the binary, polarization and outflow position angles in Herbig AeBe stars.

In Table 5.4, the relative orientations of binary, polarization and outflow position angles are presented for individual stars. Columns in Table 5.4 give respectively, (1) object identification, (2) $|\Delta_{po} - 90|$, where $\Delta_{po} = \theta_p - \theta_o \pm n\pi$, (3) $|\Delta_{bp} - 90|$, where $\Delta_{bp} = \theta_b - \theta_p \pm n\pi$, (4) $|\Delta_{bo} - 90|$, where $\Delta_{bo} = \theta_b - \theta_o \pm n\pi$. $\theta_b, \theta_p, \theta_o$ are the observed binary, polarization and outflow position angles respectively and π stands for 180°. In Table 5.4, 17 ($\approx$ 85%) of the 20 outflow sources have outflow position angle within 30° of being either perpendicular or parallel to the polarization position angle. Histogram (a) shown in Figure 5.1 gives the frequency distribution of the difference in polarization and outflow position angles. Sources with outflow position angle within 30° of being perpendicular to polarization position angle ($|\Delta_{po} - 90| \leq 30°$) are found to be 55%. Polarization position angle can be perpendicular to outflow if the circumstellar disk is

Table 5.4: Relative orientations of binary, polarization and outflow position angles for Herbig AeBe stars.

Object	$\lvert\Delta_{po} - 90\rvert$ (°)	$\lvert\Delta_{bp} - 90\rvert$ (°)	$\lvert\Delta_{bo} - 90\rvert$ (°)
V633 Cas	61	84	67
V376 Cas	6	-	-
XY Per	-	41	-
V892 Tau	-	70	-
UX Ori	-	73	-
HD 35187	-	50	-
CO Ori	-	25	-
HK Ori	89	29	28
T Ori	-	63	-
V380 Ori	55,32	23	58,35
LkHα 208	65	1	24
GGD 18	21	83	14
R Mon	1	30	61
GU CMa	-	70	-
Z CMa	23	40	27
HD 53367	-	13	-
NX Pup	-	78	-
HD 76534	-	81	-
Her 4636	76	38	24
HD 141569	-	47	-
HD 144432	-	88	-
HR 5999	-	84	-
HD 150193	-	87	-
KK Oph	-	23	-
HD 163296	28	-	-
AS 310	-	-	8
R CrA	31	-	-
T CrA	42	4	52
Par 21	10	-	-
V1685 Cyg	-	82	-
MWC 349	74	16	0
LkHα 234	13,13	76	27,1
PV Cep	2	-	-
HD 200775	84	2	4
AS 477	22	89	21
LkHα 233	17,23	-	-
HD 216629	-	55	-
MWC 1080	0	26	64

optically thick and the outflow is perpendicular to it. As can be seen from Table 5.3, six sources, namely, V376 Cas, GGD 18, R Mon, Par 21, PV Cep and LkHα 233 with polarization position angle perpendicular to outflow direction (within 30°) have polarization value greater than 3%. This can happen when highly polarized scattered light from the optically thin polar regions superimposed on strongly attenuated unpolarized direct light from the central star reaches the observer whose line of sight is close to being edge-on. Five sources given in Table 5.3, namely, Z CMa, HD 163296, LkHα 234, AS 477 and MWC 1080 with polarization position angle perpendicular to the outflow (within 30°) have polarization value less than 3%. This situation can arise when polarized scattered light from the optically thin polar regions superimposed on weakly attenuated direct light from the central star reaches the observer whose line of sight is relatively away from

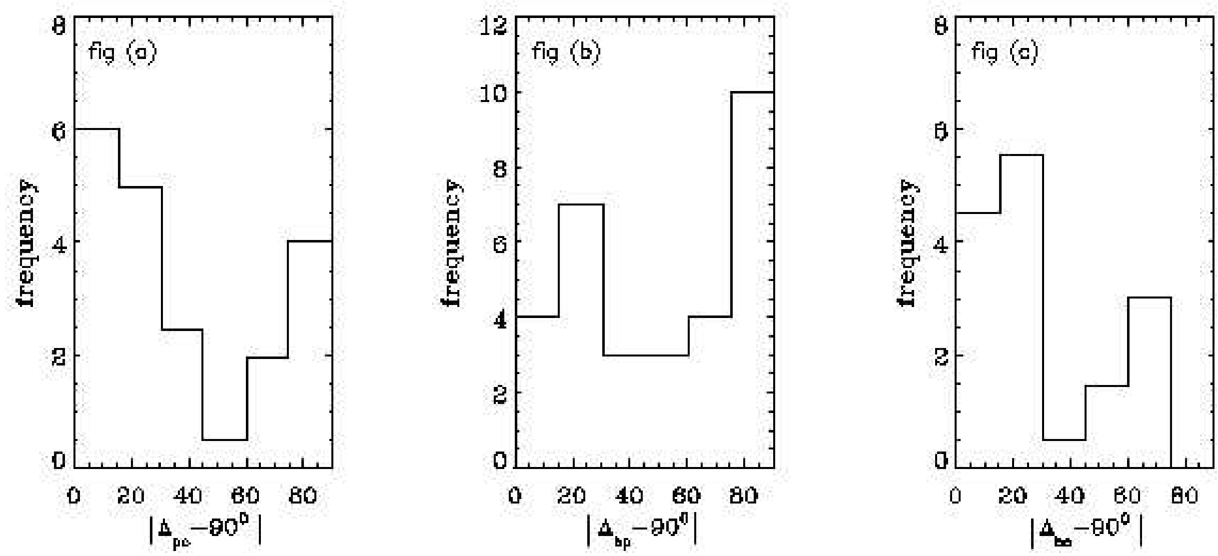

Figure 5.1: Figure (a), the frequency distribution of the difference in polarization and outflow position angles. Figure (b), the frequency distribution of the difference in polarization and binary position angles. Figure (c), the frequency distribution of the difference in binary and outflow position angles.

the equatorial region. From Table 5.4, the sources with outflow position angle within 30° of being parallel to polarization position angle ($|\Delta_{po} - 90| \geq 60°$) are found to be 30%. Such a situation can arise when star has an oblate envelope or an optically thin disk. Sources satisfying this condition namely, V633 Cas, HK Ori, LkHα 208, Her 4636 and HD 200775 have polarization values less than 3% except for MWC 349. Polarization values larger than ≈ 2% are hard to obtain owing to the presence of direct unpolarized light from the star and probably also because extremely oblate envelope do not occur (McLean & Brown, 1978). However, we note here that the interpretation in terms of optically thin dust distribution may not be correct for some of these stars. Three of these stars (HK Ori, LkHα 208 and HD 200775) were also studied by Hillenbrand et al. (1992) and were found to have Group I SEDs indicative of optically thick disks. Scattering off the surface of the optically thick disk (Whitney & Hartmann, 1992) may be responsible for the observed polarization for these objects. Among the 11 sources with polarization vectors perpendicular to the outflow, 7 are in common with Hillenbrand et al. (1992). Four of these (V376 Cas, R Mon, Par 21 and LkHα 233) show Group II SEDs indicative of optically thick disks surrounded by extended envelopes, and 3 (HD 163296, LkHα 234 and MWC 1080) show Group I SEDs. Three sources namely, V380 Ori, R CrA and T CrA have outflow position angle neither parallel nor perpendicular to the polarization position angle. This can happen when the outflow direction is not perpendicular to the circumstellar/circumbinary optically thin/thick disk. Fendt & Zinnecker (2000) showed that in some cases, protostellar jets and counter jets are misaligned and the reason they suggest for the misalignment is the bending of jets due to the motion of jet source in a binary system. Similar effects could be responsible for the outflow being neither perpendicular nor parallel to the polarization position angle in the binary systems V380 Ori and T CrA. R CrA is suggested to have an interstellar disk (Ward-Thompson et al. 1985) around it which bends the outflow originating from it. V380 Ori, LkHα 234 and LkHα 233 have outflows associated with them in two directions. Each of them is counted 1/2 in the histogram. A two sided Kolmogorov-Smirnov test shows that the frequency distribution shown in Figure 5.1(a) is different from a random distribution to 97%. In Figure 5.2 the difference in polarization and outflow position angles ($|\Delta_{po} - 90|$) is plotted against intrinsic polarization P_i. Error bars shown in Figure 5.2 result from probable errors in polarization measurements, uncertainties in the estimation for interstellar polarizarion, dispersions in multi-epoch values and the uncertainties in the outflow position angles. The probable errors in the outflow position angles are typically 5-20° (Bastien 1987) depending on the method of outflow detection (optical/NIR, radio) but are not given explicitly by the authors for most of the sources. Where not available, we have taken a value 5° for optical/NIR and 20° for radio observation. From Figure 5.2 it can be seen that objects with $|\Delta_{po} - 90| \leq 30°$ tend to exhibit large values of polarization indicative of optically thick disks with extended envelopes. These results strengthen the correlation found by Bastien (1987).

Histogram (b) in Figure 5.1 shows the frequency distribution of difference in polarization position angle and binary position angle. In Table 5.4, 25 ($\approx$ 81%) out of 31 binary systems have polarization position angle within 30° of being either perpendicular or parallel to the binary position angle. Among 31 sources, 10 ($\approx$ 32%) have polarization position angle within 15° of being parallel to the binary position angle while 45% of the sources show the two position angles parallel to within 30°. Parallelity of the two posi-

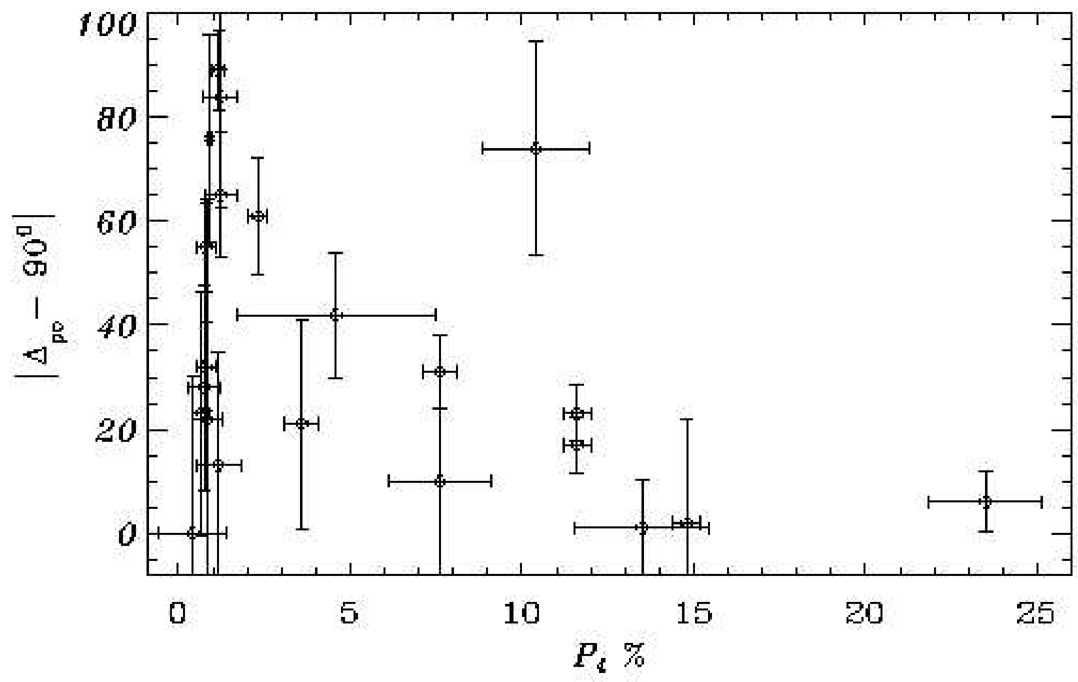

Figure 5.2: Difference in polarization and outflow position angles plotted against intrinsic polarization P_i.

tion angles can result if the binary component is coplanar with an optically thick disk since polarization arises due to the scattering of stellar light by the dust distributed in the polar regions. In 35% of the sources given in Table 5.4 polarization position angle is perpendicular to the binary position angle within 30°. This situation can arise when the binary component is coplanar with an optically thin disk where polarization arises due to the scattering of stellar light by the dust distributed in equatorial region. Alternatively, polarization could be caused by scattering off the surface of an optically thick disk (Whitney & Hartmann, 1992). A two sided Kolmogorov-Smirnov test shows that the frequency distribution shown in Figure 5.1(b) is different from a random distribution to 84%. However, the binary component position angle does not in a strict sense represent the orbital plane (except in edge-on systems) owing to the projection effects and this will weaken the correlation. We find here that there exists a correlation between binary position angle and polarization position angle inspite of the projection effect. This indicates that in actual case there exist a correlation that is even stronger than observed.

Histogram (c) in Figure 5.1 shows the frequency distribution of difference in binary and outflow position angles. Among binary systems, there are 15 sources which are associated with outflows also. It can be seen that 10 ($\approx 67\%$) of the 15 binary sources have the binary position angle within 30° of being perpendicular to outflow position angle. A two sided Kolmogorov-Smirnov test shows that the frequency distribution shown in Figure 5.1(c) is different from a random distribution to 96%. Here again it should be noted that the projection effects on the binary orbital planes would weaken even a perfect correlation (perpendicularity) between the outflow and binary position angles. So the observed correlation is relatively more significant.

The results presented in Figure 5.1, the various correlations and their interpretation discussed above must be viewed with caution as they are based on relatively small number statistics (17/20, 25/31, 10/15). In particular, for the restricted sample of binary sources with outflows, only 7($\approx 50\%$) are compatible with the interpretation of their polarization position angle relative to the outflow and binary position angles. Also, projection effects on binary orbital planes, as noted earlier, tend to reduce the observed correlations. Correlations between the different position angle differences and binary component separation were also investigated. For $|\Delta_{po} - 90|$, $|\Delta_{bp} - 90|$ and $|\Delta_{bo} - 90|$ as a function of log (projected linear separation in AU) we obtain very low linear correlation coefficients (0.26, 0.17, 0.20 respectively) indicating poor correlation.

5.5 Discussion

The geometrical relationships between binary position angle, polarization position angle and outflow position angle studied here can be compared with those expected from different mechanisms of formation of binary system, circumstellar disks and YSOs. The favoured binary formation mechanisms are: (1) capture process - in which two independently formed stars can be captured into orbits under certain conditions (Hills 1976; Boss 1988; Hills & Day 1976; Mansbach 1970); (2) fission process - in which as a star contracts towards mainsequence it spins up and the ratio of rotational to gravitational energy (β) increases. When (β) increases beyond a certain critical value, the star becomes unstable to non-axisymmetric perturbations. It has been hypothesized that breakup into orbiting subcondensations then occurs (Ruzmaikina 1981a,b; Williams & Tohline 1988); (3) fragmentation - in which a cloud that is initially differentially rotating (Myhill & Kaula 1991), or has a milder exponential-type density profile (Boss 1991), fragments. Another mode of fragmentation was suggested by Zinnecker (1990) where he proposed that since most of the interstellar clouds often show an elongated, filamentary structure, it rotates about an axis perpendicular to the cylindrical axis. After fragmentation of the cylinder (Bastein 1983) the fragments move towards each other along the cylindrical axis until they reach a keplerian orbit. This mechanism results in the formation of binary systems with wide separation; (4) disk fragmentation - in which a relatively slowly rotating protostar collapses through the adiabatic phase without fragmentation and will form a disk-like structure. Equilibrium keplerian disks around central stars have the possibility of fragmenting due to gravitational instabilities (Adams, Ruden & Shu 1989; Shu et al. 1990). In all the above mentioned binary formation mechanisms except the capture, one would expect the disk around each component or the circumbinary disk and the binary orbit to be coplanar. Results presented in this work support those binary formation mechanisms in which disk around each component or circumbinary disk and the binary orbital plane are coplanar. While polarization position angle could be either parallel or perpendicular to the circumstellar disk depending on the optical depth and the presence of extended envelopes, the outflow direction is expected to be always perpendicular to the disk. If the disks are coplanar with binary orbital plane, then the outflow position angle should be perpendicular to the binary position angle except for any projection effect. From Table 5.4 it is seen that out of 15 outflows listed here 10 of them have difference in binary component and outflow to be within 30° of being perpendicular to each other. The polarimetric observations used in this work have generally been made with large apertures ($\approx 10 - 15''$) encompassing both the components of the Herbig AeBe binaries (with typical angular separation of $\leq 2''$). Since the optical light is dominated by the primary component the observed polarization is determined by the distribution of scattering matter around it. The outflow in a binary Herbig AeBe star could be driven by either the primary or even the secondary which is generally a low mass infrared object, having its own circumstellar disk. The results on the correlations between the various position angles discussed above therefore indicate coplanarity of the disks around the individual components. For low mass T Tauri binaries, polarimetry on individual component stars (Jensen et al. 2000; Wolf et al. 2001 and Monin et al. 2000) have shown that in a majority of the binary systems the linear polarization vectors from individual stars are within 30° of being parallel. Resolved polarimetric measurements of the Herbig AeBe binary components will be needed to confirm the results presented here.

5.6 Conclusions

Circumstellar matter around Herbig AeBe stars causes polarization in the light from these objects due to scattering from dust. The position angle of the observed polarization depends on whether the scattering is dominated by optically thin disk or by optically thin/thick scattering dust distributed perpendicularly to an optically thick disk. Bipolar outflows are generally constrained to be perpendicular to the disks. In binary Herbig AeBe stars, the binary orbital plane may also be correlated with the polarization and outflow directions if the binary formation mechanism derives the binary orbital angular momentum and the individual star's circumstellar disk from the angular momentum of the same rotating clouds. In this chapter we have studied the observed correlation between the different position angles. Our results can be summarized as follows:

- Out of 20 outflow sources, 17 sources ($\approx$ 85%) have the outflow position angle within 30° of being either parallel or perpendicular to the polarization position angle.

- In 25 ($\approx$ 81%) out of 31 sources, the direction of binary position angle is within 30° of being either parallel or perpendicular to the polarization position angle.

- In 10 ($\approx$ 67%) out of 15 outflow sources, the binary position angle is within 30° of being perpendicular to the outflow position angle.

These results are consistent with binary star formation senarios in which the circumstellar disk planes are parallel to the binary orbital plane. However, it must be noted that these results are subject to small number statistics as they are based on samples that are small and need to be enlarged.

Bibliography

[1] Adams, F. C., Emerson J. P., & Fuller G. A., 1990, ApJ 357, 606

[2] Adams, F. C., Ruden, S. P., Shu, F. H., 1989, ApJ 347, 959

[3] Ageorges, N., Eckart, A., Monin, J. -L., Menard, F., 1997, A&A 326, 632

[4] Asselin, L., Menard, F., Bastien, P., 1996, ApJ 472, 349

[5] Bailey, J., 1998, MNRAS 301, 161

[6] Barbier, R., Swings, J. P., 1982, IAUS 98, 103

[7] Bastien, P., 1982, A&AS 48, 159

[8] Bastien, P., 1982, ApJS 59, 277

[9] Bastien, P., 1983, A&A 119, 109

[10] Bastien, P., 1987, ApJ 317, 231

[11] Beckwith, S. V. W., Sargent, A. I., Chini, R. S. & Gusten, R. 1990, AJ 99, 924

[12] Berrilli, F., Corciulo, G., Ingrosso, G. et al., 1992, ApJ 398, 254

[13] Bertout, C., Basri, G. & Bouvier, J., 1988, ApJ 330, 350

[14] Bertout, C., Robichon, N., Arenou, F., 1999, A&A 352, 574

[15] Bessell and Eggen, 1972, ApJ 177, 209

[16] Boss, A. P., 1988, ComAp 12, 169

[17] Boss, A. P., 1991, Nature 351, 298

[18] Brandner, W., Bouvier J., Grebel E. K., et al., 1995, A&A 298, 818

[19] Breger, M., 1974, ApJ 188, 53

[20] Brown, J. C., & McLean I. S., 1977, A&A 57, 141

[21] Cabrit, S., Lagage, P. -O., McCaughrean, M., Olofsson, G., 1997 A&A 321, 523

[22] Canto, J., Rodriguez, L. F., Calvet, N., Levreault, R.M., 1984, ApJ 282, 631

[23] Chelli, A., Cruz-Gonzalez I., Reipurth B., 1995 A&As 114, 135

[24] Close, L. M., Roddier, F., Hora J. L,. et al., 1997, ApJ 489, 210

[25] Cohen, M., Kuhi, L. V., 1979, ApJS 41, 743

[26] Corcoran, M. & Ray, T. P., 1998, A&A 336, 538

[27] Devine, D., Grady, C. A., Kimble, R. A., et al., 2000, ApJ 542, L115

[28] Dommanget J., Nys O., 1994, CoORB (Components of Double and Multiple stars,CCDM) 115, 1D

[29] Draper, P. W., Warren-Smith, R. F., Scarrott, S. M., 1985, MNRAS 212 P1

[30] Dunkin, S. K., Crawford, I. A., 1998, MNRAS 298, 275

[31] Elsasser, H. & Staude, H. J., 1978, A&A 70, L3

[32] Fendt, C., Zinnecker, H., 2000, IAUS 200, 112

[33] Finkenzeller, U., Mundt, R., 1984, A&AS 55, 109

[34] Garrison, L. M. & Anderson, C. M., 1978, ApJ 221, 601

[35] Gnedin, Y. N., Kiselev, N. N., Pogodin, M. A., Rozenbush, A. E., Rozenbush, V. K., 1992, SvAL 18, 182

[36] Goodrich, R. W., 1993, ApJS 86, 499

[37] Hall, J. S., Pub. U.S.Naval Obs. 17/VI

[38] Herbig, G. H., 1960, ApJS 4, 337

[39] Heiles, C., 2000, AJ 119, 923

[40] Hillenbrand, L. A., Strom, S.E., Vrba, F. J. & Keene, J., 1992, ApJ 397, 613

[41] Hills, J. G., 1976, MNRAS 175, 1

[42] Hills, J. G., and Day, C. A., 1976, ApL 17, 87

[43] Hodapp, K. -W., 1984, A&A 141, 255

[44] Hsu, J. C. & Breger, M., 1982, ApJ 262, 732

[45] Hutchinson, M. G., Albinson, J. S., Barrett, P., et al. 1994 A&A 285, 883

[46] Jain, S. K., Bhatt, H. C. & Sagar R., 1990, A&AS 83, 237

[47] Jain, S. K. & Bhatt, H. C., 1995, A&AS 111, 399

[48] Jain, S. K. & Srinivasulu, G., 1991, opt. Eng. 30, 1415

[49] Jensen, Eric, L. N., Donar, Arianne X., Mathieu, Robert D., 2000, IAUS 200, 85

[50] Konigl, A., 1982, ApJ 261, 115

[51] Lada, C. J., Gautier, T. N., 1982 ApJ 261, 161

[52] Larson, R. B., 1990, in Physical processes in fragmentation and star formation, eds. R. Capuzzo-Dolcetta et al., Kluwer, Dordrecht 389

[53] Leinert, C., Richichi A., Haas M., 1997, A&A 318, 472

[54] Lenzen, R., Hodapp, K. -W., Reddmann, T., 1984, A&A 137, 365

[55] Mansbach, P., 1970, ApJ 160, 135

[56] Manset, N., Bastien, P., 2000, AJ 120, 413

[57] Marraco, H. G., Forte, J. C., 1978 ApJ 224, 473

[58] McLean, I. S., Brown, J. C., 1978 A&A 69, 291

[59] Menard, F., Bastien, P., 1992, AJ 103, 564

[60] Meyer, M. J., Nordsieck,K. H., Hoffman, J. L., 2001, 2002, AJ, 123, 1639

[61] Monin,J.-L., Menard, F., Peretto, N., 2001, The Messenger 104, 29

[62] Mundt, R., and Fried, J. W., 1983, ApJ 274, L83

[63] Myhill, E. M., Kaula, W. M., In NASA, Washington, Reports of Planetary

[64] Geology and Geophysics Program, 1990, 420

[65] Nagata, T., Sato, S., Kobayashi, Y., 1983, A&A 119, L1

[66] Natta, A., Palla, F., Butner, H.M., et al., 1993, ApJ 406, 674

[67] Oudmaijer, R. D., Palacios, J., Eiroa, C., et al., 2001, A&A 379, 564

[68] Palla, F., Stahler S. W., 1991, ApJ 375, 288

[69] Pirzkal, N., Spillar, E. J., Dyck, H. M., 1997, ApJ 481, 392

[70] Poetzel, R., Mundt, R., Ray, T. P., 1989, A&A 224, L13

[71] Poetzel, R., Mundt, R., Ray, T. P., 1992, A&A 262, 229

[72] Ray, T. P., Poetzel, R., Solf, J., 1990, ApJ 357, L45

[73] Reipurth, Bo., Bally, J., Devine, D., 1997, AJ 114, 2708

[74] Ruzmaikina, T.V., 1981a, Adv. Space Res. 1, No 7, 49

[75] Ruzmaikina, T.V., 1981b, Pisma Astr. J. U.S.S.R. 7, 188

[76] Rydgren, A.E., Strom, S. E. & Strom K.E., 1976, ApJS 30, 307

[77] Sato, S., Nagata, T., Nakajima, T., et al., 1985, ApJ 291, 708

[78] Scarrott, S. M. Draper, P. W., Warren-Smith, R. F., 1989 MNRAS 237, 621

[79] Serkwoski, K., 1974, in Planets, Stars and Nebulae studied with photopolarimetry, ed. T. Gehrels, Univ. Arizona Press, Tucson 135

[80] Serkwoski, K., Mathewson, D. S., Ford, V. L., 1975, ApJ 196, 261

[81] Shu, F.H., Tremaine, S., Adams, F.C., and Ruden, S.P., 1990, ApJ 358, 495

[82] Strom, K. M., Strom, S. E., Kenyon S. J. & Hartmann L., 1988, AJ 95,534

[83] Strom, K. M., Strom, S. E., Wolff S. C., Morgan J. & Wenz M., 1986, ApJS 62, 39

[84] Strom, S. E., Strom, K. M., Yost J. Carrasco L., Grasdalen G., 1972, ApJ 173, 353

[85] Thé, P. S., de Winter D., Pe'rez M.R. 1994, A&AS 104, 315

[86] van den Ancker, M.E., de Winter, D., Tjin A Djie, H. R. E., 1998, A&A 330, 145

[87] Vrba, F. J., 1975, ApJ 195, 101

[88] Vrba, F. J., Schmidt, G. D., Hintzen, P. M., 1979, ApJ 227, 185

[89] Ward-Thomson, W. D., Warren-Smith, R. F., Scarrott, S. M., 1985, MNRAS 215,537

[90] Watt, G. D., Burton, W. B., Choe, S. U., Liszt, H. S., 1986, A&A 163, 194

[91] Weintraub, D. A., Sadnell G. & Duncan W.D., 1989 ApJ 340, L69

[92] White, G. J., 1993, A&A 274, L33

[93] White, R. L., Becker, R. H., 1985 ApJ 297, 677

[94] Whittet, D. C. B., Martin, P. G., Hough, J. H., et al., 1992, ApJ 386, 562

[95] Whitney, B. A., Hartmann Lee, 1992, ApJ 395, 529

[96] Whitney, B. A., Hartmann Lee, 1993, ApJ 402, 605

[97] Williams, P. M., Brand P. W. J. L., Longmore A. J, et al. 1977, MNRAS 180, 709

[98] Williams, H. A., and Tohline, J. E., 1988, ApJ 334, 449

[99] Wolf, S., Stecklum, B., Henning, Th., 2001.IAUS 200, 295

[100] Yudin, R., 1994, ASP con. 62, 82

[101] Yudin, R. V., 1996, A&A 312, 234

[102] Yudin, R. V. & Evans A., 1998, A&AS 131, 401

[103] Zinnecker, H., 1990, in Low Mass Star Formation and Pre-Main-Sequence objects, ed. B. Reipurth, 447

Chapter 6

Summary

In this thesis, we have studied star forming cometary globules, as examples of triggered star formation, and the properties of young stellar objects associated with these and other galactic star forming regions. The cometary globules which are studied in this thesis are chosen from an updated list of CGs, presented in chapter 1, prepared from the literature survey and from a search made by us using 100μm IRAS images to identify additional clouds with cometary morphology. From the search we have identified the cometary shape of a cloud LBN 131.54-08.16.

In chapter 2 we have presented a detailed study carried out on cometary globule CG 12. This chapter is subdivided into three parts: Part I, Part II and Part III.

In Part I, we have determined the distance to CG 12 using a method which is based on the broad-band optical and near-IR photometry. In this method, we compute intrinsic colour indices of stars projected towards the direction of the cloud by dereddening the observed colour indices using various trial values of extinction A_V and a standard extinction law. These computed intrinsic colour indices for each star are then compared with the intrinsic colour indices of normal main-sequence stars and a spectral type is assigned to the star for which the computed colour indices best match with the standard intrinsic colour indices. Distances (d) to the stars are determined using the A_V and absolute magnitude (M_V) corresponding to the spectral types thus obtained. A distance versus extinction plot is made and the distance at which A_V undergoes a sharp rise is taken to be the distance to the cloud. Using this method we have estimated a distance of 550 pc to CG 12. This distance to CG 12 implies that it is at a height of $\sim$ 200 pc above the Galactic midplane.

In Part II, we have presented a polarization map representing the geometry of the magnetic field lines in CG 12 by making optical linear polarization measurements of stars projected towards the region containing the cloud. We find that in the lower-density outer parts of the cloud, the field is more or less parallel to the cometary tail, with position angle $\theta \sim 130°$. The orientation of other elongated structures, like the bipolar molecular outflow from near the infrared source IRAS 13547-3944 and the nebulosity around star 2 embedded in the cloud are also found to be in the same direction. Polarization vectors for the more highly reddened stars in the head region of the globule are found to be more or less parallel to the long axis of the elliptical, high-density $C^{18}O$ core of the CG head, with position angle $\theta \sim 7°$. This indicates that the orientation of magnetic field in the high-density core is parallel to the long axis of the CG head. These results show that the expanding supernova remnant, suggested to have caused the cometary morphology of CG 12, which blew the lower density outer parts of the globule into a cometary tail is likely to have dragged the ambient magnetic field lines in the same direction while the original magnetic field in the higher density inner parts of the globule head is preserved.

In Part III, the results of a multi-wavelength study carried out to investigate the cloud morphology and star formation activity in CG 12 are presented. We have made the dust colour temperature (T_d), optical depth and extinction maps of CG 12 using IRAS data. T_d computed from the long-wavelength flux ratio ($F_{60\mu m}/F_{100\mu m}$) in CG 12 varies from 21 to 33 K. T_d is found to peak at the position of $h4636$. The minimum value of the T_d is found towards the north of $h4636$ which coincides with the peak emission of $C^{18}O$. T_d towards the tail region is found to be nearly constant at 24 - 25 K. The influence of $h4636N$, the most luminous star in CG 12, was found to be negligible in heating the dust towards the tail. Of the four stars associated with nebulosities, only northern component of the double star $h4636$ shows emission features in its spectrum. We find B4 and B7 spectral types for the northern and southern components of the double star $h4636$. The northern component, $h4636N$ shows Hα and Hβ Balmer lines in emission, whereas, these lines are in absorption in the southern component, $h4636S$. The presence of Hα and Ca II triplet lines ($\lambda\lambda$8498, 8542, 8662) in emission and O I λ7774 ($W_\lambda \sim 2.3$ Å) in absorption in the spectrum of $h4636N$ are presented as evidence for an extended, highly turbulent envelope or disk around it. Combining both spectroscopic and photometric evidences, we conclude that both $h4636N$ and $h4636S$ have significant amounts of circumstellar material probably in shell geometries. The presence of an additional disk around $h4636N$ is highly likely through which the star is still accreting matter. We have identified a number of of PMS star candidates which are in addition to those already known towards CG 12 [a couple of near-IR embedded sources detected by Santos et al. (1998) and molecular outflow source by White (1993)]. We have selected 7 sources as the probable PMS star candidates with $K < 14$ magnitude, on the basis of their locations in $J-H$, $H-K$ colour-colour (c-c) and K, $J-K$ colour magnitude (c-m) diagrams. Again on the basis of the locations of X-ray sources found towards CG 12 in $J-H$, $H-K$ c-c and K, $J-K$ c-m diagrams, we have identify 3 X-ray detections which are found inside the cloud boundaries and not identified with previously known sources and 5 X-ray detections located outside the cloud boundaries as the low-mass PMS star candidates with their ages in the range 1 - 7 Myr. More recent radio maps confirm the existence of an HI shell centred at $l = 315°, b = 30°$ with CG 12 near its boundary and its tail pointing away from the centre of the shell. As suggested by Williams et al. (1977) a supernova explosion near the centre of the HI shell may have been responsible for the cometary morphology and triggering star formation in CG 12 with a relatively high efficiency ($\gtrsim$ 16 % to as large as $\sim$ 33 %). The spatial distribution of the PMS star candidates and the sources already recognized as PMS stars or candidates indicate a wave of star formation with X-ray sources which are lying outside the cloud boundaries might have formed first due to the initial trigger and then propagated inside the CG head where star formation is still continuing.

In chapter 3 we have presented the results from an investigation carried out to study the maximum luminosity of young stellar objects as a function of the parent cloud mass in CGs and then compared them with those in isolated dark clouds (opacity class 6). Protostars (IRAS sources) forming in CGs are found to be more luminous than those in opacity class 6 clouds which are relatively more isolated and away from the influences of any external forces. The mass of the most luminous visible stars currently associated with CGs, whose masses were estimated from the their spectral types, are found also to be larger. These results suggest that the external forces which are responsible for the cometary morphology have also influenced the internal properties as well as the star formation in CGs.

In chapter 4, the results of a study which was aimed at identifying potential high galactic latitude YSO candidates among Stephenson Hα objects on the basis of our spectroscopic observations, near-infrared excess form 2MASS observations and their detection in IRAS and/or ROSAT observations are presented. The YSOs amongst StHα stars that are already known or confirmed as such in this study (StHα 48), and objects (StHα 52, 125 and 129) suggested in this study to be YSOs all belong to well known star-forming regions like Taurus, Orion and Ophiuchus. YSOs at high galactic latitudes in other parts of the sky are therefore rare.

In chapter 5, we present the results of an investigation carried out to understand the geometrical relationship between the distribution of circumstellar matter, observed optical linear polarization, outflows and binary orbital planes in Herbig Ae/Be stars which are young stellar objects with masses ranging between $2M_{\odot} - 8M_{\odot}$. In 25 ($\approx 81\%$) out of 31 sources, the direction of binary position angle is within 30° of being either parallel or perpendicular to the polarization position angle. In 10 ($\approx 67\%$) out of 15 outflow sources, the binary position angle is within 30° of being perpendicular to the outflow position angle. These results indicate the presence of correlations between the position angles of polarization, outflows and binary companions for Herbig Ae/Be stars. These results are consistent with binary star formation scenarios in which the circumstellar disk planes are parallel to the binary orbital plane.

Appendix A

Spectra of stars associated with CGs

In this appendix we present the instrumental setup used for the spectroscopic observations of the stars associated with CGs and their spectra discussed in chapter 3. In Table A.1, the columns give: (1) the telescope and the instrumental setup used for the observations, (2) the objects observed using the setup. The object identifications are same as given in the text of chapter 3. The H_α source found adjecent to L1622 star 1 was extracted from the slit-less spectrum of the field containing L1622 star 1.

Table A.1: Instrumental setup used for the spectroscopic observations of stars associated with CGs.

Telescope and instrumental setup	Object observed with the setup
HCT + HFOSC slit width $\sim 2''$ Resolution $(\lambda/\Delta\lambda) \sim 2000$	LBN 131.54-08.16 (star 1 & 2), L1616 (stars 1, 2a, 2b, 3), CPM 16 (1 & 2) L1622 (stars 2, 3, 4, 5 & 8) LkH$_\alpha$ 230, LkH$_\alpha$ 231, LkH$_\alpha$ 232, LkH$_\alpha$ 230
VBT + OMR slit width $\sim 2''$ Resolution $(\lambda/\Delta\lambda) \sim 1200$	RNO 6, L1616 (stars 1, 4, 5, 6, & 7), NX Pup, Sao 53209

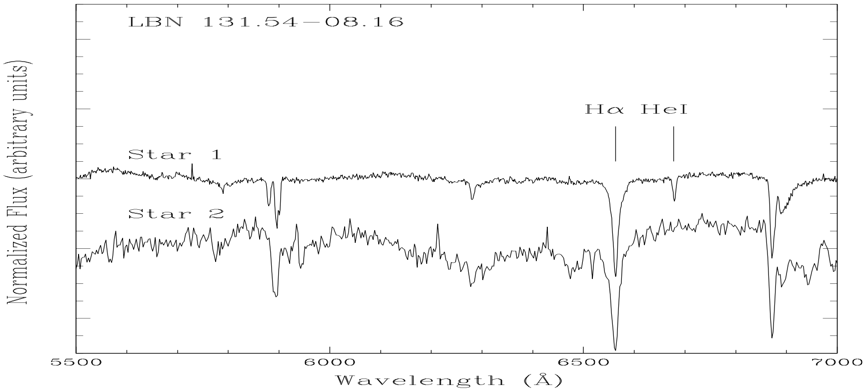

Figure A.1: Spectrum of stars found towards LBN 131.54-08.16 which are marked as 1 and 2 in Figure 3.3.

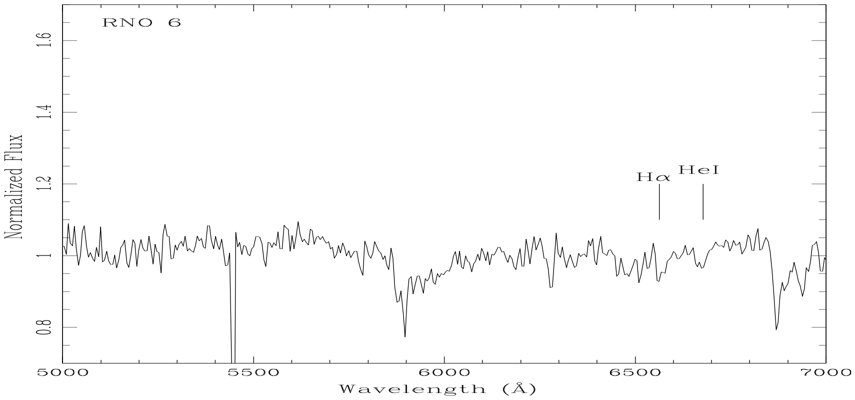

Figure A.2: Spectrum of RNO 6.

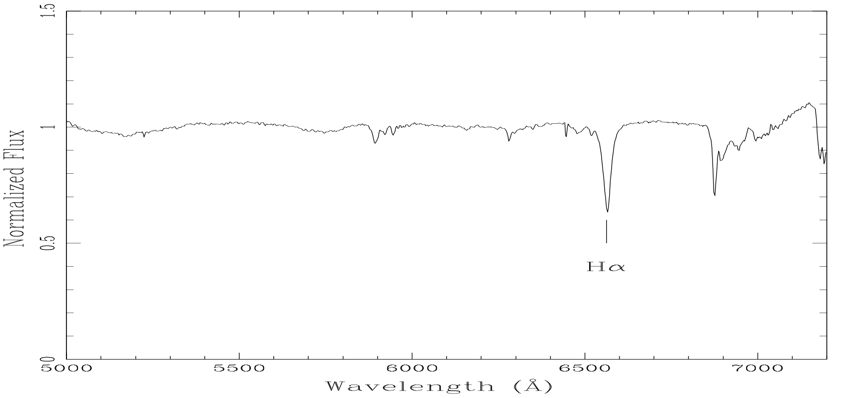

Figure A.3: Spectrum of L1616 - 1.

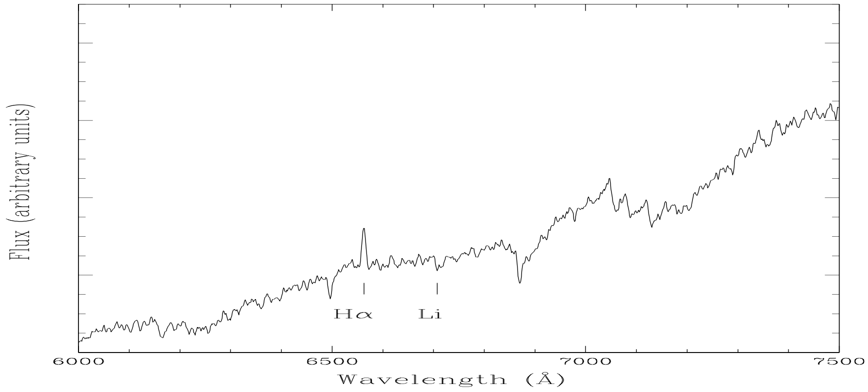

Figure A.4: Spectrum of L1616 - 2a.

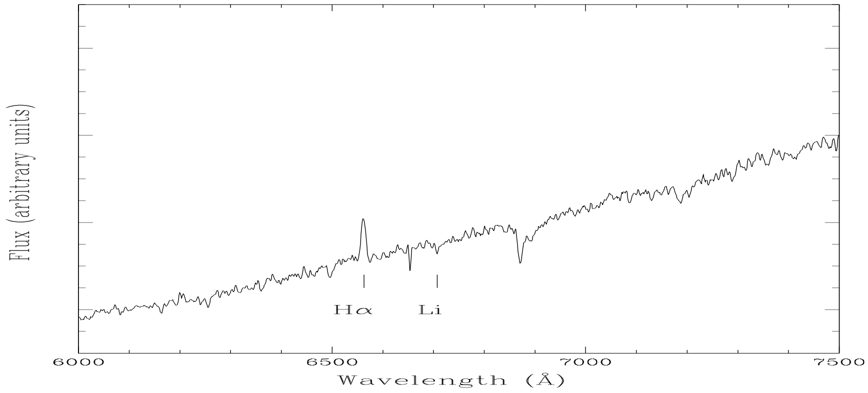

Figure A.5: Spectrum of L1616 - 2b.

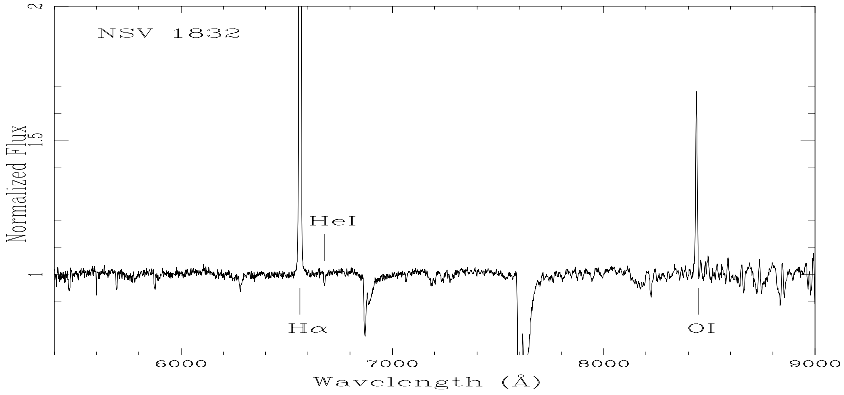

Figure A.6: Medium resolution spectrum of NVS 1832 in the range 5400-9000 Å.

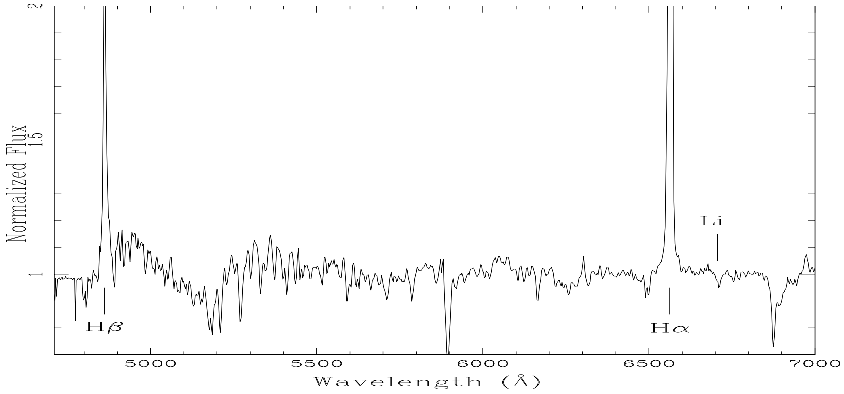

Figure A.7: Spectrum of L1616 - 4.

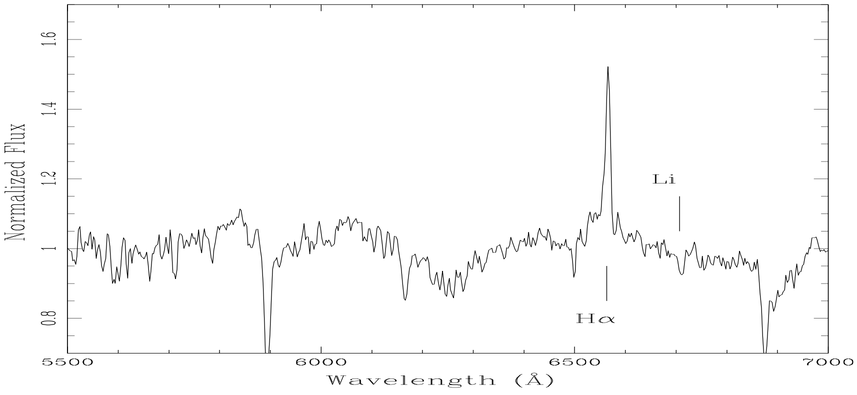

Figure A.8: Spectrum of L1616 - 5.

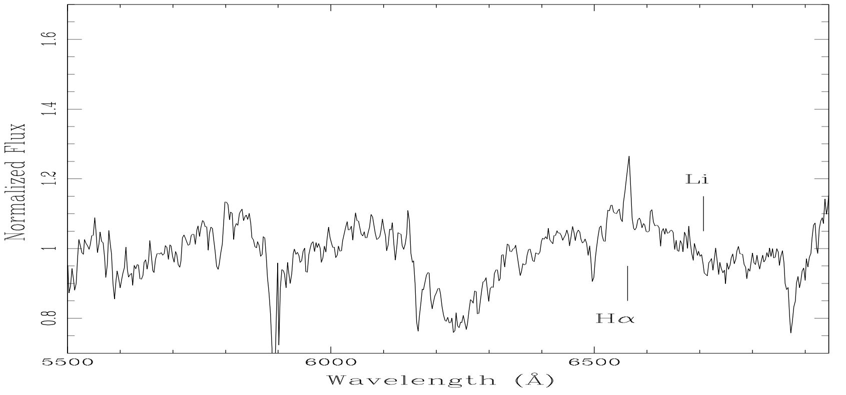

Figure A.9: Spectrum of L1616 - 6.

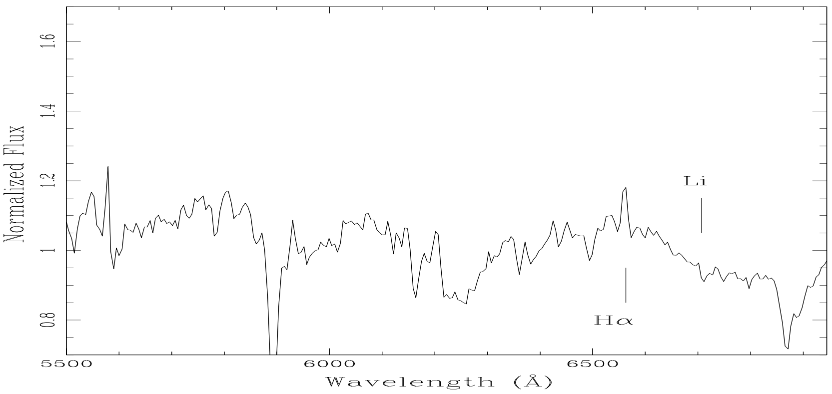

Figure A.10: Spectrum of L1616 - 7.

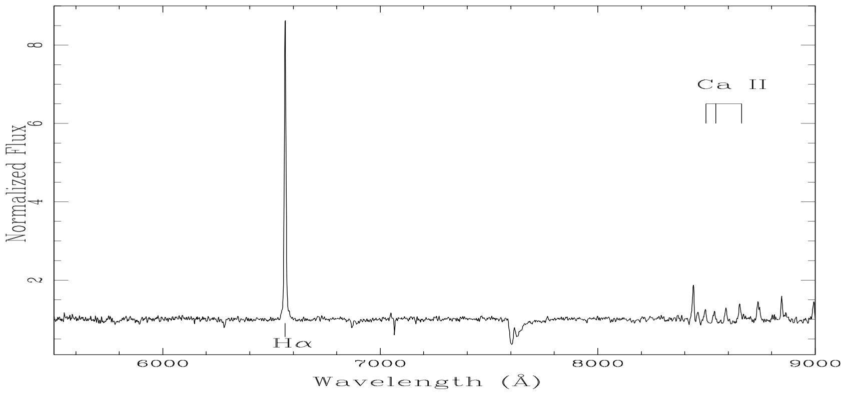

Figure A.11: Spectrum of CPM 16 - 1.

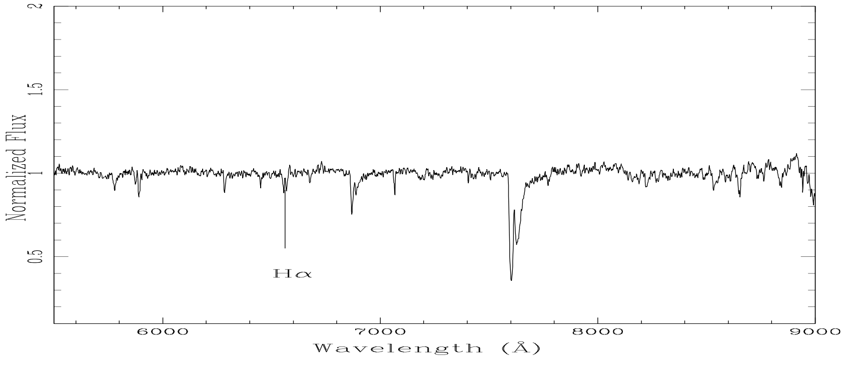

Figure A.12: Spectrum of CPM 16 - 2.

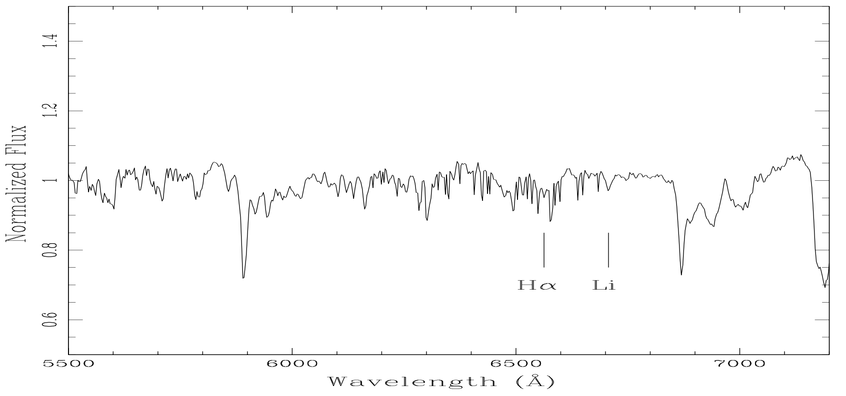

Figure A.13: Spectrum of L1622 - 1.

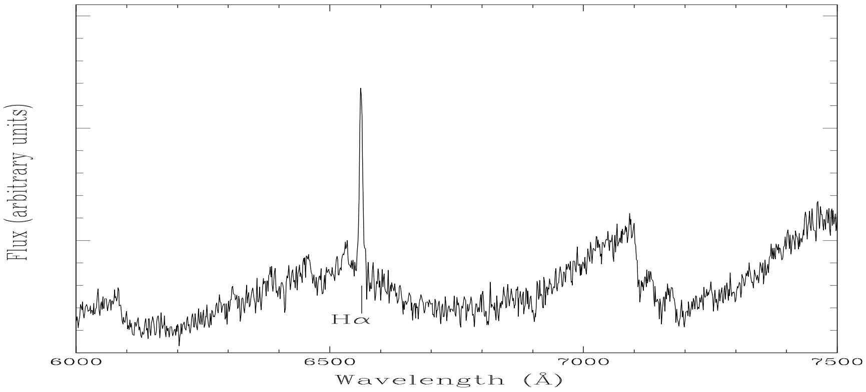

Figure A.14: Spectrum of star adjecent to star 1 which was identified as Hα emission source by Ogura & Hasegawa (1983).

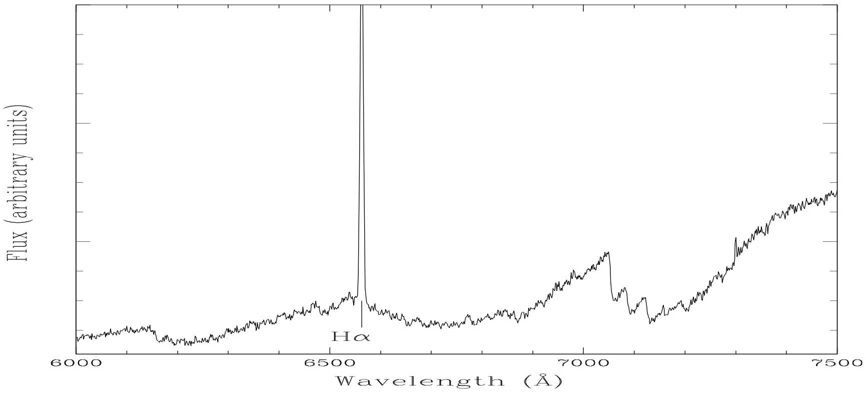

Figure A.15: Spectrum of L1622 - 2.

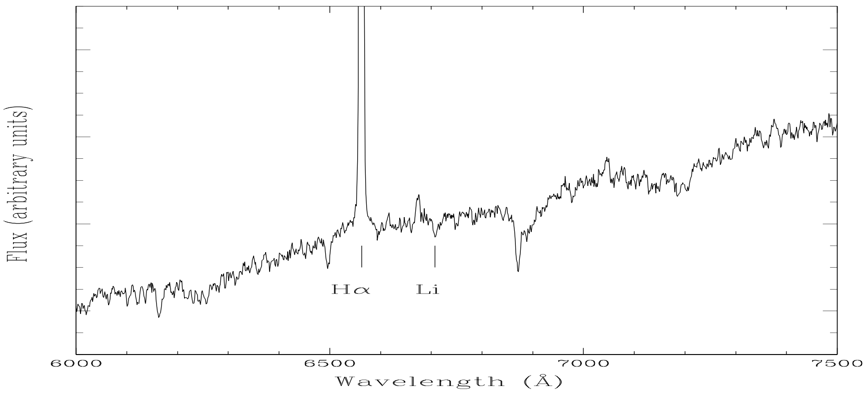

Figure A.16: Spectrum of L1622 - 3.

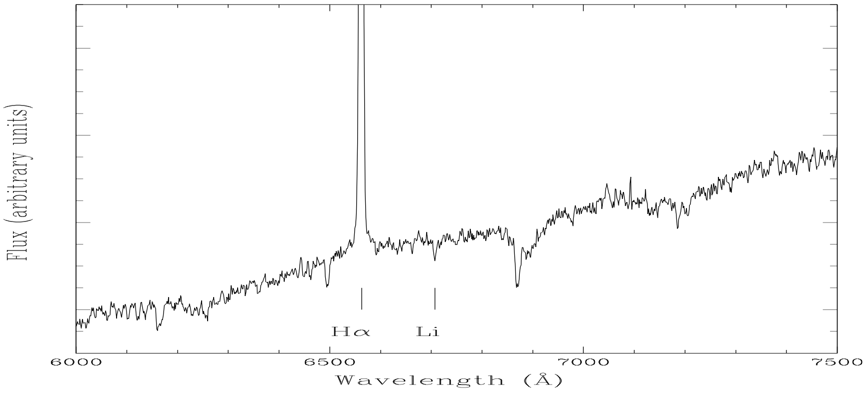

Figure A.17: Spectrum of L1622 - 4.

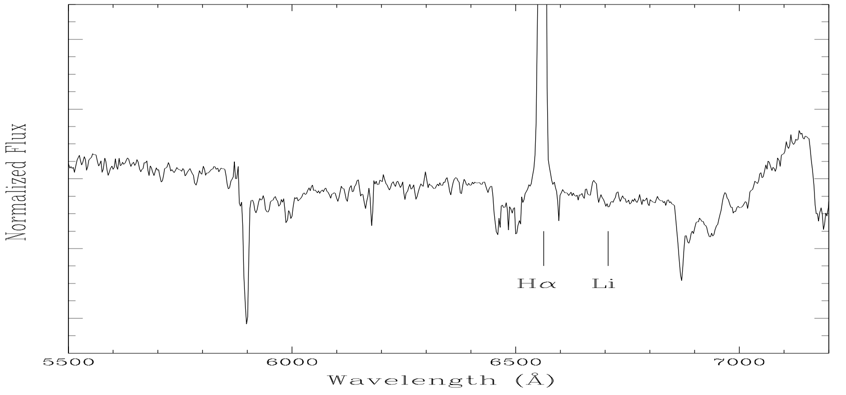

Figure A.18: Spectrum of L1622 - 5.

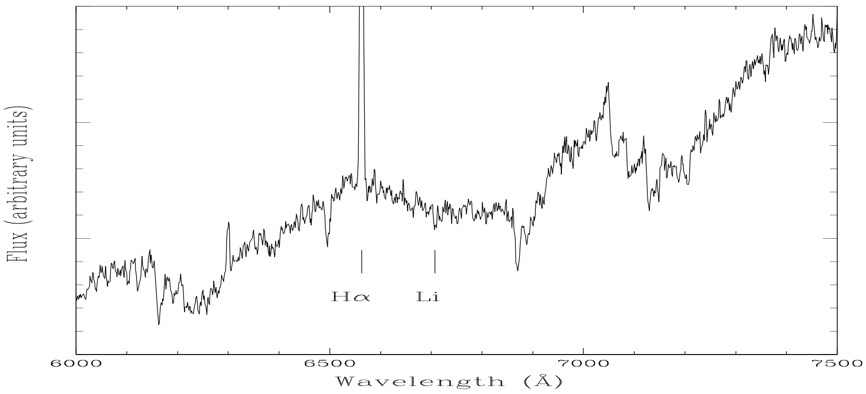

Figure A.19: Spectrum of L1622 - 8.

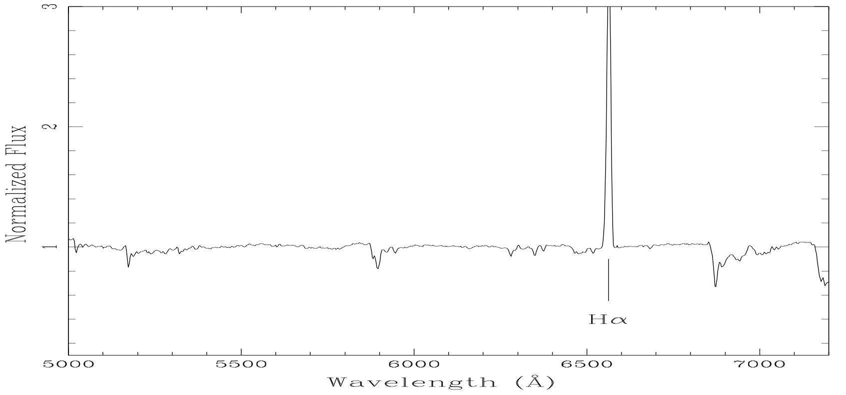

Figure A.20: Spectrum of Nx Pup.

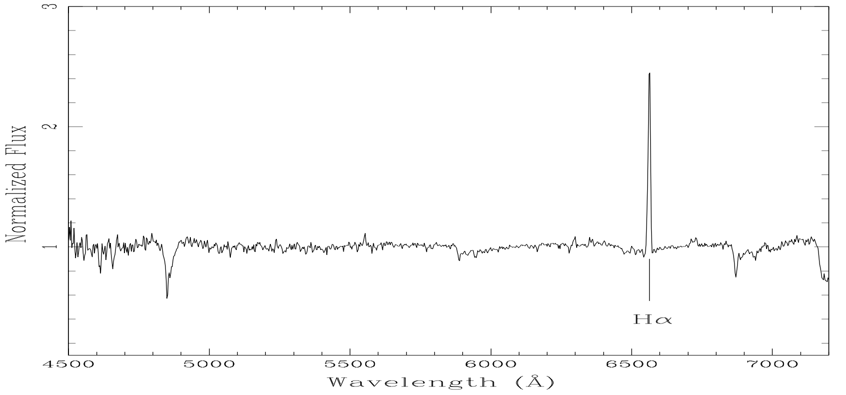

Figure A.21: Spectrum of LkHa 233.

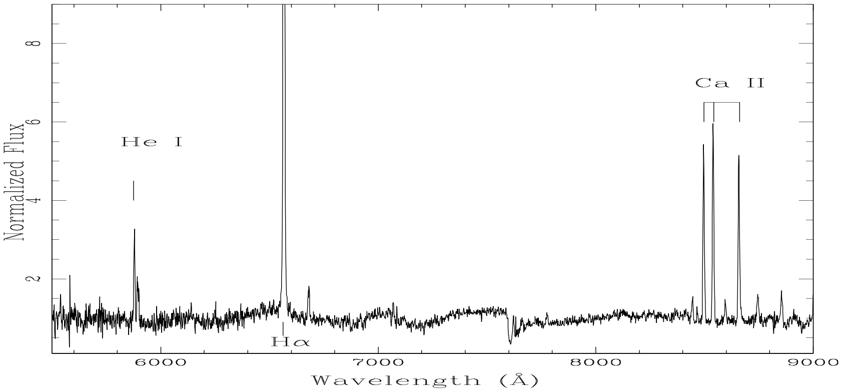

Figure A.22: Spectrum of LkHa 230.

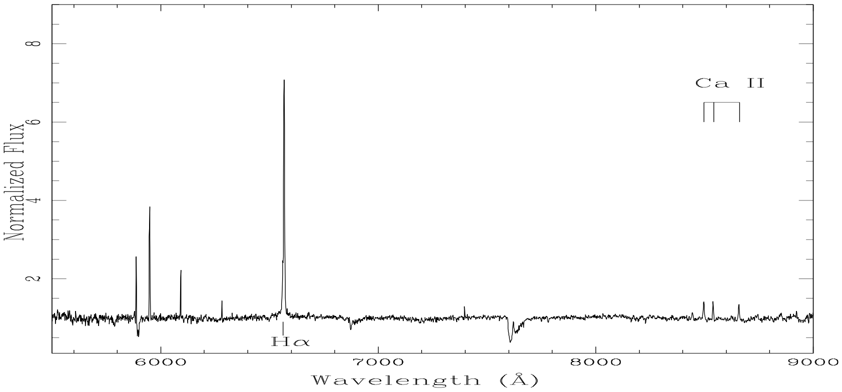

Figure A.23: Spectrum of LkHa 231.

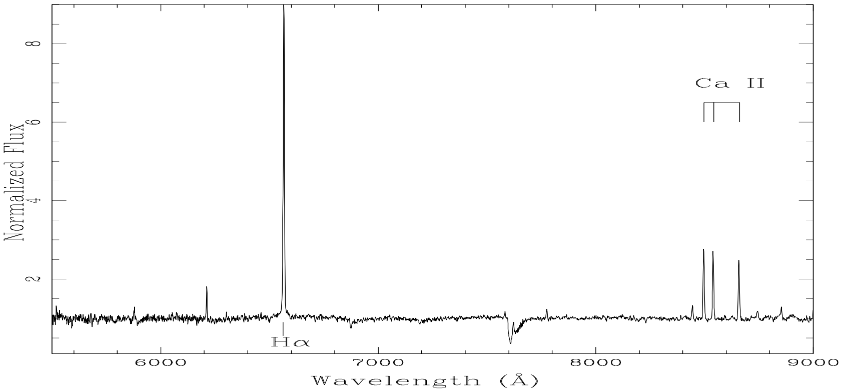

Figure A.24: Spectrum of LkHa 232.

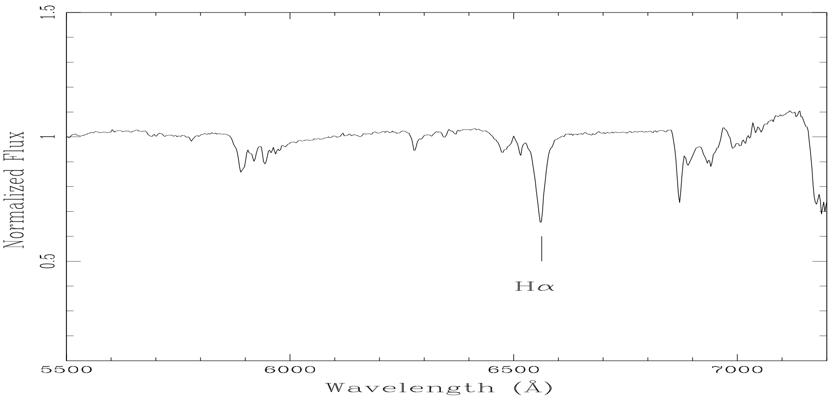

Figure A.25: Spectrum of Sao 53209.

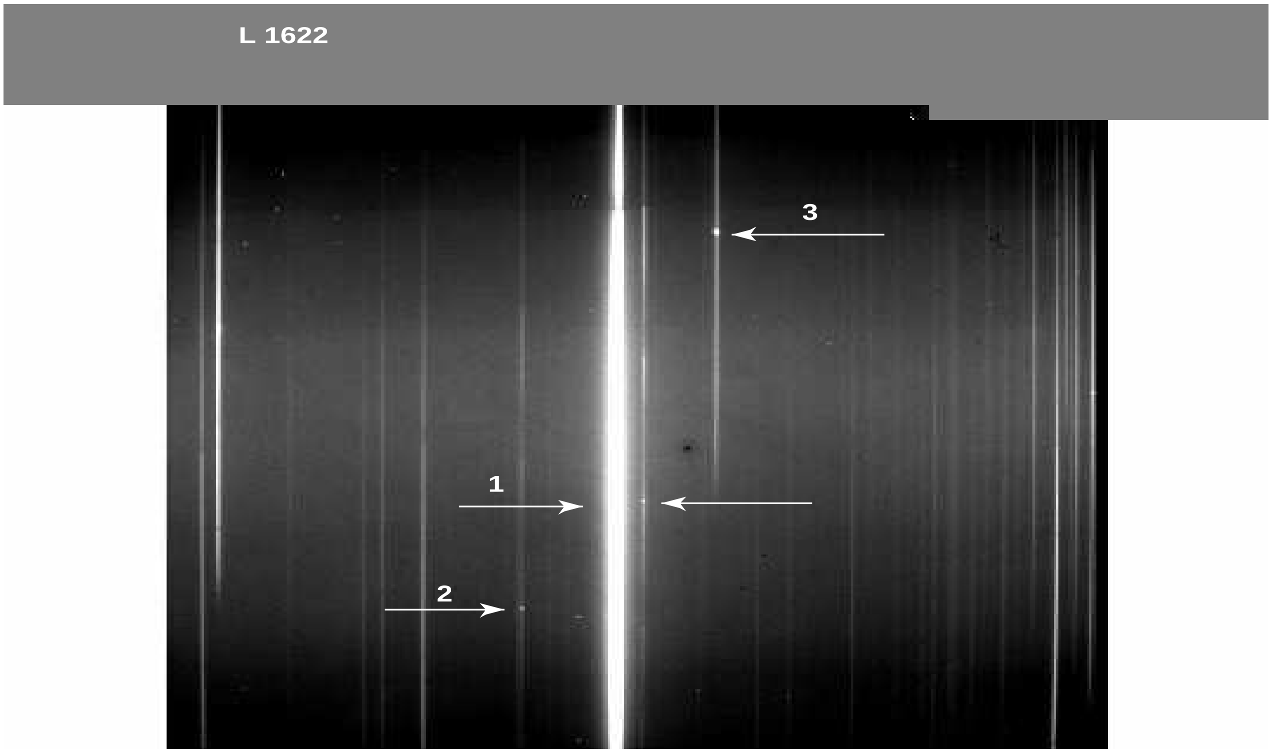

Figure A.26: Slit-less spectrum of field containing L1622 star 1. Numbers are same as in Figure 3.6.